University of Rijeka
Faculty of Civil Engineering

Nina Čeh

A Contribution to Dynamic Characterisation of Ordered Blocky Systems

Doctoral Thesis

Rijeka, 2018

University of Rijeka
Faculty of Civil Engineering

Nina Čeh

A Contribution to Dynamic Characterisation of Ordered Blocky Systems

Doctoral Thesis

2013-2016

Supervisor: prof. dr. sc. Nenad Bićanić
Co-supervisor: prof. dr. sc. Gordan Jelenić

2016-2018

Supervisor: prof. dr. sc. Gordan Jelenić

Rijeka, 2018

2013-2016

Supervisor: prof. dr. sc. Nenad Bićanić
Co-supervisor: prof. dr. sc. Gordan Jelenić

2016-2018

Supervisor: prof. dr. sc. Gordan Jelenić

Doktorski rad obranjen je dana _____ na Građevinskom fakultetu Sveučilišta u Rijeci pod povjerenstvom u sastavu:

1. prof. dr. sc. Željana Nikolić, Sveučilište u Splitu, Fakultet građevinarstva, arhitekture i geodezije

2. prof. dr. sc. Ivica Kožar, Sveučilište u Rijeci, Građevinski fakultet

3. prof. dr. sc. Roberto Žigulić, Sveučilište u Rijeci, Tehnički fakultet

Acknowledgement

Veliko hvala...

mojim mentorima:
Nenadu, mentoru koji me uveo u svijet razigrane znanosti i znatiželje. Mentoru koji me naučio mnogo više od onoga što spada u domenu doktorskog studija i čiji jedinstven pogled na svijet i ljude nikada neću zaboraviti. Gordanu, mentoru koji je iznenada preuzeo ovo mentorstvo i imao stvarno velike cipele za popuniti, a čiju količinu podrške, razumijevanja i strpljenja svaki doktorski student može samo poželjeti.
Nenad i Gordan, jedina bolja opcija bi bila da ste me zajedno doveli do ovog cilja.

kolegama s Katedre za tehničku mehaniku - bolju radnu okolinu teško mogu zamisliti.

Nildi i Marini u referadi na ljubaznosti i neizostavnom osmijehu na licu.

svima vama koji ste uljepšali trenutke provedene na fakultetu: Sara, Maja, Edita, Leo, Paulo, Nino, Ivana, Miran, Tea.

svima vama koji ste smijehom, druženjem, glupiranjem i beskrajnim razumijevanjem uljepšali trenutke izvan fakulteta: Denia, Sanja, Olja, Tanja, Žigo, Kristina, Dani, Mario, Mateja, Tomislav, Zlatan, Fere, Mate.

mojim Čehovima:
Mama i tata, hvala vam na svemu u ovih 29 godina. Na potpori, savjetima, životnim lekcijama, veselom djetinjstvu, ljubavi, razumijevanju.
Ivan, hvala na inspiraciji, razgovorima, savjetima, ljubavi.
Čehovi, da ste bilo koju stvar učinili drukčije, danas ne bih bila ovdje gdje jesam.

Abstract

In this work, dynamic characterisation of blocky structures is investigated. First, rocking of blocks is investigated. By this model, the behaviour of historical monuments, dry-stones, blocks in nuclear power plants, and masonry structures after the failure of the mortar may be described.

Non-linear equations of motion are derived and solved numerically. The exact time of impact is detected and the kinematic contact conditions after the impact are derived. Experimentally obtained energy loss is introduced. The algorithm is validated using a specially designed set of experiments, which also represent benchmark cases for validation of rocking. Conditions for complete or partial overturning of a dual-block stack are investigated experimentally and numerically.

Second, organisation of an ordered multiple-block assembly inside a basin due to harmonic excitation is investigated. The parameters for detection of diverse modes of organisation and characterisation of undesirable events are defined from experimental observation.

Keywords: dynamic characterisation; blocky structures; single block; rocking, coefficient of restitution; overturning; dual-block stack; experimental validation; multiple-block assembly; shaking platforms; optical measurement

Prošireni sažetak

U ovom radu se istražuje dinamička karakterizacija blokovskih sustava. Ponašanje blokovskih sustava može opisati ponašanje povijesnih spomenika, suhozidanih konstrukcija, blokova u nuklearnim elektranama i zidanih konstrukcija nakon popuštanja veziva.

Najprije se istražuje ljuljanje samo jednog bloka pod utjecajem pobude baze na kojoj se blok nalazi. Nelinearne jednadžbe kretanja koje opisuju ljuljanje jednog bloka su izvedene i riješene numerički koristeći Newmarkovu metodu za numeričku integraciju i Newton-Raphsonovu metodu za iterativno rješavanje nelinearnih jednadžbi. Detektirano je točno vrijeme sudara između tijela, što omogućuje određivanje brzine i ubrzanja sustava neposredno prije sudara. Izvedene su i brzine neposredno nakon sudara iz uvjeta da je moment količine kretanja sustava tijekom sudara održan obzirom na točku koja predstavlja novi centar rotacije. Odnos između brzine neposredno prije i neposredno nakon sudara je definiran koeficijentom restitucije. Posebno osmišljenom i provedenom serijom eksperimentalnih ispitivanja slobodnog ljuljanja, uz pomoć sustava za beskontaktno optičko mjerenje pomaka i deformacija GOM Aramis i Pontos, dobivene su stvarne vrijednosti koeficijenta restitucije. Pokazano je da tako dobivene vrijednosti potvrđuju potrebu za korištenjem modificirane formule za izračun koeficijenta restitucije. Eksperimentalno dobivene vrijednosti su uvedene u numerički model. Algoritam je eksperimentalno potvrđen pomoću posebno osmišljenog skupa pokusa, koji također predstavljaju *benchmark* primjere za validaciju simulacija ljuljanja: ljuljanje (i prevrtanje) bloka prilikom konstantnog ubrzanja podloge određenog trajanja (provedeno na *air-track* uređaju), te ljuljanje (i prevrtanje) prilikom jednog vala sinusoidalnog ubrzanja podloge (provedeno na preciznoj potresnoj platformi Quanser ST-III).

Stupac koji se sastoji od dva bloka jednakih širina koji stoje jedan na drugome se prilikom ljuljanja može naći u osam različitih konfiguracija.

Nelinearne jednadžbe kretanja za ljuljanje u svih osam konfiguracija su izvedene iz Lagrangevih jednadžbi. Definirani su prelasci između konfiguracija, koji se događaju ukoliko su kinematički uvjeti za aktivaciju 'više' konfiguracije zadovoljeni, ili ukoliko je došlo do sudara između tijela u sustavu (ili između gornjeg i donjeg bloka ili između donjeg bloka i podloge). Na temelju navedenog je napisan numerički algoritam pomoću Newmarkove metode za integraciju i Newton-Raphsonove iterativne metode, te procedure za detektiranje točnog vremena svakog sudara između tijela. Brzine u sustavu nakon sudara su izvedene iz uvjeta da moment količine kretanja gornjeg bloka te moment količine kretanja cijelog stupca obzirom na točke koje predstavljaju centre rotacije nakon sudara moraju biti održani pri sudaru. Algoritam je eksperimentalno potvrđen serijom ispitivanja ljuljanja stupca od dva bloka prilikom jednog vala sinusoidalnog ubrzanja podloge. Uvjeti za potpuno (oba bloka) ili djelomično (samo gornji blok) prevrtanje stupca su istraženi numerički i eksperimentalno.

Stupac koji se sastoji od tri bloka je eksperimentalno ispitan na posebno osmišljenoj platformi za dvostruki impuls ROORI1 na Sveučilištu u Oxfordu. Ispitani su uvjeti (posebice vrijeme između dva impulsa pobude baze) pod kojima dolazi do prevrtanja samo najgornjeg bloka, dva gornja bloka i cijelog stupca.

Na kraju, istražena je organizacija uređene skupine od više blokova unutar posude prilikom horizontalne harmonijske pobude. Parametri za detekciju različitih oblika organizacije, periodično ponašanje te karakterizaciju nepoželjnih događaja, poput položaja težišta sustava te momenta inercije sustava s obzirom na težište, su definirani na temelju eksperimentalnih promatranja.

Ključne riječi: dinamička karakterizacija; blokovske konstrukcije; jedan blok; ljuljanje; koeficijent restitucije; prevrtanje; stupac od dva bloka; eksperimentalna validacija; skupina od više blokova; potresne platforme; optičko mjerenje.

Contents

Chapter 1

Introduction

1.1 Motivation

There is a number of structures that are inherently discontinuous, either as a matter of convenience (e.g. ease of construction in structural masonry [5] or dry stone walling [6]) or as a deliberate strategy to avoid extensive thermal stresses (e.g. graphite cores in Advanced Gas-cooled Reactors, AGR, in nuclear power plants [7]). Often these structures are organised as stacked and/or interlocked assemblies with a regular pattern and technologically intended gaps and clearances, allowing for limited sliding and rocking in between contacts during their dynamic response. Frequently, these structural assemblies represent by themselves a vital safety-critical component (or form a crucial part thereof) of an entire structural system and there is a growing need for methods capable to predict their behaviour under both static and dynamic (impact, seismic) conditions. This is particularly true with ageing and degradation of such systems (e.g. AGR cores), where the safety considerations with respect to their life extension may be paramount for the integrity assessment process of the entire plant operation. Moreover, some of the safety critical non-structural components (e.g. large control cabinets) need to be treated as un-anchored or partially anchored blocky structures in their seismic assessment. There is also a rising interest in utilising rocking as a means for seismic isolation of tall slender buildings [6].

Direct extension of the structural reliability and integrity assessment procedures developed for continuous structures to include also discontinuous structural assemblies is clearly not appropriate. Considerations of blocky systems therefore often rely on some form of a homogenisation technique (simplified or complex), leading to a whole series of equivalent nonlinear continuum models. Such idealisations then follow well established routes, developed for continuum structures and supported by a series of well recognised benchmarks, both computational and experimental. In particular,

the homogenisation process allows for a reasonably straightforward dynamic characterisation (e.g. spectral signature, eigenfrequencies and mode shapes for response spectrum techniques in earthquake considerations are easily evaluated) of systems which are in reality discontinuous, 'blocky' structures, for which no eigen-problem can be formulated.

Therefore, dynamic behaviour of continuous deformable structures can be a priori characterised for a given class of dynamic excitation functions. Seismic assessment procedures for such structures are well known and clearly provide extensive guidelines to be used in practical application.

In contrast, dynamic characterisation of discontinuous structures that consist of multiple rigid bodies that are not inter-connected is not investigated enough owing to the fact that the dynamic response of such structures is geometrically nonlinear and non-smooth.

The dynamic response and insight into the dynamic characterisation for two classes of discontinuous structures will be here investigated in more detail: rocking structures and confined ordered multiple-block assemblies. This work focuses on a class of blocky structures which are either designed with deliberate discontinuities or start to behave as such after the failure of a certain structural component. The structures chosen here are a single block or a stack of two or three blocks in rocking motion, and a confined multiple-block assembly, all subjected to an arbitrary horizontal base acceleration function.

1.1.1 Rocking and dynamic characterisation of blocky structures

Rocking in combination with sliding, jumping, sliding and jumping, deformable base, and 3D behaviour is already analysed in the literature (presented ij more detail later in Chapter 2). We re-visit the simplest model of pure rocking with only one degree-of-freedom (DOF) and check whether such model describes the experimentally obtained behaviour satisfactorily. The interest here lies in determining the influence of chosen parameters of a rocking system to its response.

There are three main reasons for our focus on this simple model problem:

1. A simple 1-DOF model that is properly validated experimentally enables us to use multiple runs of the model and provide a benchmark solution for further validation of simulation platforms based on more complex paradigms (such as the non smooth contact dynamics - NSCD - or discrete element method - DEM).

A number of such robust simulation platforms is still not fully validated (in particular for rocking motion) and a trusting simple numerical model provides a cheaper way to obtain a wide set of benchmarks in comparison to conducting experiments for each new case of interest.

2. Such validation model can simulate rocking due to an arbitrary base excitation which enables performing multiple runs with perturbation of system parameters, thus providing information about the effect of each parameter to the system's dynamic response. This leads to detecting parameters for dynamic characterisation of rigid blocky structures.

3. The simple 1-DOF model can be generalized to rocking of a stack comprising two blocks, which is a more complex dynamic problem and is rarely addressed in the literature. Such dual-block stack model enables determining the conditions for partial and total failure, and thus provides an insight into its dynamic characterisation.

1.1.2 Self-organisation

In other fields, research into dynamic behaviour and pattern formation of particulate systems has been widely studied for vertically excited constrained columns or containers of both loosely and densely packed granular materials, where the excitation frequency and the amplitude dependent free surface wave patterns and convection rolls have been observed (presented ij more detail later in Chapter 2).

In practical cases, where the ordered discontinuous block assemblies with clearances represent and form a meaningful structural system (often safety-critical, as in multi-block graphite cores) any a priori insight into dynamic sensitivities would be beneficial both in terms of safety assessment and in the design of scaled experiments, as they are usually very costly and time-consuming.

We intent to primarily experimentally address the periodicity in dynamic behaviour of horizontal assemblies consisting of a given number of blocks inside a basin subject to a harmonic excitation. The emphasis is put on detecting repeatable configuration patterns and presenting the system parameters which depict periodicity in such an assembly's behaviour.

1.1.3 Undesirable events

An undesirable event is characterised here as any configuration occurring during dynamic response of a structure which is unwanted and disrupts stability and/or Functionality of the structure. In terms of discontinuous blocky structures we address two classes of structures: a vertically standing block or a stack of blocks, and horizontally assembled group of blocks (resembling tiles).

Regarding the first class of blocky structures observed, an undesirable event can be overturning of a block or a stack consisting of multiple blocks. For a stack of multiple blocks it is important to distinguish between conditions that lead to partial overturning (where the upper blocks overturns, while the bottom block is stable) and total overturning (where the whole stack overturns).

Regarding the second class of blocky structures observed, an undesirable event can be a configuration that significantly differs from the initial configuration, such as a rarified or a densified configuration.

In both cases, a undesirable event can also be such dynamic response that produces a large number of impacts between bodies. The number of impacts can be related to material fatigue and failure, as well as the formation of cracks.

All the mentioned events can lead to an unsafe state of a structure, thus representing a situation that ought to be investigated in more detail and avoided if possible.

1.2 Hypotheses

There are two main hypotheses of this research.

The first hypothesis:
A classical rocking model (the so called inverted-pendulum model) with rotational degrees of freedom can satisfactorily describe rocking behaviour and predict failure conditions of a single block and a dual-block stack.

The second hypothesis:
The global parameters such as the moment-of-inertia index and the mass centroid position of a constrained ordered multiple-block assembly enable characterisation of the dynamic response of the assembly.

1.3 Objectives

The objectives of this research are:

1. Develop a numerical model of dynamic response of a rigid single-block and a dual-block system subjected to arbitrary ground acceleration function capable of simulating the physically attainable post-impact behaviours.

2. Define energy loss mechanism during rocking motion without sliding and jumping.

3. Characterise the dynamic stability and modes of overturning of a dual-block system with respect to its geometry and parameters of excitation.

4. Characterise the dynamic behaviour of a constrained ordered multiple-disc assembly.

5. Investigate scalability of failure mechanisms/undesirable events in dynamic response of ordered blocky systems.

Chapter 2

Literature review

2.1 Rocking

Rocking of rigid bodies is a vitally important mode of motion when describing behaviour of historical structures (such as monuments or drystone walls, where multiple rigid bodies are freely standing one on top of another) [6], graphite cores inside nuclear power plants (which consist of a large number of rigid bodies deliberately designed with gaps and clearances between them so that thermal expansion is enabled) [7], or masonry structural elements after failure of the binding component [5].

2.1.1 Analytical and numerical investigation

In-plane rocking motion was first addressed by Housner [1] fifty-five years ago. He gave the set of two analytical piece-wise governing equations of rocking motion of a single rigid rectangular block on a rigid base due to horizontal base excitation. The two equations of motion describe the rotation around the two bottom edges and a transition between these two motions happens when the block hits the base. He linearised the equations of motion and derived the conditions for overturning due to a constant acceleration, a sinusoidal acceleration, and an earthquake motion of the ground. In this seminal work he concluded that *the larger of two geometrically similar blocks is more stable than the smaller* (which he called the *unexpected scale effect*).

Scientists later dealt with the rocking problem by solving the equation of motion in its linearised [1, 8, 9, 10, 11, 12, 13] as well as fully nonlinear form using the state-space procedure and built-in ODE solvers [10, 11, 12, 13, 14, 15, 5, 16, 17].

The analytical conditions for minimum ground acceleration of a specific acceleration function necessary to overturn a single block obtained from the fully linearised

equation of motion were first given in [1], and later corrected using a more conservative condition in [8, 11, 12]. These conditions were limited to slender blocks with small rotations and to simple overturning cases without the impact with the base or with only one impact. Rocking motion (with or without additional degrees of freedom, such as jumping and/or sliding) was also modelled by means of the discrete element method (DEM) in [14, 18, 19] and the non-smooth contact dynamics (NSCD) in [20].

Following Housner's work, the analytical condition for initiation of rocking and the minimum ground acceleration of a specific acceleration function necessary to overturn a block have been further derived from the linearised equation of motion [21, 11, 12, 8, 1], while the fully nonlinear equation of motion using the state-space procedure and built-in ODE solvers has been addressed in [11, 12, 14, 15, 10, 22].

In an attempt to characterise rocking motion more completely, transient and steady-state dynamic response of a single rigid block due to earthquakes [8], random-noise excitations [23] and pulse-type excitations [15] have been investigated.

From a mathematical point of view, points of bifurcation during rocking motion and Poincare points in the phase-plane view were addressed in [24, 25, 26, 27]. The latter work showed that, while the results of rocking motion are usually depicted as time histories of the degrees of freedom and their time derivatives, the phase plane views alternatively represented a good insight into the overall rocking response (by clearly indicating periodicity and attractor points) [27, 4].

Regarding classical analytical approach to modelling rocking, the effect of size and slenderness on the overall dynamic stability of a rigid block was already briefly addressed in [1]. Further investigation of the scaling of rocking motion is presented in [6, 28, 29, 30].

The high sensitivity of the rocking response to the slenderness angle and to initial conditions (in terms of initial ideal verticality) was addressed in [29, 24, 31]. The authors in [29] concluded that *the stability of the block did not necessarily increase monotonically with the increasing size or decreasing slenderness ratio.*

The research on pure rocking was later broadened to models taking into account relative sliding with respect to the base [32] (and references therein), and jumping (detachment) of the block from the base [32] (and references therein), as additional degrees of freedom. Rocking, sliding and jumping were addressed in [9]. The states of rest, sliding, rotation, slide-rotation, translation-jump, and rotation-jump are all addressed in [32], as well as recently in [5]. The latter work concluded that the nonlinear effects were not negligible for a slenderness ratio lower than three.

In the recent years a 3D rocking model of a block on a deformable (modelled with concentrated spring at the corners, as well as with Winkler's spring model) base was introduced by [33].

2.1.2 Restitution and energy-loss

The conditions during the impact/contact between the block and the base were usually accounted for using classical Housner's approach of introducing an instant energy loss at the time of the impact by means of a coefficient of restitution [1] obtained from the angular-momentum balance as an upper limit on the actual physical restitution. Housner's restitution coefficient was not validated experimentally throughout the years. Most of the experiments conducted showed that in reality less energy is lost than Housner's model predicted [34, 35, 36, 37, 38, 39, 40, 41].

The coefficient of restitution was taken as suggested in [1] or calculated by fitting the numerically obtained curves to the experimentally obtained ones. In the past few years, researchers in [42] concluded that the physically attainable post-impact motions are rocking, bouncing, translation and jumping motion. Researchers in [43, 42] investigated these post-impact motions from the non-smooth-contact-dynamics point of view and tried to relate it to Housner's restitution during pure rocking. The said treatment of the contact problem belongs to the event-tracking time-stepping schemes which are based on accurate detection of contacts and description of changes in velocities and transitions between different motions [44]. The use of these schemes is justifiable in cases when a relatively small number of contacts is expected, such as rocking of systems consisting of small number of blocks.

In the recent years, a modified restitution formula was introduced independently in [2] and [3], which took into account the fact that the impact impulse may act at an arbitrary point along the contact between the block and the base, not necessarily at the very edge. The modified restitution showed to be larger than Housner's and as such more suitable for modelling the real rocking behaviour.

In addition, energy-loss in terms of damping proportional to the angular velocity is introduced in [23].

2.1.3 What about more than just a single block?

The attempts to generalise the equation of motion of a single rigid block to a stack of rigid rectangular blocks have not gone beyond the case of a two-block stack. For the two-block stack it becomes necessary to write eight different (sets of) equations

of motion that describe eight different possible configurations of such a system [4, 30, 45]. During rocking the two-block stack keeps switching between these eight configurations. So, the description of rocking motion of a two-block stack involves transitions between the configurations due to initiation of configurations [45], contacts closing, and impacts between bodies followed by further rocking [30, 45]. Overturning conditions of a two-block stack obtained from the linearised form of the equations of motion and for simple ground acceleration functions are given in [4, 46]. A number of numerical examples of dynamic response to ground acceleration are given in [30, 45, 4, 46], but without detailed presentation of the methods used for the numerical integration and iterative solution procedure.

The description of rocking of a three-block stack would require the total of 27 equations of motion to describe possible configurations [47] and would most certainly turn out to be too cumbersome for analytical treatment.

Beside that, rocking of a trilith structures (consisting of two slender vertically aligned blocks with a horizontal rigid body upon them) was analysed in [48, 6, 49].

2.1.4 Experiments

Experimentally, rocking behaviour is not easy to investigate and there has not been a wide set of experimental investigations dealing with rocking. Rocking of a single block was experimentally investigated in [50], and a stack of two blocks and a frame structure were addressed in [18]. Some experiments showed limited repeatability [51]. Motion of stacks of two and three blocks was measured by means of accelerometers in [14], and asymmetric single rocking block was experimentally tested in [10]. Experimentally, an insight into the sensitivity of rocking response to non-ideal initial conditions was given in [18] and restitution during rocking was discussed in [34, 35, 36, 37, 38, 39, 40, 41]. Another set of experiments was performed and compared to Housner's model earlier this year [41].

Shi et al. [10] conducted a more extensive experimental program, which was specifically focused on asymmetric blocks subject to sine pulses. They concluded two important things: that the vertical component of the ground motion plays far less important role in the overturning behaviour than the horizontal component, and that *the rocking response of rigid bodies subject to ground motion is quite different from the typical response associated with vibrations of elastic systems since the rocking frequency is a strong function of the rocking amplitude.*

A more extensive experimental research program is difficult to perform for the following reasons:

- it is difficult to ensure pure rocking behaviour with no sliding and/or jumping between the bodies,

- monitoring the dynamic behaviour has to be performed in a way which is not affecting the dynamic response (non-intrusiveness of the measurement, for example as suggested in [52]), especially for smaller-scale specimens,

- failure (defined as complete or partial overturning) has to be monitored as well, which can lead to measurement devices in contact with the specimens being broken (the continuity of the measurement).

For these reasons, there exists a clear need for well-documented experimental program of rocking benchmarks. In general, research aims in the past few years have moved from the description of dynamic response of nonlinear structures to a specific excitation to a more general prediction of overall response (and stability/failure) of structures to a class of excitation functions [28]. Based on an extensive numerical, analytical and experimental investigation of simple rocking structures, evidence based dynamic characterisation of such structures should be performed.

2.2 Self-organisation

Confined ordered multiple-disc assemblies make a model to describe of the behaviour of engineering structures classified as discrete with deliberate gaps or clearances such as dry stone walls or graphite cores in nuclear power plants [7]. These assemblies are frequently constrained within a certain container system, thus subject to the container movement. Furthermore, the dynamic behaviour of these assemblies involves both changing contact conditions among themselves and with the confinement. Such ordered discontinuous systems cannot be a priori characterised using an eigenvalue analysis, and there is a need for better understanding of their dynamic response.

The dynamic behaviour of granular systems has been researched by studying vertically excited constrained columns of granular material in [53, 54]. The authors have observed certain pattern formation in such systems and related them to the excitation parameters. These are not specifically ordered assemblies, and rearrangement and mixing of the large number of elements is both physically possible and allowed. Nevertheless, surface wave patterns and convection rolls have been observed . Based on this idea, a characterisation of the dynamic response of confined ordered assemblies, where rearrangement and mixing is not possible, could be performed.

The experimental research of confined ordered multiple-disc assemblies faces the same problems as experimental research of rocking (with the exception of the need to ensure pure rocking) and a thorough and well-documented experimental analysis of such assemblies is still missing.

Chapter 3

Numerical analysis of a single block rocking

This chapter is partially based on the results and discussion from paper [55]:
Čeh, N., and Jelenić, G., "Rocking motion of a single rigid rectangular block - analysis of the block slenderness assumption", 8ᵗʰ International Congress of Croatian Society of Mechanics

A rigid rectangular block standing freely on top of a rigid horizontal base subjected to a base excitation in form of an acceleration function or to tilted initial conditions is analysed here. The block and the base are assumed to be completely rigid. The connection between the base and the block is such that no relative sliding or jumping (detachment) between the two can occur. This means that there is at least one contact point between the block and the base at any time.

3.1 Equation of motion

Dynamic behaviour of a single rigid prismatic block standing on a rigid base, with the assumption that friction between the block and the base is high enough to prevent sliding, was first described by Housner [1]. If sliding is prevented, a rigid block subjected to dynamic base excitation either moves translationally with the base or it rotates around one of its bottom corners.

For a relatively small base acceleration, the block will move along with the base without rocking.
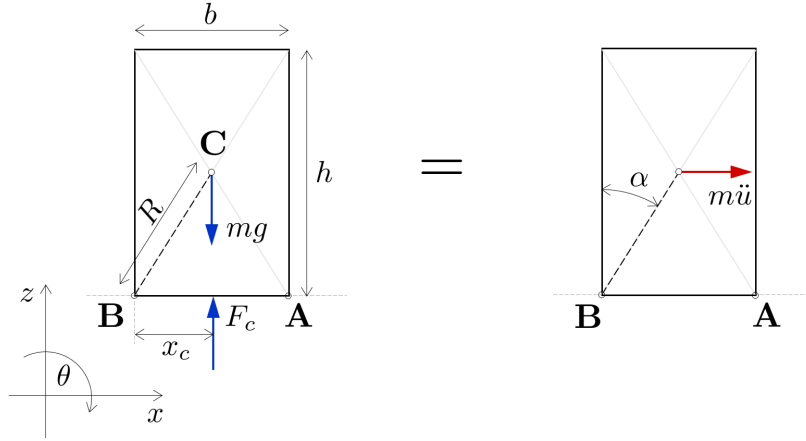
Figure 3.1: Free-body and mass-acceleration diagrams of block translating along with the base

From Figure 3.1 the equation of motion describing such behaviour follows as

$$\Sigma M_B = m\ddot{u}R\cos\alpha \tag{3.1}$$

or

$$mgR\sin\alpha - F_c x_c = m\ddot{u}R\cos\alpha, \tag{3.2}$$

where F_c is the vertical reaction from the base, x_c is the distance between the point at which the resultant reaction acts and edge B, m is the mass of the block, g is the gravity acceleration, $R = \frac{1}{2}\sqrt{h^2 + b^2}$ is the half-diagonal, $\alpha = \tan^{-1}\frac{b}{h}$ is the angle of slenderness of the block, and $\ddot{u}$ is the horizontal base acceleration function. In the limiting case, when the block is about to start rocking, $x_c \to 0$ and the corresponding ground acceleration $\ddot{u}_0$ is

$$\ddot{u}_0 = g\tan\alpha. \tag{3.3}$$

When the actual base acceleration $\ddot{u}$ becomes larger than $\ddot{u}_0$ rocking motion is initiated, which is described via (see Figure 3.2)

$$I_A\ddot{\theta} + mgR\sin(\alpha - \theta) + m\ddot{u}R\cos(\alpha - \theta) = 0 \tag{3.4}$$

and

$$I_A\ddot{\theta} - mgR\sin(\alpha + \theta) + m\ddot{u}R\cos(\alpha + \theta) = 0 \tag{3.5}$$

for $\theta > 0$ and $\theta < 0$, i.e. for rocking around corner A and rocking around corner B, respectively (see Figure 3.3). In the above equations $I_A = I_C + mR^2 = \frac{4}{3}mR^2$ is the moment of inertia with respect to one of the base corners, I_C is the moment of inertia with respect to its centre of mass C, and θ is the angle of rotation. The superimposed

14

dot and double dot indicate the differentiations with respect to time, i.e. the angular velocity $\dot{\theta}$ and the angular acceleration $\ddot{\theta}$.
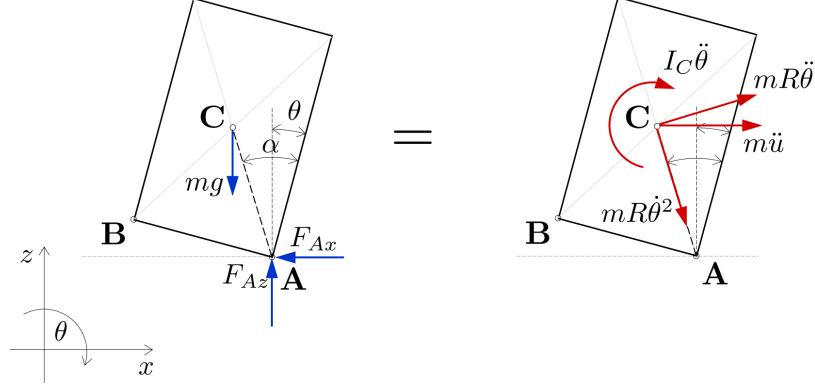
Figure 3.2: Free-body and mass-acceleration diagrams of the block rocking around its contact point A $(\theta > 0)$ [1]
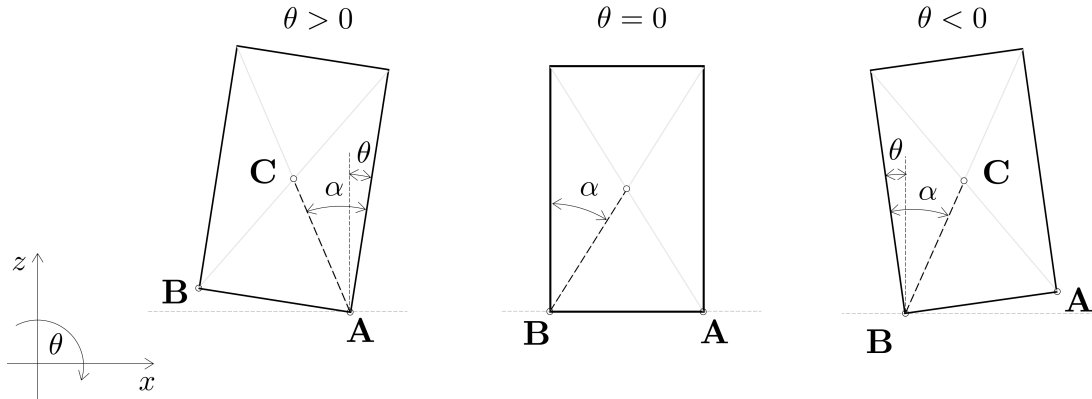
Figure 3.3: Three possible configurations during rocking

In order to use one equation to describe rocking in both directions, the following piece-wise governing equation is derived [28]:

$$I_A \ddot{\theta} \pm mgR \sin{(\alpha \mp \theta)} + mR\ddot{u} \cos{(\alpha \mp \theta)} = 0. \tag{3.6}$$

The ground acceleration function $\ddot{u}$ can be any arbitrary function. However, only a constant ground acceleration of finite duration

$$\ddot{u} = \begin{cases} a_0 & \text{if } t \leq t_a \\ 0 & \text{if } t > t_a \end{cases} \tag{3.7}$$

and a harmonic acceleration function

$$\ddot{u} = \begin{cases} a_0 \sin{(\omega t + \psi)} & \text{if } t \leq t_a \\ 0 & \text{if } t > t_a \end{cases} \tag{3.8}$$

15

with a_0 as the amplitude, ω as the natural frequency and ψ as the phase lag of the excitation will be analysed in this research.

If equation (3.6) is divided by I_A we get

$$\ddot{\theta} \pm p^2 \sin\left(\alpha \mp \theta\right) + p^2 \frac{\ddot{u}}{g} \cos\left(\alpha \mp \theta\right) = 0, \qquad (3.9)$$

where

$$p = \sqrt{\frac{mgR}{I_A}} = \sqrt{\frac{3g}{4R}} \qquad (3.10)$$

is the so-called frequency parameter of the block [1, 28].

When the block switches from the rotation around corner A to the rotation around corner B (or the other way around) it experiences an impact with the base. This impact is taken into account via a new quantity - coefficient of restitution - describing the energy balance during the impact. It is assumed that due to the impact between the block and the base there is an instant loss in kinetic energy, i.e. an instant loss in angular velocity of the block. A coefficient of restitution is usually defined as the ratio between the post-impact and the pre-impact kinetic energy or the squares of the post-impact and the pre-impact angular velocities

$$r = \frac{\left(\dot{\theta}^+\right)^2}{\left(\dot{\theta}^-\right)^2} \qquad (3.11)$$

where $\dot{\theta}^-$ and $\dot{\theta}^+$ are the angular velocities immediately before and after the impact. An alternative way to define the coefficient of restitution is

$$\eta = \frac{\dot{\theta}^+}{\dot{\theta}^-}, \qquad (3.12)$$

where the restitution is defined as the ratio between the post-impact and the pre-impact angular velocities, rather than the ratio between the post-impact and the pre-impact kinetic energies. The coefficient of restitution given in equation (3.12) is used in this work.

3.1.1 Quasi-linear equation of motion

In the literature, a linearised version of equation (3.6) is often solved analytically [1, 28]. However, it is important to distinguish between two separate steps in the procedure of linearising this fundamental equation of motion. In the first step, the sine and cosine functions in equation (3.6)

$$\sin\left(\alpha \mp \theta\right) = \sin\left(\alpha\right)\cos\left(\theta\right) \mp \cos\left(\alpha\right)\sin\left(\theta\right) \tag{3.13}$$

and

$$\cos\left(\alpha \mp \theta\right) = \cos\left(\alpha\right)\cos\left(\theta\right) \pm \sin\left(\alpha\right)\sin\left(\theta\right), \tag{3.14}$$

can be substituted with the following if the block experiences small rotations (i.e. if $\sin\theta \to \theta$ and $\cos\theta \to 1$):

$$\sin\left(\alpha \mp \theta\right) = \sin\left(\alpha\right) \mp \theta\cos\left(\alpha\right) \tag{3.15}$$

and

$$\cos\left(\alpha \mp \theta\right) = \cos\left(\alpha\right) \pm \theta\sin\left(\alpha\right). \tag{3.16}$$

Equation (3.6) becomes

$$I_A\ddot{\theta} \pm mgR\left(\sin\alpha \mp \theta\cos\alpha\right) + m\ddot{u}R\left(\cos\alpha \pm \theta\sin\alpha\right) = 0 \tag{3.17}$$

which can also be written as

$$I_A\ddot{\theta} = mR\theta\left(g\cos\alpha \mp \ddot{u}\sin\alpha\right) - mR\left(\pm g\sin\alpha + \ddot{u}\cos\alpha\right). \tag{3.18}$$

or

$$\ddot{\theta} - \left(\cos\alpha \mp \frac{\ddot{u}}{g}\sin\alpha\right)p^2\theta = -p^2\left(\pm\sin\alpha + \frac{\ddot{u}}{g}\cos\alpha\right). \tag{3.19}$$

In the above equation no limits are put on the geometry of the block, but it is still linear with respect to the unknown rotation θ. This equation will be referred to as the quasi-linear equation of motion of the rigid rectangular block.

3.1.2 Linearised equation of motion

In the second step, assuming that the block is slender (the angle of slenderness, α, is small) and the rotations are also small, equation (3.18) further simplifies to the following form:

$$I_A\ddot{\theta} = mgR\theta \mp mR\ddot{u}\theta\alpha \mp mgR\alpha - mR\ddot{u}, \tag{3.20}$$

where the product $\alpha\theta \to 0$. Equation (3.20) divided by I_A becomes

$$\ddot{\theta} - p^2\theta = -p^2\left(\pm\alpha + \frac{\ddot{u}}{g}\right). \tag{3.21}$$

The above equation is a linear second-order non-homogeneous differential equation with constant coefficients.

3.1.3 Analytical solutions of the linearised equation of motion

3.1.3.1 Analytical solution for free rocking

Free rocking describes the situation when the block is initially tilted and left from a quiescent initial position. The analytical solution of differential equation (3.21) in case of free rocking with initial conditions at time $t = 0$ given as $\theta(0) = \theta_0$ and $\dot{\theta}(0) = 0$ is

$$\theta(t) = (\theta_0 - \alpha)\cosh(pt) + \alpha, \tag{3.22}$$

while its derivative with respect to time is

$$\dot{\theta}(t) = p(\theta_0 - \alpha)\sinh(pt). \tag{3.23}$$

From the analytical solution describing free rocking for slender blocks, a conclusion about the 'period of rocking' T can be derived. The period of rocking theoretically corresponds to four durations between the instant when the block is set in motion from the initially tilted position and the instant when the block impacts the base, i.e. $\theta \equiv 0$ at time $t = \frac{T}{4}$, provided there is no energy loss due to impacts. Introducing this condition into equation 3.22 gives [1]

$$\cosh\frac{pT}{4} = \frac{1}{1 - \frac{\theta_0}{\alpha}} \tag{3.24}$$

or

$$\frac{T}{4} = \frac{1}{p}\cosh^{-1}\left(\frac{1}{1 - \frac{\theta_0}{\alpha}}\right). \tag{3.25}$$

This indicates that the period of rocking depends on the initial rotation, i.e. on the initial amplitude of rocking. The relation between the non-dimensional period of rocking pT and the initial rotation normalised with respect to the angle of slenderness α for free rocking is shown in Figure 3.4. Under the kinematic conditions considered (no sliding or bouncing at the time of contact), however, the kinetic energy at impact is bound to decrease and T should never be understood as the real period of rocking. We may only claim that the right-hand side of equation (3.25) accurately defines the time elapsed from the beginning of motion until the first contact of the block with the base.
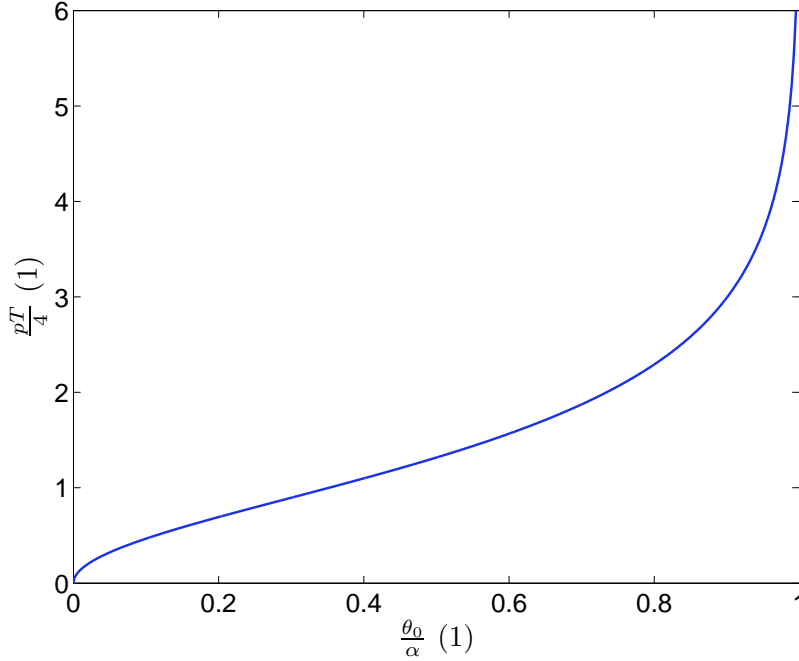
Figure 3.4: Period T and amplitude θ_0 of free rocking according to [1]

After the impact between the block and the base happens (at time $t = t_{imp}$), the solutions given in equations (3.22) and (3.23) are no longer valid. From $t = t_{imp}$ on the equation of motion (3.21) describing negative rotations should be linearised and solved, taking into account the initial conditions as $\theta(t_{imp}) = 0$ and $\dot{\theta}(t_{imp})$ calculated from equations (3.22) and (3.23). This procedure should be repeated after each subsequent impact between the block and the base in order to assess free rocking. Mathematically, this equation will never result in block settling to rest, the rotations will just decrease until they reach a value small enough that can be rounded as zero.

3.1.3.2 Analytical solution for forced rocking due to a constant acceleration function

Forced rocking describes the situation when the block is usually initially in its vertical position of static equilibrium and as such subjected to a ground acceleration function. When the value of the ground acceleration exceeds the limit value as described in equation (3.3) rocking is initiated.

Here the analytical solution of the linearised equation of motion (3.21) with a constant acceleration function as given in equation (3.7) is derived. This analytical solution with initial conditions at time $t = 0$ given as $\theta(0) = 0$ and $\dot{\theta}(0) = 0$ is

$$\theta(t) = \left(\frac{a_0}{g} + \alpha\right)[1 - \cosh(pt)], \tag{3.26}$$

19

and as its derivative with respect to time is

$$\dot{\theta} = -\left(\frac{a_0}{g} + \alpha\right) p \sinh\left(pt\right). \tag{3.27}$$

The derived analytical solution is valid for $t \leq t_a$ (provided no contact with the base has taken place before), after which the block enters in its free-rocking stage. During the free-rocking stage defined by the initial conditions $\theta\left(t_a\right)$ and $\dot{\theta}\left(t_a\right)$ calculated from equations (3.26) and (3.27) the solutions of equation (3.3) with $\ddot{u} = 0$ is

$$\theta\left(t\right) = \alpha\left[1 - \cosh\left(pt\right)\right] + \frac{a_0}{g}\left\{\left[\cosh\left(pt_a\right) - 1\right]\cosh\left(pt\right) - \sinh\left(pt_a\right)\sinh\left(pt\right)\right\} \tag{3.28}$$

and its derivative with respect to time is

$$\dot{\theta}\left(t\right) = -\alpha p \sinh\left(pt\right) + \frac{pa_0}{g}\left\{\left[\cosh\left(pt_a\right) - r\right]\sinh\left(pt\right) - \sinh\left(pt_a\right)\cosh\left(pt\right)\right\}. \tag{3.29}$$

It is important to notice that the solutions derived above for rocking with $\theta > 0$ due to a constant acceleration function of finite duration are valid until the impact of the block with the base occurs (at time $t = t_{imp}$). After the impact the block transitions into rocking with $\theta < 0$ and the linearised equation of motion (3.21) should be solved taking into account the proper sign with the initial conditions as $\theta\left(t_{imp}\right)$ and $\dot{\theta}\left(t_{imp}\right)$ calculated from equations (3.28) and (3.29).

3.1.3.3 Analytical solution for forced rocking due to a harmonic acceleration function

The analytical solution of the linearised equation of motion (3.21) with a harmonic acceleration function as given in equation (3.8) is also derived. With the initial conditions at time $t = 0$ as $\theta\left(0\right) = 0$ and $\dot{\theta}\left(0\right) = 0$ and assuming that $\psi = 0$ the rotation of the block is

$$\theta\left(t\right) = -\alpha \cosh\left(pt\right) - \frac{\omega p \frac{a_0}{g}}{\omega^2 + p^2} \sinh\left(pt\right) + \alpha + \frac{p^2 \frac{a_0}{g}}{\omega^2 + p^2} \sin\left(\omega t\right), \tag{3.30}$$

and its derivative with respect to time is

$$\dot{\theta}\left(t\right) = p\left[-\alpha \sinh\left(pt\right) - \frac{\omega p \frac{a_0}{g}}{\omega^2 + p^2} \cosh\left(pt\right) + \frac{\omega p \frac{a_0}{g}}{\omega^2 + p^2} \cos\left(\omega t\right)\right], \tag{3.31}$$

all valid for $t \leq t_a$ and $t \leq t_{imp}$, where t_{imp} is the time of the impact of the block with the base. This solution enables defining an analytical condition for overturning of the block due to the given base acceleration function during motion with positive rotation. Starting with the instant when the block hits the base and the block rotates

around the other corner, the above equation and its analytical solution do not longer apply. Provided this happens at time $t \leq t_a$, the differential equation such as equation (3.21), but with the signs corresponding to a negative rotation and initial conditions written at time of impact with the base, i.e. $\theta(t_{imp})$ and $\dot{\theta}(t_{imp})$ calculated from equations (3.30) and (3.31), can be likewise solved in order to obtain the analytical solution in that case.

3.1.4 Analytical solutions of the quasi-linear equation of motion

3.1.4.1 Analytical solution for free rocking

The analytical solution of equation (3.18) for free rocking ($\ddot{u} = 0$) with the initial conditions at time $t = 0$ as $\theta(0) = \theta_0$ and $\dot{\theta}(0) = 0$ is

$$\theta(t) = (\theta_0 - \tan \alpha) \cosh\left(pt\sqrt{\cos \alpha}\right) + \tan \alpha \tag{3.32}$$

and its derivative with respect to time is

$$\dot{\theta}(t) = (\theta_0 - \tan \alpha) p\sqrt{\cos \alpha} \sinh\left(pt\sqrt{\cos \alpha}\right), \tag{3.33}$$

which is valid until the impact between the block and the base occurs, i.e. for $t < t_{imp}$. After that, the corresponding quasi-linear equation of motion obtained from the equation with negative θ should be solved with initial conditions $\theta(t_{imp})$ and $\dot{\theta}(t_{imp})$ calculated from equations (3.32) and (3.33). This should be repeated at every subsequent impact between the block and the base until the blocks reaches small enough rotations which can be considered settling to rest.

3.1.4.2 Analytical solution for forced rocking due to a constant acceleration function

For a block subjected to a constant ground acceleration of finite duration as given in equation (3.7) the analytical solution of the equation (3.18) is

$$\theta(t) = \frac{\sin \alpha + \frac{a_0}{g} \cos \alpha}{\cos \alpha - \frac{a_0}{g} \sin \alpha} \left[1 - \cosh\left(pt\sqrt{\cos \alpha - \frac{a_0}{g} \sin \alpha}\right) \right] \tag{3.34}$$

and its time-derivative

$$\dot{\theta}(t) = -\frac{\sin \alpha + \frac{a_0}{g} \cos \alpha}{\cos \alpha - \frac{a_0}{g} \sin \alpha} \left[p\sqrt{\cos \alpha - \frac{a_0}{g} \sin \alpha} \sinh\left(pt\sqrt{\cos \alpha - \frac{a_0}{g} \sin \alpha}\right) \right], \tag{3.35}$$

for $t < t_a$. After the ground acceleration expires the block enters into its free rocking stage with the initial conditions at time $t = t_a$ for $\theta(t_a) = \theta_a$ and $\dot{\theta}(t_a) = \dot{\theta}_a$ calculated from equations (3.34) and (3.35). The solution for rotation of the block in this stage is

$$
\theta(t) = \left[(\theta_a - \tan\alpha)\cosh(rt_a) - \frac{\dot{\theta}_a}{r}\sinh(rt_a) \right]\cosh(rt)
$$

$$
+ \left[\frac{\dot{\theta}_a}{r}\cosh(rt_a) - (\theta_a - \tan\alpha)\sinh(rt_a) \right]\sinh(rt) + \tan\alpha, \quad (3.36)
$$

where $r = \frac{mgR}{I_A}\cos\alpha$, which is valid until the block hits the base and the edge acting as the centre of rotation has changed.

3.1.4.3 Forced rocking due to a harmonic acceleration function

In an attempt to derive an analytical solution of the equation of motion due to a harmonic acceleration function which is not limited to slender blocks but only to small rotations, i.e. the quasi-linearised equation of motion, equation (3.18) becomes

$$
\ddot{\theta} - \frac{mR}{I_0}\left[g\cos(\alpha) + a_0\sin(\alpha)\sin(\omega t) \right]\theta = -\frac{mR}{I_0}\left[g\sin(\alpha) - a_0\cos(\alpha)\sin(\omega t) \right],
$$

$$
(3.37)
$$

which is a second-order non-homogeneous differential equation with non-constant coefficients.

In general, the quasi-linear equation of motion can sometimes be applied to analyse the rocking behaviour of bulky blocks. However, overturning of bulky blocks occurs at large rotations (when $\theta \geq \alpha$) and we should hence bear in mind that the quasi-linear equation of motion is not applicable to assess rocking stability and overturning conditions of bulky blocks.

3.2 Numerical procedure

In order to find a solution for rocking of blocks or arbitrary geometry due to an arbitrary given ground excitation a numerical procedure based of solving the equations of motion is written in the programming environment Matlab. Both the linearised and the nonlinear equation of motion are discretised and integrated numerically using Newmark's formula for numerical integration. The fully nonlinear equation of motion (3.6) is solved at each time step using the Newton-Raphson iterative procedure. Furthermore, a contact detection algorithm is built into the numerical code. The procedures are described below.

3.2.1 Newmark's method and numerical solution of linearised equation of motion

Newmark's method of direct numerical integration of equation of motion for dynamic systems is one of the most general approaches for solving dynamic responses of structural systems. The most fundamental idea of direct integration methods, such as Newmark's method, is the attempt to satisfy dynamic equilibrium at discrete time steps after the solution has been defined at time zero [56].

Newmarks used Taylor's series to obtain two additional equations to the equation of motion [56]:

$$x_t = x_{t-\Delta t} + \Delta t \dot{x}_{t-\Delta t} + \frac{\Delta t^2}{2}\ddot{x}_{t-\Delta t} + \frac{\Delta t^3}{6}\dddot{x}_{t-\Delta t} + ... \tag{3.38}$$

and

$$\dot{x}_t = \dot{x}_{t-\Delta t} + \Delta t \ddot{x}_{t-\Delta t} + \frac{\Delta t^2}{2}\dddot{x}_{t-\Delta t} + ... \tag{3.39}$$

In the above equations x_t and $\dot{x}_t$ are the unknown displacement and velocity at time t, respectively, $x_{t-\Delta t}$, $\dot{x}_{t-\Delta t}$, $\ddot{x}_{t-\Delta t}$ and $\dddot{x}_{t-\Delta t}$ are the known displacement, velocity, acceleration and jerk at time $t - \Delta t$, respectively, and Δt is the size of the time step. Newmark truncated equations (3.38) and (3.39) and presented them in the following form [56]:

$$x_t = x_{t-\Delta t} + \Delta t \dot{x}_{t-\Delta t} + \frac{\Delta t^2}{2}\ddot{x}_{t-\Delta t} + \beta \Delta t^3 \dddot{x} \tag{3.40}$$

and

$$\dot{x}_t = \dot{x}_{t-\Delta t} + \Delta t \ddot{x}_{t-\Delta t} + \gamma \Delta t^2 \dddot{x}. \tag{3.41}$$

In the above equations β and γ are Newmark's integration parameters and $\dddot{x}$ is the jerk between time steps $t - \Delta t$ and t. If acceleration is assumed to be linear within

the time step [56], the following can be written:

$$\dddot{x} = \frac{(\ddot{x}_t - \ddot{x}_{t-\Delta t})}{\Delta t}. \tag{3.42}$$

The substitution of equation (3.42) into equations (3.40) and (3.41) gives Newmark's equations in standard form [56]:

$$x_t = x_{t-\Delta t} + \Delta t \dot{x}_{t-\Delta t} + \left(\frac{1}{2} - \beta\right) \Delta t^2 \ddot{x}_{t-\Delta t} + \beta \Delta t^2 \ddot{x}_t \tag{3.43}$$

and

$$\dot{x}_t = \dot{x}_{t-\Delta t} + (1 - \gamma) \Delta t \ddot{x}_{t-\Delta t} + \gamma \Delta t \ddot{x}_t. \tag{3.44}$$

Newmark's method with average acceleration inside every time step and integration parameters $\beta = \frac{1}{2}$ and $\gamma = \frac{1}{4}$ (the so-called trapezoidal rule) is used in this work. It is a single-step, implicit and unconditionally stable numerical method for linear problems [56].

Using Newmark's method of integration, equation of motion (3.20) can be numerically solved for each discrete time step. The time domain has to be divided into a number of discrete time steps. Equation (3.20) written at the end of a given time step n is:

$$I_A \ddot{\theta}_{n+1} - mgR\theta_{n+1} = \mp mgR\alpha - mR\ddot{u}_{n+1}. \tag{3.45}$$

Using Newmark's "d" approach and equation (3.43) in the form

$$\ddot{x}_t = \frac{x_t - x_{t-\Delta t} - \Delta t \dot{x}_{t-\Delta t} - \left(\frac{1}{2} - \beta\right) \Delta t^2 \ddot{x}_{t-\Delta t}}{\beta \Delta t^2}, \tag{3.46}$$

the angular acceleration ($\ddot{\theta}_i$, in equation (3.45)) can be written as

$$\ddot{\theta}_{n+1} = \frac{\theta_{n+1} - \theta_n - \Delta t \dot{\theta}_n - \left(\frac{1}{2} - \beta\right) \Delta t^2 \ddot{\theta}_n}{\beta \Delta t^2}, \tag{3.47}$$

which gives the following equation:

$$I_0 \frac{\theta_{n+1} - \theta_n - \Delta t \dot{\theta}_n - \left(\frac{1}{2} - \beta\right) \Delta t^2 \ddot{\theta}_n}{\beta \Delta t^2} - mgR\theta_{n+1} = \mp mgR\alpha - mR\ddot{u}_{n+1}. \tag{3.48}$$

In the above equation θ_n, $\dot{\theta}_n$ and $\ddot{\theta}_n$, the rotation, angular velocity and angular acceleration of the block at the beginning of the time step n are known, and θ_{n+1}, the rotation of the block at the end of the time step n, is the only unknown.

This procedure is used to integrate both the linear and the nonlinear equation of motion (the former is described above).

3.2.2 Newton-Raphson method and numerical solution of non-linear equation of motion

When the assumption of small unknown rotations are not justifiable, nonlinear equation (3.6) needs to be solved. In order to find a solution at each time step using Newmark's method of integration, equation (3.47) can be substituted into equation (3.6) to obtain equation:

$$F\left(\theta_{n+1}\right) \equiv \frac{I_A}{\beta \Delta t^2} \left[\theta_{n+1} - \theta_n - \Delta t \dot{\theta}_n - \left(\frac{1}{2} - \beta\right) \Delta t^2 \ddot{\theta}_n\right]$$
$$\pm mgR \sin\left(\alpha \mp \theta_{n+1}\right) + mR\ddot{u}_{n+1} \cos\left(\alpha \mp \theta_{n+1}\right) = 0. \quad (3.49)$$

The above equation is the nonlinear equation of rocking motion of a single rigid rectangular block with one unknown, rotation of the block at the end of the time step $n+1$, θ_{n+1}. To solve the nonlinear equation it is necessary to use an iterative procedure.

Newton-Raphson iterative method [57] is one of the methods used to find the roots of nonlinear equations. The method is based on the unknown solution which is expanded into Fourier series around the last known solution. All the higher-order terms in Fourier series are ignored, therefore the nonlinear function is approximated by a tangent between the last known solution and the first iteration of the new unknown solution (Figure 3.5).
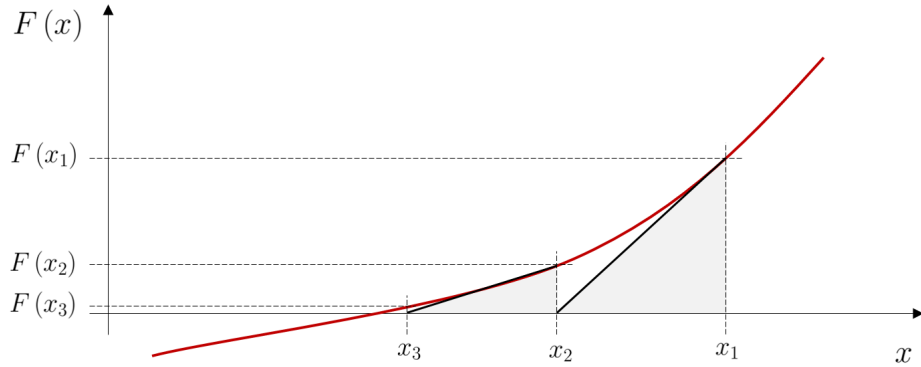
Figure 3.5: Newton-Raphson iterative method scheme

The Newton-Raphson iterative method has quadratic convergence [57], provided that the function is continuous and smooth within the reference interval (i.e. the function is two times differentiable with respect to the unknown variable).

When using the Newton-Raphson iterative method to solve the nonlinear equation (3.49), rotation, θ_1, and angular velocity, $\dot{\theta}_1$, are the input values at the first time

step. Angular acceleration, $\ddot{\theta}_1$, is calculated using equation (3.6). At every subsequent time step Newton-Raphson iterative procedure is used. For a given time step $n + 1$, the value of rotation in the first iteration is the converged rotation from the previous time step:

$$\theta_{n+1,1} = \theta_n. \tag{3.50}$$

Inside each iteration, j, the function $F(\theta_{n+1,j})$ given in equation (3.49) needs to be calculated. If the value of this function is lower than a given tolerance, *tol*, solution from the last iteration, $\theta_{n+1,j}$, is the value of the rotation at that time step, θ_{n+1}. Otherwise, the first derivative of the function $F(\theta_{n+1,j})$ with respect to the unknown $\theta_{n+1,j}$ needs to be calculated as:

$$F'(\theta_{n+1,j}) = \frac{I_0}{\beta \Delta t^2} - mgR\cos(\alpha \mp \theta_{n+1,j}) \mp mR\ddot{u}_{n+1}\sin(\alpha \mp \theta_{n+1,j}) \tag{3.51}$$

for every value of $\theta_{i,j}$.

In order to calculate the value of the unknown rotation $\theta_{n+1,j+1}$ in the next iteration $j+1$, the function $F(\theta_{n+1,j+1})$ given in equation 3.49) is expanded into Taylor's series:

$$\begin{aligned} F(\theta_{n+1,j+1}) = F(\theta_{n+1,j}) \\ + F'(\theta_{n+1,j})(\theta_{n+1,j+1} - \theta_{n+1,j}) + \frac{1}{2}F''(\theta_{n+1,j})(\theta_{n+1,j+1} - \theta_{n+1,j})^2 \\ + ... + \frac{1}{n!}F^{(n)}(\theta_{n+1,j})(\theta_{n+1,j+1} - \theta_{n+1,j})^n \equiv 0. \end{aligned} \tag{3.52}$$

If all the higher-order terms are ignored, Taylor's series results in a linear approximation of the function

$$F(\theta_{n+1,j+1}) = F(\theta_{n+1,j}) + F'(\theta_{n+1,j})(\theta_{n+1,j+1} - \theta_{n+1,j}), \tag{3.53}$$

or

$$F(\theta_{n+1,j+1}) = F(\theta_{n+1,j}) + F'(\theta_{n+1,j})\delta_j \equiv 0. \tag{3.54}$$

A correction of rotation, $\delta_{n+1,j}$, is, therefore, calculated as

$$\delta_{n+1,j} = -\frac{F(\theta_{n+1,j})}{F'(\theta_{n+1,j})}. \tag{3.55}$$

The new (improved) value of unknown rotation in iteration $j + 1$ is:

$$\theta_{n+1,j+1} = \theta_{n+1,j} + \delta_j. \tag{3.56}$$

The above procedure is repeated within each time step until the absolute value of the function $F(\theta_{n+1,j})$ becomes lower than the given tolerance. When this condition is satisfied the value of rotation at that time step is finally taken as $\theta_{n+1} = \theta_{n+1,j}$, and the iterative procedure continues with the next time step.

3.2.3 Contact detection procedure

To make the transition from one of the equations of motion to the other, which occurs when the block impacts the base without any constraint violation, it becomes important to detect the time of the contact precisely. Such treatment of the contact belongs to the event-tracking time-stepping schemes which are based on accurate detection of contacts (see e.g. [44]). The use of these schemes is justified in cases when a relatively small number of contacts is expected, such as rocking of a system consisting of a small number of blocks, where there is no risk of numerical inefficiency. At the same time, such contact treatment enables a detailed analysis of the energy-loss mechanism during contact.

We propose a technique in which the rotation at the end of a time step is monitored throughout the analysis for the change of sign. When such change is detected, say at a time t_{n+1}, the dynamic equilibrium over the time step is repeated for an *unknown modified time-step length* $\Delta t'$ under the condition that $\theta_{n+1} := 0$ in equation (3.49). Let us emphasize the fact that this equation is nonlinear with respect to the unknown $\Delta t'$ and needs to be solved iteratively, following the Newton-Raphson iterative procedure described in Section 3.2.2, but with $\Delta t'$ as the unknown instead of θ_{n+1}.

In the special case when $\ddot{u} = 0$ and the block is in free rocking we can obtain a quadratic equation with respect to the unknown $\Delta t'$, i.e. the following equation (obtained from (3.49) written at time instant $n+1$ taking into account the condition for zero rotation)

$$I_A \left[\frac{1}{\beta} \left(-\theta_n \right) - \frac{\Delta t'}{\beta} \dot{\theta}_n - \frac{\frac{1}{2} - \beta}{\beta} \Delta t'^2 \ddot{\theta}_n \right] + mRg\Delta t'^2 \sin\alpha = 0 \qquad (3.57)$$

needs to be solved for the unknown $\Delta t'$.

Following the condition that the unknown $\Delta t' \geq 0$ because it should belong to the interval $[0, \Delta t]$, the roots of the equation (3.57) are

$$\Delta t' = 2\frac{\dot{\theta}_n + \sqrt{\dot{\theta}_n^2 + \left(p^2 \sin\alpha - \ddot{\theta}_n \right) \theta_n}}{p^2 \sin\alpha - \ddot{\theta}_n} \qquad (3.58)$$

for $\theta_n > 0$ and

$$\Delta t' = 2\frac{-\dot{\theta}_n + \sqrt{\dot{\theta}_n^2 + \left(p^2 \sin\alpha + \ddot{\theta}_n \right) \theta_n}}{-p^2 \sin\alpha - \ddot{\theta}_n} \qquad (3.59)$$

for $\theta_n < 0$.

Once the modified time step size is calculated, the pre-impact (for time t^-) angular velocity, $\dot{\theta}^-$, and angular acceleration, $\ddot{\theta}^-$ are calculated using Newmark's scheme as

$$\dot{\theta}^- = \frac{\gamma}{\beta \Delta t'}(0 - \theta_n) - \left(\frac{\gamma}{\beta} - 1\right)\dot{\theta}_n - \left(\frac{\gamma}{2\beta} - 1\right)\Delta t' \ddot{\theta}_n \qquad (3.60)$$

$$\ddot{\theta}^- = \frac{1}{\beta \Delta t'^2}(0 - \theta_n) - \frac{1}{\beta \Delta t'}\dot{\theta}_n - \frac{\frac{1}{2} - \beta}{\beta}\ddot{\theta}_n. \qquad (3.61)$$

After the impact, the original time-step length Δt is restored and the time-stepping procedure switches to the other equation of motion. The initial post-impact acceleration $\ddot{\theta}^+$ is then calculated from the corresponding equation of motion. Before proceeding, however, the angular velocity $\dot{\theta}^+$ at the beginning of the first post-impact time step has to be determined, taking into account the coefficient of restitution as defined in equation (3.12). This coefficient of restitution is addressed in Chapter 4.

3.2.4 Numerical algorithm

The numerical algorithm based on the nonlinear equation of motion and following the explained approach is shown graphically in Figure 3.6.
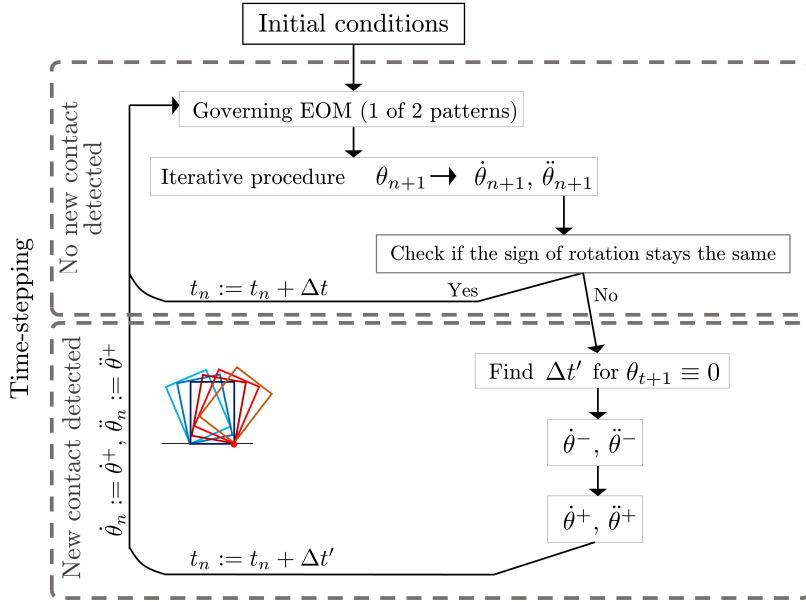

Figure 3.6: Algorithm for simulation of rocking of a rigid prismatic block

The numerical algorithm based on the linearised equation of motion follows the same flowchart, with the exception of the iterative procedure to find θ_{n+1}.

3.3 Numerical results

The Matlab codes are developed - based on the linearised equation of motion (referred to as linearised analysis), and the nonlinear equation of motion (nonlinear analysis) for the analysis of a single rigid rectangular block on rigid base subjected to horizontal base acceleration function.

3.3.1 Slender block

First, the analyses are carried out for a slender rigid block of width $0.06\ m$, height $0.27\ m$ and mass $2.5692\ kg$ (Figure 3.7, reffered to as B6L later in Chapter 4). The angle of slenderness of the block is $\alpha = 0.2187\ rad$, slenderness ratio is $\frac{h}{b} = 4.5$, half-diagonal is $R = 0.1383\ m$ and frequency parameter is $p = 7.2940\ \frac{rad}{s}$.
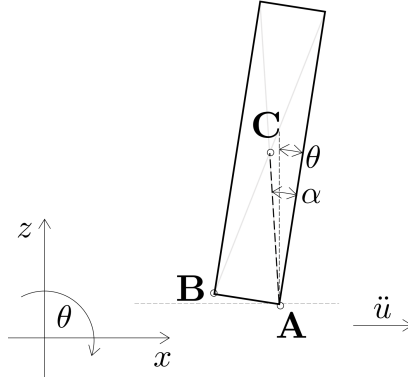
Figure 3.7: Slender rigid rectangular block analysed

3.3.1.1 Free rocking for $t \leq t_{imp}$

Rotation time histories during rocking of a slender block obtained from the solution of the linearised equation of motion (given in Section 3.1.3.1) and the numerically solved nonlinear equation of motion (described in Section 3.2) are shown in Figure 3.8 for rotation until the block impacts the base, i.e. for $t \leq t_{imp}$. Initial rotation of the block is $\theta_0 = 0.15\ rad$ here. The iterative procedure is carried out with the tolerance of the dynamic residual

$$|F\left(\theta_{n+1}\right)| \leq 1 \cdot 10^{-8}. \tag{3.62}$$

The numerical analyses are carried out with time step size $\Delta t = 1 \cdot 10^{-3}$ s.

Figure 3.8: Rotation time-histories of free rocking of a slender rigid rectangular block for $t \leq t_{imp}$ obtained from the linearised and the nonlinear analysis

A comparison between the results from the linearised and the nonlinear analysis shows that the nonlinear procedure results in barely noticeable larger periods of rotation than the linearised procedure. Periods of rocking are comparable to the results from the analytical solution of the equation of motion given by Housner [1] (Table 3.3.1.1):
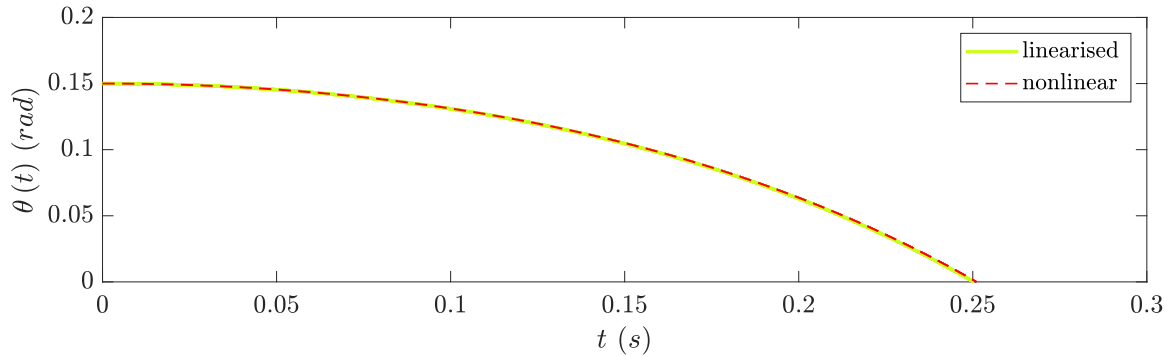
$$T_{Housner} = \frac{4}{p} \cosh^{-1} \left(\frac{1}{1 - \frac{\theta_0}{\alpha}} \right). \tag{3.63}$$

Calculation method	Marking	Value
Housner's solution [1]	$T_{Housner}/4$	0.2503 s
Nonlinear numerical analysis	$T_{nonlin}/4$	0.2510 s

Table 3.1: Rocking period using approximate analytical solution [1] and the nonlinear numerical analysis for a slender rigid block

The linearised analysis can obviously provide sufficiently accurate results for slender blocks.

3.3.1.2   Free rocking for $t > t_{imp}$

The comparison between the linear and the nonlinear solution is here continued after the block impacts the base. When such impact between the block and the base occurs, a decrease in the angular velocity of the block needs to be accounted for by a coefficient of restitution (as defined in equation (3.12)). All the analyses in this section are carried out using Housner's coefficient of restitution η_H [1], which is calculated from the angular momentum balance principle with respect to the point acting as the centre of rotation after the impact. This procedure is explained in more

detail in Chapter 4, which deals with restitution treatment. For the observed block the restitution coefficient is $\eta_H = 0.9294$.

First example shows the results from the linearised and the nonlinear numerical analyses for a rigid block with initial rotation $\theta_0 = 0,15\ rad$, which is approximately 69 % of the angle of slenderness α of the observed block (Figure 3.9). As seen in the previous section, the nonlinear solution tends to result in slightly longer periods of motion. Additionally, from Figure 3.9 is seems that more time is needed before the block reaches the state of rest. Mathematically, the block never really settles, but it actually experiences smaller and smaller rotations for an infinite time.
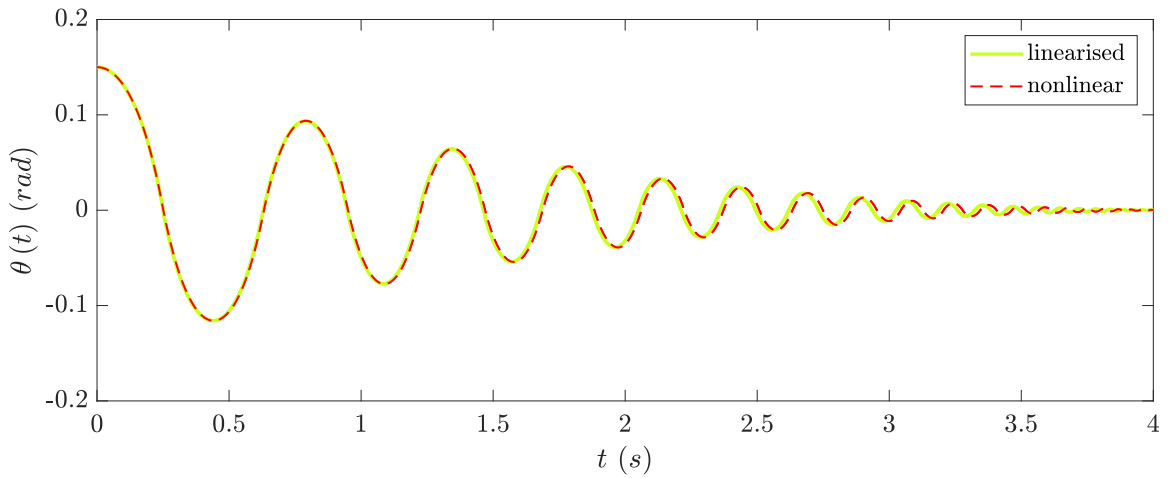
Figure 3.9: Rotation time-histories of free rocking of a slender block (linearised and nonlinear solution)

Furthermore, a phase plane view of the same motion, obtained from the nonlinear analysis, is given in Figure 3.10. A phase-plane view is obtained by tracing the points that mark angular velocity versus rotation in each time step. Such a view provides an easier insight into periodicity of rocking and existence of attractor points.
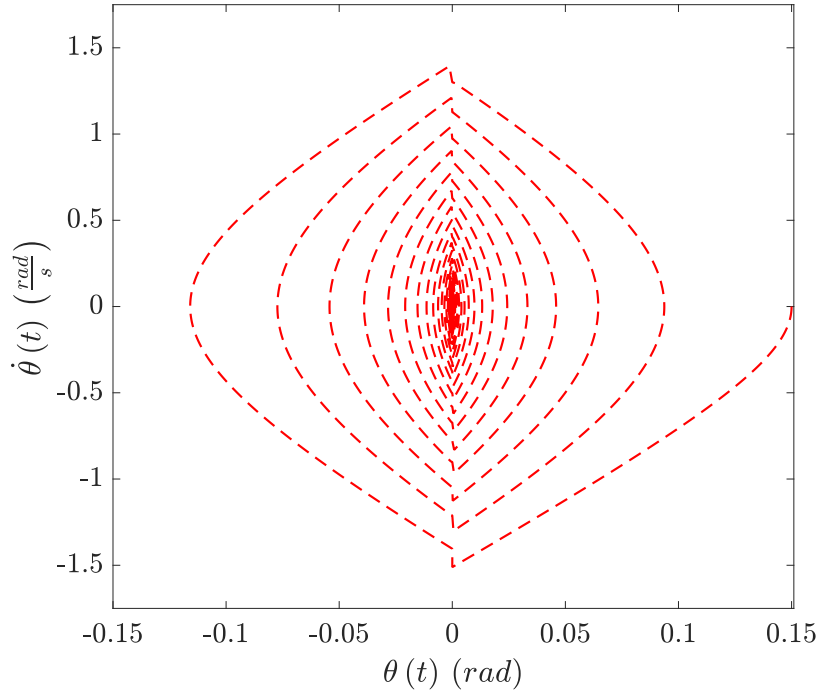
Figure 3.10: Phase plane view of free rocking of a slender block (linearised and nonlinear solution)

3.3.1.3 Forced rocking

Forced rocking is caused by a given dynamic excitation. Here it is considered that the rectangular block is subjected to either a single-wave or a lasting horizontal harmonic base acceleration function. The dynamic analyses are run for the rigid rectangular block specified earlier, which is initially ideally vertical and at rest, with η_H taken into account. The numerical analyses are again carried out with the time step size $\Delta t = 0.001 \ s$.

First, a series of analysis of overturning or stable rocking caused by a single-wave excitation function is run for 10 seconds, with excitation amplitudes ranging between $0.1g \tan \alpha$ and $10g \tan \alpha$ and frequencies ranging between $0.1p$ and $10p$. Overturning is characterised as the position when the block's vertical side hits the ground, i.e. when $\theta = \frac{\pi}{2}$. Stable rocking is characterised as any rocking where $\theta_{max} < \frac{\pi}{2}$ Figures 3.11 and 3.12 show these results obtained from the linearised and the nonlinear analysis.

Figure 3.11: Overturning/non-overturning area due to a single-wave sine excitation in the linearised analysis of a slender block

Figure 3.12: Overturning/non-overturning area due to a single-wave sine excitation in the nonlinear analysis of a slender block

The two analyses are now repeated for the same span of excitation amplitudes and frequencies but for the case when the excitation lasts during the full 10 seconds of the analysis. Figures 3.13 and 3.14 show these results obtained from the linearised
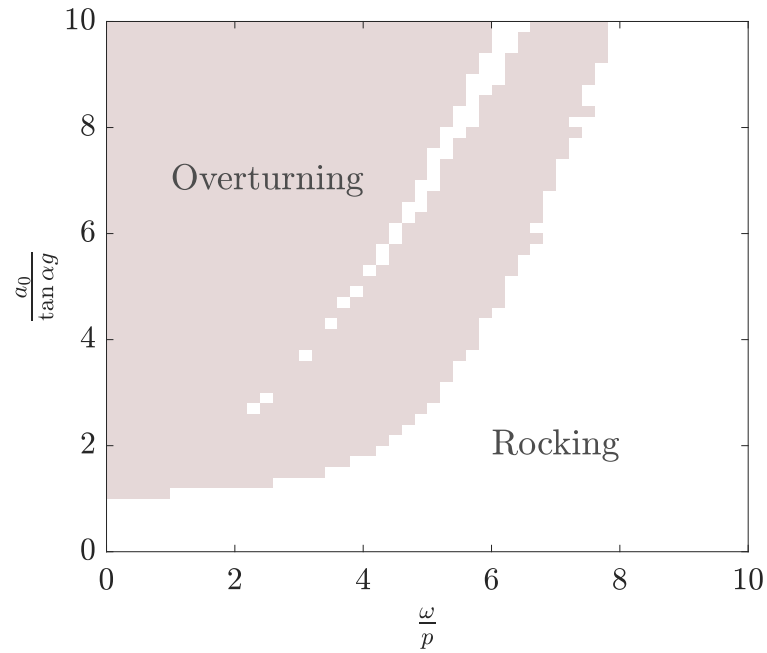
Figure 3.13: Overturning/non-overturning area due to lasting sine excitation in the linearised analysis of a slender block

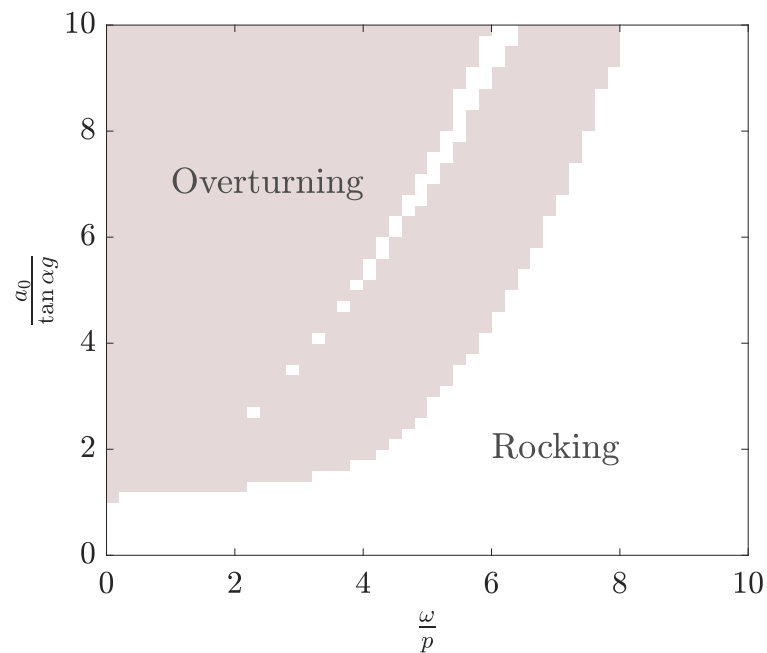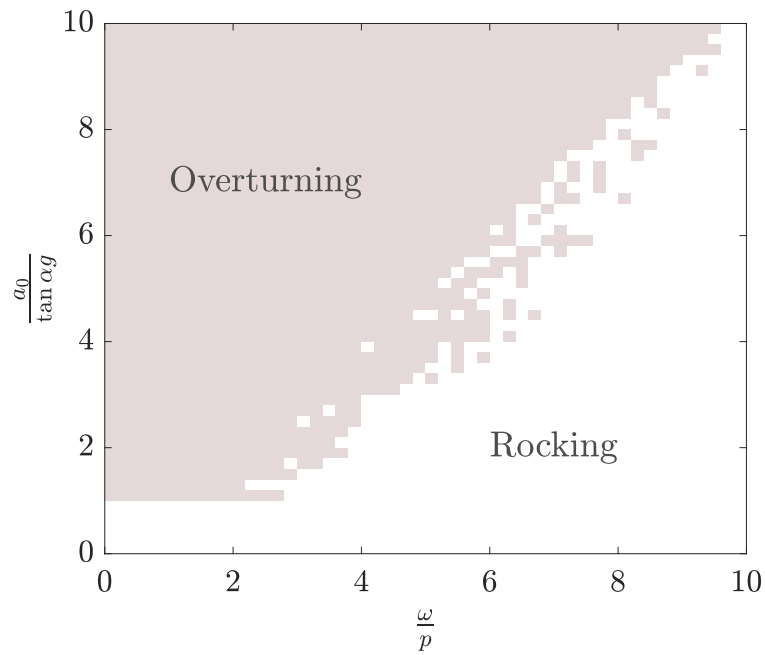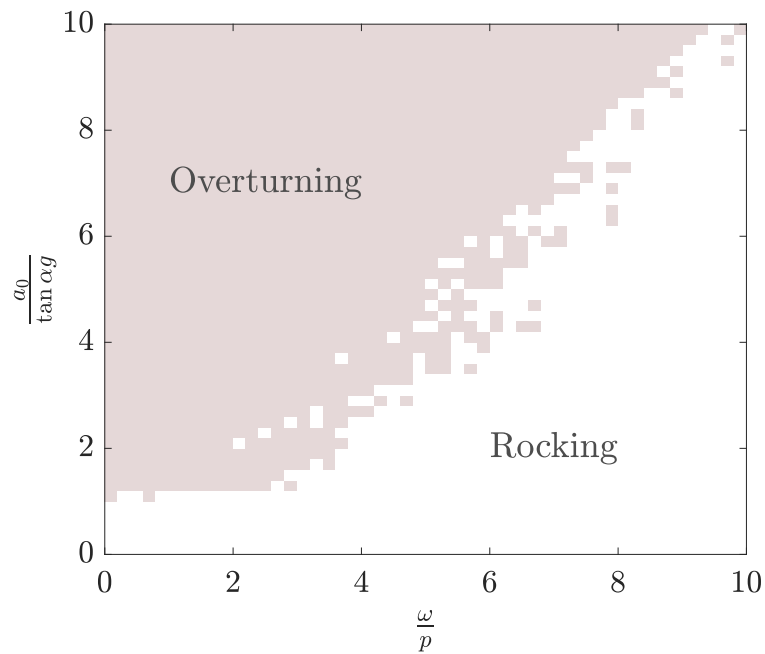and the nonlinear simulation procedure.

Figure 3.14: Overturning/non-overturning area due to lasting sine excitation in the nonlinear analysis of a slender block

Comparing the linearised and the nonlinear analysis for a single-wave excitation

(Figures 3.11 and 3.12), as well as the linearised and the nonlinear analysis for a lasting excitation (Figures 3.13 and 3.14), we see that the linearised and the nonlinear analysis results in similar overturning areas. Slight differences between the results obtained from the two analysis are visible, but in general even linearised procedure is sufficient to assess rocking stability of significantly slender blocks.

3.3.2 Bulky block

All the analyses carried out in the previous section have dealt with rigid rectangular blocks that can be considered slender. Blocks with slenderness ratio lower than 2.8 have large angle of slenderness according to [1], therefore they cannot be considered slender, and can experience large rotations even during stable rocking, while that certainly happens when they are close to overturning (i.e. when $\alpha \leq \theta \leq \frac{\pi}{2}$). Such blocks are referred to as bulky. It is expected that the linearised analysis of rocking of bulky blocks would show greater deviation from the nonlinear analysis than in the case of slender blocks.

All the analyses in this section are carried out for a bulky block with width 0.06 m, height 0.09 m and mass 0.8566 kg. The angle of slenderness of the block is $\alpha = 0.5880\ rad$, the slenderness ratio $\frac{h}{b} = 1.5$, the half-diagonal is $R = 0.0541\ m$ and the frequency parameter is $p = 11.662\ \frac{rad}{s}$.
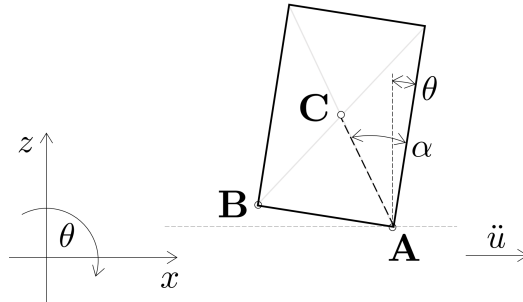
Figure 3.15: Model of the analysed bulky block

3.3.2.1 Free rocking for $t \leq t_{imp}$

First, rotation time histories during free rocking of the bulky block obtained from the analytical solution of the linearised equation of motion (given in Section 3.1.3.1) and from the numerical solution of the nonlinear equation of motion (described in Section 3.2) before the block impacts the base are given. The initial rotation here is $\theta_0 = 0.5$ rad. Again slightly larger period of rocking is observed in the nonlinear analysis than in the linearised analysis.
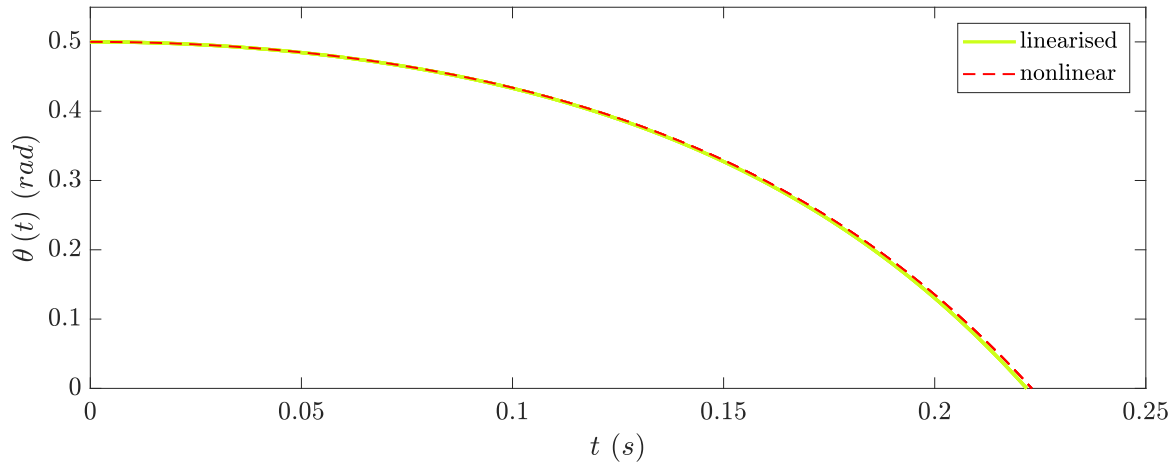
Figure 3.16: Rotation time-histories of free rocking of a bulky block for $t \leq t_{imp}$ obtained from the linearised and the nonlinear analysis

3.3.2.2   Free rocking for $t > t_{imp}$

The results from the linearised and the nonlinear numerical analysis of a bulky block rocking until settling to rest are shown here (see Figure 3.17). Housner's restitution is used in the procedure, which is $\eta_H = 0.5795$ for the observed bulky block. Initial rotation of the block is $\theta_0 = 0.5 \; rad$. The nonlinear numerical analysis (red dashed line in Figure 3.17) results in the period of rocking motion somewhat longer than in the linearised analyses (Table 3.3.2.2).
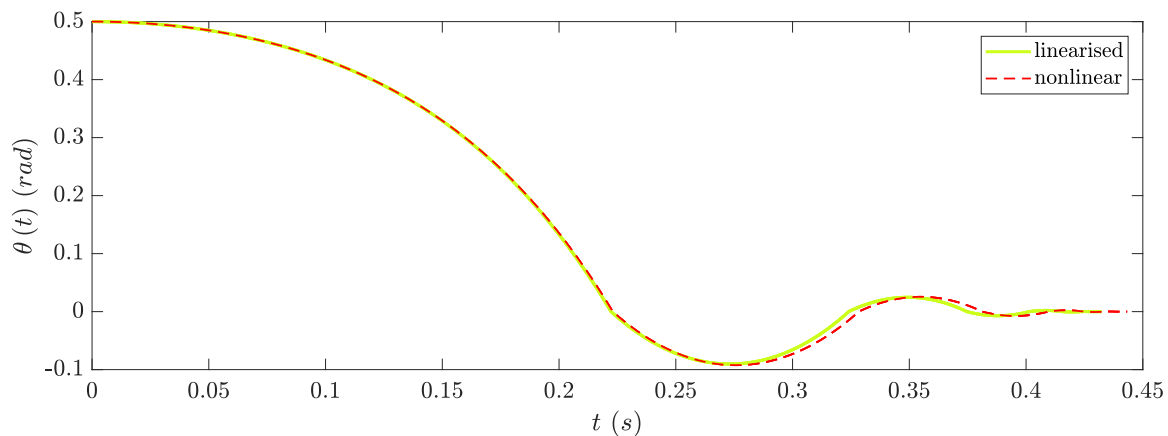
Figure 3.17: Rotation time histories of free rocking of bulky block (linearised and nonlinear analysis)

Phase plane view of free rocking of the bulky block obtained from the nonlinear analysis is shown in Figure 3.18.

36
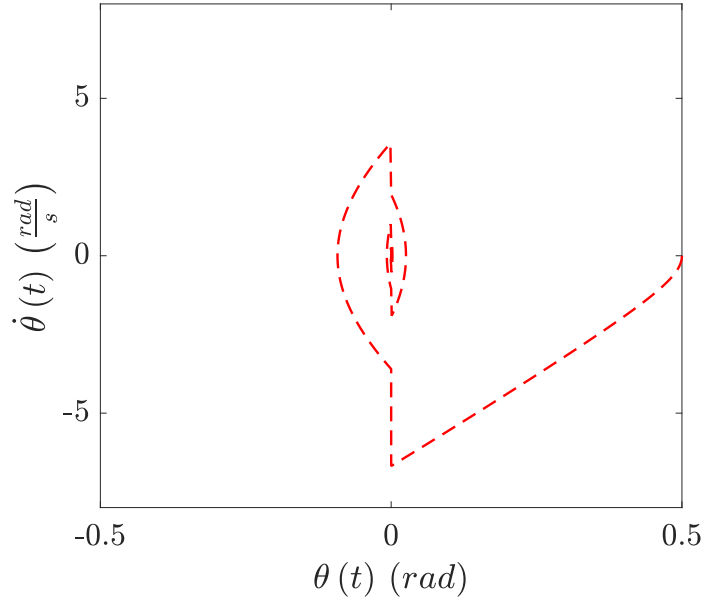
Figure 3.18: Phase plane view of free rocking of single block

Calculation method	Marking	Value
Housner's solution [1]	$T_{Housner}/4$	$0.2223\ s$
Nonlinear numerical analysis	$T_{nonlin}/4$	$0.223\ s$

Table 3.2: Period of free rocking using approximate numerical solution [1] and the nonlinear numerical analysis for non-slender rigid block

Considering the results shown above, it is expected that the difference between the linearised and the nonlinear solution will be significant when the bulky rigid block is subject to ground acceleration, too.

3.3.2.3 Forced rocking

A number of analyses of forced rocking of the bulky block carried out using the linearised and the nonlinear procedure show significantly different outcomes (overturning and non-overturning zones) obtained from the two different analyses.

Differences between the results of the linearised and nonlinear analyses can be easily noticed when monitoring a number of analyses against a maximum rotation (to indicate overturning) due to a single sine-wave horizontal harmonic base acceleration function with amplitudes between $0.1\alpha g\ \frac{m}{s^2}$ and $10\alpha g\ \frac{m}{s^2}$ and frequencies between $0.1p$ $\frac{rad}{s}$ and $10p\ \frac{rad}{s}$. Figures 3.19 and 3.20 show these results for the linearised and the nonlinear numerical analysis, respectively.
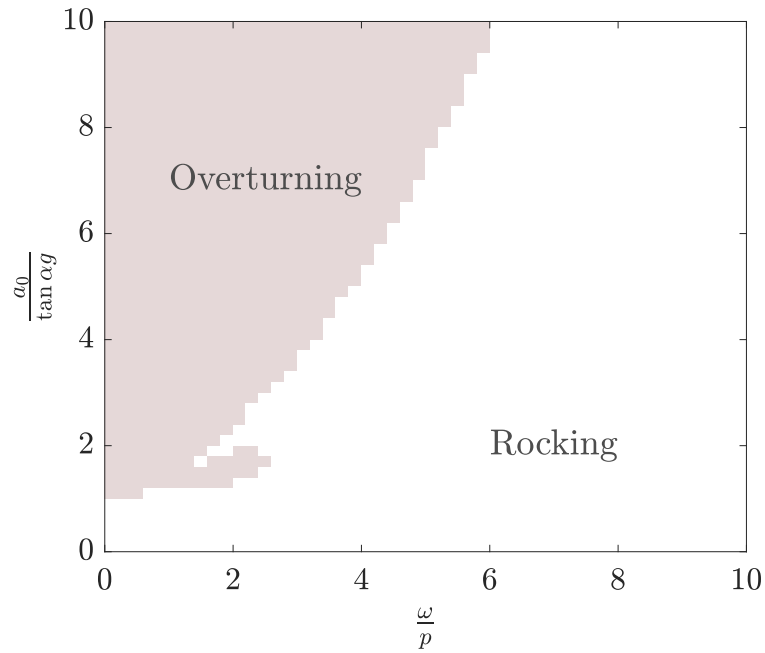
Figure 3.19: Overturning/non-overturning area due to a single-wave sine excitation obtained from the linearised analysis for a bulky block
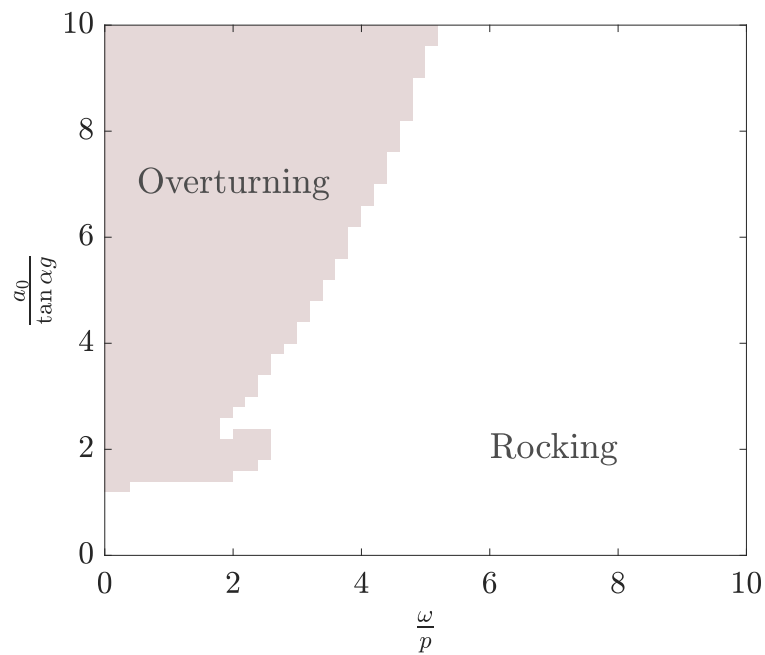
Figure 3.20: Overturning/non-overturning area due to a single-wave sine excitation obtained from the nonlinear analysis for a bulky block

The two analyses are now repeated for the same span of excitation amplitudes and frequencies but for the case when excitation lasts during the whole 10 seconds of

analysis. Figures 3.21 and 3.22 show these results for the linearised and the nonlinear numerical analysis during 10 seconds, respectively.
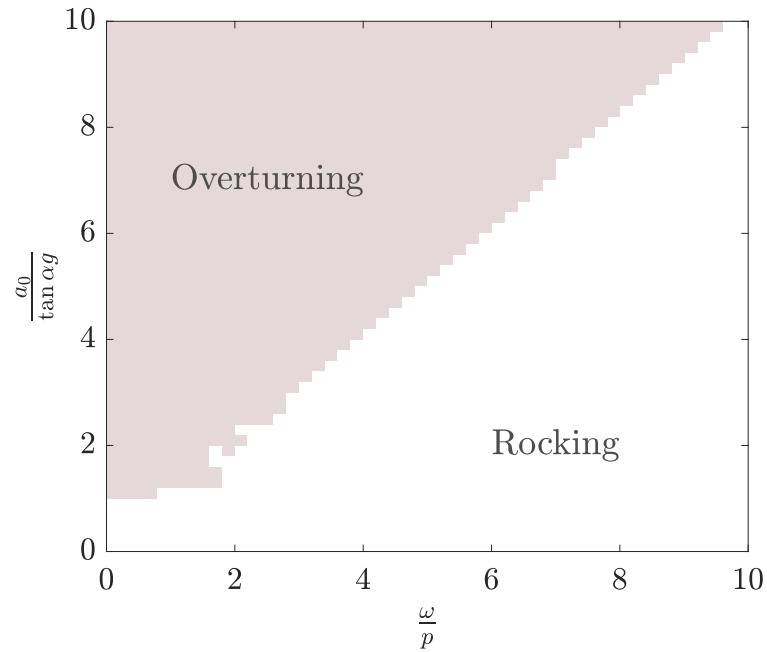
Figure 3.21: Overturning/non-overturning area during 10 seconds of the linearised analysis of rocking for a bulky block
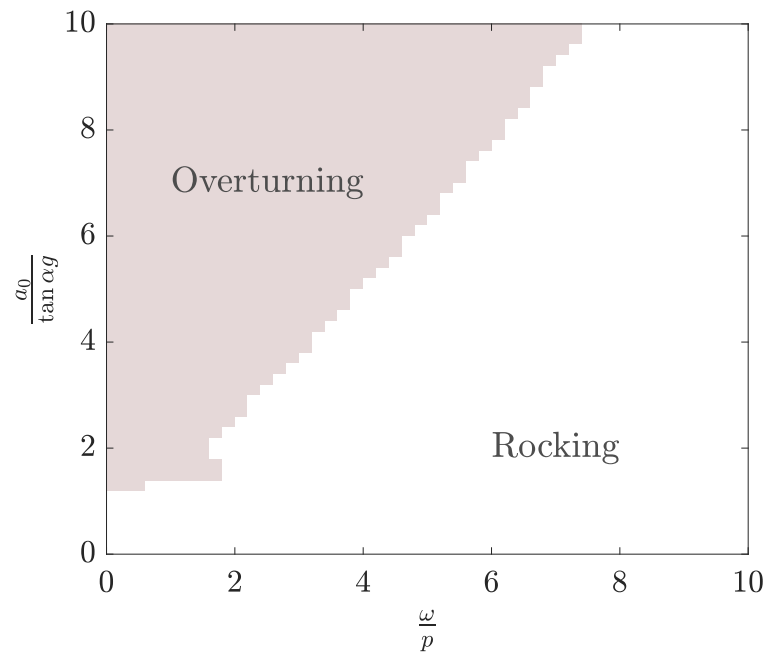
Figure 3.22: Overturning/non-overturning area during 10 seconds of the nonlinear analysis for a bulky block

In contrast to the slender block, a significantly narrower overturning area in the nonlinear analysis may be now observed, both for the single-wave excitation and for the excitation lasting throughout the analysis. This analyses carried out suggest that the linearised procedure in general underestimates the stability of the block.

3.4 Comparison of the linearised, the quasi-linear and the nonlinear analysis for different initial conditions

The linearised solution of equation of motion with the assumption that the block is slender is usually used in literature, even though there are cases when rotations and angle of slenderness (or both) should not be considered as small values. A solution based on these assumptions can be more or less accurate, depending on the initial conditions of the dynamic system.

When the value of $\alpha - \theta$ in the nonlinear equation of motion is initially really small (i.e. when block's initial rotation is close to the value of its angle of slenderness) the linearised equation of motion with the assumption that block is slender gives better results than the quasi-linear equation of motion with the bulky geometry of the block taken into account (Figure 3.23), even though the analysed block is bulky (with width $0.06\ m$, height $0.09\ m$ and angle of slenderness $0,5880\ rad$). Initial rotation of the block is $\theta_0 = 0.5\ rad$ and there is no acceleration of the base.
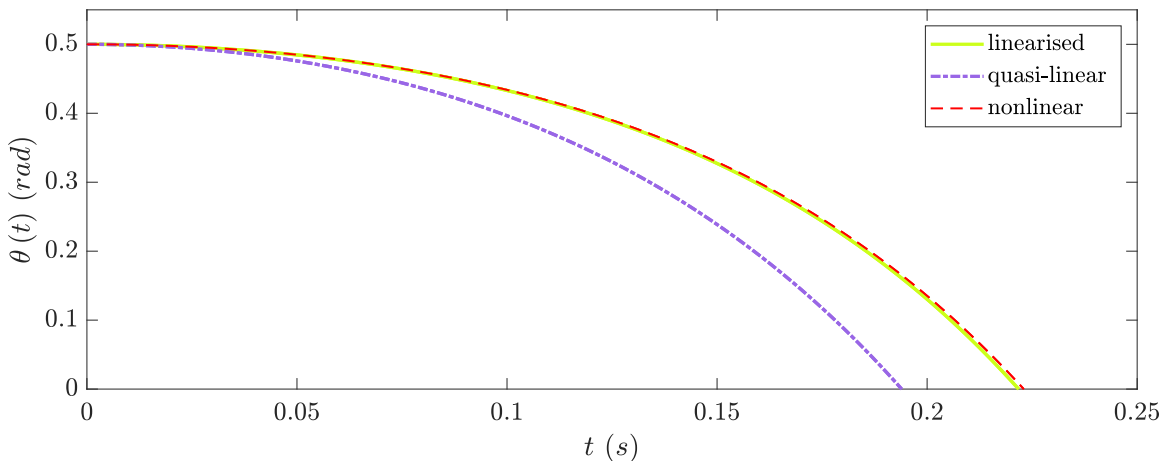
Figure 3.23: Rotation time-histories of free rocking of initially tilted bulky block for $t \leq t_{imp}$ ($\theta_0 = 0.5\ rad$)

In Figure 3.23 the analytical solutions of the linearised and the quasi-linear equation of motion are shown in green and purple, respectively. The analytical solution

of the linearised equation of motion is given in equation (3.22) while the analytical solution of the quasi-linear equation of motion is given in equation (3.32).

When the value of $\alpha - \theta$ is initially large (i.e. when a bulky block is initially slightly tilted) the quasi-linear equation of motion gives better results than the linearised equation of motion with the assumption that the block is slender (Figure 3.24). Initial rotation of the bulky block (with above stated dimensions) is $\theta_0 = 0.1\,rad$ here.
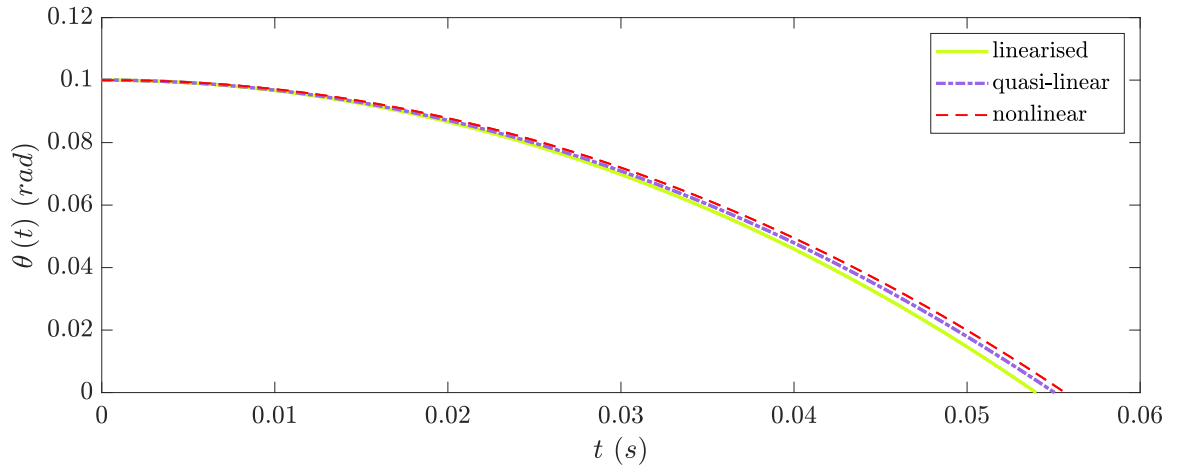
Figure 3.24: Rotation time-histories of free rocking of initially tilted bulky block for $t \leq t_{imp}$ $(\theta_0 = 0.1\,rad)$

The results presented in this section show that there are cases when the quasi-linear equation of motion gives better results for rocking of bulky blocks than the linearised equation of motion, as expected. However, that is true always when bulky blocks are observed. In conclusion, the fully nonlinear equation of motion, which takes into account the real geometry of the block via an arbitrary α and large rotations should be used to assess rocking stability of the block.

3.5 Sensitivity to perturbation of initial conditions to forced rocking

The sensitivity of the results to perturbation of initial conditions for a rocking block is discussed in [29]. This perturbation means that a really small initial angle is given to the block. This is an approximation used to model the case where the block is initially not ideally vertical due to an imperfection of its bottom surface or the base beneath it, or due to small fractions of dust or other material existing at the contact.

Clearly, this models appropriately only the case where the block overturns immediately (before an impact with the base) due to rotation in the same direction as the

initial tilt. If the initial tilt is in one direction and the block enters rocking, impacts the base and changes the edge acting as the centre of rotation, the imperfection causing the initial tilt would cause additional changes in the dynamic model, thus should be modelled differently.

The effect of perturbation of initial conditions on the dynamic response obtained from the numerical solution of the equation of motion is investigated here. The slender block with $h = 0.27\ m$, $b = 0.06\ m$ and mass $m = 2.5692\ kg$ is observed (the same as in Section 3.3.1).

Most dynamic (analytical and numerical) analyses of rocking of a rigid block in the literature are carried out with the assumption that the block is initially quiescent and ideally vertical ([28, 1, 11] and the references therein). These assumptions highly idealise the real situation in which the blocks can be, especially due to the fact that the ideal verticality can rarely be provided. This happens both with real structures as well as in the laboratory experiments. Aiming to assess the effect of small perturbations in initial verticality of the block to its rockign response, a study with a series of dynamic analyses of block's behaviour due to a single sine-wave harmonic ground excitation is carried out. The study is repeated for a range of excitation amplitudes a_0 ranging from $0.1g \tan \alpha$ to $10g \tan \alpha$ and frequencies ω ranging from $0.1p$ to $10p$ with different initial conditions, i.e. different initial tilt of the block $\theta_0 = (-0.05; -0.01; 0; 0.005; 0.01; 0.05)$ rad. This analyses show that small perturbations in initial conditions significantly affect the dynamic response and the overturning or stable rocking outcome. The rotation, angular velocity and angular acceleration time-histories are different when obtained from different initial tilt, but the more important are the significant differences in the overall outcome of the analyses (see Figure 3.25).
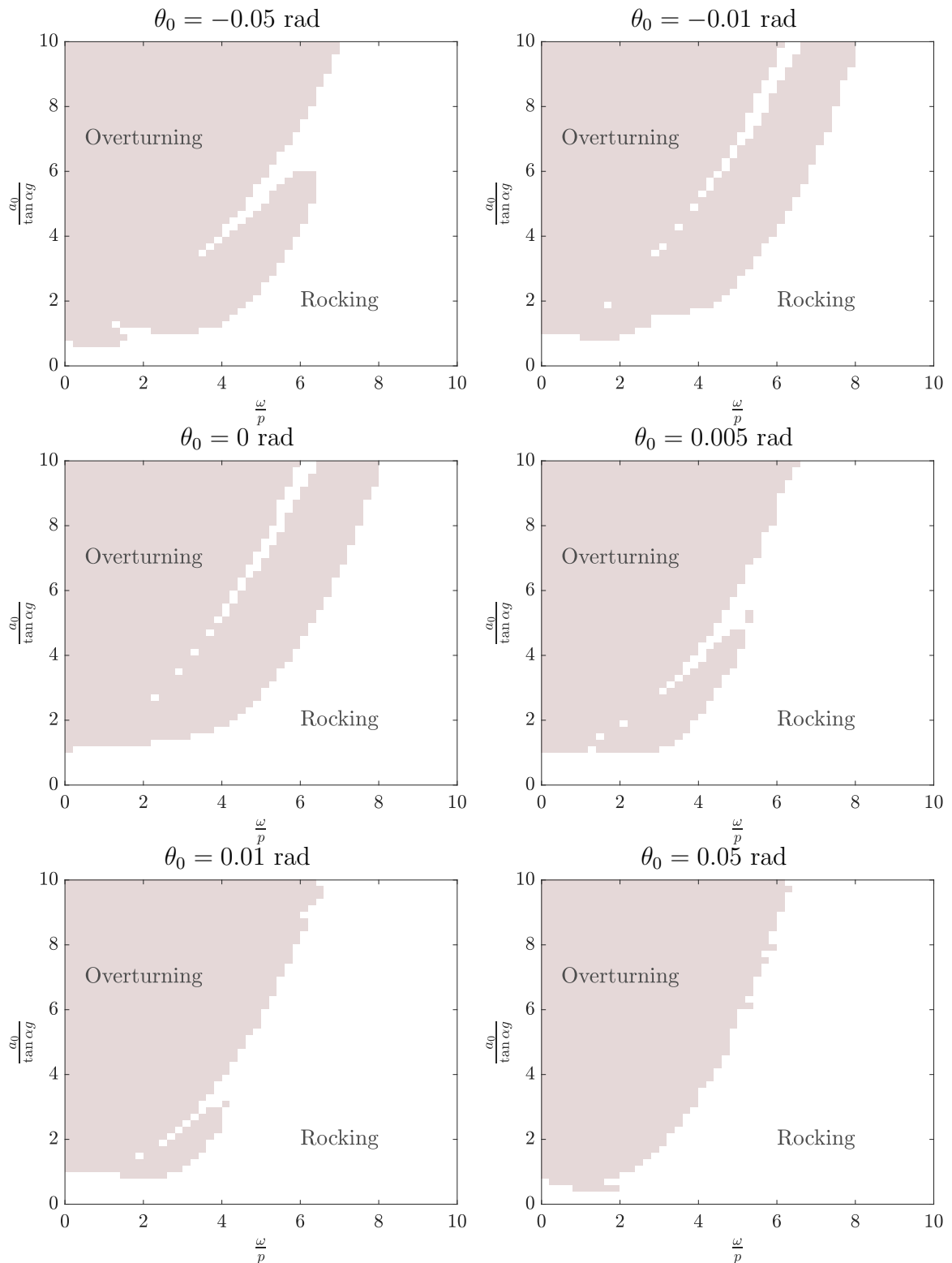
Figure 3.25: Overturning/non-overturning area depending on frequency and amplitude of ground acceleration function obtained during 10 seconds of nonlinear analysis of rocking motion of a slender rigid rectangular block with various initial rotation

The overturning area in Figure 3.25 expands in the direction of smaller amplitudes. In case of initially ideally vertical block the overturning area is bound by a line corresponding to the amplitude $a_0 = g \tan \alpha$, while when the block is initially slightly tilted lower excitation amplitudes can result in rocking and overturning. Furthermore, the boundary between the overturning and the non-overturning conditions changes significantly in the direction of higher excitation frequencies when a small perturbation in initial verticality is introduced.

The perturbation of initial verticality, as one of the fundamental assumptions usually introduced into the dynamic analysis in the literature, is an idealisation of the real state of a structure or a physical model. Here it is evident that really small perturbations of the initial position affect the dynamic response and the possibility of overturning. Perturbations up to 0.05 rad (nearly 2.86°) affect both the nature of the dynamic response and completely eliminate the safe area where the block should not event initiate rotating. Therefore, significantly lower amplitudes of the ground acceleration function than the limit value $g \tan \alpha$ can cause block to overturn if its initial position is not ideally vertical.

These conclusions represent an important issue which needs to be taken into account when it comes to designing laboratory experiments to validate the dynamic behaviour of rigid blocks, especially in terms of assuring the repeatability of the experiments.

3.6   Discussion and conclusion

Rocking of a single rigid rectangular block is investigated analytically where applicable (for slender block, as well as and for small rotations, regardless of the slenderness).

In order to be able to assess rocking of single blocks of any arbitrary geometry which can succumb large rotations, a numerical procedure based on the fully nonlinear equations of motion is developed. The dime domain is discretised and the equation of motion is written at a discrete time step, with the time-derivatives approximated using Newmark's integration formula. The nonlinear equation is solved at each time step using Newton-Raphson iterative procedure and the exact time of each contact of the block with the base is detected.

The differences between the obtained linearised and nonlinear (from the presented algorithm) rotation time-histories, as well as stability due to harmonic excitation, are presented. By comparing the results obtained from the linearised procedure with the results obtained from the nonlinear procedure, we come to a conclusion that

the nonlinear equation of motion provides a more suitable estimate of the rocking response of a single rigid rectangular block of an arbitrary geometry and is used in the rest of this research.

Furthermore, an assessment of rocking stability of a single block subject to a single-sine wave excitation with perturbation of the initial verticality of the block, we show that the rocking response is sensitive to such perturbation. This fact needs to be in mind when designing experiments.

Chapter 4

Restitution

This chapter is based on the results and discussion from paper [58]:
Čeh, N., Jelenić, G., and Bićanić, N., "Analysis of restitution in free rocking of single rigid rectangular block", submitted for publication

4.1   Impact of the block with the base

During rocking a block makes transition from rocking around one corner (for example corner A in Figure 3.2) to the other corner (for example corner B in Figure 3.2) and back. At every transition an impact between the block and the base takes place. During this impact the corner acting as the centre of rotation changes and the motion is described by a new governing equation of motion (either equation (3.4) or equation (3.5).

Due to the fact that no sliding or jumping (detachment) of the block from the base is allowed, a certain amount of kinetic energy is lost from the system at each impact and such a pure rocking is inherently a non-conservative dynamic problem. This statement is explained in more detail further on.

The energy loss at each impact is described using a coefficient of restitution defined as the ratio between either the post-impact and the pre-impact kinetic energy (as given in equation (3.11)) or the ratio between the post-impact and the pre-impact angular velocities (as given in equation(3.12)). The latter definition is used here.

4.2   Restitution models

Two different restitution models addressed in this work are presented below.

4.2.1 Housner's original restitution description [1]

Housner [1] obtained the coefficient of restitution using the angular momentum balance between the instant just before and immediately after the impact with respect to the corner which acts as the centre of rotation after the impact. He assumed that the resultant impact impulse acts at that edge. Based on the velocity plans shown in Figure 4.1, he obtained the angular momentum with respect to point A before the impact (at time t^-) as

$$J_A^- = I_C \dot{\theta}^- + m\dot{u}^- R \cos\left(\alpha + \theta^-\right) + mR^2 \dot{\theta}^- \cos^2\left(\alpha + \theta^-\right)$$
$$- mR\dot{\theta}^- \sin\left(\alpha + \theta^-\right) \left[b - R\sin\left(\alpha + \theta^-\right)\right], \quad (4.1)$$

and after the impact (at time t^+) as

$$J_A^+ = I_C \dot{\theta}^+ + m\dot{u}^+ R \cos\left(\alpha - \theta^+\right) + mR^2 \dot{\theta}^+. \quad (4.2)$$
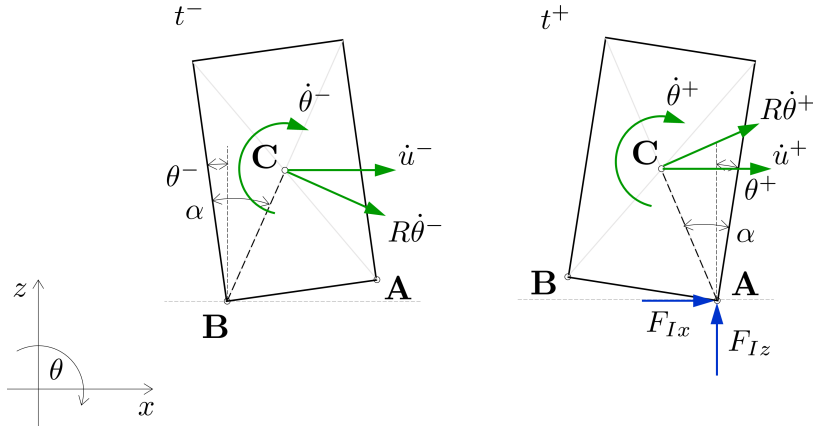
Figure 4.1: Pre-impact and post-impact velocity plans during transition from rocking around point B to rocking around point A

The momentum with respect to that point between the time instants just before and immediately after the impact must be conserved, i.e.

$$J_A^- = J_A^+, \quad (4.3)$$

and since $I_C = \frac{1}{3}mR^2$, $\dot{u}^+ \to \dot{u}^-$ and $\theta^+ \to \theta^-$ (both $\theta^- \to 0$ and $\theta^+ \to 0$), the coefficient of restitution $\eta_H = \frac{\dot{\theta}^+}{\dot{\theta}^-}$ [1] follows as

$$\eta_H = 1 - \frac{3}{2}\sin^2\alpha. \quad (4.4)$$

48

Housner's restitution coefficient depends only on the geometry, or rather slenderness, of the block and is the highest value of restitution coefficient possible in the considered model [1]. The real coefficient of restitution is to be lower that η_H due to material dissipation, deformation of the block and the base and other effects, which are not taken into account in the present rigid body rocking model.

The experimentally obtained results available in the literature [34, 35, 36, 37, 38, 39, 40, 41], however, show that Housner's model clearly underestimates the actual coefficient of restitution and thus overestimates the stability of the block, see also Figure 4.2 and Table 4.1.

Table 4.1: An overview of previously conducted experiments and the resulting restitution η_H

Reference	$\frac{h}{b}$	materials in contact	η_e	η_H
Muto et al., 1960 [39]	4.33	steel - wood	0.96	0.94
Ogawa, 1977 [34]	2	wood - steel	0.79	0.70
	3	wood - steel	0.88	0.85
	4	wood - steel	0.94	0.91
Aslam et al., 1980 [37]	4	concrete - steel	0.93	0.91
Pristley et al., 1987 [35]	2	concrete - aluminium	0.87	0.80
Lipscombe, 1990 [40]	4	steel - steel	0.92	0.91
Fielder et al., 1997 [38]	4	wood - aluminium	0.95	0.91
Pena et al., 2007 [36]	2.85	granite - granite	0.93	0.94
	4	granite - granite	0.94	0.91
	5.88	granite - granite	0.97	0.96
	8.33	granite - granite	0.98	0.98
Bachmann et al., 2017 [41]	6.67	aluminium - aluminium	0.98	0.97
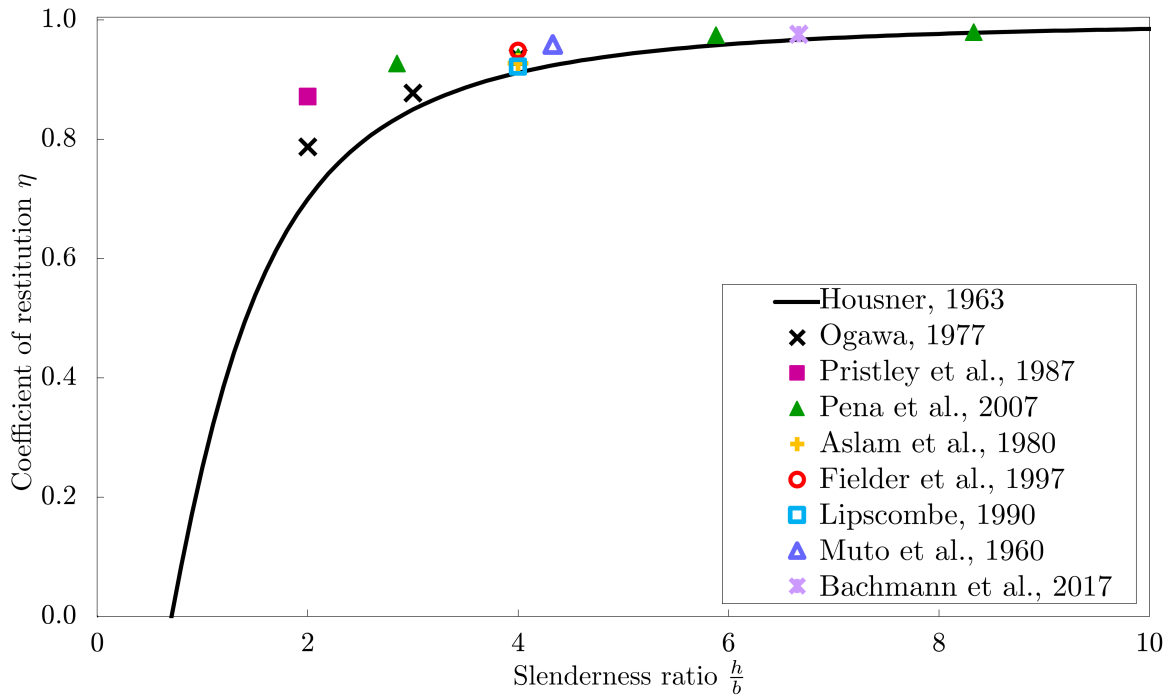
Figure 4.2: Coefficient of restitution from Housner's formula [1], and previous experiments [34, 35, 36, 37, 38, 39, 40, 41]

4.2.2 The improved restitution description [2, 3]

Addressing the fact that the experimental results showed that the widely used Housner's restitution tends to overestimate the energy loss and thus overestimate block's stability during an excitation, Kalliontzis et al. [2] and Chatzis et al. [3] independently introduced an improved coefficient od restitution. The work of Kalliontzis et al. [2] is followed here. They based their restitution formula on the observation that the resultant impact impulse can act at any point along the base of the block other than the corner point.
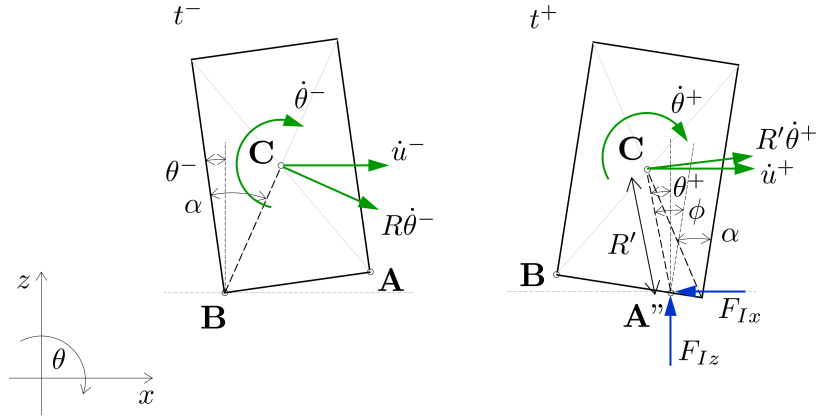
Figure 4.3: Pre-impact and post-impact velocity plans during transition from rocking around point B to rocking around an arbitrary point A"
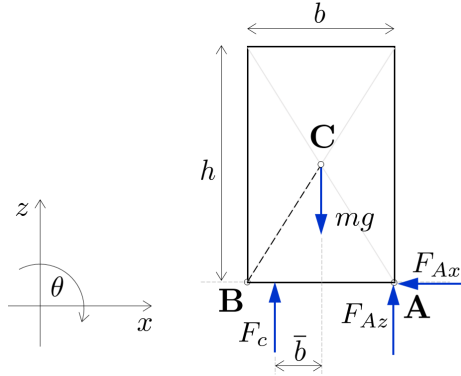
Figure 4.4: Free-body diagram of the model due to Kalliontzis et al. [2] and Chatzis et al. [3] at the time of impact following rotation around corner A

From Figure 4.3, the improved coefficient of restitution is

$$\eta_M = \frac{4 - 3\sin^2\alpha\,(1 + k^2)}{4 - 3\sin^2\alpha\,(1 - k^2)}, \tag{4.5}$$

as is given in [2], although the same formula with slightly different notation is also given in [3]. In the above formula $k = \frac{2\bar{b}}{b}$, and $\bar{b}$ is the distance between the middle of the block and the point at which the resultant impulse acts as shown in Figure 4.4, where F_c is the resultant impact force. The restitution coefficient obtained in this way is shown with respect to block's slenderness $\frac{h}{b}$ for four different values of k in Figure 4.6. Housner's coefficient of restitution is, therefore, a special case in the improved description when $k = 1$.

51
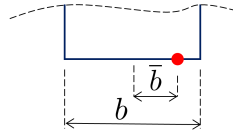
Figure 4.5: $\bar{b}$ for calculating k from equation (4.5)
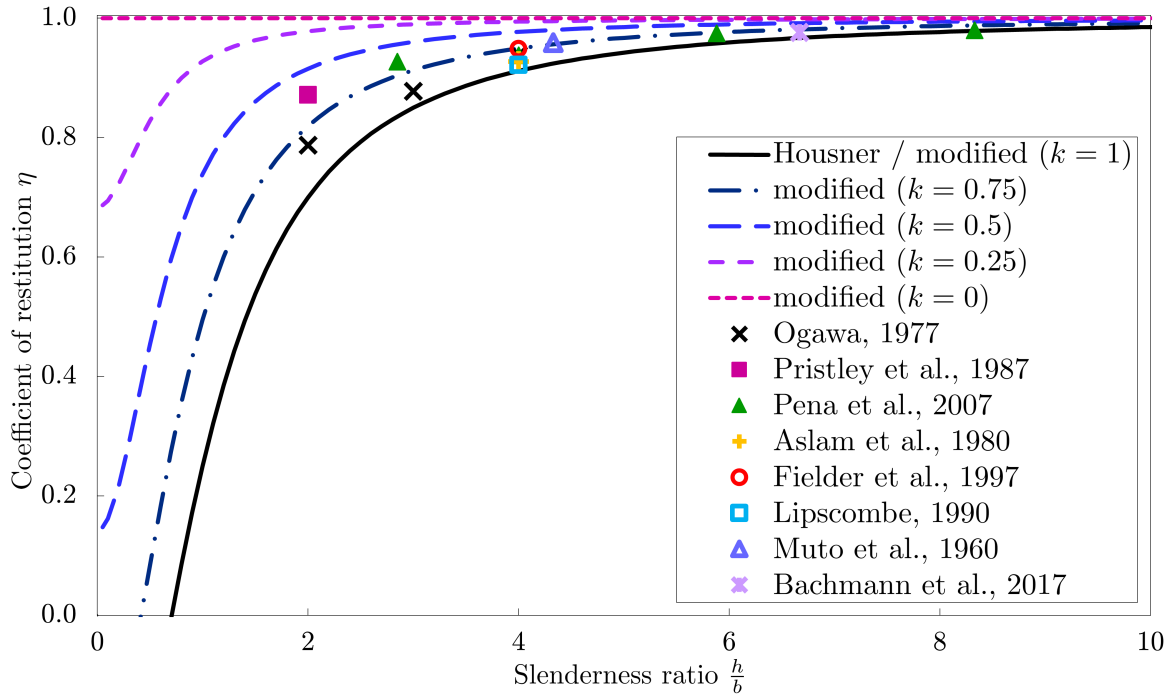
Figure 4.6: Coefficient of restitution from Housner's formula [1], modified formula [2, 3] and previous experiments [34, 35, 36, 37, 38, 39, 40, 41]

Obviously the improved restitution coefficient [2, 3] is in better agreement with the experimental results, but there does not exist a plausible proposal of how to estimate the extra parameter in the model. We will make such a proposal in Section 4.4.2 based on the analysis of the experiments conducted in Sections 4.4.1.1 and 4.4.1.2.

4.3 Experimental setup

An extensive experimental programme has been designed aiming to investigate the energy-loss mechanism in free rocking. The emphasis has been put on examining the coefficient of restitution and overall post-impact behaviour with respect to slenderness and scale of the block as well as the contact conditions between the block and the base.

4.3.1 Sample preparation

The blocks of ten different slenderness ratios $\frac{h}{b}$ (B1 - B10) on three different scales (S-small, M-medium, L-large) have been used as samples in the experimental programme and their properties are shown in Table 4.2. Thickness of all the blocks is equal to their width apart from blocks B1, which have larger thickness, and block B0M, which has smaller thickness. All the blocks are made from aluminium material.

Table 4.2: Geometric characteristics and masses of the tested blocks

Block	m [g]	b [m]	h [m]	$\frac{h}{b}$	$\alpha[rad]$	$R[m]$
B1S	113.3	0.03	0.03	1	0.7854	0.0212
B2S	113.3	0.03	0.045	1.5	0.5880	0.0270
B3S	161.2	0.03	0.0675	2.25	0.4182	0.0369
B4S	226.6	0.03	0.09	3	0.3218	0.0474
B5S	274.5	0.03	0.1125	3.75	0.2606	0.0582
B6S	339.6	0.03	0.135	4.5	0.2187	0.0691
B7S	453.2	0.03	0.18	6	0.1651	0.0912
B8S	500.8	0.03	0.2025	6.75	0.1471	0.1024
B9S	614.1	0.03	0.2475	8.25	0.1206	0.1247
B10S	727.4	0.03	0.2925	9.75	0.1022	0.1470
B0M	47.9	0.045	0.02	0.44	1.1526	0.0246
B1M	363.6	0.045	0.045	1	0.7854	0.0318
B2M	363.6	0.045	0.0675	1.5	0.5880	0.0406
B3M	544.4	0.045	0.10125	2.25	0.4182	0.0554
B4M	727.2	0.045	0.135	3	0.3218	0.0712
B5M	907.7	0.045	0.16875	3.75	0.2606	0.0873
B6M	1089.6	0.045	0.2025	4.5	0.2187	0.1037
B7M	1453.2	0.045	0.27	6	0.1651	0.1369
B8M	1634.0	0.045	0.30375	6.75	0.1471	0.1535
B9M	1997.6	0.045	0.37125	8.25	0.1206	0.1870
B10M	2361.2	0.045	0.43875	9.75	0.1022	0.2205
B1L	856.6	0.06	0.06	1	0.7854	0.0424
B2L	856.6	0.06	0.09	1.5	0.5880	0.0541
B3L	1284.3	0.06	0.135	2.25	0.4182	0.0739
B4L	1713.2	0.06	0.18	3	0.3218	0.0949
B5L	2140.9	0.06	0.225	3.75	0.2606	0.1164
B6L	2569.2	0.06	0.27	4.5	0.2187	0.1383
B7L	3425.8	0.06	0.36	6	0.1651	0.1825
B8L	3853.5	0.06	0.405	6.75	0.1471	0.2047
B9L	4710.1	0.06	0.495	8.25	0.1206	0.2493
B10L	5566.7	0.06	0.585	9.75	0.1022	0.2940

To prevent sliding and jumping as well as any out-of-plane motion of the blocks during testing a system of very thin plastic tapes attached to both the samples and the base beneath them is used (Figure 4.7). In this way only rocking or bouncing back of the block is enabled. The tapes provide no rotational resistance during rocking.
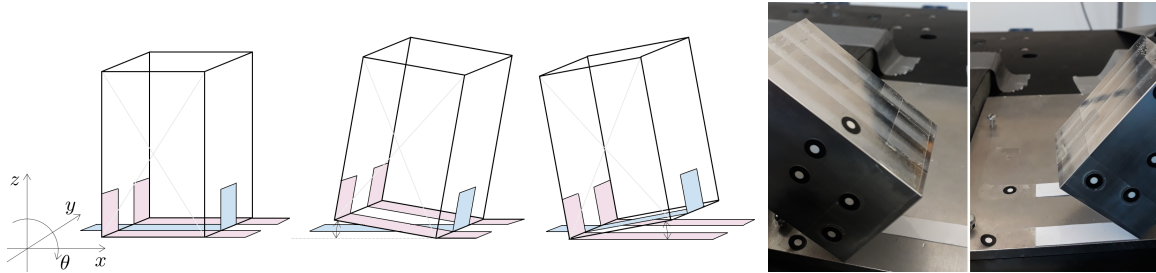
Figure 4.7: System of tapes designed to avoid sliding and/or jumping of the block on the base

To investigate the effect of the correction of Housner's restitution coefficient [1] due to Kalliontzis et al. given in [2] and Chatzis et al. [3] two different sets of contact conditions - full contact and edge contact - are designed as shown in Figure 4.8. In the full-contact set-up the actual point of impact between the block and the base is fully unknown, while in the edge-contact set-up this point is bound to be in the narrow region (here $l_c = 1.5$ mm wide) near the edges of the block. Modifying the block in order to make Housner's assumption for the position of impact impulse more accurate is also suggested in Chatzis et al. [3]. In our work, however, the base was modified instead of the rocking body itself.
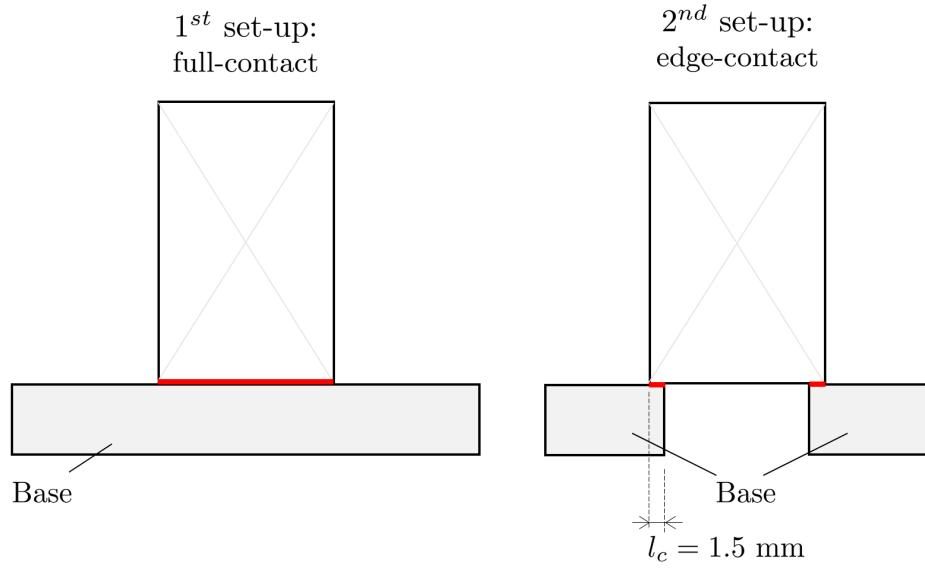
Figure 4.8: Two experimental set-ups with different contacts between the block and the base

4.3.2   Initiation of free rocking

The free rocking is initiated by setting the block into an initially tilted position (such that the initial rotation θ_0 is not greater than the block's angle of slenderness α) with zero initial angular velocity, and releasing it. The condition of zero initial velocity is provided by designing a special release system: the initially tilted block, connected to the base with a set of tapes described in the previous section and to another body with a piece of string, is set in motion by burning the string at the beginning of the experiment (Figure 4.9).
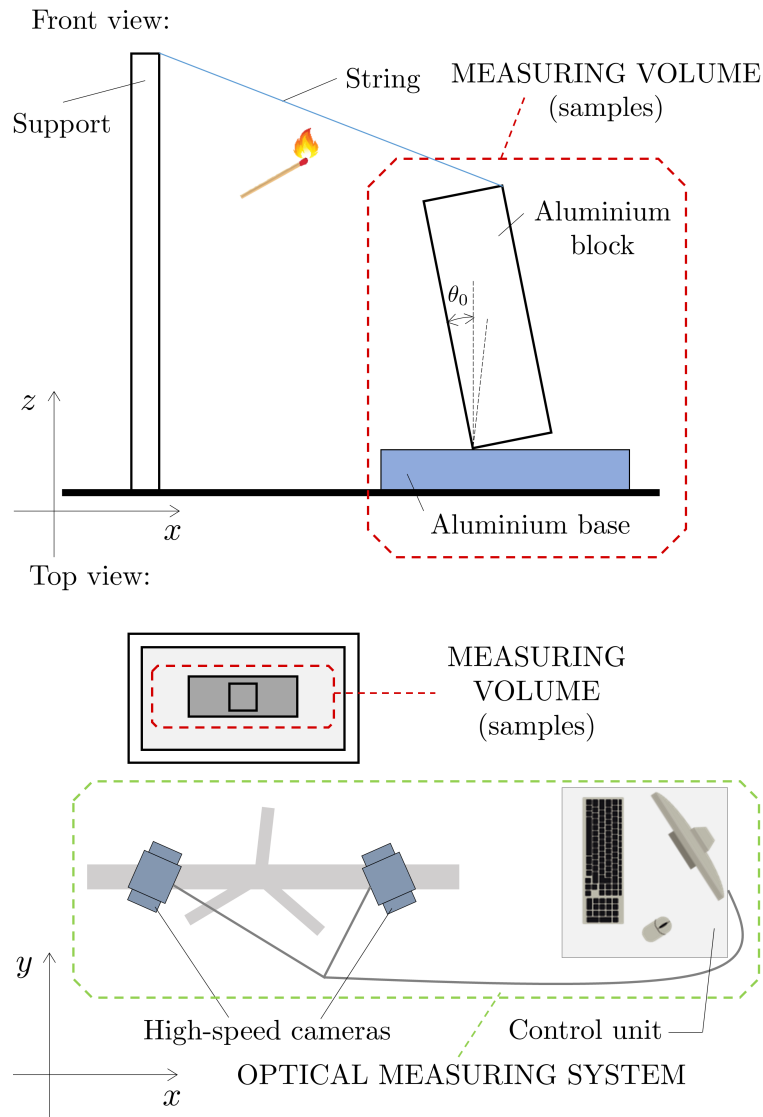
Figure 4.9: The free-rocking experimental set-up and measuring system: block in its tilted initial position (left) and top view showing the position of the measuring system (right)

4.3.3 Measurement

Motion of the samples is monitored using the 3D contactless optical measuring system GOM Pontos (version 6.3 and 8.0). The system comprises a set of two high-speed full-resolution cameras, an acquisition unit and post-processing software Aramis and Pontos. GOM Aramis and Pontons software are based on dividing the image of the experiment into facets (rectangular units with a unique arrangement of dark and light pixels) which are traced through the set of images extracted from the video in order to conduct the information of displacements and deformations on the surface of the

tested sample [59]. Choice for the facet size needed to be optimised, as it depends on the sample surface speckle pattern, pixel size and the scale of observation.

The system is shown inside a green dashed line on the right in Figure 4.9. Every experiment is filmed in full resolution (2400 x 1728 pixels) with 150 frames-per-second (fps) frequency. The positions of the testing samples in time (including the initial position) are obtained by post-processing the videos from the experiments. The initial rotation obtained in this way is then given as an input for the numerical simulation described in the previous section.

4.4 Examining the restitution in free rocking

4.4.1 Results and analysis

The time histories from each experiment are compared to the time histories from the numerical simulation for the block with the same geometry and initial conditions. The coefficient of restitution initially used in the numerical simulations is η_H [1] and η_M [2, 3], as given in equations (4.4) and (4.5).

This experiment is designed to question the conditions for rocking/sticking and the relation between η_H, η_M and the actual restitution in the physical model. The effects of slenderness and size, as well as the effect of different contacts between the block and the base to the restitution, are investigated.

4.4.1.1 Full contact experiments

First, the results obtained using Housner's restitution for four representative blocks from the group of blocks $0, 045$ m wide (medium scale) spanning the full range of possible slendernesses (blocks B0M, B2M, B6M and B10M in Table 4.2) are shown in Figure 4.10.
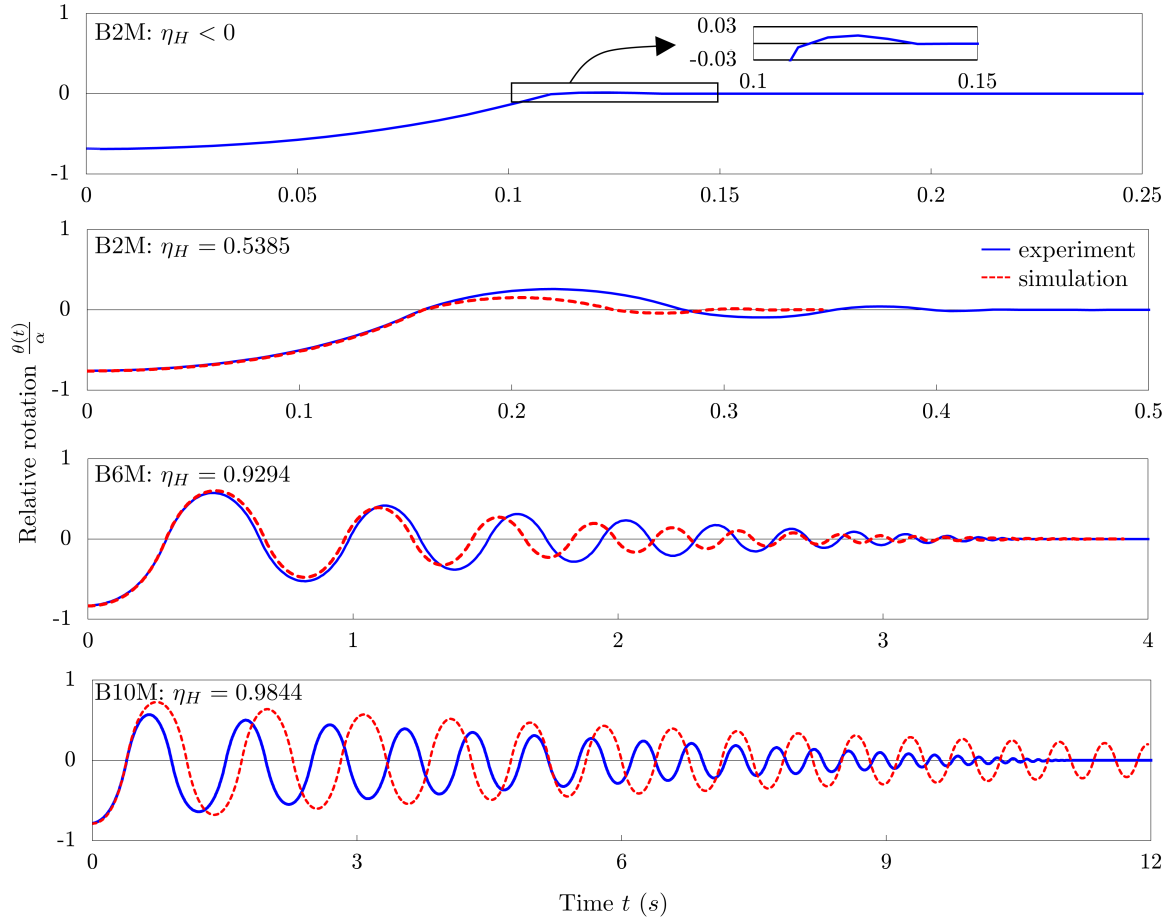
Figure 4.10: Comparison between full-contact experiments and simulation using η_H

For the three blocks with positive η_H (B2M, B6M and B10M) post-impact rocking is both observed experimentally and computed numerically. Given that no material dissipation is included in the computation of η_H, we would expect that the experimentally obtained amplitudes should be smaller than those from the numerical simulation, and, correspondingly, that the periods from the experiment should be also smaller than those from the simulation. This indeed happens for the relatively slender block B10M, but not for the stockier blocks B6M and B2M, which raises concerns about appropriateness of η_H in real situations.

Furthermore, following Housner's approach and the angular momentum conservation principle from (4.4), rocking behaviour should not occur when $\frac{h}{b} < \frac{1}{\sqrt{2}}$, as is the case for the presently considered block B0M. The experiment still shows (minor) rocking for that case (top graph in Figure 4.10). We presume that this happens owing to a relative ineffectiveness of the system of tapes used to prevent sliding and/or jumping for bulky blocks, which is unable to completely eliminate jumping when $\frac{h}{b} \leq$.

58

To preliminarily test if a constant coefficient of restitution is able to model rocking at all, we next try to find a "real" coefficient of restitution by running the simulation with a variety of restitution coefficients and choosing the one which fits the experimental results best, which we denote as η_e. The best fitting is defined by the criteria that both the amplitudes and the periods of rocking fit graphically well during the middle 50% of the response. Figure 4.11 shows the corresponding results for block B2M, where the green dashed line shows the numerical results obtained by fitting the experimental results with a constant value of coefficient of restitution $\eta_e = 0.67$ throughout the duration of rocking. Note that, as discussed earlier, for this block $\eta_e > \eta_H$.1

To preliminarily test if a constant coefficient of restitution is able to model rocking at all, we next try to find a "real" coefficient of restitution by running the simulation with a variety of restitution coefficients and choosing the one which fits the experimental results best, which we denote as η_e. The best fitting is defined by the criteria that both the amplitudes and the periods of rocking fit graphically well during the middle 50% of the response. Figure 4.11 shows the corresponding results for block B2M, where the green dashed line shows the numerical results obtained by fitting the experimental results with a constant value of coefficient of restitution $\eta_e = 0.67$ throughout the duration of rocking. Note that, as discussed earlier, for this block $\eta_e > \eta_H$.
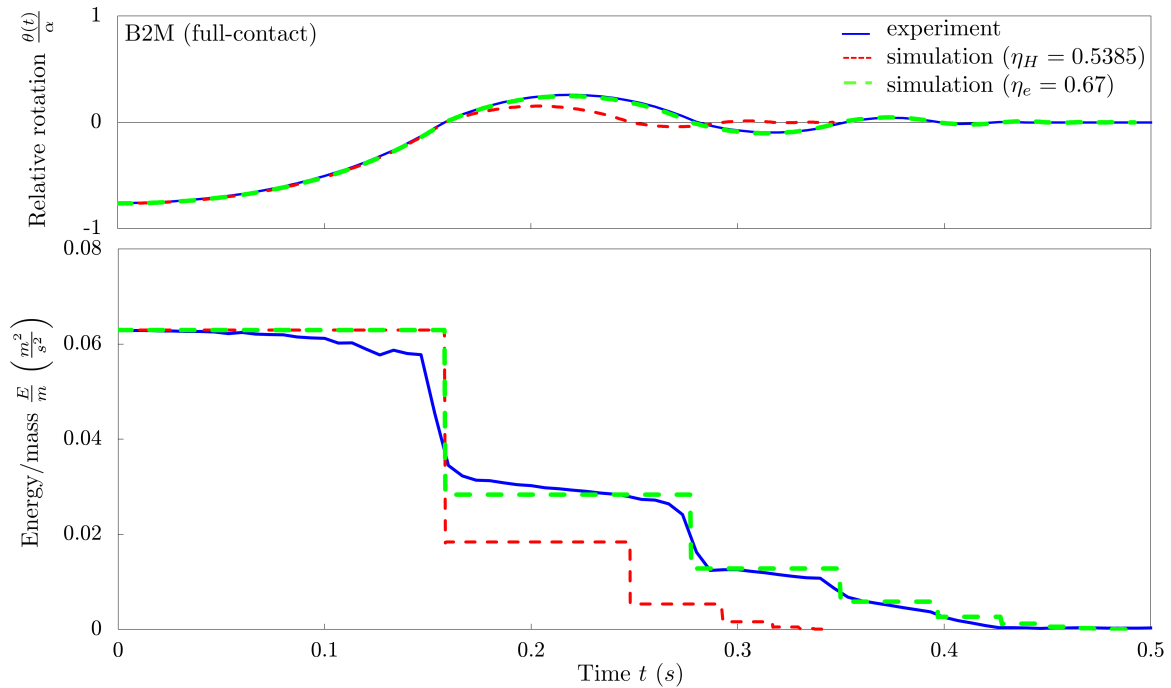
Figure 4.11: Comparison between full-contact experiments and simulation using η_H and η_e for block B2M

The comparison between experimentally and numerically obtained energy time histories for block B2M in Figure 4.11 shows that the assumption that energy loss is instantaneous at impacts can simulate the real energy-loss sufficiently well. For this block a constant value of coefficient of restitution models the experimental behaviour quite well.

However, not quite so good an agreement between the numerically and experimentally obtained results may be obtained by fitting the coefficient of restitution for significantly slenderer blocks. This is illustrated for block B10M in Figure 4.12. This figure indicates that *the restitution coefficient should not be assumed as constant* throughout the duration of free rocking. The green dashed line shows the results obtained using the coefficient of restitution η_e determined by fitting the overall response and it is obvious that, in contrast to the results for block B2M, the experimentally observed changes in the rocking periods may not be accurately followed. To gain more insight, we also show the results (the orange dashed line) for a coefficient of restitution η'_e obtained by fitting only the first post-impact half-period of rocking. The results are blown out for the first two seconds of motion for both the relative rotation and the angular velocity in the lower parts of Figure 4.12.
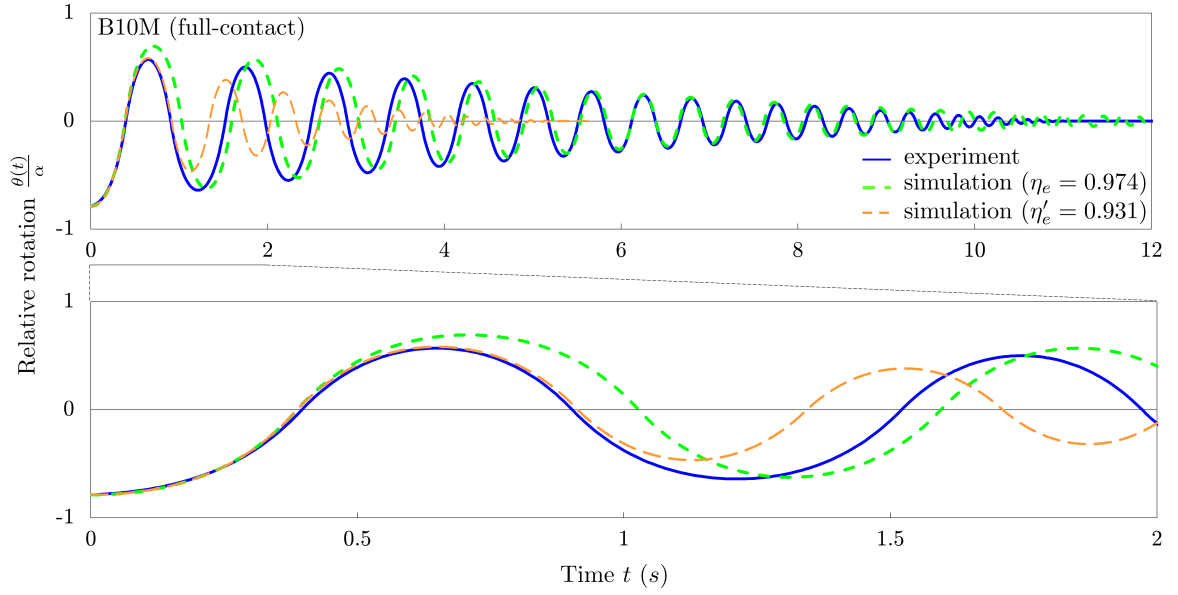
Figure 4.12: Experimental and numerical results for block B10M and different restitution coefficients

If we take the difference between η_e and η'_e as a measure of variability of the restitution coefficient during rocking, and repeat the analysis for ten different slenderness ratios (blocks B1M-B10M), we observe two interesting phenomena. Firstly, as already noted earlier, Housner's restitution coefficient η_H underestimates the actual restitution (i.e. is overly dissipative) for bulky blocks, but the actual restitution for the analysed problems appears to be constant (see Figure 4.13 for slenderness ratios below cca 4). Secondly, while for the relatively slender blocks (slenderness ratio above cca 6) Housner's restitution is now larger than the actual one (which is physically justified), the latter may not any more be considered as constant. Figure 4.13 shows that the difference between η_e and η'_e increases as the slenderness increases, in turn indicating an increase in variability of the actual restitution during rocking. As an estimate for the actual restitution we will from now on take η_e, as the one on the safe side when assessing stability of a block against overturning.
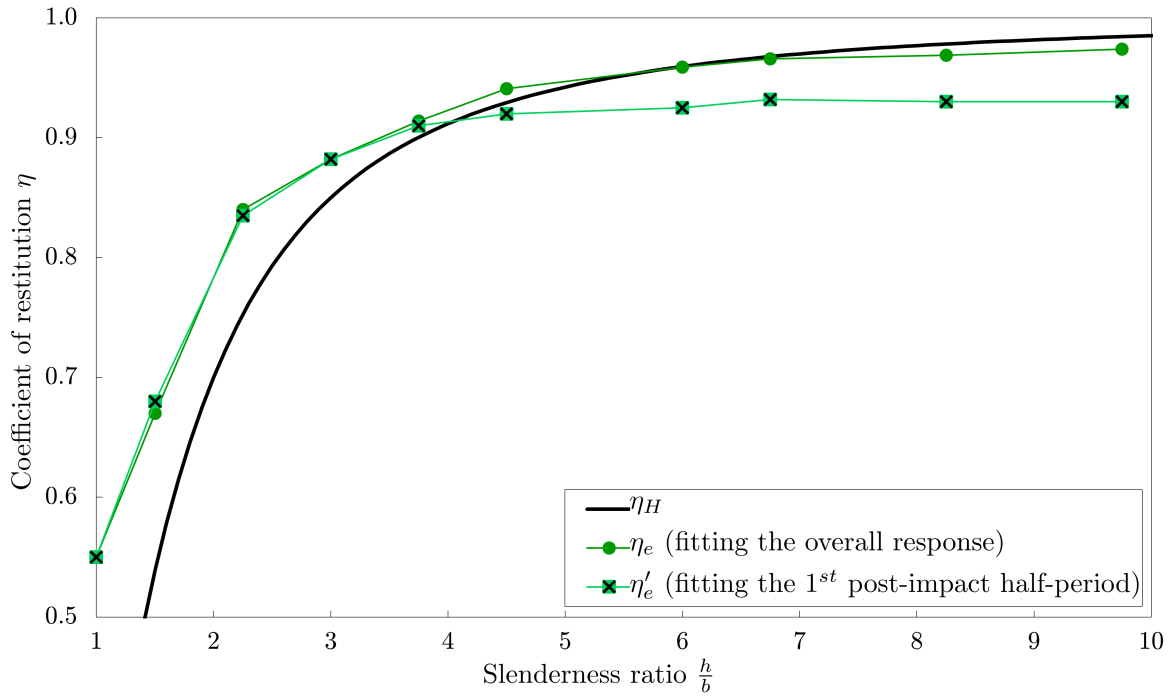
Figure 4.13: Coefficient of restitution from Housner's formula [1] and full-contact experiments for blocks B1M - B10M (medium scale) with different fitting

The inappropriateness of Housner's restitution estimate, especially for bulky blocks (which is way too liberal and thus unsuitable for design purposes), is also observed in the experiments performed on the other two scales in this work (see Table 4.3), as well as noticed by other researchers as shown in Figure 4.14.

Figure 4.14: η_H [1] and coefficient of restitution obtained from full-contact experiments [34, 35, 36, 37, 38, 40, 39, 41]

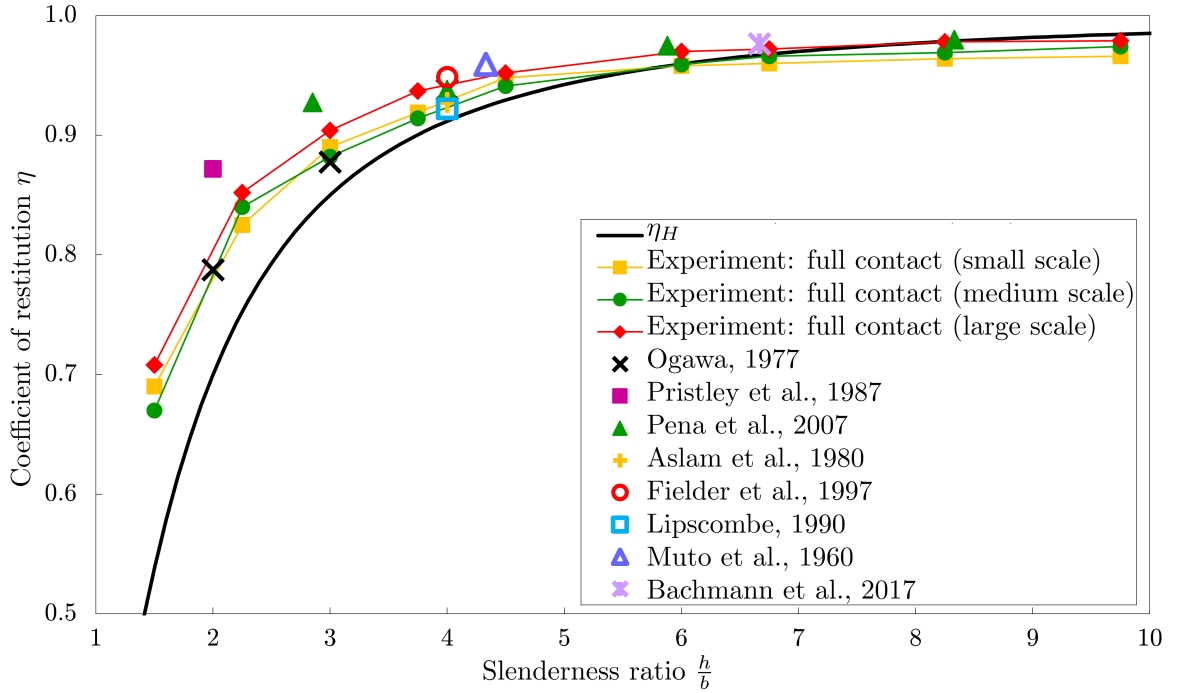With the decrease in size of the block, η_H seems to describe restitution somewhat better - it overestimates the energy-loss for slenderness ratios lower than 6 for scale S and lower than 8 for scale L.

Table 4.3: Coefficient of restitution $\eta_{e,full}$ from full-contact experiments

Block	$\eta_{e,full}$	Block	$\eta_{e,full}$	Block	$\eta_{e,full}$
B2S	0.690	B2M	0.670	B2L	0.708
B3S	0.825	B3M	0.840	B3L	0.852
B4S	0.890	B4M	0.882	B4L	0.904
B5S	0.919	B5M	0.914	B5L	0.937
B6S	0.948	B6M	0.941	B6L	0.952
B7S	0.958	B7M	0.959	B7L	0.970
B8S	0.960	B8M	0.966	B8L	0.972
B9S	0.964	B9M	0.969	B9L	0.978
B10S	0.966	B10M	0.974	B10L	0.979

4.4.1.2   Edge-contact experiments

To test if the reason for unsuitability of Housner's restitution estimate applied to bulky blocks lies in an increased uncertainty in the position of the actual contact

impulse as the slenderness decreases (as suggested both by Kalliontzis et al. [2] and by Chatzis et al. [3]) we will now repeat our analysis on a different set of suitably designed experiments. To this end, we provide different contact conditions in which this position may be determined much more accurately - the edge-contact conditions shown in Figure 4.8.

The analysis with the edge-contact conditions is first repeated for block B2M. The results are shown in Figure 4.15, along with those obtained earlier using the full-contact conditions. Clearly, in the case of edge contact, η_H enables a much better simulation than in the case of full contact. As noted above, this is expected since the edge contact experiments provide conditions that are much closer to the assumptions of Housner's impact model. Still, η_H in this case slightly underestimates the actual restitution (see inset in Figure 4.15) and the analysis will be performed next to see if Housner's estimate may be improved following the modified formula due to Kalliontzis et al. [2] and Chatzis et al. [3].
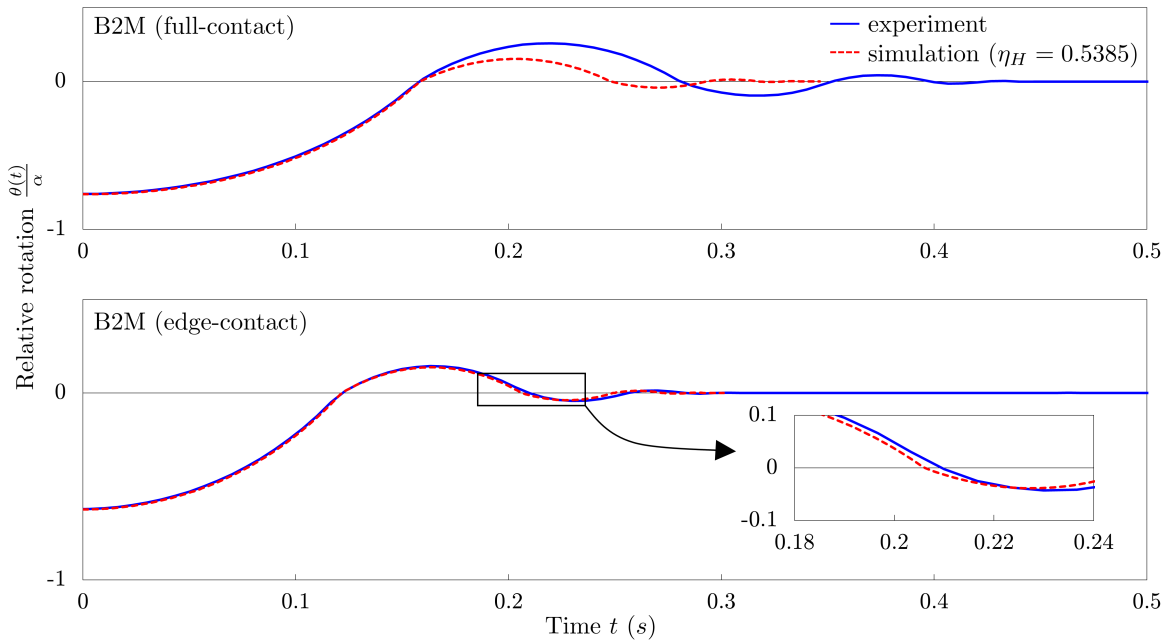

Figure 4.15: Experimental and numerical results for block B2M and different contact conditions

The two series of experiments have been carried out for all the blocks from B1S to B10L. For the purpose of comparison between experimentally and numerically obtained results, the experimentally obtained coefficient of restitution η_e is used for all the blocks, i.e. the coefficient of restitution calculated by fitting the numerical curve to the experimentally obtained one over the whole response time. The results

for block of width 4.5 cm (medium scale) and both full- and edge-contact conditions are given in Figure 4.16, which shows a very significant effect of the size of the contact area on the restitution during free rocking.
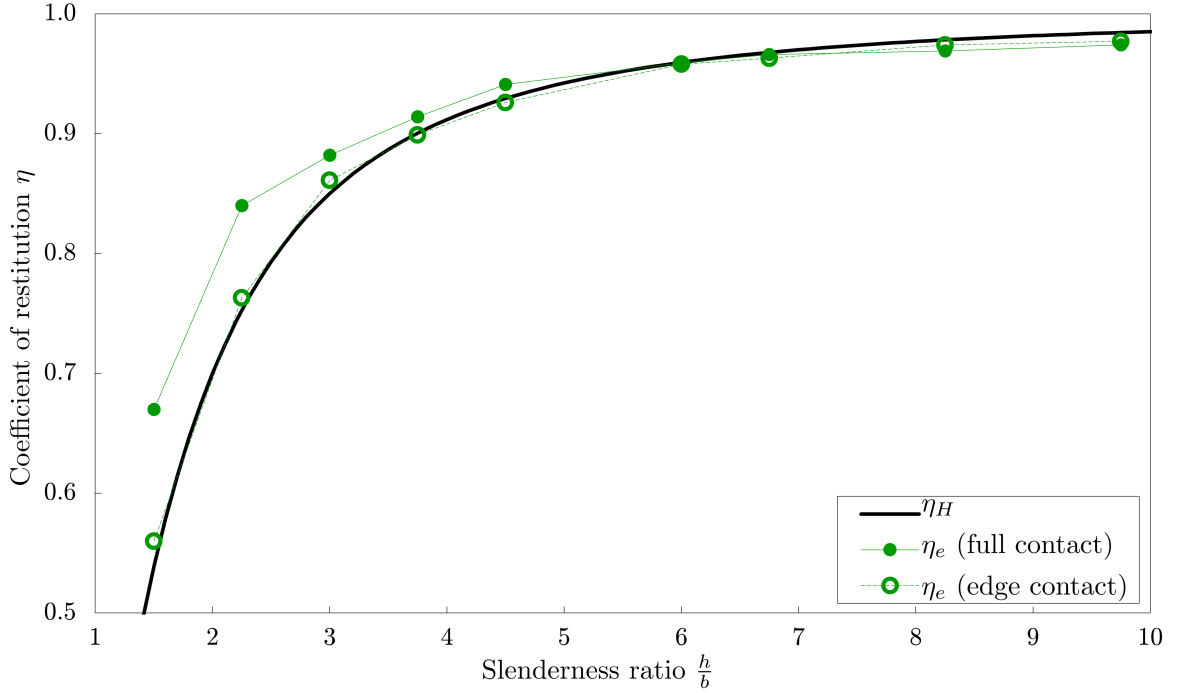

Figure 4.16: Experimentally obtained results from full- and edge-contact experiments (medium scale, $b = 4.5$ cm)

Below, the results are presented with respect to block's slenderness $\frac{h}{b}$ separately for each of the three scales. If the contact is assumed to take place between the block and the inner edge of the base ($l_c = 1.5$ mm in Table 4.4), we can compute the upper bound for the restitution coefficient η_M. On the other hand, the contact can be assumed to take place midway between the inner edge of the base and the edge of the block, in which case $l_c = \frac{1.5}{2}$ mm. Parameters k necessary to compute η_M obtained from these two approaches using (4.5) are given in Table 4.4 for the three scales.

Table 4.4: Values of the parameter k in edge-contact experiments

Scale	k_1	k_2
small	0.9	0.95
medium	$0.9\dot{3}$	$0.9\dot{6}$
large	0.95	0.975

The experimentally obtained results for blocks B1S to B10S from Table 4.2 are shown in Figure 4.17. Coefficient η_H is shown in the full black line, which clearly underestimates block's restitution for slenderness ratio lower than 4.5, while η_M calculated using $k = 0.9$ and $k = 0.95$ give improved estimates which are almost always higher than the corresponding values from the edge-contact experiments for all the slenderness ratios analysed.
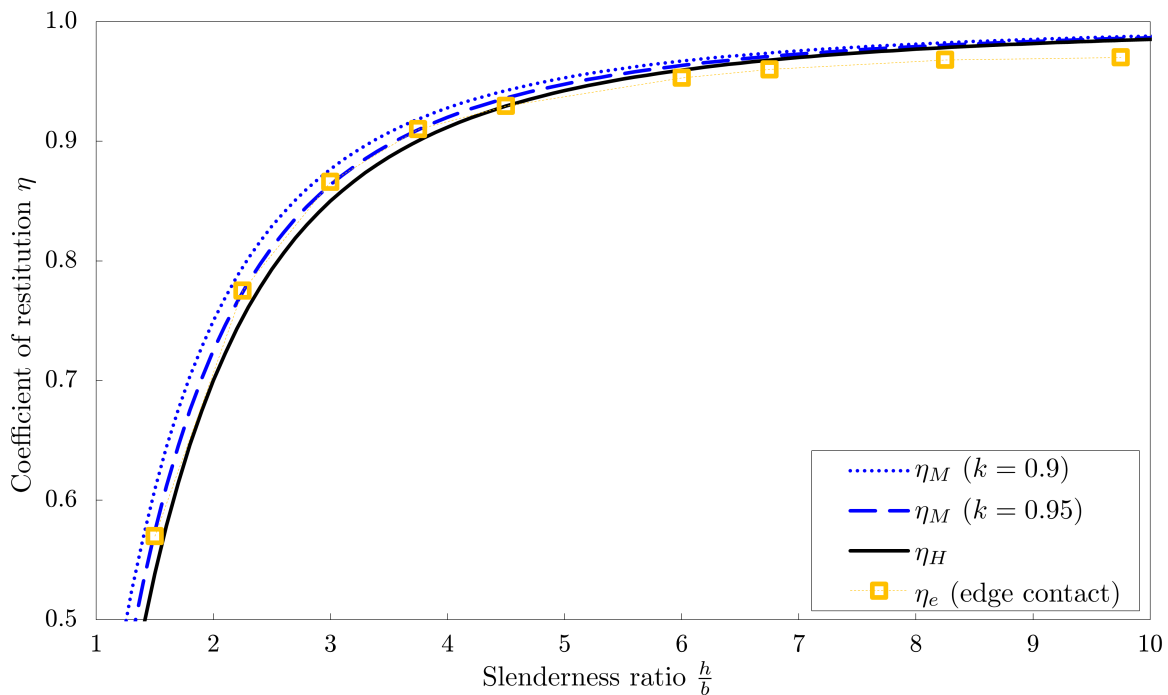

Figure 4.17: Coefficient of restitution for blocks B1S - B10S (small scale, $b = 3$ cm) with full- and edge-contact conditions

The corresponding results for blocks B1M to B10M are shown in Figure 4.18. Coefficient η_H again underestimates the restitution for slenderness ratios lower than

4.5. Coefficients η_M with $k = 0.9\dot{3}$ and $k = 0.9\dot{6}$ again almost always return higher restitution estimates than those experimentally obtained for all the slenderness ratios.
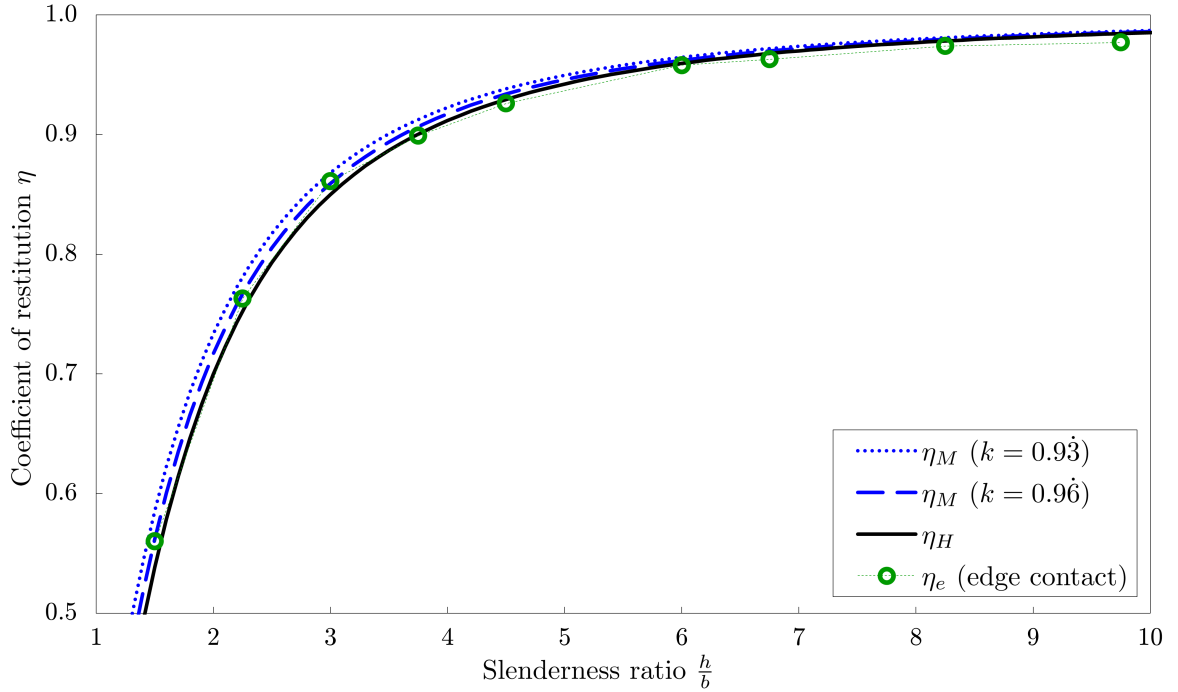

Figure 4.18: Coefficient of restitution for blocks B1M - B10M (medium scale, $b = 4.5$ cm) with full- and edge-contact conditions

Likewise, the results for blocks B1L to B10L are shown in Figure 4.19. For this largest scale, η_H overestimates the energy-loss for slenderness ratios lower than 3. In contrast, coefficients η_M calculated with $k = 0.95$ and $k = 0.975$ are higher than those experimentally obtained for the complete range of slenderness ratios analysed.
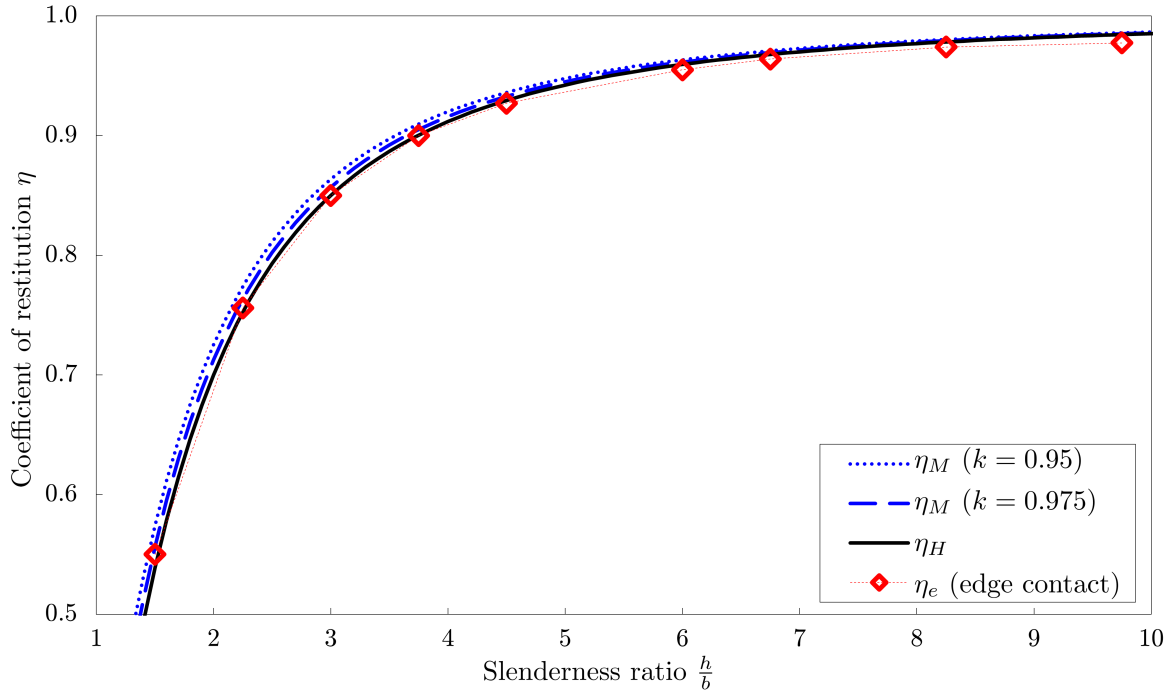
Figure 4.19: Coefficient of restitution obtained for blocks B1L - B10L (large scale, $b = 6$ cm) with full- and edge-contact conditions

Clearly, the results in Figures 4.17 - 4.19 show that Housner's restitution estimate is much more suitable when we know that the impact actually takes place near the edge of the block. In addition, they show that the modified restitution estimate given in [2, 3] for the position of the impact as away from the edge of the block as applicable are always higher than those experimentally observed and may be thus taken to be the upper limit of the restitution coefficient. In practical situations, however, this position is unknown and in the following we suggest a method to determine it.

4.4.1.3 Estimate of material dissipation from edge-contact experiments

An analysis is now performed so that an insight into the additional energy-loss due to material dissipation is provided: the ratio between the experimentally obtained restitution η_e and the η_M from (4.5) should provide a quantitative information about material dissipation:

$$\eta_{mat} = \frac{\eta_e}{\eta_M} \iff \eta_e = \eta_M \eta_{mat} \tag{4.6}$$

and from Figures 4.17 - 4.19 we expect that for the edge-contact experiments η_{mat} obtained in this way should be approximately constant.

The ratio between the experimentally obtained restitution η_e and the corresponding η_M is plotted in Figure 4.20 taking into account the two approaches from Table

4.4 for all the edge-contact experiments carried out. This ratio is near-constant for the slenderness ratio higher than 3 if we assume that the contact takes place at the inner edge of the base ($\eta_{mat} = \frac{\eta_e}{\eta_M} \simeq 0.989$), which indicates that η_M gives consistent results for such geometries and contact conditions. On the other hand, this ratio is near-constant for all the observed slendernesses if we assume that the contact takes place midway between the inner edge of the base and the edge of the block ($\eta_{mat} = \frac{\eta_e}{\eta_M} \simeq 0.994$), but in this case it reaches unacceptable values higher than 1 for slenderness ratios between 2 and 4 on scale S, as well as for slenderness ratio 3 on scale M. This indicates that the contact point has to be assumed further from the edge of the block.
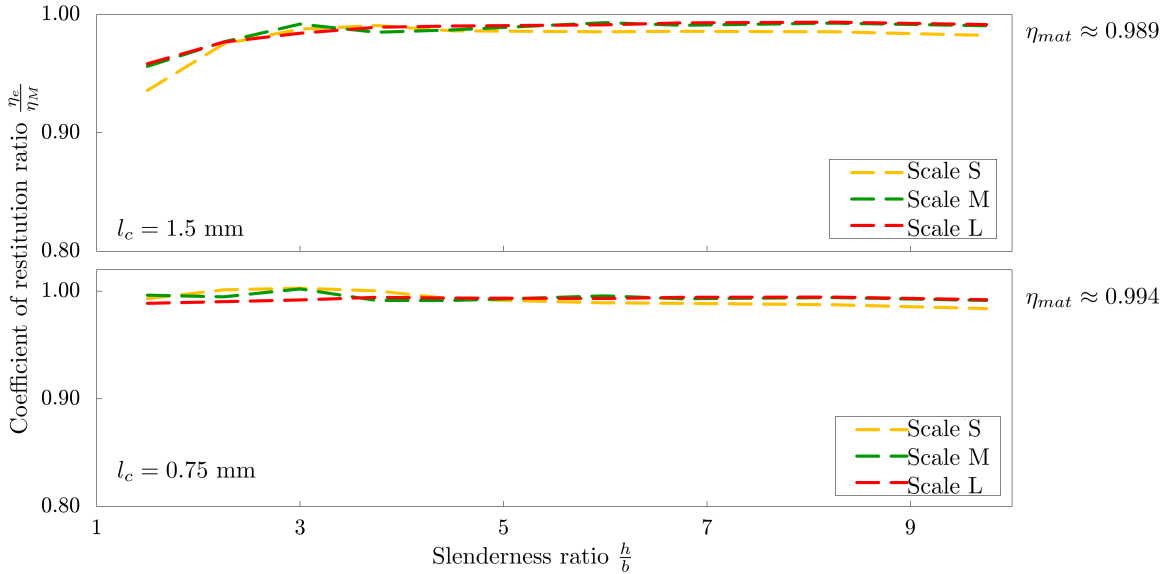

Figure 4.20: Ratio between the experimentally obtained coefficient of restitution η_e and η_M [2, 3] for the edge-contact experiments

The approach where the contact is assumed to take place on the inner edge of the base is on the safe side and it is clearly to be preferred.

4.4.2 Inverse analysis for assessment of k in equation (4.5) for full-contact experiments

Since generally we are not able to detect the point at which the contact takes place in full-contact experiments, here we suggest an inverse analysis which enables assessment of the approximate values k (and thus also the contact point) for the full-contact rocking conditions. Fundamentally, η_{mat} is assumed to be purely a measure of material dissipation, not dependent on contact conditions. Then, its value calculated

from the edge-contact experiments is also valid for the full-contact conditions, which supplies an estimate for the amount of rigid-body restitution η_{RB} in the full-contact experiments:

$$\eta_{mat} = \frac{\eta_{e,full}}{\eta_{RB}} \rightarrow \eta_{RB} = \frac{\eta_{e,full}}{\eta_{mat}}. \tag{4.7}$$

Bearing in mind that η_M in (4.5) is also a coefficient of rigid-body restitution but such one computed from the angular-momentum balance in which k is the parameter defining the position of the resultant contact impulse, substituting η_{RB} for η_M in (4.5) provides a result for this position as

$$k = \sqrt{\frac{(1 - \eta_{RB})\left(4 - 3\sin^2\alpha\right)}{(1 + \eta_{RB})\, 3\sin^2\alpha}}, \; \bar{b} = \frac{b}{2}k, \tag{4.8}$$

where $\bar{b}$ is shown in Figure 4.5. The values of the parameter k and the position $\bar{b}$ for each block obtained in this way are given in Table 4.5. Note that the values for k and $\bar{b}$ for blocks B9S and B10S obtained in this way are larger than the maximum possible values ($k = 1$, $\bar{b} = b/2$; see Figure 4.5). We suggest that this occurs due to the system of tapes designed to prevent jumping and sliding: the tapes act as an additional dissipation mechanism which has the biggest influence on the smallest scale due to the smallest mass of the block. This additional dissipation cannot be fully taken into account with η_{mat} obtained as the average of η_e/η_M in Section 5.3 over all scales and slendernesses.

The results show that the average parameter k needed to calculate the position of the impact impulse tends to decrease with the increase in block's size, which means that the position of the impact impulse moves away from the edge and the restitution coefficient increases with the increase in block's size.

Table 4.5: Parameter k in (4.5) and position $\bar{b}$ of the contact impulse in Figure 4.5 for $\eta_{mat} = 0.989$ for the full-contact experiments

| Block	k	$\bar{b}$	Block	k	$\bar{b}$	Block	k	$\bar{b}$	Average k
B2S	0.7704	0.0116	B2M	0.8805	0.0180	B2L	0.7429	0.0223	0.7713
B3S	0.8001	0.0120	B3M	0.7595	0.0171	B3L	0.7259	0.0218	0.7619
B4S	0.8059	0.0121	B4M	0.8397	0.0189	B4L	0.7440	0.0223	0.7965
B5S	0.8364	0.0125	B5M	0.8670	0.0195	B5L	0.7175	0.0215	0.8070
B6S	0.7602	0.0114	B6M	0.8241	0.0185	B6L	0.7214	0.0216	0.7685
B7S	0.8766	0.0131	B7M	0.8621	0.0194	B7L	0.6838	0.0205	0.8075
B8S	0.9526	0.0143	B8M	0.8468	0.0191	B8L	0.7266	0.0218	0.8420
B9S	1.0787	0.0162	B9M	0.9634	0.0217	B9L	0.7121	0.0214	0.9181
B10S	1.2214	0.0183	B10M	0.9838	0.0221	B10L	0.8016	0.0240	0.9181
Average	0.9003	0 0135	Average	0.8608	0.0194	Average	0.7306	0.0219	0.8306
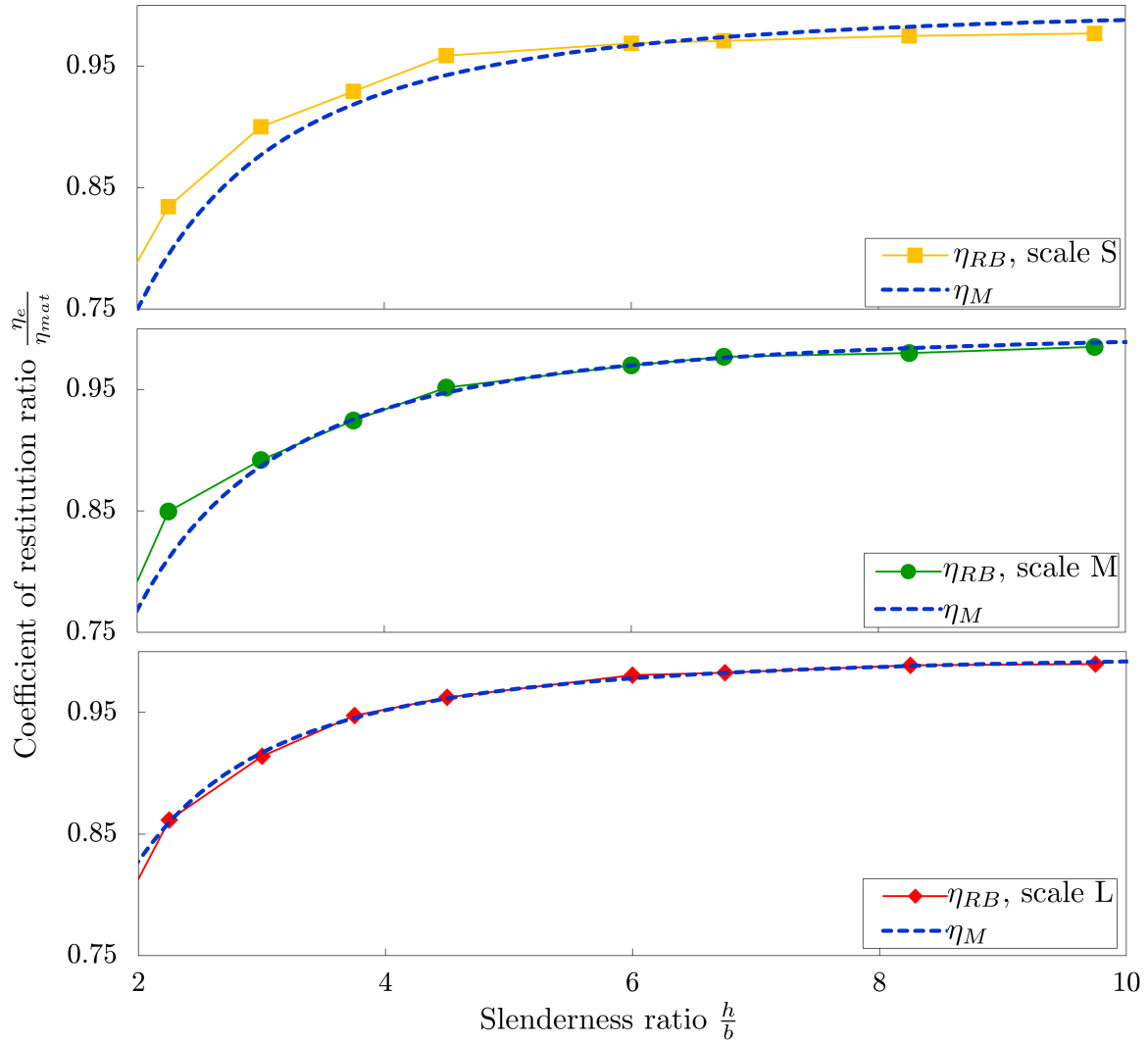
Figure 4.21: Coefficient of restitution η_{RB} and η_M [2, 3]

The assumed constant value of k models the experiment very well for the largest scale, as shown in Figure 4.21. However, with the decrease in scale there is an increasing difference between η_M and η_{RB} which indicates that the value k is increasingly related to the slenderness of the block as size decreases.

4.5 Discussion and conclusion

In this chapter the dynamic response of a single rigid prismatic blocks in free rocking without sliding and jumping has been treated numerically and experimentally. The emphasis is put on the analysis of the post-impact behaviour and energy-loss mechanism during impacts. To enable analysis of both slender and bulky blocks in

large-amplitude rocking, full nonlinearity of the rocking behaviour is taken into account in numerical simulations. A time-stepping numerical procedure is developed with built-in contact detection algorithm, which enables a precise investigation of energy-loss during impact. Two different impact models and restitution estimates are considered: Housner's classical model (η_H) [1] and the improved model (η_M) given by Kalliontzis et al. [2] and Chatzis et al. [3].

An extensive controlled experimental study of free rocking behaviour with ten different slenderness ratios, three scales (sizes) and two different contact conditions which prevent sliding and jumping is conducted. The comparison between the experimentally and numerically obtained results shows that bouncing or remaining still after the impact is unlikely to occur in reality because it is not easy to completely prevent detachment of bulky blocks from the ground. The restitution coefficient is shown to change during rocking, but the overall response can still be modelled with sufficient accuracy with a constant restitution coefficient.

Housner's restitution coefficient η_H is widely reported to overestimate the energy-loss and should be used with caution in seismic stability assessment, especially for bulky blocks, which is confirmed by the present analysis. The numerical results obtained using the improved restitution coefficient η_M due to Kalliontzis et al. and Chatzis et al. are in much better agreement with the experimentally obtained values. Their suggestion that the impact between the block and the base takes place at some point between the corners of the block is verified by experiments where the contact between the block and the base is designed so that the actual contact region is controlled and known (the edge-contact experiments).

Finally, an approach for estimating restitution due to material dissipation η_{mat} and the position of the contact point in full-contact experiments is presented. With this position known, the corresponding improved restitution [2, 3] models the full-contact rocking behaviour significantly better than Housner's model and provides an accurate estimate of the energy loss in rocking, which is always on the conservative side and thus suitable for assessment of rocking stability.

Based on the present results, further numerical and experimental analysis of rocking due to an arbitrary base acceleration function is conducted in Chapter 5.

Chapter 5

Forced rocking of a single block due to ...

Forced rocking of a rigid rectangular block standing freely on a rigid base subject to a base acceleration function is addressed here. The equations of motion for such forced rocking are derived in Chapter 3 and the energy loss at each impact during free rocking is defined and investigated in Chapter 4. Now rocking response of a single block to a specific base excitation is addressed by combining a specially designed experimental program with numerical simulations (and analytical results where applicable). Rocking due to two different classes of base excitation is investigated: constant acceleration function of finite duration, and harmonic excitation.

5.1   ... constant acceleration of finite duration

This chapter is based on the results and discussion from paper [60]:
Čeh, N., Jelenić, G., and Bićanić, N., "Rocking of single and dual rigid-block systems subject to ground excitation: experimental and computational analysis of overturning conditions", 25th UKACM Conference on Computational Mechanics

A constant base acceleration of finite duration is the simplest base excitation and we want to fully understand rocking behaviour of the single block under this kind of excitation. For this reason, rocking response and stability are investigated in detail analytically, numerically and experimentally before going into the assessment of rocking stability due to more complex base excitation functions.

A rigid rectangular block subject to a constant base acceleration function a_0 of finite duration t_a (described in equation (3.7) in Chapter 3 and shown in Figure 5.1)
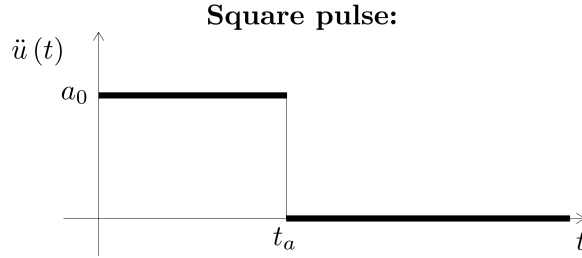
is observed here.

Figure 5.1: Constant acceleration of finite duration

As described in Section 3.1, for a relatively small a_0 the block translates along with the base. When $a_0 > \ddot{u}_0$ the block starts to rotate around one of its corners. We investigate the conditions under which the block overturns due to the influence of constant base acceleration of various duration analytically, numerically and experimentally. The case where sliding between the block and the base, as well as jumping (detachment) of the block from the base is prevented is observed. This is assured experimentally with the help of a set of tapes attached to both the block and the base, as described in Section 4.3.1 (Figure 4.7).

5.1.1 Analytical and numerical conditions for overturning

The analytical condition for overturning is derived from the analytical solutions for rotation due to a constant base acceleration given in Section 3.1.3.1. These solutions are derived from the linearised equation of motion, which is only valid for significantly slender blocks. In Figure 5.2 the vertical green line follows the boundary between rocking and translation defined by $a_0 \geq g\alpha$ which approximates the condition given in equation (3.3) for really slender blocks, while the curved green line follows the boundary between stable rocking and overturning. The boundary between rocking and overturning is derived from the analytical solution for rotation of the block due to a constant base acceleration of finite duration, i.e. from equation (3.28). In order for overturning due to a constant ground acceleration to occur, the rotation θ needs to exceed the value of the angle of slenderness α and the least critical case is when this takes place at time $t > t_a$. This means that

$$\alpha \left[1 - \cosh\left(pt\right)\right] + \frac{a_0}{g}\left\{\left[\cosh\left(t_a p\right) - 1\right]\cosh\left(tp\right) - \sinh\left(t_a p\right)\sinh\left(tp\right)\right\} > \alpha, \quad (5.1)$$

from which we can obtain

$$\frac{\alpha - \frac{a_0}{g}\left[\cosh\left(1 - t_a p\right)\right]}{\frac{a_0}{g}\sinh\left(t_a p\right)} > \tanh\left(tp\right). \quad (5.2)$$

Since $\tanh{(t_a p)} < 1$ always,

$$t_a p > -\ln\frac{\frac{a_0}{g\alpha} - 1}{\frac{a_0}{g\alpha}}. \tag{5.3}$$
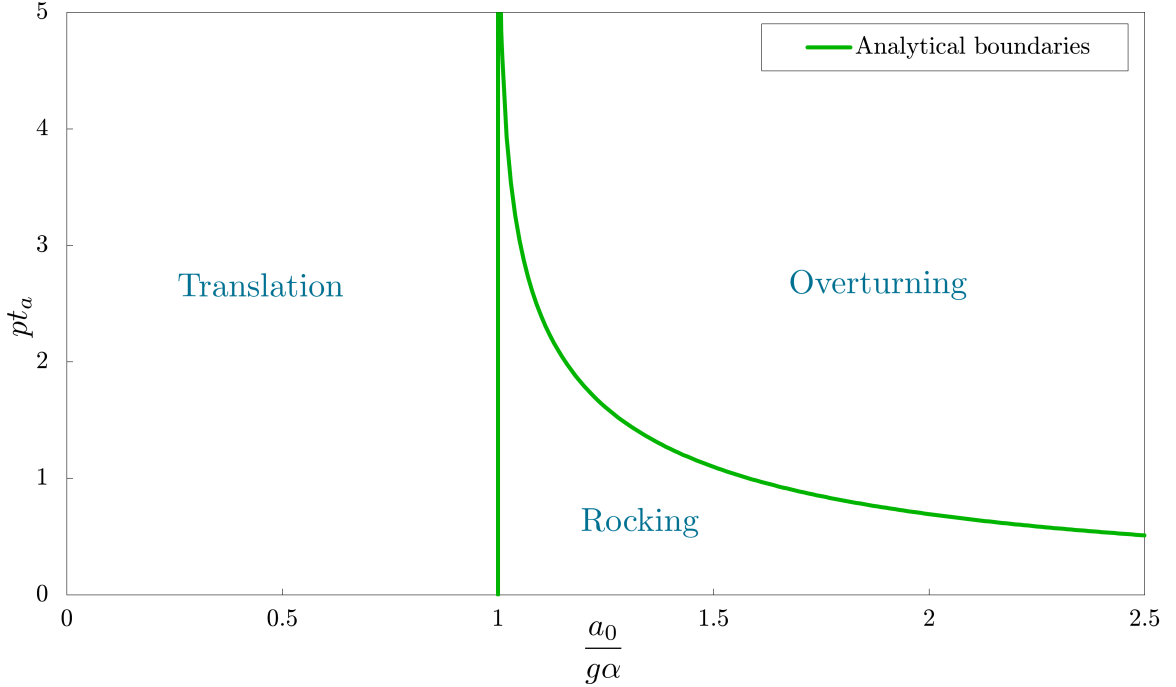

Figure 5.2: Analytical boundaries between overturning, rocking and translation conditions due to a constant acceleration

The numerical solution for overturning conditions is obtained from the numerical procedure based on solving the nonlinear equation of motion by means of Newmark's integration formula and Newton-Raphson iterative procedure, with contact detection procedure built-in, described in Section 3.2 (Figure 3.6). The nonlinear numerical analysis is run multiple times for a range of base accelerations a_0 between $0.1g\alpha$ and $2.5g\alpha$ and durations of the accelerations t_a between $0.1/p$ and $5/p$. The results obtained that way are shown in Figure 5.3, along with the previously presented analytical results. The numerical analysis takes into account the real geometry of the block (i.e. α is not considered small), and, since $\tan\alpha > \alpha$, the results obtained from the numerical analysis show that slightly larger acceleration a_0 is necessary to overturn the block than the linearised analysis predicts.
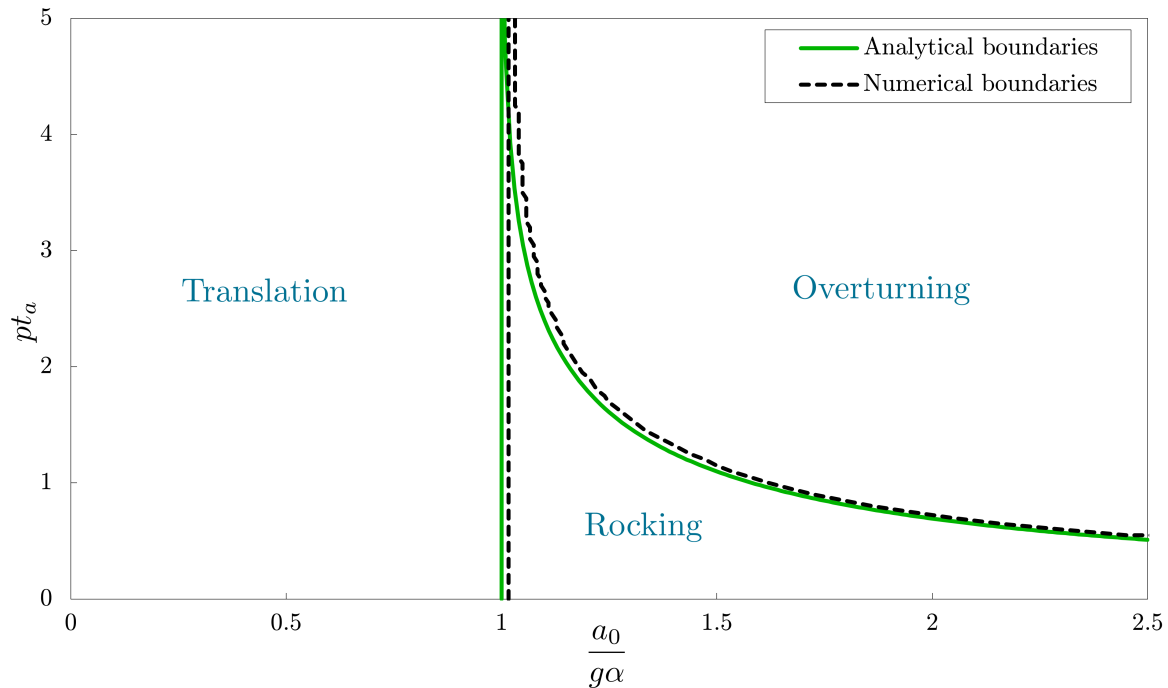
Figure 5.3: Numerical boundaries between overturning, rocking and translation conditions due to a constant acceleration

5.1.2 Experimental set-up

To validate the theory and assess the numerical procedure, a test rig is set up and a set of measurements is conducted on a near frictionless air track device (shown in Figures 5.4 and 5.5). The air track device enables a constant acceleration of a chosen magnitude to be applied to a slider (which represents the base) for a prescribed duration in a fully controlled manner. The near-absence of friction is obtained by means of an air cushion between the air track and the slider. This is achieved by pumping air via the compressor, which escapes the air track device through a large set of tiny holes drilled on its top surface. When the ground acceleration drops to zero, the slider remains free to move uniformly without any horizontal disturbances thus completely reproducing the problem stated.
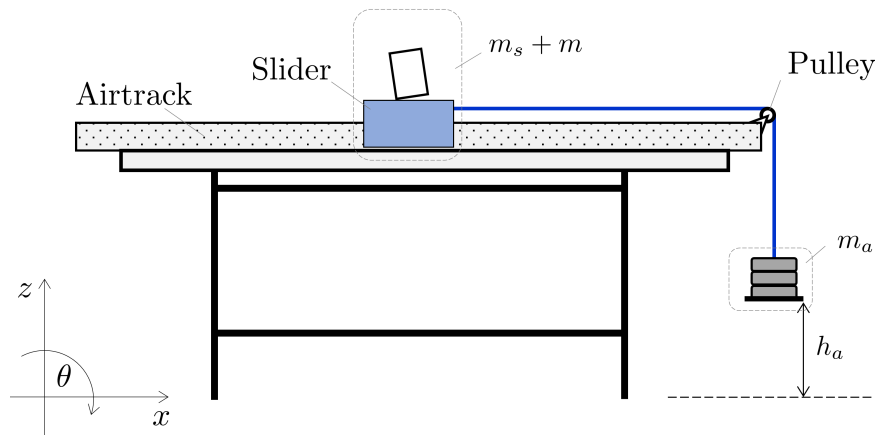
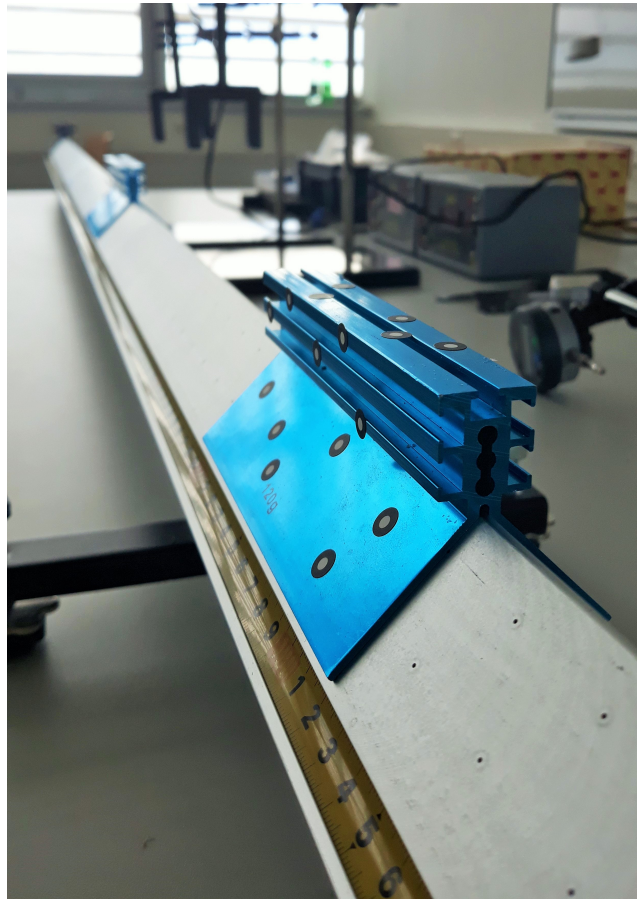Figure 5.4: Scheme of the experimental set-up with the air track device

Figure 5.5: Photo of the experimental set-up with the air track device

Before the analysis, the block of mass m is placed on the slider of mass m_s and the system is set floating by supplying sufficient air pressure to the air track. The slider–block system is kept in equilibrium through a force in the string attached to

the slider and running over a pulley (see Figure 5.4) on the right-hand side of the air track and supporting a hanging mass m_a, which is counter-balanced by the force in the second string securing the slider in a fixed position by connecting it to the left-hand side of the air track. The three-mass mechanical system in the initial position is also shown in Figure 5.5.

The kinematic contacts condition needed (continuous contact between the block and the slider/base without slipping or jumping) are provided by attaching the block to the slider via a set of plastic tapes as described in Section 4.3.1 (Figure 4.7) enabling free rotation of the block around both bottom corners without sliding and vertical detachment from the slider.

The slider–block system is set in motion by cutting the left-hand string, thus subjecting the initially resting system to a constant acceleration of magnitude $a_0 = \frac{m_a g}{m_s + m + m_a}$. For the given slider–block system, therefore, the constant acceleration a_0 is completely defined by the hanging mass m_a which may be freely varied.

The exposure t_a of the system to such acceleration is defined by this mass *and* the initial distance from the bottom of the hanging mass to the floor h_a as $t_a = \sqrt{\frac{2h_a}{g} \frac{m_s + m + m_a}{m_a}}$. In other words, for the chosen m_a defining a_0, varying the distance h_a provides different durations t_a of base acceleration function.

The air track device used should be long enough so that the slider can move uniformly after the acceleration function drops to zero before the block either overturns or settles to rest. In this way the shock occurring when the slider finally impacts the stopper at the end of the air track device does not affect the experimentally obtained results.

5.1.3 Results

A range of measurements is then made for given mass of the slider $m_s = 120\,\text{g}$ and the block with width $b = 0.02$ m, height $h = 0.09$ m, mass $m = 95.5\,\text{g}$, its half-diagonal $R = 0.0461\,\text{m}$, angle of slenderness $\alpha = 0.2187$ rad, and different values of the input data $(m_a, h_a) \Leftrightarrow (a_0, t_a)$, for which the block motion is characterised as translation, rocking or overturning by visual observation. The hanging masses are chosen from within the range $m_a \in [0.015\,\text{g}, 0.115\,\text{g}]$ and the vertical distances from within the range $h_a \in [0.2\,\text{cm}, 25.5\,\text{cm}]$. The results of the experiment are shown in Figure 5.6 for a variety of input data.

5.1.3.1 Slender block

The regions describing the excitation conditions resulting in pure translation, rocking and overturning theoretically predicted from equation (5.3) and shown in Figure 5.2 are to a certain extent confirmed by the tests conducted (see Figure 5.6).
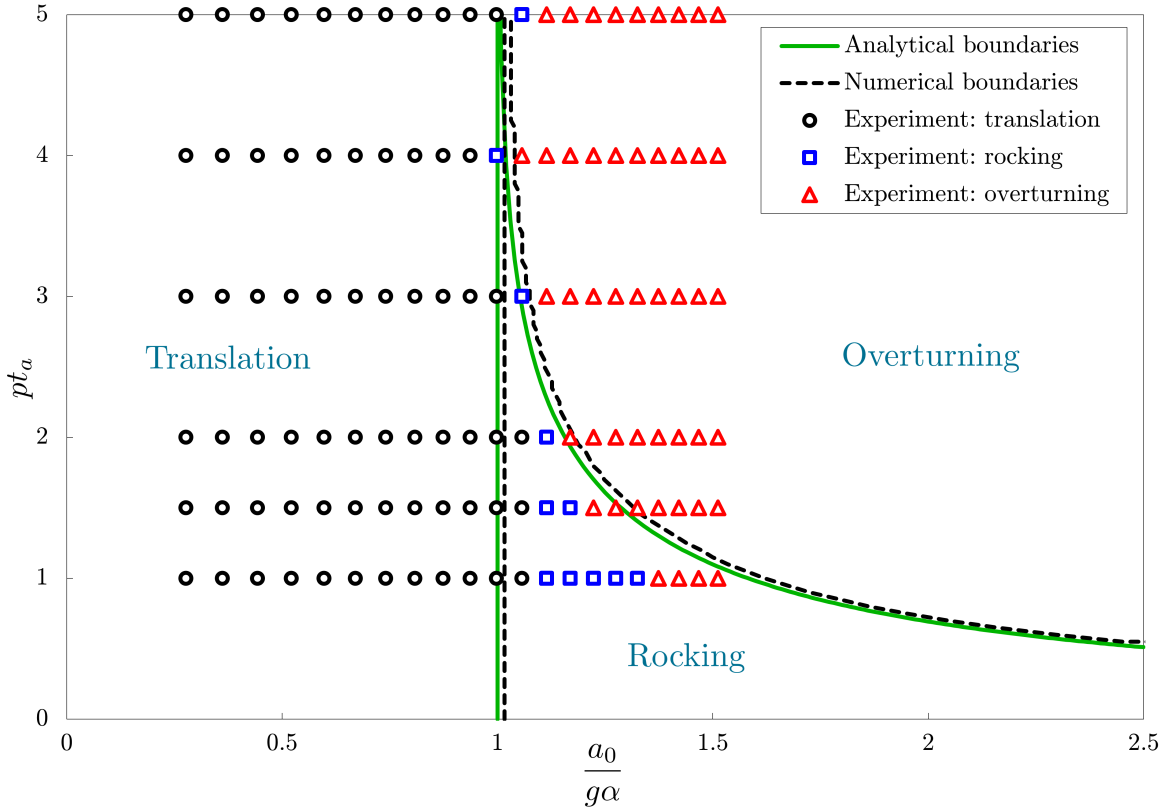

Figure 5.6: Experimental results for overturning/rocking/translation of the block due to a constant acceleration of finite duration

In the experiments the blocks sometimes overturn when subject to excitation which results in stable rocking in the numerical analysis and is outside the boundary leading to overturning conditions obtained from the analytical solution (the red marks sometimes appear on the left side of the black and green boundaries between rocking and overturning). One of the reasons for that is that the air resistance in not accounted for in the equations of motion, while it affects the dynamic behaviour of such small blocks.

5.1.4 Conclusion

Clearly, the experimentally obtained results in general agree quite well with the analytically and the numerically obtained results. The small differences can be accredited

to already stated air resistance as well as caused by an imperfect manual input of the problem parameters.

It is important to notice that the coefficient of restitution does not affect the outcome of the dynamic analysis for a block subject to constant ground acceleration of finite duration owing to the fact that the block starts rotating around one corner and if overturning occurs it happens around the same corner, without any impact with the base. If the block sways back and then goes into rotation around the other corner after the acceleration drops to zero (i.e. $t_{imp} > t_a$), the block cannot go through larger rotations, and does never overturn.

5.2   ... single-wave harmonic excitation

This section is based on the results and discussion from paper [61]:
Čeh, N., and Jelenić, G., "Rocking stability of rigid prismatic blocks during single-wave harmonic excitation: numerical investigation and experimental validation", submitted for publication

Although a number of authors have addressed the case of a single block rocking due to a single-wave base acceleration function, such rocking and its outcome in terms of overturning or no-overturning, is still not characterised accounting for the real energy-loss during rocking via an appropriate coefficient of restitution. Also, the overturning outcome during a certain acceleration function is not experimentally validated.

For this reason, here we analyse the stability of a block during simple harmonic ground acceleration function numerically and validate the results experimentally. The improved estimate of the restitution coefficient, introduced independently by Kalliontzis et al. [2] and by Chatzis et al. [3], is employed. The improved estimate, which is derived from the assumption that the resultant impulse at the time of impact acts at some other point than the corner of the block, proves to be a better approximation of the real restitution [58] than the widely used Housner's restitution [1].

The effect of the uncertainty of the position of the impact impulse to the rocking stability due to sine- and cosine-wave excitation is addressed in [3]. The objective here is to derive the conditions under which a block overturns when subjected to a single sine-wave or cosine-wave acceleration, which are safer than those available in the literature [6].

The two restitution formulas become increasingly similar with the increase in block's slenderness, but in general η_H overestimates block's stability, sometimes significantly (as shown in Chapter 4). On the other hand, η_M involves an additional parameter, for which a method to determine it has to be devised. Such a method is presented and used in Chapter 4.

5.2.1 Rocking stability

Stability of the block is characterised based on whether the block overturns or rocks in a stable fashion (and finally settles) during the excitation or after it drops to zero. Rocking stability is assessed using the described numerical procedure based on the nonlinear equation of motion by running the algorithm multiple times for different excitation frequencies and amplitudes and documenting the outcome in the frequency-amplitude space. In this way the areas with the excitation conditions under which overturning occurs and those under which rocking in stable fashion occurs are obtained. The boundary between these areas in the case of sine-wave acceleration is presented in Figures 5.7 and 5.8 for two slenderness ratios using both restitution formulas (with $k = 0.75$ in case of η_M). The results in Figures 5.7 and 5.8 and in the rest of the paper are presented in terms of the normalised angular frequency $\frac{\omega}{p}$ on the horizontal axis and the normalised acceleration amplitude $\frac{a_0}{\alpha g}$ on the vertical axis. These figures stress the importance of the improved restitution estimate η_M, as it is clear that η_H may seriously overestimate a block's stability against overturning.
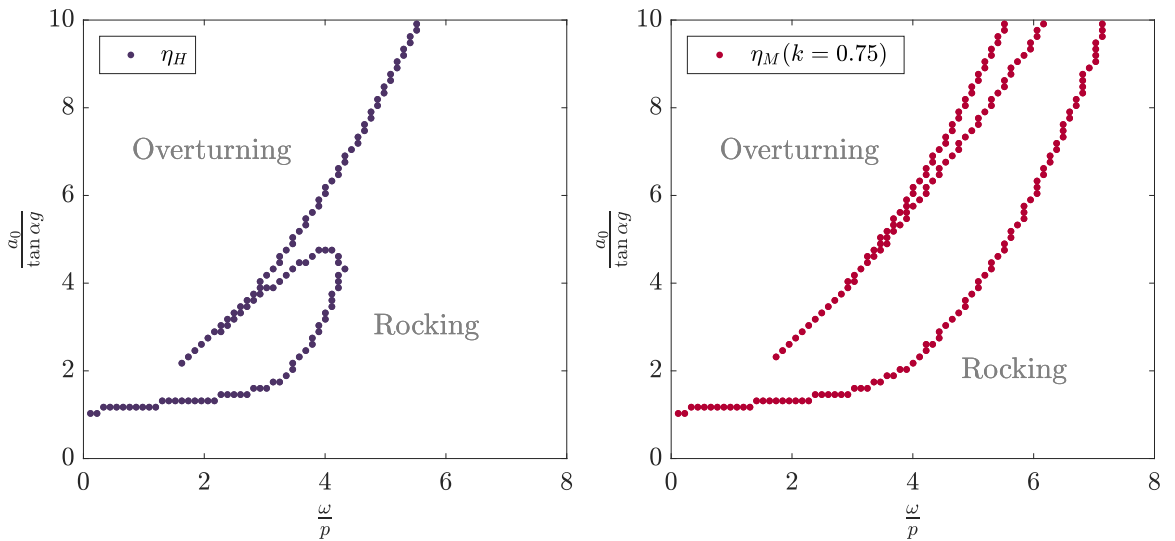

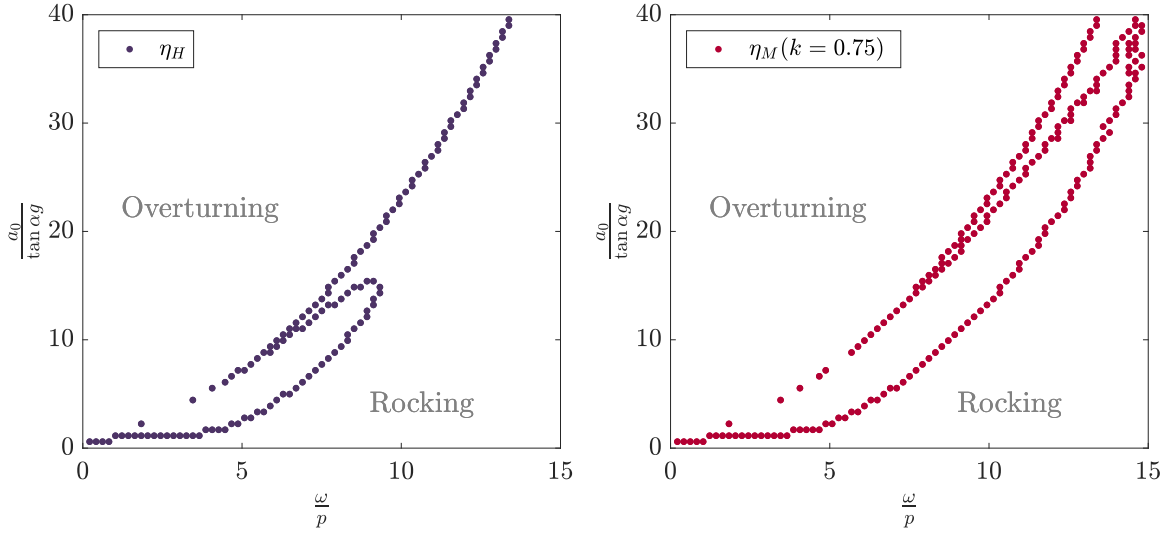Figure 5.7: Stability graph due to a single sine wave for blocks with $h/b = 2.25$

Figure 5.8: Stability graph due to a single sine wave for blocks with $h/b = 4.5$

It is usually assumed that such graphs can be applied to estimate rocking stability of a block with slenderness angle α regardless of the size of the block. This is acceptable if the restitution coefficient is independent of the size of the block since an increase in the restitution coefficient causes a significant increase in the overturning area [3], as can be seen when comparing the two graphs either in Figure 5.7 or Figure 5.8.

A previous study of free rocking [58] has shown that the restitution coefficient decreases with the increase in block's size. Following on from there, the objective here is to assess stability of blocks of different geometries subject to the pulse excitation described with an improved restitution estimate from [58] taken into account.

5.2.2 Rocking stability using an improved restitution estimate

Here we try to characterise the rocking more precisely using an estimate for k in equation (4.5) obtained from the series of free rocking experiments reported in [58] and described in detail in Chapter 4.

5.2.2.1 Geometry

Stability of the blocks of two different slendernesses and two different sizes are examined here so that both the slenderness effect and the size effect may be investigated. The properties and the corresponding Housner's restitution coefficients of the four blocks examined in this study are shown in Table 5.1, where the thickness of the

blocks is equal to their width b. The actual denotation used for the blocks follows that introduced in [58] and in Chapter 4.

Table 5.1: Geometry, η_H, and η_M for the analysed blocks

Block	m [g]	b [m]	h [m]	$\frac{h}{b}$	α [rad]	R [m]	p	η_H	η_M
B3M	544.4	0.045	0.10125	2.25	0.4182	0.0554	11.524	0.7526	0.8106
B6M	1089.6	0.045	0.2025	4.5	0.2187	0.1037	8.423	0.9294	0.9472
B3L	1284.3	0.06	0.135	2.25	0.4182	0.0739	9.978	0.7526	0.8598
B6L	2569.2	0.06	0.27	4.5	0.2187	0.1383	7.294	0.9294	0.9617

For the blocks in Table 5.1 the unknown parameter k necessary to calculate η_M in (4.5) is obtained in [58] as $k = 0.8608$ for a set of nine medium-sized blocks ($b = 0.045$ m) with slenderness ranging from $\frac{h}{b} = 1.5$ to $\frac{h}{b} = 9.75$ and $k = 0.7306$ for the corresponding set of large blocks ($b = 0.06$ m), obtained as average values. The corresponding η_M are shown in Table 5.1.

5.2.2.2 Single sine-wave acceleration

Rocking stability and overturning conditions for a rigid block due to a single sine-wave acceleration excitation highly depend on the restitution coefficient. The overturning condition obtained from the numerical procedure described earlier using $\Delta t = 0.001$ s and the Newton-Raphson convergence norm $1 * 10^{-9}$ for the blocks and the corresponding restitution coefficients given in Table 5.1 are shown in Figures 5.9 and 5.10 for the blocks with slenderness ratio $\frac{h}{b}$ of 2.25 and 4.5 , respectively.
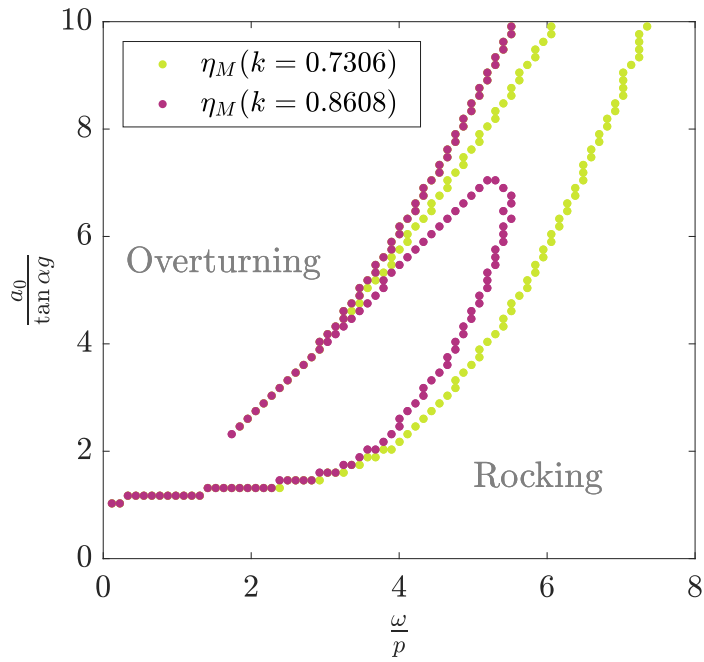
Figure 5.9: Stability graph for a single sine wave acceleration excitation for blocks with $\frac{h}{b} = 2.25$: B3M and B3L
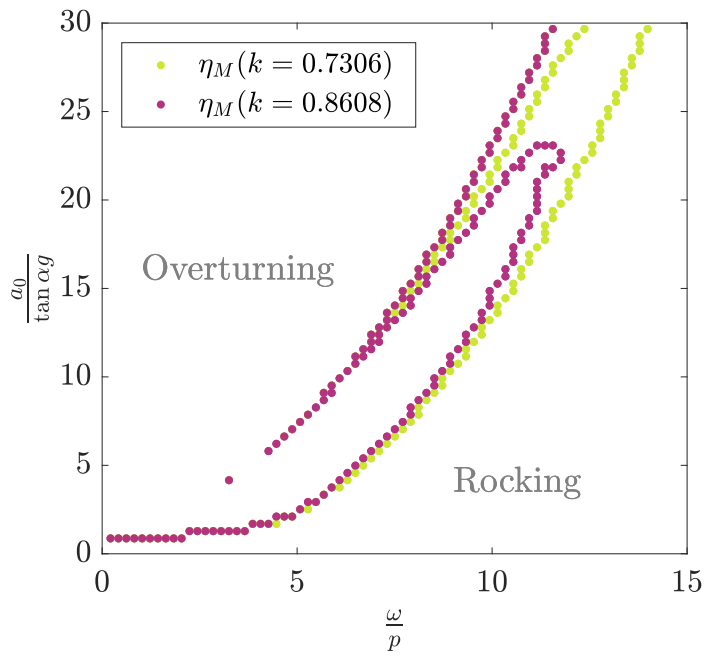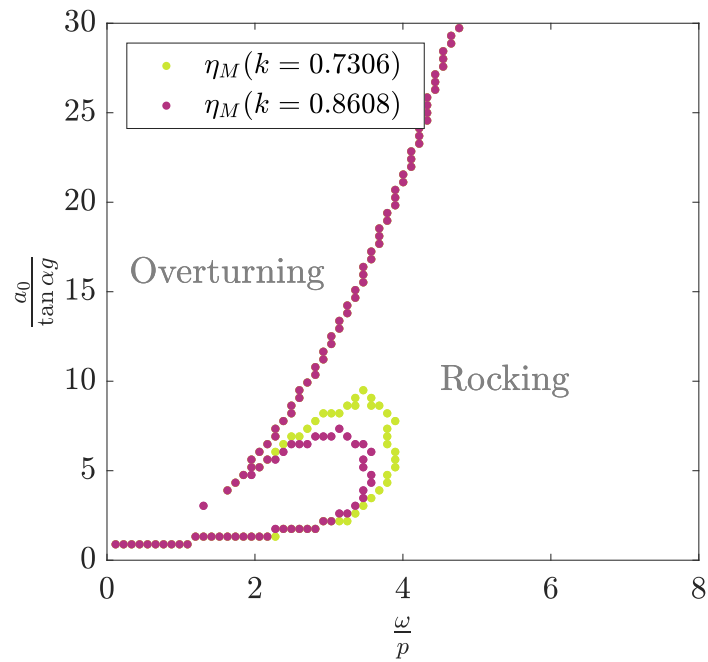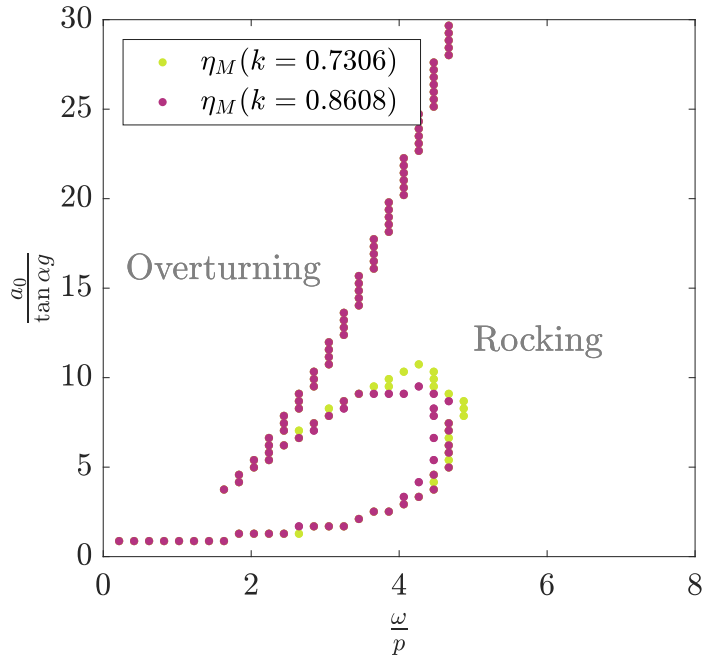

Figure 5.10: Stability graph for a single sine wave acceleration excitation for blocks with $\frac{h}{b} = 4.5$: B6M and B6L

5.2.2.3 Single cosine-wave acceleration

The overturning conditions for a rigid block due to a single cosine-wave excitation acceleration obtained from the described numerical procedure vary only slightly with variation in block's size. Also, the overturning conditions are not strongly dependent of the restitution coefficient, which can be seen in Figures 5.11 and 5.12 for the blocks with slenderness ratio $\frac{h}{b}$ of 2.25 and 4.5, respectively.

Figure 5.11: Stability graph for a single cosine wave acceleration excitation for blocks with $\frac{h}{b} = 2.25$: B3M and B3L

Figure 5.12: Stability graph for a single cosine wave acceleration excitation for blocks with $h/b = 4.5$: B6M and B6L

5.2.3 Experimental set-up

5.2.3.1 Contact conditions in the model

In order to avoid slipping and jumping (detachment) and to assure only rocking motion, a specially designed system of tapes described in Section 4.3.1 (Figure 4.7) is also used here.

5.2.3.2 Excitation and shaking table capacities

The excitation is experimentally performed by means of a biaxial shaking table Quanser ST-III run by a LabWiev-based software, which controls the position of the table.

The desired acceleration excitation function, which is a part of the equation of motion in the simulations, should be integrated twice to get the position excitation function and as such given to the shaking table for the experimental tests. Due to the inertia of the table itself, the initial velocity of the system can only be equal to zero and rise gradually after that. For this reason, we can experimentally simulate

either a cosine-wave acceleration excitation $\ddot{u}(t) = a_0 \cos(\omega t)$ leading to

$$\dot{u}(t) = \frac{a_0}{\omega} \sin(\omega t),$$ (5.4)

$$u(t) = \frac{a_0}{\omega^2} [1 - \cos(\omega t)],$$

or a sine-wave acceleration excitation $\ddot{u}(t) = a_0 \sin(\omega t)$ leading to

$$\dot{u}(t) = \frac{a_0}{\omega} [1 - \cos(\omega t)],$$ (5.5)

$$u(t) = \frac{a_0}{\omega} \left[t - \frac{1}{\omega} \sin(\omega t) \right].$$

These functions are shown in Figure 5.13.
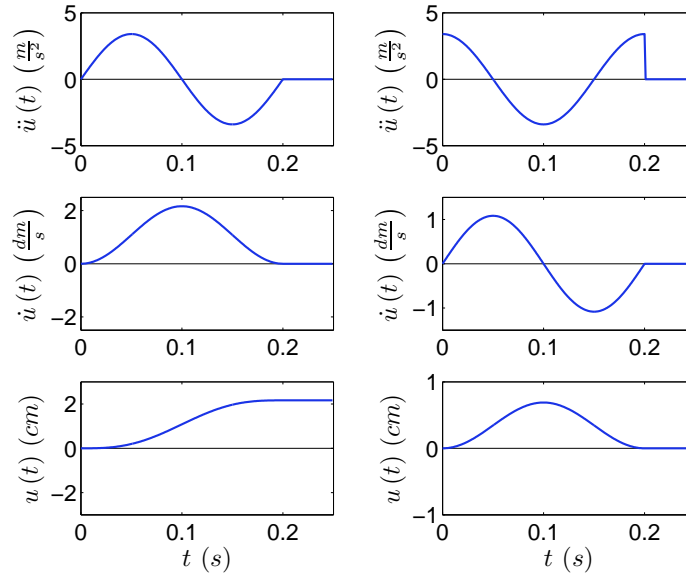
Figure 5.13: Sine- (left) and cosine-wave (right) acceleration excitation with the corresponding velocity and position functions

The shaking table system (Quanser ST-III) has the total gait of 10.8 cm in both directions, it can reach a velocity of 2.58 m/s and an acceleration of $3.21g$ with the load-mass roughly corresponding to our heaviest samples.

The experiments are carried out so that the two blocks of the same slenderness are put on top of the shaking table and excited at the same time with exactly the same acceleration function, as can be seen in Figure 5.14.
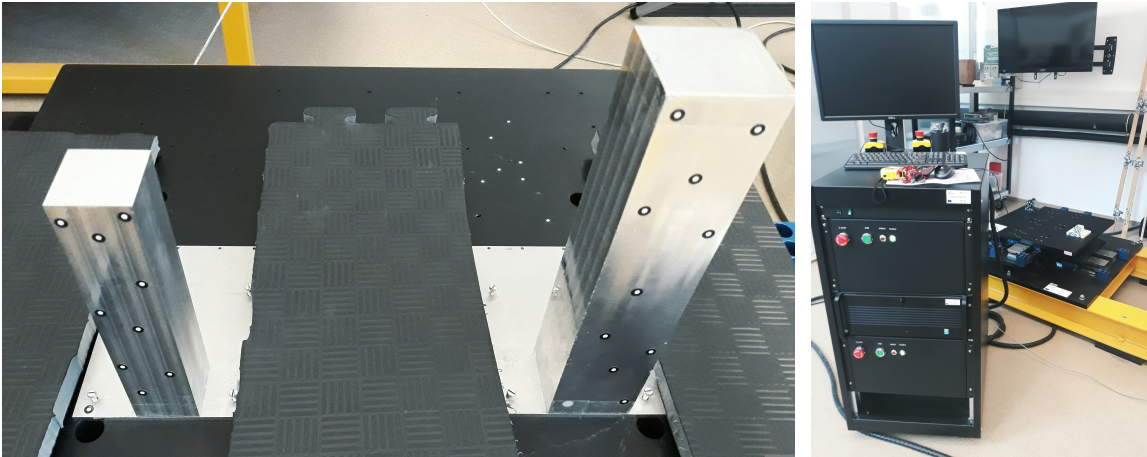
Figure 5.14: Two blocks of the same slenderness ratio but different size (left) on the shaking table system Quanser ST-III (right)

5.2.3.3 Measurement of the output excitation function

In each experiment the displacement function actually performed by the shaking table slightly differs from the input displacement function, owing to the inertia of the table and the samples. The displacement is measured by a linear encoder with one million counts per meter each 0.002 seconds. These results are numerically differentiated with respect to time twice (using the mid-point rule) to check for the 'real' amplitude and frequency of the acceleration function of the table. Furthermore, the acceleration is measured by a biaxial accelerometer embedded in the shaking table system each 0.002 seconds. The results obtained from post-processing the encoder measurement and from accelerometers measurement has shown to be close to the input values given to the shaking table. For this reason the experimental results in the rest of this work are presented with respect to the input amplitude and acceleration function.

5.2.4 Experimental validation of the algorithm for sine-wave acceleration

The set of four blocks - two bulky blocks with slenderness ratio $\frac{h}{b} = 2.25$ and two slender blocks with slenderness ratio $\frac{h}{b} = 4.5$ - subjected to a sine-wave acceleration function is chosen for experimental validation. The acceleration function is input via a single sine-wave displacement function added to a linear displacement function (5.5), which satisfies the condition of zero initial velocity of the shaking table, as described in the previous section. The sine-wave excitation described in Section 5.2.3.2 is the only one chosen in the experimental analysis because it is much more suitable for

testing sensitivity to overturning upon variation of the restitution coefficient (see Section 5.2.2.2).

The experiments are performed for each acceleration amplitude starting from the highest acceleration frequency and after each experiment resulting in stable rocking the frequency is lowered. This is repeated until overturning is reached. The experiments close to the boundary between overturning and not-overturning regions are repeated at least three times and the outcome has proven to be repeatable.

5.2.4.1 Slender blocks $\left(\frac{h}{b} = 4.5\right)$

The experimentally obtained results for both slender blocks B6M and B6L are shown in Figures 5.15 and 5.16, along with the simulation results with the average parameter k for each size of the block. These experiments strongly validate the numerically obtained overturning conditions with the restitution coefficient as reported in [58] based on the free rocking tests.
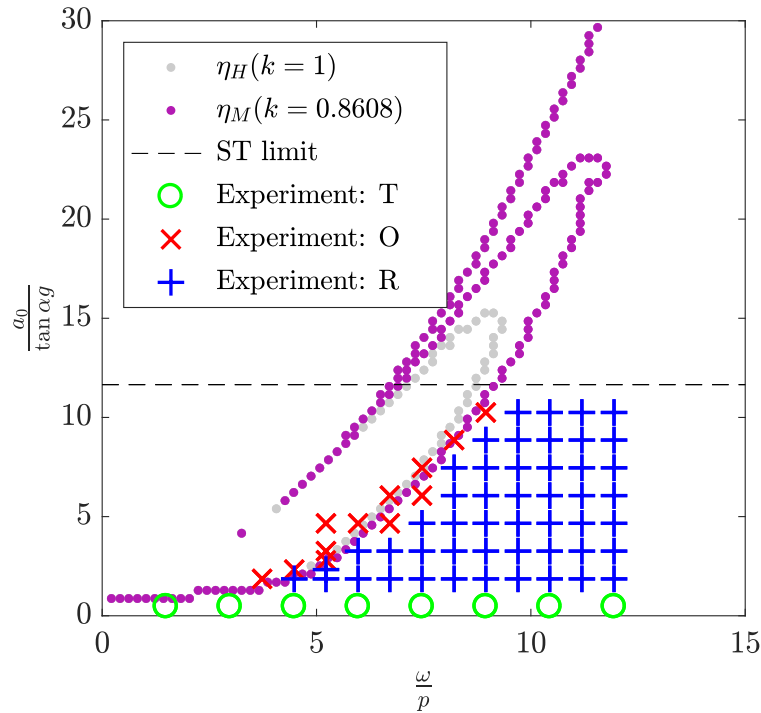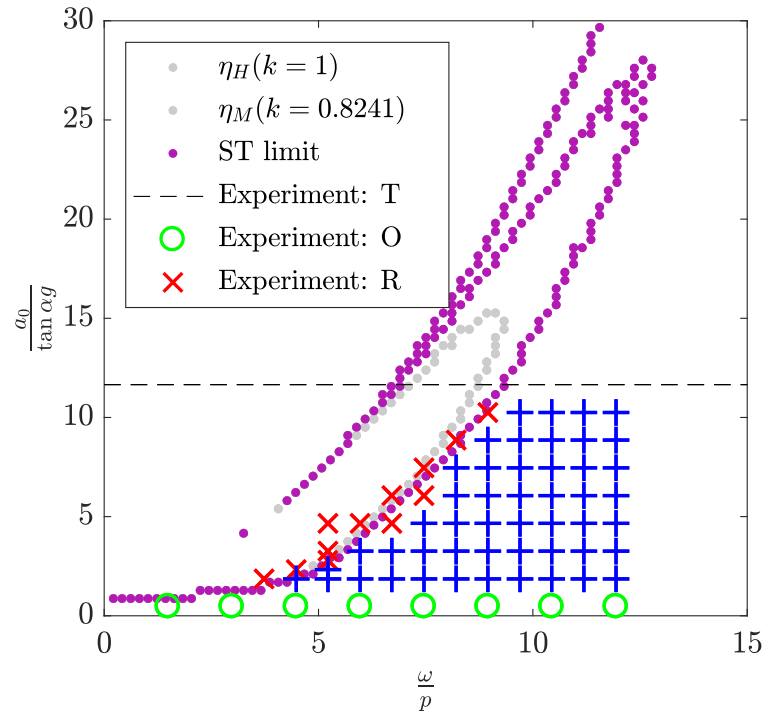

Figure 5.15: Stability graph due to a single sine wave for block B6M with $h/b = 4.5$ (T - translation, O - overturning, R - rocking)
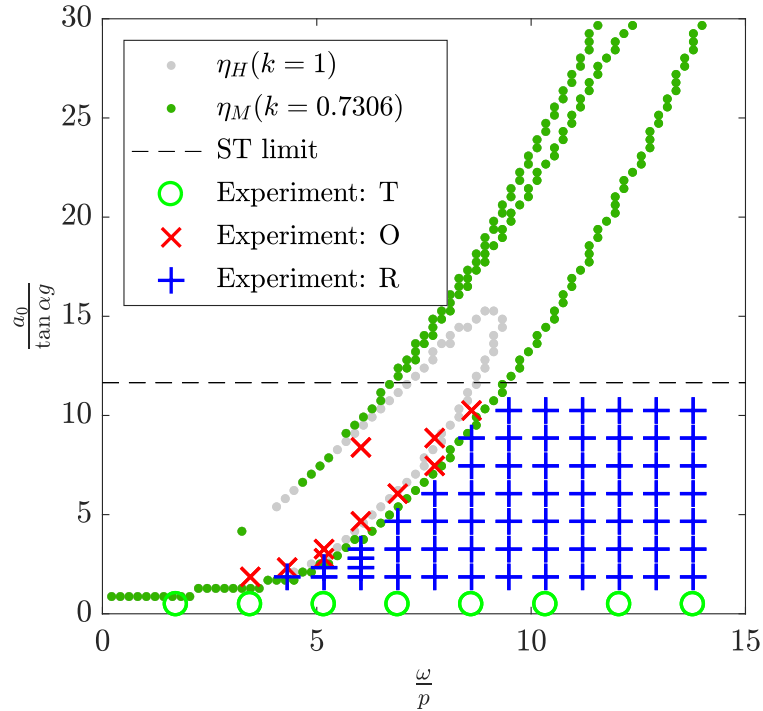
Figure 5.16: Stability graph due to a single sine wave for block B6L with $h/b = 4.5$ (T - translation, O - overturning, R - rocking)

The shaking table system limit is declared as $3.21g$ but, even before reaching the limit, the actual acceleration output starts to resemble a double constant function more than a single sine-function. This prevents us from checking the overturning conditions for the amplitudes of acceleration functions larger that cca $25 \frac{m}{s^2} \approx 2.55g$ (black dashed line in Figures 5.15 and 5.16).

In Figures 5.17 and 5.18 the experimental results are also compared to the simulation results with the parameter k taken as the exact value obtained for that specific block in Chapter 4 ($k = 0.8241$ for B6M, $k = 0.7214$ for B6L). The boundary between overturning and non-overturning regions has now somewhat changed - specifically, the overturning area is noticeably larger for the smaller block, but for the acceleration range tested, the experimental results compare equally well with the simulation results.

Figure 5.17: Stability graph due to a single sine wave for block B6M with $h/b = 4.5$ (T - translation, O - overturning, R - rocking)
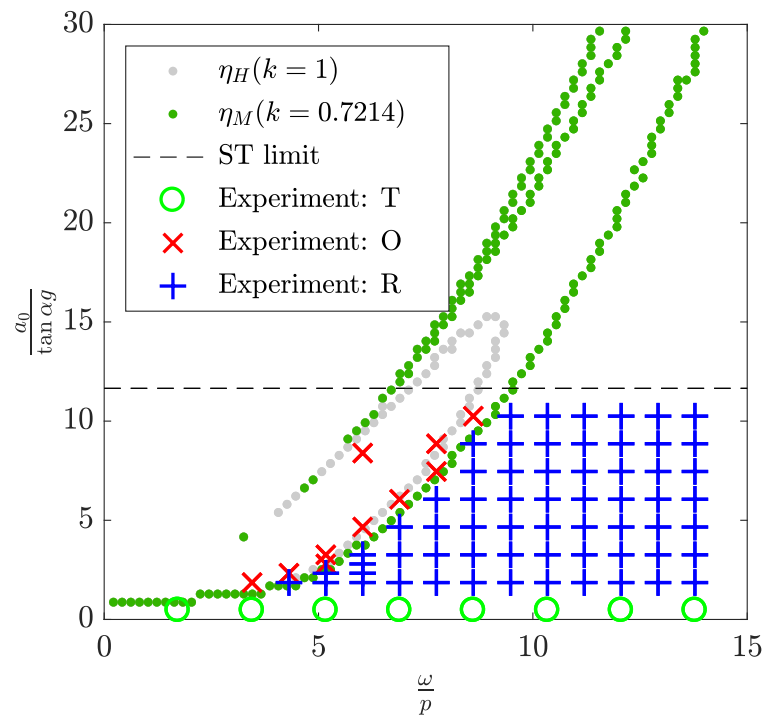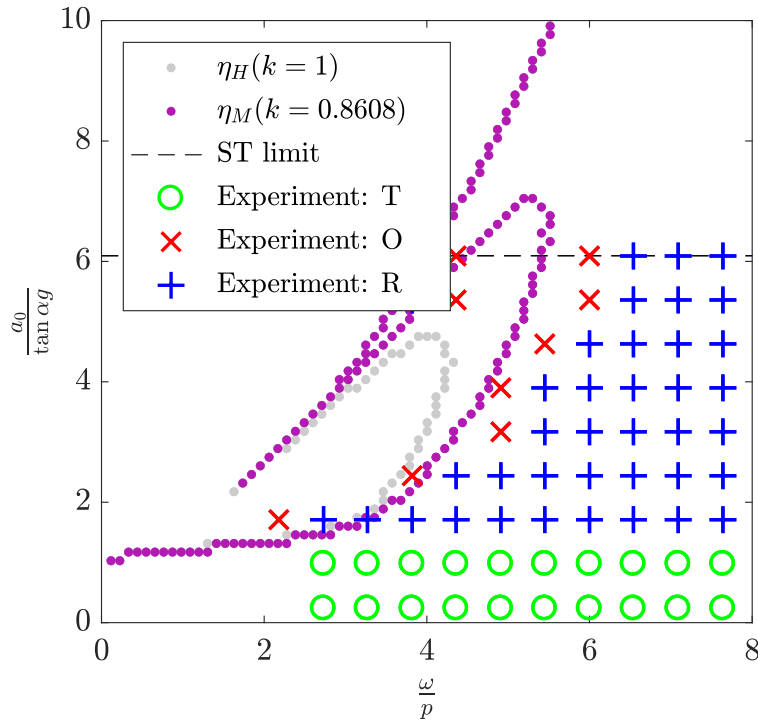

Figure 5.18: Stability graph due to a single sine wave for block B6L with $h/b = 4.5$ (T - translation, O - overturning, R - rocking)

5.2.4.2 Bulky blocks $\left(\frac{h}{b} = 2.25\right)$

The experimentally obtained results for both bulky blocks B3M and B3L are shown in Figures 5.19 and 5.20 along with the simulation results with the average restitution for each size from Chapter 4 taken into account. The experimental results strongly validate the simulation results in case of the larger block B3L. However, the smaller block B3M overturns in the experiments in the area where the simulations show that stable rocking should occur.

Figure 5.19: Stability graph due to a single sine wave for block B3M with $h/b = 2.25$ (T - translation, O - overturning, R - rocking)

In Figures 5.21 and 5.22 the experimental results are again compared to the simulation results with the exact value of the parameter k for each block from the free-rocking study in Chapter 4 ($k = 0.7595$ for B3M, $k = 0.7259$ for B3L). The overturning area for block B3M is now substantially larger and such a simulation agrees with the experimental results much better.
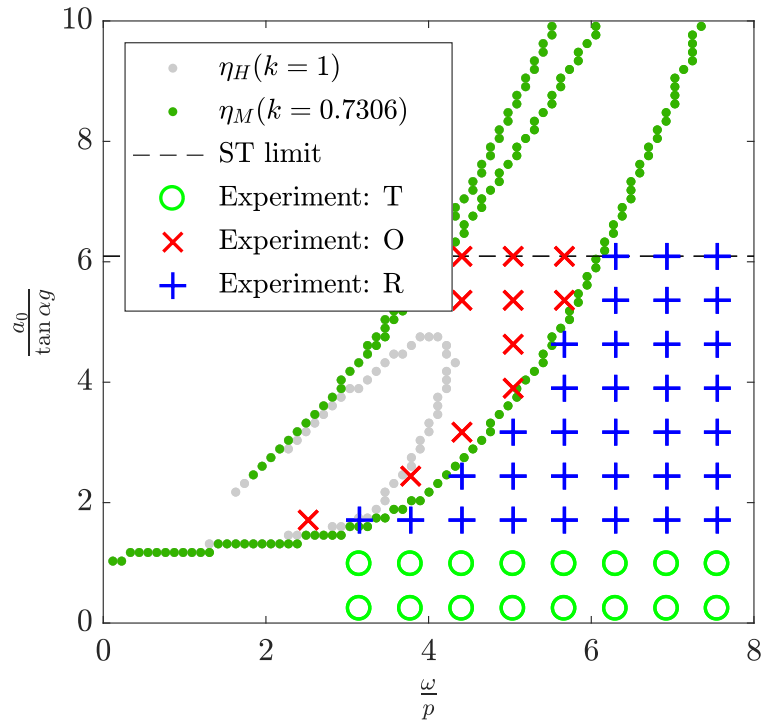
Figure 5.20: Stability graph due to a single sine wave for block B3L with $h/b = 2.25$ (T - translation, O - overturning, R - rocking)
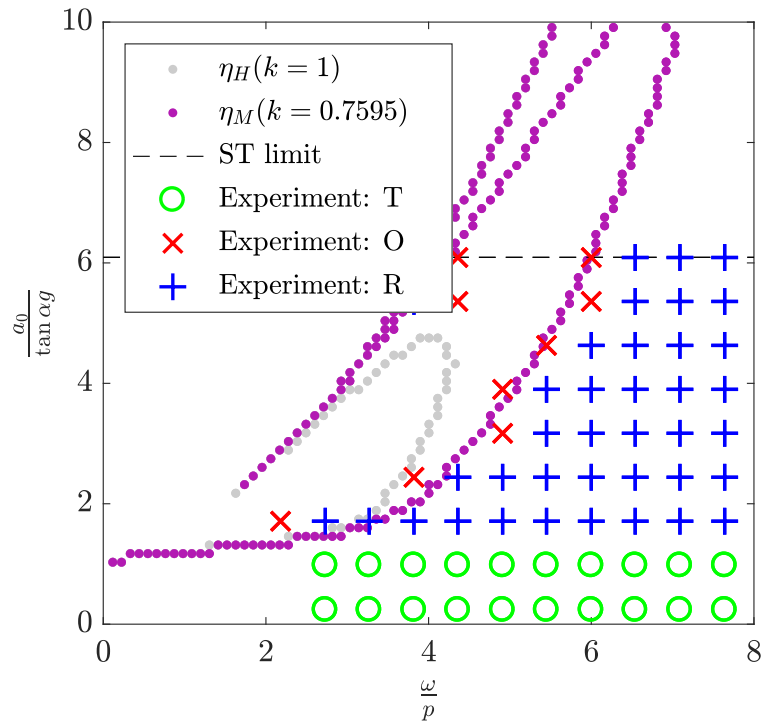

Figure 5.21: Stability graph due to a single sine wave for block B3M with $h/b = 2.25$ (T - translation, O - overturning, R - rocking)
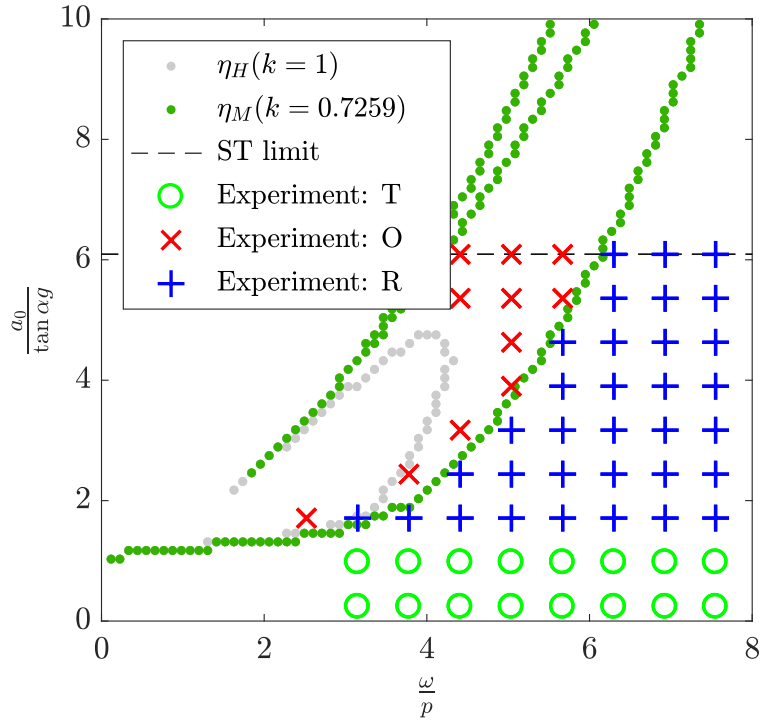
Figure 5.22: Stability graph due to a single sine wave for block B3L with $h/b = 2.25$ (T - translation, O - overturning, R - rocking)

5.2.5 Discussion and conclusion

A numerical procedure to obtain overturning conditions for a single rigid block rocking on top of a rigid base, without sliding or jumping, due to a single harmonic wave excitation acceleration is developed and validated against experiments. The code involves an impact detection procedure, and takes into account energy loss during each impact of the block with the base via a restitution coefficient as described in Chapter 4. Both the well-known Housner's restitution coefficient [1], and a recently reported modified restitution coefficient [2, 3] are analysed for their predictive power as stability estimates. The actual point of impact, needed in the latter, is taken from a free rocking series of tests described in Chapter 4.

A series of controlled experiments with aluminium blocks on a shaking table subjected to a single sine-wave acceleration function is designed and carried out. The experiments are conducted for two bulky blocks (slenderness $\frac{h}{b} = 2.25$) and two slender blocks (slenderness $\frac{h}{b} = 4.5$) of different sizes.

The experimental validation proves that Housner's restitution formula is overly liberal and should be avoided in practical use. The modified formula [2, 3] is clearly a better fit to describe real energy loss during rocking, and is strongly encouraged if

the position of the impact impulse may be appropriately estimated. In this Chapter this has been performed in conjunction with the free rocking tests conducted earlier in Chapter 4.

The simulation involving larger blocks and the restitution coefficient [2, 3] with the additional parameter obtained in this way agree with the experiment very nicely, in contrast with the results using the original Housner's restitution, which is particularly visible for the bulky block.

The simulation involving smaller blocks is less precise but still supportive of the use of the modified restitution formula. It also shows that the method to estimate the impact position should be improved, which is what we plan to address in the future.

Chapter 6

Numerical analysis of rocking of a dual-block stack

A stack of two rigid rectangular blocks (of the same width) standing freely one on top of the other and lying on a rigid horizontal base is analysed here. The stack is exposed to a base excitation acceleration or is initially tilted and left to rock. The blocks and the base are assumed to be completely rigid. All the connections between the bodies in the system, which includes the connection between the top and the bottom block as well as the connection between the bottom block and the base, are such that no relative sliding or jumping (detachment) between them can occur. Thus, there is at least one contact point between the top and the bottom block, and between the bottom block and the base at any time.

6.1   Introduction

A stack comprised of two blocks where one is on top of the other is called a dual-block stack, a two-block stack, or a bi-block structure. When subjected to ground excitation, the dual-block structure starts to move. If the following assumptions are introduced the dual-block structure can succumb to either rocking rocking or translational motion along with the base [1]:

- the block and its base are rigid,

- the ground surface is horizontal,

- the block is symmetric with respect to the vertical central axis,

- the friction between the block and the ground, as well as between the two blocks, is high enough to prevent sliding at any time (or sliding can be prevented in some other way),

- only planar motion is considered,

- the impact of the block on the ground, as well as the impact between the two blocks, is not elastic, thus there is no jumping of the blocks and at least one contact point always exists between the bottom block and the ground, as well as between the top block and the bottom block.

If the base acceleration $\ddot{u}$ is lower than certain conditions (which are presented later in Section 6.4) the dual-block stack translates along with the base (see Figure 6.1). The blocks are defined by their widths, in this work taken to be equal, i.e. $b_1 = b_2 = b$, their heights h_1 and h_2, and their masses m_1 and m_2. The geometry of the blocks can also be defined by their angles of slenderness as $\alpha_1 = \tan^{-1} \frac{b}{h_1}$ and $\alpha_2 = \tan^{-1} \frac{b}{h_2}$, and their size via the lengths of their half-diagonals $R_1 = \frac{1}{2}\sqrt{h_1^2 + b}$ and $R_2 = \frac{1}{2}\sqrt{h_2^2 + b}$.
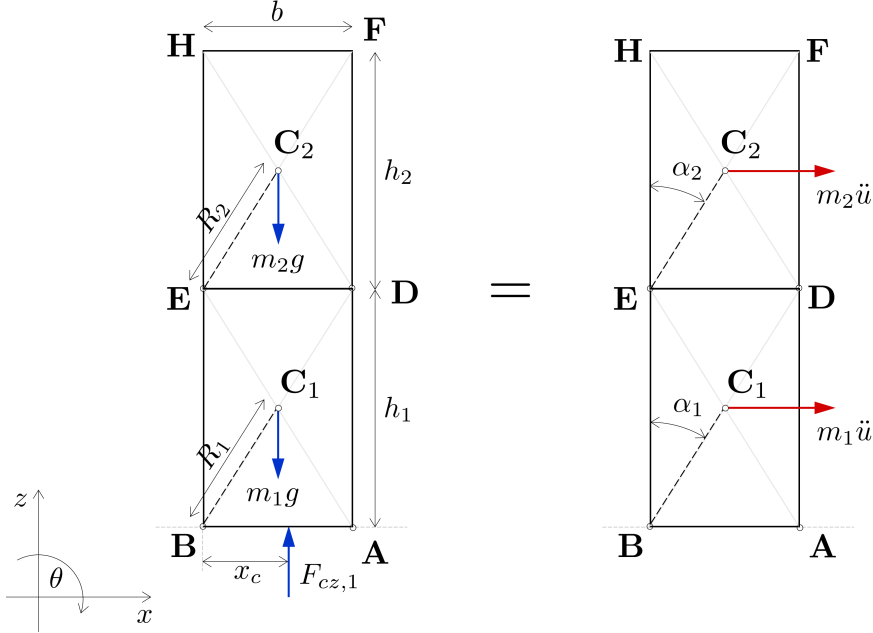

Figure 6.1: Free-body and mass-acceleration diagrams of a dual-block stack translating along with the base

On the other hand, if the acceleration $\ddot{u}$ exceeds these conditions, rocking is initiated. There are four different rocking configurations and each configuration consists

of two sub-configurations [45, 30, 4]. The total of eight different configurations during rocking of the stack are shown in Figure 6.2.
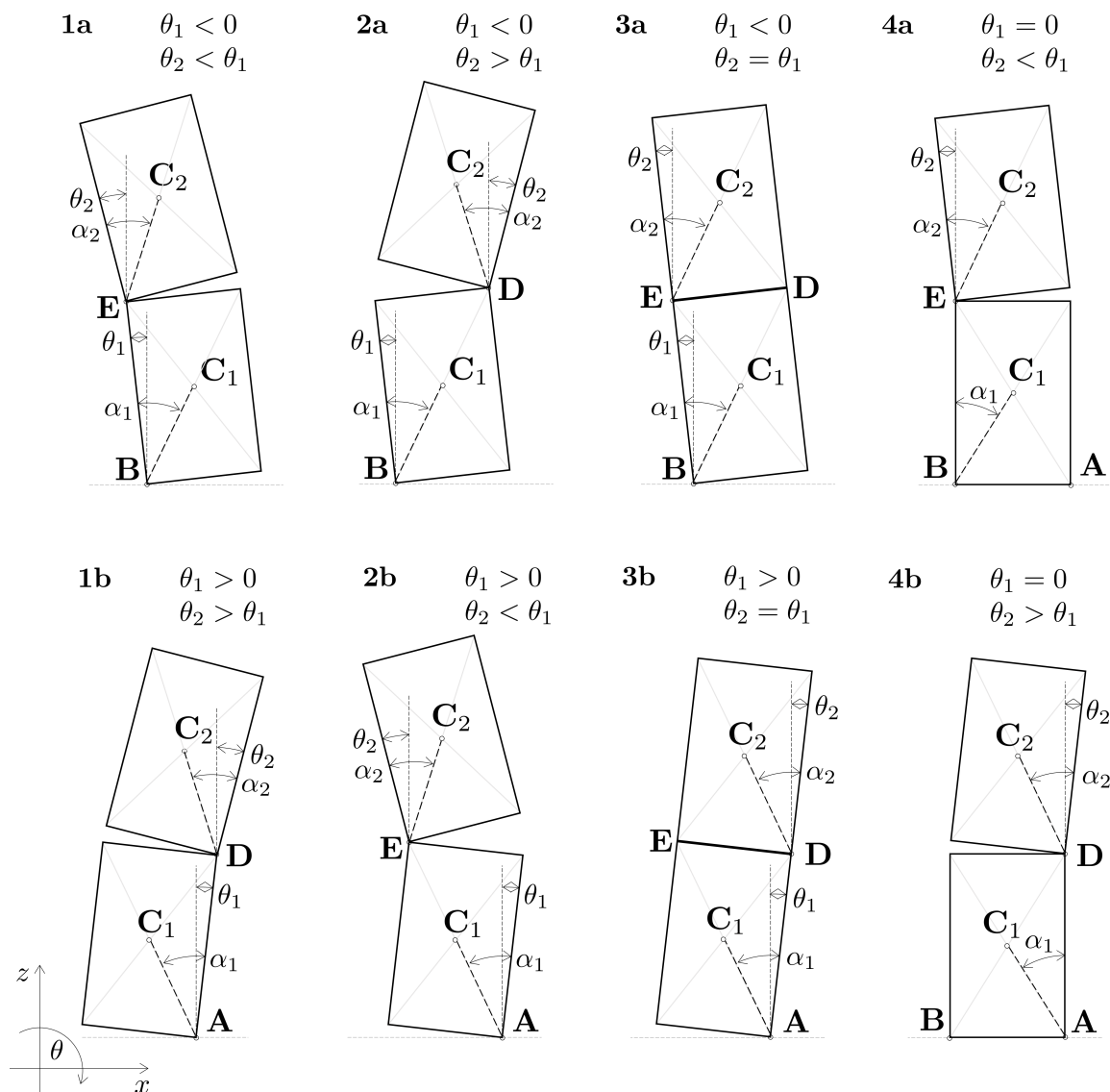

Figure 6.2: Possible configurations during rocking of a dual-block stack

The eight configurations are characterized by the sign of rotation of the lower block and the relative rotation of the bottom block with respect to the upper block. If the rotation of the bottom block is θ_1 and the rotation of the upper block is θ_2, then:

- **configuration 1a** occurs when $\theta_1 < 0$ and $\theta_2 < \theta_1$ and **configuration 1b** occurs when $\theta_1 > 0$ and $\theta_2 > \theta_1$,

- **configuration 2a** occurs when $\theta_1 < 0$ and $\theta_2 > \theta_1$ and **configuration 2b** occurs when $\theta_1 > 0$ and $\theta_2 < \theta_1$,

- **configuration 3a** occurs when $\theta_1 < 0$ and $\theta_2 = \theta_1$ and **configuration 3b** occurs when $\theta_1 > 0$ and $\theta_2 = \theta_1$,

- **configuration 4a** occurs when $\theta_1 = 0$ and $\theta_2 < 0$ and **configuration 4b** occurs when $\theta_1 = 0$ and $\theta_2 > 0$.

Rocking in each of the eight configurations is described with a separate set of equations of motion for the two-degree-of-freedom system.

Below, the set of equations of motion of each configuration is derived first and after that the conditions for initiation of each configuration and/or transition between different configurations are derived.

6.2   Configurations and equations of motion

Let the equations of motion be derived from Lagrange's equation of motion [62]

$$\frac{d}{dt}\left(\frac{\partial L}{\partial \dot{\theta}_i}\right) - \frac{\partial L}{\partial \theta_i} = 0, \tag{6.1}$$

where

$$L = E_K - E_P, \tag{6.2}$$

i.e. the Lagrangian L is the difference between the kinetic energy E_K and the potential energy E_P of the system. Equation (6.2) can be substituted into equation (6.1) which gives

$$\frac{d}{dt}\left(\frac{\partial E_K}{\partial \dot{\theta}_i} - \frac{\partial E_P}{\partial \dot{\theta}_i}\right) - \frac{\partial E_K}{\partial \theta_i} + \frac{\partial E_P}{\partial \theta_i} = 0. \tag{6.3}$$

Below, the equations of motion for each configuration are derived (following [4], taking into account large rotations θ_1 and θ_2, as well as an arbitrary geometry of the blocks defined by α_1 and α_2 (which can be slender or bulky).

6.2.1   Nonlinear equations of motion

The equations of motion for each configuration are derived below step by step. All the equations below are restricted to the case when both blocks have the same width $(b_1 = b_2 = b)$.

6.2.1.1 Configuration 1a

The dual-block system has two degrees of freedom: the angle of rotation of the bottom block, θ_1, and the angle of rotation of the top block, θ_2, hence the equation (6.3) has to be written for $i = 1, 2$. Let us derive the kinetic and potential energy of the system moving in configuration 1a, based the kinematics shown in Figure 6.3.
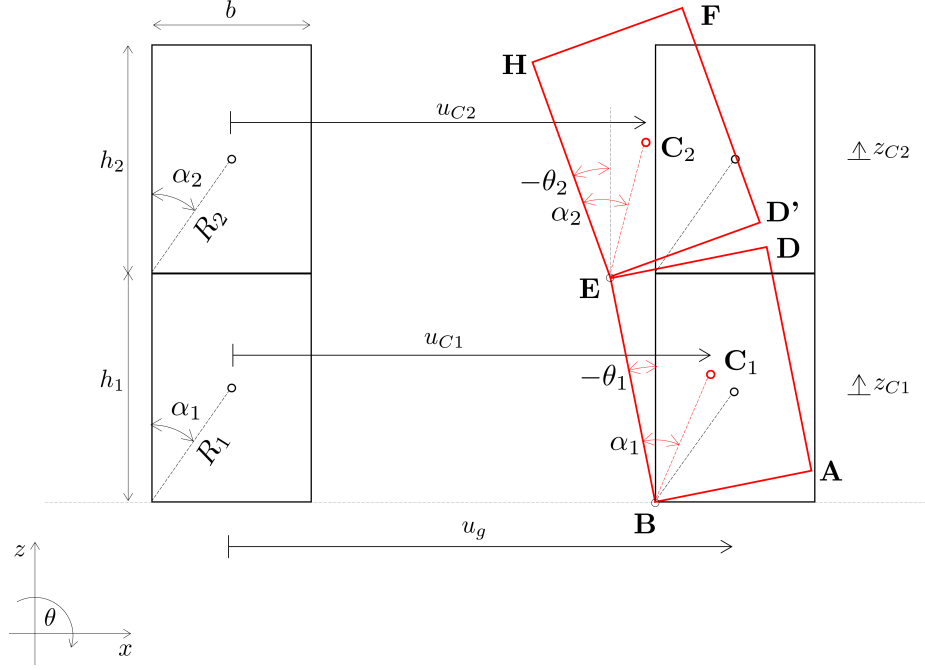

Figure 6.3: Displacements of the dual-block stack: translation and rotation in configuration 1a

The displacements of the blocks' centroids C_1 and C_2 in the referent coordinate system shown are

$$u_{C1} = u_g - \frac{b}{2} + R_1 \sin(\alpha_1 + \theta_1) \tag{6.4}$$

$$z_{C1} = R_1 \cos(\alpha_1 + \theta_1) - \frac{h_1}{2} \tag{6.5}$$

and

$$u_{C2} = u_g - \frac{b}{2} - h_1 \sin(-\theta_1) + R_2 \sin(\alpha_2 + \theta_2) \tag{6.6}$$

$$z_{C2} = h_1 \cos(-\theta_1) + R_2 \cos(\alpha_2 + \theta_2) - \left(h_1 + \frac{h_2}{2}\right). \tag{6.7}$$

The time derivatives of these displacements – the velocities – are

$$\dot{u}_{C1} = \dot{u}_g + R_1 \dot{\theta}_1 \cos(\alpha_1 + \theta_1) \tag{6.8}$$

$$\dot{z}_{C1} = -R_1\dot{\theta}_1 \sin\left(\alpha_1 + \theta_1\right) \tag{6.9}$$

and

$$\dot{u}_{C2} = \dot{u}_g + h_1\dot{\theta}_1 \cos\left(-\theta_1\right) + R_2\dot{\theta}_2 \cos\left(\alpha_2 + \theta_2\right) \tag{6.10}$$

$$\dot{z}_{C2} = h_1\dot{\theta}_1 \sin\left(-\theta_1\right) - R_2\dot{\theta}_2 \sin\left(\alpha_2 + \theta_2\right). \tag{6.11}$$

The total kinetic energy E_K of the dual-block stack is then

$$E_K = \frac{1}{2}m_1\left(\dot{u}_{C1}^2 + \dot{z}_{C1}^2\right) + \frac{1}{2}I_{C1}\dot{\theta}_1^2 + \frac{1}{2}m_2\left(\dot{u}_{C2}^2 + \dot{z}_{C2}^2\right) + \frac{1}{2}I_{C2}\dot{\theta}_2^2, \tag{6.12}$$

where $I_{C1} = \frac{m_1 R_1^2}{3}$ and $I_{C2} = \frac{m_2 R_2^2}{3}$ are the mass moments of inertia of the bottom and the top block with respect to their centroids C_1 and C_2, respectively. After a little bit of algebra equation (6.12) can be rewritten as

$$\begin{aligned} E_K = {} &\frac{1}{2}I_{O1}'\dot{\theta}_1^2 + \frac{1}{2}I_{O2}\dot{\theta}_2^2 + \frac{1}{2}m_1\left[\dot{u}_g^2 + 2R_1\dot{u}_g\dot{\theta}_1 \cos\left(\alpha_1 + \theta_1\right)\right] + \\ &\frac{1}{2}m_2\left[\dot{u}_g^2 + 2\dot{u}_g h_1\dot{\theta}_1 \cos\left(-\theta_1\right) + 2\dot{u}_g R_2\dot{\theta}_2 \cos\left(\alpha_2 + \theta_2\right)\right. \\ &\left. \qquad\qquad\qquad\qquad + 2h_1 R_2\dot{\theta}_1\dot{\theta}_2 \cos\left(-\theta_1 + \alpha_2 + \theta_2\right)\right], \quad (6.13) \end{aligned}$$

where the moments of inertia are

$$I_{O1}' = \frac{4}{3}m_1 R_1^2 + m_2 h_1^2 \tag{6.14}$$

and

$$I_{O2} = \frac{4}{3}m_2 R_2^2, \tag{6.15}$$

written in this form so that they can be easily compared to the results from the literature [4].

The total potential energy E_P of the dual-block stack measured from the position $\frac{h_1}{2}$ above the ground is

$$E_P = m_1 g z_{C1} + m_2 g\left(\frac{h_1}{h_2} + z_{C2}\right) \tag{6.16}$$

or

$$E_p = m_1 g\left[R_1 \cos\left(\alpha_1 + \theta_1\right) - \frac{h_1}{2}\right] + m_2 g\left[h_1 \cos\left(-\theta_1\right) + R_2 \cos\left(\alpha_2 + \theta_2\right) - \frac{h_1}{2}\right]. \tag{6.17}$$

The partial derivatives of E_K and E_P with respect to the unknown rotations θ_1 and θ_2 needed in equation (6.1) are

$$\frac{\partial E_K}{\partial \theta_1} = -m_1 R_1 \dot{u}_g \dot{\theta}_1 \sin\left(\alpha_1 + \theta_1\right) + m_2 \dot{u}_g h_1 \dot{\theta}_1 \sin\left(-\theta_1\right)$$
$$+ m_2 h_1 R_2 \dot{\theta}_1 \dot{\theta}_2 \sin\left(-\theta_1 + \alpha_2 + \theta_2\right),$$

$$\frac{\partial E_K}{\partial \theta_2} = -m_2 \dot{u}_g \dot{\theta}_2 R_2 \sin\left(\alpha_2 + \theta_2\right) - m_2 h_1 R_2 \dot{\theta}_1 \dot{\theta}_2 \sin\left(-\theta_1 + \alpha_2 + \theta_2\right), \qquad (6.18)$$

$$\frac{\partial E_P}{\partial \theta_1} = -m_1 g R_1 \sin\left(\alpha_1 + \theta_1\right) + m_2 g h_1 \sin\left(-\theta_1\right),$$

$$\frac{\partial E_P}{\partial \theta_2} = -m_2 g R_2 \sin\left(\alpha_2 + \theta_2\right).$$

The partial derivatives of E_K and E_P with respect to the unknown angular velocities $\dot{\theta}_1$ and $\dot{\theta}_2$ are

$$\frac{\partial E_K}{\partial \dot{\theta}_1} = m_1 R_1 \dot{u}_g \cos\left(\alpha_1 + \theta_1\right) + I'_{O1} \dot{\theta}_1 + m_2 h_1 \dot{u}_g \cos\left(-\theta_1\right)$$
$$+ m_2 h_1 R_2 \dot{\theta}_2 \cos\left(-\theta_1 + \alpha_2 + \theta_2\right),$$

$$\frac{\partial E_K}{\partial \dot{\theta}_2} = m_2 \dot{u}_g R_2 \cos\left(\alpha_2 + \theta_2\right) + I_{O2} \dot{\theta}_2 + m_2 h_1 R_2 \dot{\theta}_1 \cos\left(-\theta_1 + \alpha_2 + \theta_2\right), \qquad (6.19)$$

$$\frac{\partial E_P}{\partial \dot{\theta}_1} = 0,$$

$$\frac{\partial E_P}{\partial \dot{\theta}_2} = 0.$$

The time derivatives of (6.19) are

$$\frac{d}{dt}\left(\frac{\partial E_K}{\partial \dot{\theta}_1}\right) = m_1 R_1 \ddot{u}_g \cos\left(\alpha_1 + \theta_1\right) - m_1 R_1 \dot{u}_g \dot{\theta}_1 \sin\left(\alpha_1 + \theta_1\right) + I'_{O1} \ddot{\theta}_1$$
$$+ m_2 h_1 \ddot{u}_g \cos\left(-\theta_1\right) + m_2 h_1 \dot{u}_g \dot{\theta}_1 \sin\left(-\theta_1\right)$$
$$+ m_2 h_1 R_2 \ddot{\theta}_2 \cos\left(-\theta_1 + \alpha_2 + \theta_2\right) \qquad (6.20)$$
$$+ m_2 h_1 R_2 \dot{\theta}_2 \left(\dot{\theta}_1 - \dot{\theta}_2\right) \sin\left(-\theta_1 + \alpha_2 + \theta_2\right),$$

$$\frac{d}{dt}\left(\frac{\partial E_K}{\partial \dot{\theta}_2}\right) = m_2 \ddot{u}_g R_2 \cos\left(\alpha_2 + \theta_2\right) - m_2 \dot{u}_g \dot{\theta}_2 R_2 \sin\left(\alpha_2 + \theta_2\right) + I_{O2} \ddot{\theta}_2$$
$$+ m_2 h_1 R_2 \ddot{\theta}_1 \cos\left(-\theta_1 + \alpha_2 + \theta_2\right) \qquad (6.21)$$
$$- m_2 h_1 R_2 \dot{\theta}_1 \left(-\dot{\theta}_1 + \dot{\theta}_2\right) \sin\left(-\theta_1 + \alpha_2 + \theta_2\right),$$

$$\frac{d}{dt}\left(\frac{\partial E_p}{\partial \dot{\theta}_1}\right) = 0, \qquad (6.22)$$

and

$$\frac{d}{dt}\left(\frac{\partial E_p}{\partial \dot{\theta}_2}\right) = 0. \qquad (6.23)$$

Finally, by substituting the terms given in equations (6.18) and (6.20)-(6.21) into equation (6.3), the equations of motion for configuration 1a are

$$I'_{O1}\ddot{\theta}_1 + m_2 h_1 R_2 \ddot{\theta}_2 \cos\left(-\theta_1 + \alpha_2 + \theta_2\right) - m_2 h_1 R_2 \dot{\theta}_2^2 \sin\left(-\theta_1 + \alpha_2 + \theta_2\right)$$
$$+ g\left[m_2 h_1 \sin\left(-\theta_1\right) - m_1 R_1 \sin\left(\alpha_1 + \theta_1\right)\right]$$
$$+ \ddot{u}_g\left[m_1 R_1 \cos\left(\alpha_1 + \theta_1\right) + m_2 h_1 \cos\left(-\theta_1\right)\right] = 0 \quad (6.24)$$

and

$$m_2 h_1 R_2 \ddot{\theta}_1 \cos\left(-\theta_1 + \alpha_2 + \theta_2\right) + I_{O2}\ddot{\theta}_2 + m_2 h_1 R_2 \dot{\theta}_1^2 \sin\left(-\theta_1 + \alpha_2 + \theta_2\right)$$
$$- m_2 g R_2 \sin\left(\alpha_2 + \theta_2\right) + m_2 \ddot{u}_g R_2 \cos\left(\alpha_2 + \theta_2\right) = 0, \quad (6.25)$$

for $i = 1$ and $i = 2$, respectively.

6.2.1.2 Configuration 1b

Let us derive the expressions for kinetic and potential energy of the dual-block stack moving in configuration 1b, based on Figure 6.4.
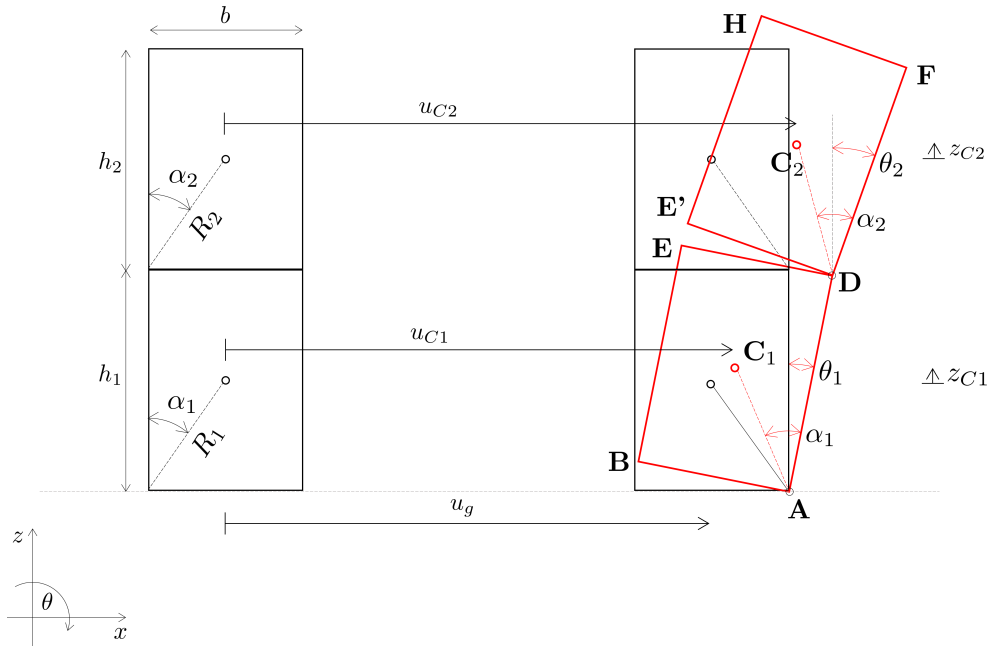
Figure 6.4: Displacements of the dual-block stack: translation and rotation in configuration 1b

The displacements of the blocks' centroids C_1 and C_2 are

$$u_{C1} = u_g + \frac{b}{2} - R_1 \sin\left(\alpha_1 - \theta_1\right) \quad (6.26)$$

106

$$z_{C1} = R_1 \cos{(\alpha_1 - \theta_1)} - \frac{h_1}{2} \qquad (6.27)$$

and

$$u_{C2} = u_g + \frac{b}{2} + h_1 \sin{(\theta_1)} - R_2 \sin{(\alpha_2 - \theta_2)} \qquad (6.28)$$

$$z_{C2} = h_1 \cos{(\theta_1)} + R_2 \cos{(\alpha_2 - \theta_2)} - \left(h_1 + \frac{h_2}{2}\right). \qquad (6.29)$$

The time derivatives of these displacements – the velocities – are

$$\dot{u}_{C1} = \dot{u}_g + R_1 \dot{\theta}_1 \cos{(\alpha_1 - \theta_1)} \qquad (6.30)$$

$$\dot{z}_{C1} = R_1 \dot{\theta}_1 \sin{(\alpha_1 - \theta_1)} \qquad (6.31)$$

and

$$\dot{u}_{C2} = \dot{u}_g + h_1 \dot{\theta}_1 \cos{(\theta_1)} + R_2 \dot{\theta}_2 \cos{(\alpha_2 - \theta_2)} \qquad (6.32)$$

$$\dot{z}_{C2} = -h_1 \dot{\theta}_1 \sin{(\theta_1)} + R_2 \dot{\theta}_2 \sin{(\alpha_2 - \theta_2)}. \qquad (6.33)$$

The total kinetic energy is

$$E_k = \frac{1}{2}m_1 \left[\dot{u}_g^2 + 2\dot{u}_g R_1 \dot{\theta}_1 \cos{(\alpha_1 - \theta_1)}\right] + \frac{1}{2}I'_{O1}\dot{\theta}_1^2 + \frac{1}{2}I_{O2}\dot{\theta}_2^2$$
$$+ \frac{1}{2}m_2 \left[\dot{u}_g^2 + 2\dot{u}_g h_1 \dot{\theta}_1 \cos{(\theta_1)} + 2\dot{u}_g R_2 \dot{\theta}_2 \cos{(\alpha_2 - \theta_2)}\right.$$
$$\left. + 2h_1 R_2 \dot{\theta}_1 \dot{\theta}_2 \cos{(\theta_1 + \alpha_2 - \theta_2)}\right], \quad (6.34)$$

while the potential energy E_P of the stack is

$$E_p = m_1 g \left[R_1 \cos{(\alpha_1 - \theta_1)} - \frac{h_1}{2}\right] + m_2 g \left[h_1 \cos{(\theta)} + R_2 \cos{(\alpha_2 - \theta_2)} - \frac{h_1}{2}\right].$$
$$(6.35)$$

After a little bit of algebra the terms $\dfrac{d}{dt}\left(\dfrac{\partial E_K}{\partial \dot{\theta}_i}\right)$ and $\dfrac{\partial (E_k - E_p)}{\partial \theta_i}$ for $i = 1, 2$ are derived and substituted into equation (6.3). Finally, the equations of motion for rocking in configuration 1b are

$$I'_{O1}\ddot{\theta}_1 + m_2 h_1 R_2 \ddot{\theta}_2 \cos{(\theta_1 + \alpha_2 - \theta_2)} + m_2 h_1 R_2 \dot{\theta}_2^2 \sin{(\theta_1 + \alpha_2 - \theta_2)}$$
$$+ g\left[m_1 R_1 \sin{(\alpha_1 - \theta_1)} - m_2 h_1 \sin{(\theta_1)}\right] + \ddot{u}_g \left[m_1 R_1 \cos{(\alpha_1 - \theta_1)} + m_2 h_1 \cos{(\theta)}\right] = 0$$
$$(6.36)$$

and

$$m_2 h_1 R_2 \ddot{\theta}_1 \cos{(\theta_1 + \alpha_2 - \theta_2)} + I_{O2}\ddot{\theta}_2 - m_2 h_1 R_2 \dot{\theta}_1^2 \sin{(\theta_1 + \alpha_2 - \theta_2)}$$
$$+ m_2 g R_2 \sin{(\alpha_2 - \theta_2)} + m_2 \ddot{u}_g R_2 \cos{(\alpha_2 - \theta_2)} = 0, \quad (6.37)$$

for $i = 1$ and $i = 2$, respectively.

6.2.1.3 Configuration 2a

Let us derive the expressions for kinetic and potential energy in configuration 2a, based on Figure 6.5.
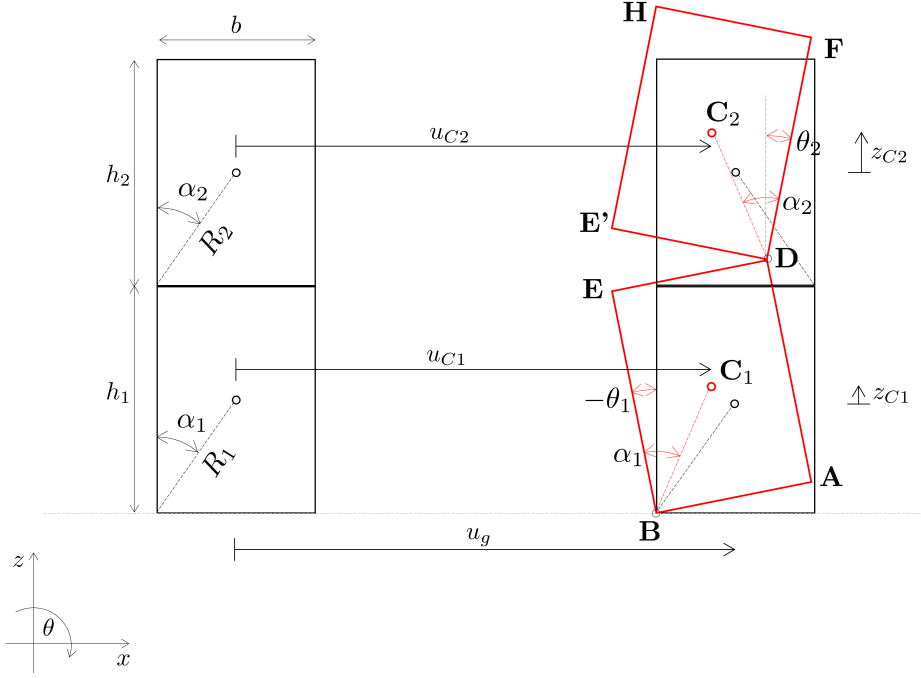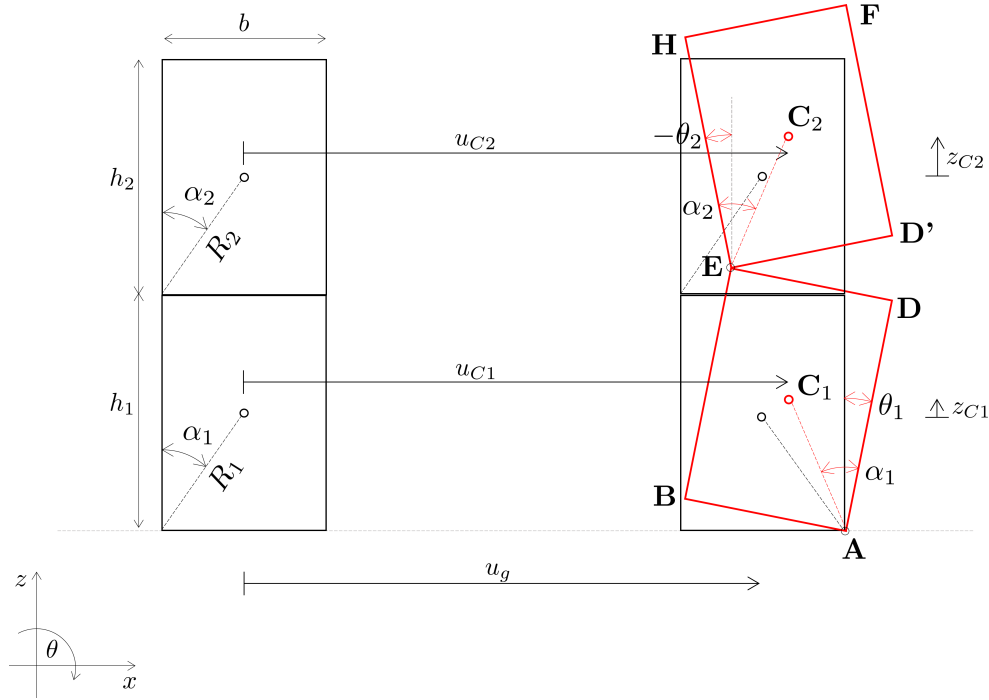

Figure 6.5: Displacements of the dual-block stack: translation and rotation in configuration 2a

The displacements of the blocks' centroids C_1 and C_2 are

$$u_{C1} = u_g - \frac{b}{2} + R_1 \sin(\alpha_1 + \theta_1) \tag{6.38}$$

$$z_{C1} = R_1 \cos(\alpha_1 + \theta_1) - \frac{h_1}{2} \tag{6.39}$$

and

$$u_{C2} = u_g - \frac{b}{2} + 2R_1 \sin(\alpha_1 + \theta_1) - R_2 \sin(\alpha_2 - \theta_2) \tag{6.40}$$

$$z_{C2} = 2R_1 \cos(\alpha_1 + \theta_1) + R_2 \cos(\alpha_2 - \theta_2) - \left(h_1 + \frac{h_2}{2}\right). \tag{6.41}$$

The time derivatives of the displacements – the velocities – are

$$\dot{u}_{C1} = \dot{u}_g + R_1 \dot{\theta}_1 \cos(\alpha_1 + \theta_1) \tag{6.42}$$

$$\dot{z}_{C1} = -R_1 \dot{\theta}_1 \sin(\alpha_1 + \theta_1) \tag{6.43}$$

$$\dot{u}_{C2} = \dot{u}_g + 2R_1 \dot{\theta}_1 \cos(\alpha_1 + \theta_1) + R_2 \dot{\theta}_2 \cos(\alpha_2 - \theta_2) \tag{6.44}$$

$$\dot{z}_{C2} = -2R_1\dot{\theta}_1 \sin(\alpha_1 + \theta_1) + R_2\dot{\theta}_2 \sin(\alpha_2 - \theta_2). \tag{6.45}$$

The total kinetic energy E_K of the stack follows as

$$E_k = \frac{1}{2}m_1\left[\dot{u}_g^2 + 2\dot{u}_g R_1\dot{\theta}_1 \cos(\alpha_1 + \theta_1)\right] + \frac{1}{2}\left(I'_{O1} + m_2b^2\right)\dot{\theta}_1^2 + \frac{1}{2}I_{O2}\dot{\theta}_2^2$$
$$+ \frac{1}{2}m_2\left[\dot{u}_g^2 + 4\dot{u}_g R_1\dot{\theta}_1 \cos(\alpha_1 + \theta_1) + 2\dot{u}_g R_2\dot{\theta}_2 \cos(\alpha_2 - \theta_2)\right.$$
$$\left. + 4R_1 R_2\dot{\theta}_1\dot{\theta}_2 \cos(\alpha_1 + \theta_1 + \alpha_2 - \theta_2)\right], \tag{6.46}$$

while the total potential energy E_P of the stack is

$$E_p = m_1 g\left[R_1 \cos(\alpha_1 + \theta_1) - \frac{h_1}{2}\right]$$
$$+ m_2 g\left[2R_1 \cos(\alpha_1 + \theta_1) + R_2 \cos(\alpha_2 - \theta_2) - \frac{h_1}{2}\right]. \tag{6.47}$$

Again after a little bit of algebra we can derive the terms $\dfrac{d}{dt}\left(\dfrac{\partial E_K}{\partial \dot{\theta}_i}\right)$ and $\dfrac{\partial L}{\partial \theta_i}$ for $i = 1, 2$ and substitute them into equation (6.1). Finally, the equations of motion for rocking in configuration 2a are

$$\left(I'_{O1} + m_2b^2\right)\ddot{\theta}_1 + 2m_2 R_1 R_2\ddot{\theta}_2 \cos(\alpha_1 + \theta_1 + \alpha_2 - \theta_2)$$
$$+ 2m_2 R_1 R_2\dot{\theta}_2^2 \sin(\alpha_1 + \theta_1 + \alpha_2 - \theta_2) - (m_1 + 2m_2)\,gR_1 \sin(\alpha_1 + \theta_1)$$
$$+ \ddot{u}_g(m_1 + 2m_2)\,R_1 \cos(\alpha_1 + \theta_1) = 0 \tag{6.48}$$

and

$$2m_2 R_1 R_2\ddot{\theta}_1 \cos(\alpha_1 + \theta_1 + \alpha_2 - \theta_2) + I_{O2}\ddot{\theta}_2 - 2m_2 R_1 R_2\dot{\theta}_1^2 \sin(\alpha_1 + \theta_1 + \alpha_2 - \theta_2)$$
$$+ m_2 g R_2 \sin(\alpha_2 - \theta_2) + m_2\ddot{u}_g R_2 \cos(\alpha_2 - \theta_2) = 0, \tag{6.49}$$

for $i = 1$ and $i = 2$, respectively.

6.2.1.4 Configuration 2b

Let us derive the expressions for kinetic and potential energy in configuration 2b, based on Figure 6.6.
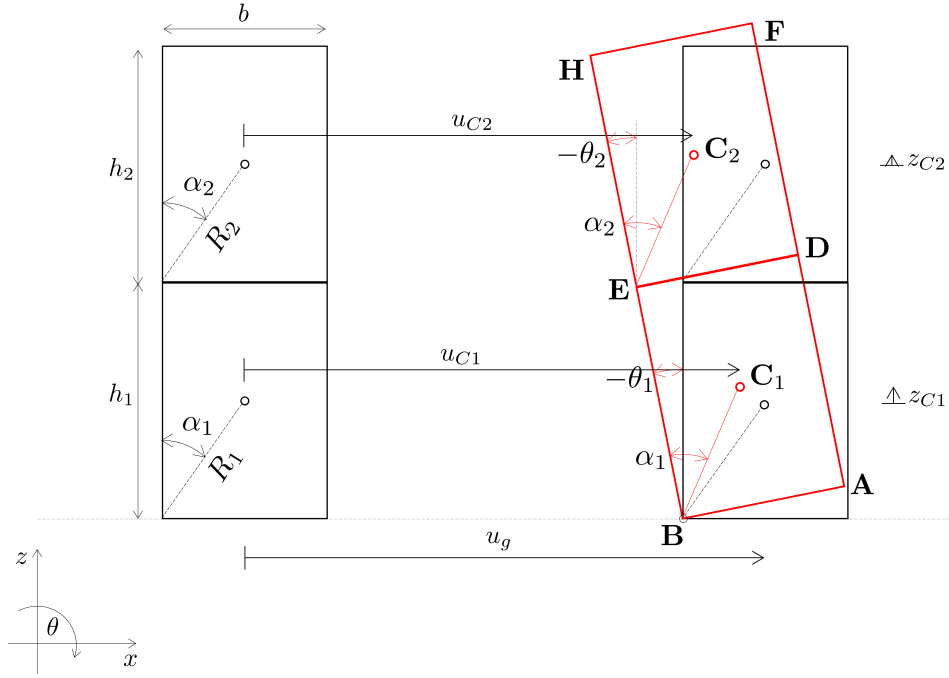
Figure 6.6: Displacements of the dual-block stack: translation and rotation in configuration 2b

The displacements of the blocks' centroids C_1 and C_2 are

$$u_{C1} = u_g + \frac{b}{2} - R_1 \sin\left(\alpha_1 - \theta_1\right) \tag{6.50}$$

$$z_{C1} = R_1 \cos\left(\alpha_1 - \theta_1\right) - \frac{h_1}{2} \tag{6.51}$$

and

$$u_{C2} = u_g + \frac{b}{2} - 2R_1 \sin\left(\alpha_1 - \theta_1\right) + R_2 \sin\left(\alpha_2 + \theta_2\right) \tag{6.52}$$

$$z_{C2} = 2R_1 \cos\left(\alpha_1 - \theta_1\right) + R_2 \cos\left(\alpha_2 + \theta_2\right) - \left(h_1 + \frac{h_2}{2}\right). \tag{6.53}$$

The time derivatives of the displacements – the velocities – are

$$\dot{u}_{C1} = \dot{u}_g + R_1 \dot{\theta}_1 \cos\left(\alpha_1 - \theta_1\right) \tag{6.54}$$

$$\dot{z}_{C1} = R_1 \dot{\theta}_1 \sin\left(\alpha_1 - \theta_1\right) \tag{6.55}$$

$$\dot{u}_{C2} = \dot{u}_g + 2R_1 \dot{\theta}_1 \cos\left(\alpha_1 - \theta_1\right) + R_2 \dot{\theta}_2 \cos\left(\alpha_2 + \theta_2\right) \tag{6.56}$$

$$\dot{z}_{C2} = 2R_1 \dot{\theta}_1 \sin\left(\alpha_1 - \theta_1\right) - R_2 \dot{\theta}_2 \sin\left(\alpha_2 + \theta_2\right). \tag{6.57}$$

110

The total kinetic energy E_K of the system is

$$E_k = \frac{1}{2}m_1 \left[\dot{u}_g^2 + 2\dot{u}_g R_1 \dot{\theta}_1 \cos(\alpha_1 - \theta_1) \right] + \frac{1}{2}\left(I'_{O1} + m_2 b^2\right)\dot{\theta}_1^2 + \frac{1}{2}I_{O2}\dot{\theta}_2^2$$
$$+ \frac{1}{2}m_2 \left[\dot{u}_g^2 + 4\dot{u}_g R_1 \dot{\theta}_1 \cos(\alpha_1 - \theta_1) + 2\dot{u}_g R_2 \dot{\theta}_2 \cos(\alpha_2 + \theta_2) \right.$$
$$\left. + 4R_1 R_2 \dot{\theta}_1 \dot{\theta}_2 \cos(\alpha_1 - \theta_1 + \alpha_2 + \theta_2) \right], \quad (6.58)$$

while the total potential energy E_P of the system is

$$E_p = m_1 g \left[R_1 \cos(\alpha_1 - \theta_1) - \frac{h_1}{2} \right]$$
$$+ m_2 g \left[2R_1 \cos(\alpha_1 - \theta_1) + R_2 \cos(\alpha_2 + \theta_2) - \frac{h_1}{2} \right]. \quad (6.59)$$

Finally, after the terms $\dfrac{d}{dt}\left(\dfrac{\partial E_K}{\partial \dot{\theta}_i}\right)$ and $\dfrac{\partial L}{\partial \theta_i}$ for $i = 1, 2$ are derived and substituted in equation (6.3), the equations of motion configuration 2b are

$$\left(I'_{O1} + m_2 b^2\right)\ddot{\theta}_1 + 2m_2 R_1 R_2 \ddot{\theta}_2 \cos(\alpha_1 - \theta_1 + \alpha_2 + \theta_2)$$
$$- 2m_2 R_1 R_2 \dot{\theta}_2^2 \sin(\alpha_1 - \theta_1 + \alpha_2 - +\theta_1) + g\left[m_1 R_1 \sin(\alpha_1 - \theta_1) + 2m_2 R_1 \sin(\alpha_1 - \theta_1)\right]$$
$$+ \ddot{u}_g(m_1 + 2m_2)R_1 \cos(\alpha_1 - \theta_1) = 0 \quad (6.60)$$

and

$$2m_2 R_1 R_2 \ddot{\theta}_1 \cos(\alpha_1 - \theta_1 + \alpha_2 + \theta_2) + 2m_2 R_1 R_2 \dot{\theta}_1^2 \sin(\alpha_1 - \theta_1 + \alpha_2 - +\theta_1)$$
$$+ I_{O2}\ddot{\theta}_2 - m_2 g R_2 \sin(\alpha_2 + \theta_2) + m_2 \ddot{u}_g R_1 \cos(\alpha_2 + \theta_2) = 0, \quad (6.61)$$

for $i = 1$ and $i = 2$, respectively.

6.2.1.5   Configuration 3a

Let us derive the expressions for kinetic and potential energy in configuration 3a (Figure 6.7).

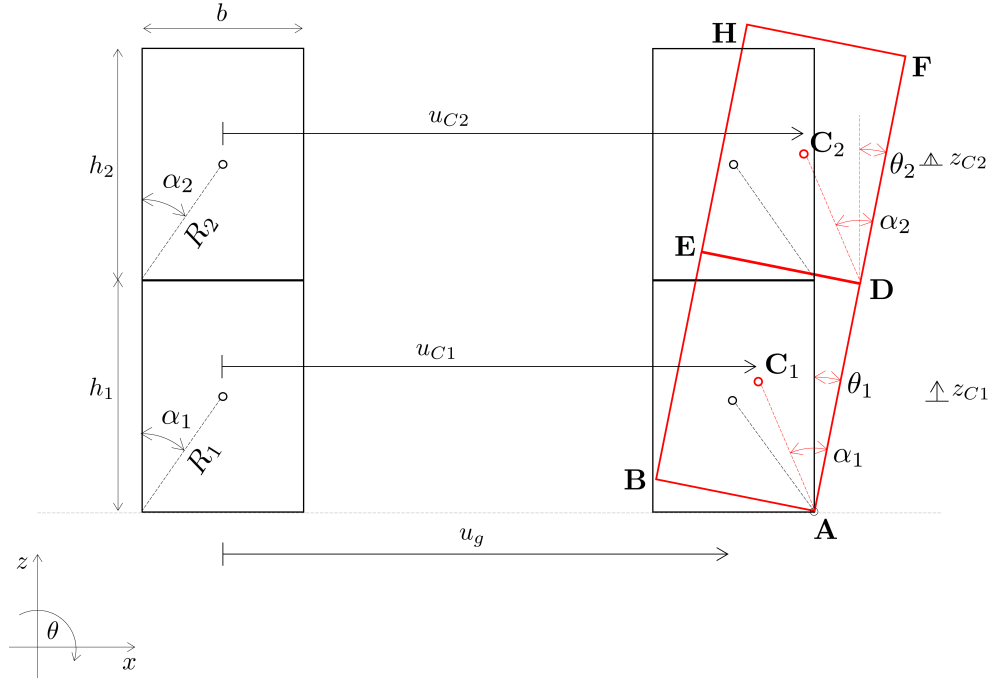Figure 6.7: Displacements of the dual-block stack: translation and rotation in configuration 3a

Configurations 3a and 3b describe rocking where both blocks rotate together ($\theta_2 = \theta_1$) and can be observed as a larger single block with dimensions $B = b$ and $H = h_1 + h_2$ rocking. The displacements of the blocks' centroids C_1 and C_2 are

$$u_{C1} = u_g - \frac{b}{2} + R_1 \sin\left(\alpha_1 + \theta_1\right) \tag{6.62}$$

$$z_{C1} = R_1 \cos\left(\alpha_1 + \theta_1\right) - \frac{h_1}{2} \tag{6.63}$$

and

$$u_{C2} = u_g - \frac{b}{2} - h_1 \sin\left(-\theta_1\right) + R_2 \sin\left(\alpha_2 + \theta_1\right) \tag{6.64}$$

$$z_{C2} = h_1 \cos\left(-\theta_1\right) + R_2 \cos\left(\alpha_2 + \theta_1\right) - \left(h_1 + \frac{h_2}{2}\right). \tag{6.65}$$

The time derivatives of the displacements – the velocities – are

$$\dot{u}_{C1} = \dot{u}_g + R_1 \dot{\theta}_1 \cos\left(\alpha_1 + \theta_1\right) \tag{6.66}$$

$$\dot{z}_{C1} = -R_1 \dot{\theta}_1 \sin\left(\alpha_1 + \theta_1\right) \tag{6.67}$$

$$\dot{u}_{C2} = \dot{u}_g + h_1 \dot{\theta}_1 \cos\left(-\theta_1\right) + R_2 \dot{\theta}_1 \cos\left(\alpha_2 + \theta_1\right) \tag{6.68}$$

$$\dot{z}_{C2} = h_1 \dot{\theta}_1 \sin\left(-\theta_1\right) - R_2 \dot{\theta}_1 \sin\left(\alpha_1 + \theta_1\right). \tag{6.69}$$

112

The total kinetic energy E_K of the system is

$$E_k = \frac{1}{2}m_1\left[\dot{u}_g^2 + 2\dot{u}_g R_1 \dot{\theta}_1 \cos(\alpha_1 + \theta_1)\right] + \frac{1}{2}I_0'\dot{\theta}_1^2 +$$
$$\frac{1}{2}m_2\left[\dot{u}_g^2 + 2\dot{u}_g h_1 \dot{\theta}_1 \cos(-\theta_1) + 2\dot{u}_g R_2 \dot{\theta}_1 \cos(\alpha_2 + \theta_1)\right], \quad (6.70)$$

where $I_0' = I_{C1} + m_1 R_1^2 + I_{C2} + m_2\left(h_1^2 + R_2^2 + 2h_1 R_2 \cos\alpha_2\right)$ is the moment of inertia with respect to the contact corner, while the total potential energy E_P is

$$E_p = m_1 g\left[R_1 \cos(\alpha_1 + \theta_1) - \frac{h_1}{2}\right] + m_2 g\left[h_1 \cos(-\theta_1) + R_2 \cos(\alpha_2 + \theta_1) - \frac{h_2}{2}\right].$$
$$(6.71)$$

Since there is only one unknown in such system, the terms $\dfrac{d}{dt}\left(\dfrac{\partial E_K}{\partial \dot{\theta}_1}\right)$ and $\dfrac{\partial(E_k - E_p)}{\partial \theta_1}$ need to be derived and substituted into equation (6.3). The final equation of motion for in configuration 3a is

$$I_0'\ddot{\theta}_1 + g\left[m_2 h_1 \sin(-\theta_1) - m_1 R_1 \sin(\alpha_1 + \theta_1) - m_2 R_2 \sin(\alpha_2 + \theta_1)\right]$$
$$+ \ddot{u}_g\left[m_1 R_1 \cos(\alpha_1 + \theta_1) + m_2 h_1 \cos(-\theta_1) + m_2 R_2 \cos(\alpha_2 + \theta_1)\right] = 0. \quad (6.72)$$

6.2.1.6 Configuration 3b

Let us derive the expressions for kinetic and potential energy in configuration 3b, based on Figure 6.8.
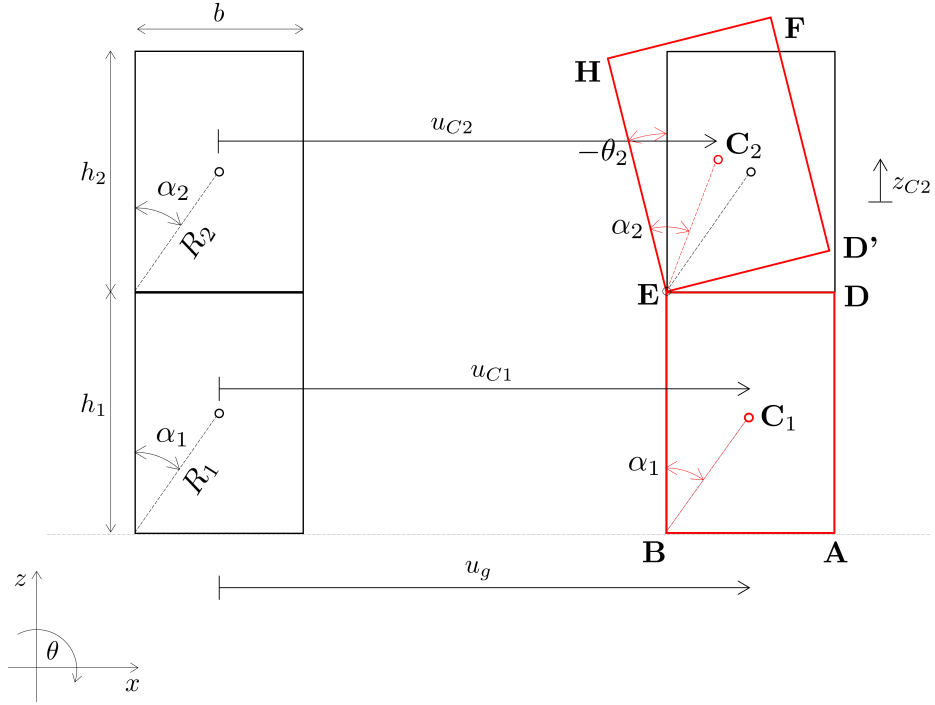
Figure 6.8: Displacements of the dual-block stack: translation and rotation in configuration 3b

The displacements of blocks' centroids C_1 and C_2 in a right-handed referent coordinate system are

$$u_{C1} = u_g + \frac{b}{2} - R_1 \sin(\alpha_1 - \theta_1) \tag{6.73}$$

$$z_{C1} = R_1 \cos(\alpha_1 - \theta_1) - \frac{h_1}{2} \tag{6.74}$$

and

$$u_{C2} = u_g + \frac{b}{2} + h_1 \sin(\theta_1) - R_2 \sin(\alpha_2 - \theta_1) \tag{6.75}$$

$$z_{C2} = h_1 \cos(\theta_1) + R_2 \cos(\alpha_2 - \theta_1) - \left(h_1 + \frac{h_2}{2} \right). \tag{6.76}$$

The time derivatives of the displacements – the velocities – are

$$\dot{u}_{C1} = \dot{u}_g + R_1 \dot{\theta}_1 \cos(\alpha_1 - \theta_1) \tag{6.77}$$

$$\dot{z}_{C1} = R_1 \dot{\theta}_1 \sin(\alpha_1 - \theta_1) \tag{6.78}$$

$$\dot{u}_{C2} = \dot{u}_g + h_1 \dot{\theta}_1 \cos(\theta_1) + R_2 \dot{\theta}_1 \cos(\alpha_2 - \theta_1) \tag{6.79}$$

$$\dot{z}_{C2} = -h_1 \dot{\theta}_1 \sin(\theta_1) + R_2 \dot{\theta}_1 \sin(\alpha_1 - \theta_1). \tag{6.80}$$

114

The total kinetic energy E_K of the system is

$$E_k = \frac{1}{2} m_1 \left[\dot{u}_g^2 + 2\dot{u}_g R_1 \dot{\theta}_1 \cos(\alpha_1 - \theta_1) \right] + \frac{1}{2} I_0' \dot{\theta}_1^2 +$$
$$\frac{1}{2} m_2 \left[\dot{u}_g^2 + 2\dot{u}_g h_1 \dot{\theta}_1 \cos(\theta_1) + 2\dot{u}_g R_2 \dot{\theta}_1 \cos(\alpha_2 - \theta_1) \right], \quad (6.81)$$

while the total potential energy E_P is

$$E_p = m_1 g \left[R_1 \cos(\alpha_1 - \theta_1) - \frac{h_1}{2} \right]$$
$$+ m_2 g \left[h_1 \cos(\theta_1) + R_2 \cos(\alpha_2 - \theta_1) - \frac{h_1}{2} \right]. \quad (6.82)$$

Since there is again only one unknown in such system, the terms $\dfrac{d}{dt}\left(\dfrac{\partial E_K}{\partial \dot{\theta}_1} \right)$ and $\dfrac{\partial (E_k - E_p)}{\partial \theta_1}$ need to be derived and substituted into equation (6.3). The final equation of motion in configuration 3b is

$$I_0' \ddot{\theta}_1 + g \left[-m_2 h_1 \sin(\theta_1) + m_1 R_1 \sin(\alpha_1 - \theta_1) + m_2 R_2 \sin(\alpha_2 - \theta_1) \right]$$
$$+ \ddot{u}_g \left[m_1 R_1 \cos(\alpha_1 - \theta_1) + m_2 h_1 \cos(\theta_1) + m_2 R_2 \cos(\alpha_2 - \theta_1) \right] = 0. \quad (6.83)$$

6.2.1.7   Configuration 4a

Let us derive the expressions for kinetic and potential energy in configuration 4a (Figure 6.9).

Figure 6.9: Displacements of the dual-block stack: translation and rotation in configuration 4a

Configurations 4a and 4b describe the situation where the bottom block is vertical and not rotating ($\theta_1 = 0$) and only the top block is rotating ($\theta_2 \neq 0$). The displacements of the blocks' centroids C_1 and C_2 are

$$u_{C1} = u_g \tag{6.84}$$

$$z_{C1} = 0 \tag{6.85}$$

and

$$u_{C2} = u_g - \frac{b}{2} + R_2 \sin\left(\alpha_2 + \theta_2\right) \tag{6.86}$$

$$z_{C2} = R_2 \cos\left(\alpha_2 + \theta_2\right) - \frac{h_2}{2}. \tag{6.87}$$

The derivatives of the displacements are

$$\dot{u}_{C1} = \dot{u}_g \tag{6.88}$$

$$\dot{z}_{C1} = 0 \tag{6.89}$$

$$\dot{u}_{C2} = \dot{u}_g + R_2 \dot{\theta}_2 \cos\left(\alpha_2 + \theta_2\right) \tag{6.90}$$

$$\dot{z}_{C2} = -R_2 \dot{\theta}_2 \sin\left(\alpha_2 + \theta_2\right). \tag{6.91}$$

116

The total kinetic energy E_K of the system is

$$E_k = \frac{1}{2}m_2\dot{u}_g^2 + \frac{1}{2}m_2\left[\dot{u}_g^2 + 2\dot{u}_g R_2\dot{\theta}_2\cos\left(\alpha_2 + \theta_2\right)\right] + \frac{1}{2}I_{02}\dot{\theta}_2^2, \tag{6.92}$$

while the total potential energy E_P is

$$E_P = m_2 g\left[R_2\cos\left(\alpha_2 + \theta_2\right) + \frac{h_1}{2}\right], \tag{6.93}$$

measured, as before, from the level $\dfrac{h_1}{2}$ above the ground.

After deriving the terms $\dfrac{d}{dt}\left(\dfrac{\partial E_K}{\partial\dot{\theta}_2}\right)$ and $\dfrac{\partial\left(E_k - E_p\right)}{\partial\theta_2}$ and substituting them in equation (6.3, the equation of motion for configuration 4a is

$$I_{02}\ddot{\theta}_2 - m_2 g R_2\sin\left(\alpha_2 + \theta_2\right) + m_2\ddot{u}_g R_2\cos\left(\alpha_2 + \theta_2\right) = 0. \tag{6.94}$$

6.2.1.8 Configuration 4b

Last, let us derive the expressions for kinetic and potential energy of the dual-block stack in configuration 4b (see Figure 6.10).
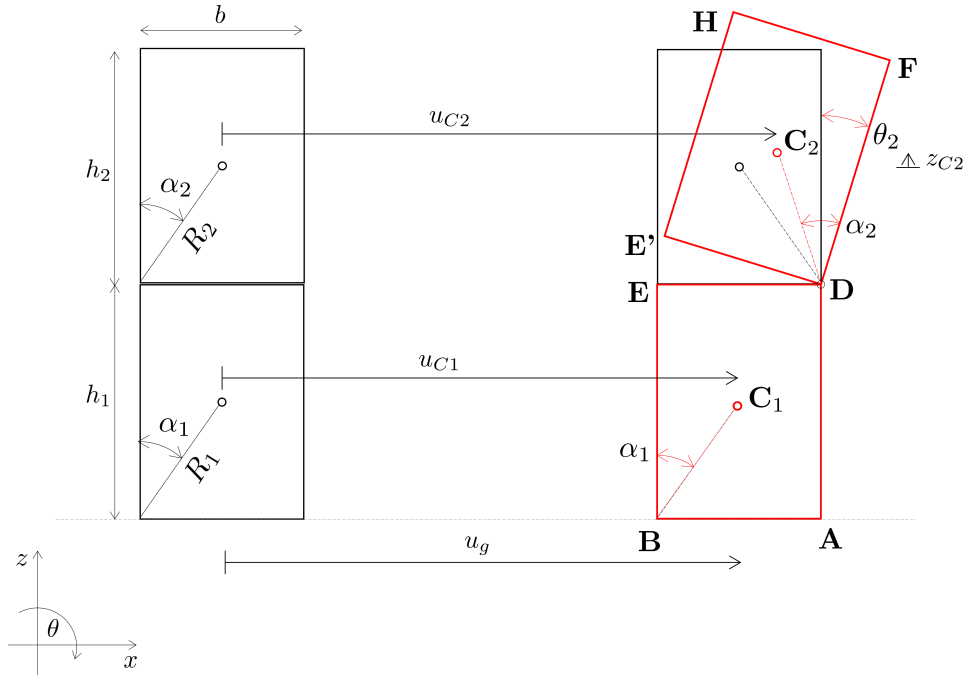
Figure 6.10: Displacements of the dual-block stack: translation and rotation in configuration 4b

The displacements of blocks' centroids C_1 and C_2 in a right-handed referent coordinate system are

$$u_{C1} = u_g \tag{6.95}$$

117

$$z_{C1} = 0 \tag{6.96}$$

and

$$u_{C2} = u_g + \frac{b}{2} - R_2 \sin(\alpha_2 - \theta_2) \tag{6.97}$$

$$z_{C2} = R_2 \cos(\alpha_2 - \theta_2) - \frac{h_2}{2}. \tag{6.98}$$

The derivatives of the displacements are

$$\dot{u}_{C1} = \dot{u}_g \tag{6.99}$$

$$\dot{z}_{C1} = 0 \tag{6.100}$$

$$\dot{u}_{C2} = \dot{u}_g + R_2 \dot{\theta}_2 \cos(\alpha_2 - \theta_2) \tag{6.101}$$

$$\dot{z}_{C2} = R_2 \dot{\theta}_2 \sin(\alpha_2 - \theta_2). \tag{6.102}$$

The total kinetic energy E_K of the system is

$$E_k = \frac{1}{2} m_2 \dot{u}_g^2 + \frac{1}{2} m_2 \left[\dot{u}_g^2 + 2\dot{u}_g R_2 \dot{\theta}_2 \cos(\alpha_2 - \theta_2) \right] + \frac{1}{2} I_{02} \dot{\theta}_2^2, \tag{6.103}$$

while the total potential energy E_P is

$$E_P = m_2 g \left[R_2 \cos(\alpha_2 - \theta_2) + \frac{h_1}{2} \right]. \tag{6.104}$$

After deriving the terms $\dfrac{d}{dt} \left(\dfrac{\partial E_K}{\partial \dot{\theta}_2} \right)$ and $\dfrac{\partial (E_k - E_p)}{\partial \theta_2}$ and substituting them in equation (6.3), the equation of motion for rocking in configuration 4b is

$$I_{02} \ddot{\theta}_2 + m_2 g R_2 \sin(\alpha_2 - \theta_2) + m_2 \ddot{u}_g R_2 \cos(\alpha_2 - \theta_2) = 0. \tag{6.105}$$

6.3   Transition between the configurations

During rocking the dual-block stack keeps transitioning between the eight possible configurations shown in Figure 6.2. The description of rocking thus involves the possible transitions between these configurations shown graphically in Figure 6.11. The transition happen due to:

1. initiation of rocking configurations from initial translation (orange lines in Figure 6.11) [45],

2. new contacts opening (green lines in Figure 6.11) [45],

118

3. impacts between bodies either between the top and the bottom block or between the bottom block and the base (red dotted lines in Figure 6.11) [45, 30].
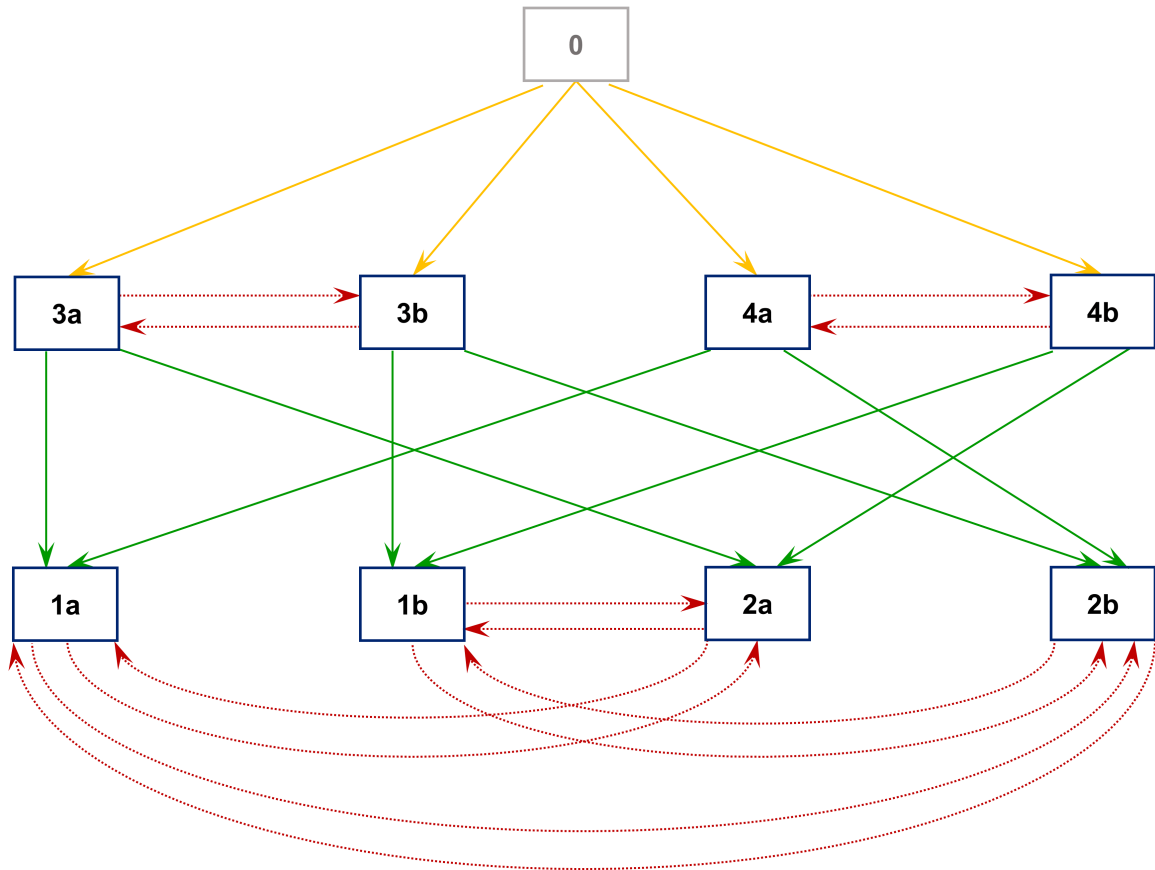
Figure 6.11: Dual-block stack: transitions between configurations

The transition criteria due to the three stated causes are all described in detail below.

6.4 Initiation of rocking

A dual-block stack that is initially ideally vertical and is translating along with the base can start rocking in one of the two 'lower' (simpler) configurations - either configuration 3a/b or configuration 4a/b. The transition criteria that need to be satisfied in order for rocking in these configuration to initiate are given below.

6.4.1 Transition from translation to configurations 3a/3b

Rocking in configuration 3a/b is initiated when the resultant force at the contact between the bottom block and the base acts at point B or A, respectively, at which

point the moment of the inertial force with respect to that point needs to exceed the moment of the weight with respect to the same point.

$$\pm \ddot{u}_g \left[m_1 h_1 + m_2 \left(2h_1 + h_2 \right) \right] > g \left(m_1 b + m_2 b \right) \tag{6.106}$$

6.4.2 Transition from translation to configurations 4a/4b

Rocking in configuration 4a/b is initiated when the resultant force at the contact between the top and the bottom acts at point E or D, respectively, at which point the moment of the inertial force of the top block with respect to that point needs to exceed the moment of its weight with respect to the same point.

$$\pm \ddot{u}_g h_2 > gb \tag{6.107}$$

6.5 Transitions without impact / initiation of 'higher' configurations

Transitions between configurations without impact occur when a new contact opens. If the stack is rocking as one body, the contact between the top and the bottom block can open due to kinematic conditions for that being satisfied. If the stack is rocking so that only the top block rocks, while the bottom one is only translating, the contact between the bottom block and the base can open due to kinematic conditions for initiation of such configuration being satisfied.

The conditions for every possible transitions between configurations due to a new contact being opened are derived below.

6.5.1 Transition from 3a to 1a

Transition from 3a to 1a takes place when the resultant force at the contact between the top and the bottom block acts at point E and the moment on the mass x acceleration diagram with respect to that point exceeds the moment of the weight with respect to the same point, while rocking in configuration 3a. The condition for this transition is:

$$\begin{aligned} m_2 \ddot{u}_g R_2 \cos \left(\alpha_2 + \theta_1 \right) > m_2 g R_2 \sin \left(\alpha_2 + \theta_1 \right) - m_2 R_2' \dot{\theta}_1^2 R_2 \sin \left(\alpha_2 - \alpha_2' \right) \\ + I_2 \ddot{\theta}_1 + m_2 R_2' \ddot{\theta}_1 R_2 \cos \left(\alpha_2 - \alpha_2' \right), \quad (6.108) \end{aligned}$$

where $R_2' = \sqrt{\left(\frac{b}{2}\right)^2 + \left(h_1 + \frac{h_2}{2}\right)^2}$ is the length of the line connecting any of the bottom corners of the stack and the centroid of the top block, while $\alpha_2' = \arctan\left(\frac{b/2}{h_1 + h_2/2}\right)$ is the angle between this line and the vertical side of the stack.

6.5.2 Transition from 3a to 2a

Transition from 3a to 2a takes place when the resultant force at the contact between the top and the bottom block acts at point D and the moment on the mass x acceleration diagram with respect to that point exceeds the moment of the weight with respect to the same point, while rocking in configuration 3a. The condition for this transition is:

$$m_2 \ddot{u}_g R_2 \cos\left(\alpha_2 - \theta_1\right) < -m_2 g R_2 \sin\left(\alpha_2 - \theta_1\right) + m_2 R_2' \dot{\theta}_1^2 \left(\alpha_2 + \alpha_2'\right)$$
$$+ I_2 \ddot{\theta}_1 + m_2 R_2' \ddot{\theta}_1 R_2 \cos\left(\alpha_2 + \alpha_2'\right). \quad (6.109)$$

6.5.3 Transition from 3b to 1b

Transition from 3b to 1b takes place when the resultant force at the contact between the top and the bottom block acts at point D and the moment on the mass x acceleration diagram with respect to that point exceeds the moment of the weight with respect to the same point, while rocking in configuration 3b. The condition for this transition is:

$$m_2 \ddot{u}_g R_2 \cos\left(\alpha_2 - \theta_1\right) < -m_2 g R_2 \sin\left(\alpha_2 - \theta_1\right) + m_2 R_2' \dot{\theta}_1^2 R_2 \sin\left(\alpha_2 - \alpha_2'\right)$$
$$+ I_2 \ddot{\theta}_1 + m_2 R_2' \ddot{\theta}_1 R_2 \cos\left(\alpha_2 - \alpha_2'\right). \quad (6.110)$$

6.5.4 Transition from 3b to 2b

Transition from 3b to 2b takes place when the resultant force at the contact between the top and the bottom block acts at point E and the moment on the mass x acceleration diagram with respect to that point exceeds the moment of the weight with respect to the same point, while rocking in configuration 3b. The condition for this transition is:

$$m_2 \ddot{u}_g R_2 \cos\left(\alpha_2 + \theta_1\right) m_2 g R_2 \sin\left(\alpha_2 + \theta_1\right) + m_2 R_2' \dot{\theta}_1^2 \left(\alpha_2 + \alpha_2'\right)$$
$$+ I_2 \ddot{\theta}_1 - m_2 R_2' \ddot{\theta}_1 R_2 \cos\left(\alpha_2 + \alpha_2'\right). \quad (6.111)$$

6.5.5 Transition from 4a to 1a

Transition from 4a to 1a takes place when the resultant force at the contact between the bottom block and the base acts at point B and the moment on the mass x acceleration diagram with respect to that point exceeds the moment of the weight with respect to the same point, while rocking in configuration 4a. The condition for this transition is:

$$
\ddot{u}_g\{m_1\frac{h_1}{2} + m_2\left[h_1 R_2 \cos\left(\alpha_2 + \theta_2\right)\right]\} >
$$
$$
g\left[m_1\frac{b}{2} + m_2 R_2 \sin\left(\alpha_2 + \theta_2\right)\right] + m_2 R_2^2 \ddot{\theta}_2 + I_2 \ddot{\theta}_2. \quad (6.112)
$$

6.5.6 Transition from 4a to 2b

Transition from 4a to 2b takes place when the resultant force at the contact between the bottom block and the base acts at point A and the moment on the mass x acceleration diagram with respect to that point exceeds the moment of the weight with respect to the same point, while rocking in configuration 4a. The condition for this transition is:

$$
\ddot{u}_g\{m_1\frac{h_1}{2} + m_2\left[h_1 + R_2 \cos\left(\alpha_2 + \theta_2\right)\right]\} < I_2 \ddot{\theta}_2 - g\{m_1\frac{b}{2} + m_2\left[b - R_2 \sin\left(\alpha_2 + \theta_2\right)\right]\}
$$
$$
+ m_2 R_2 \dot{\theta}_2^2 \left[h_1 \sin\left(\alpha_2 + \theta_2\right) + b \cos\left(\alpha_2 + \theta_2\right)\right]
$$
$$
+ m_2 R_2 \ddot{\theta}_2 \left[R_2 - b \sin\left(\alpha_2 + \theta_2\right) + h_1 \cos\left(\alpha_2 + \theta_2\right)\right]. \quad (6.113)
$$

6.5.7 Transition from 4b to 1b

Transition from 4b to 1b takes place when the resultant force at the contact between the bottom block and the base acts at point A and the moment on the mass x acceleration diagram with respect to that point exceeds the moment of the weight with respect to the same point, while rocking in configuration 4b. The condition for this transition is:

$$
\ddot{u}_g\{m_1\frac{h_1}{2} + m_2\left[h_1 R_2 \cos\left(\alpha_2 - \theta_2\right)\right]\} <
$$
$$
- g\left[m_1\frac{b}{2} + m_2 R_2 \sin\left(\alpha_2 - \theta_2\right)\right] + m_2 R_2^2 \ddot{\theta}_2 + I_2 \ddot{\theta}_2. \quad (6.114)
$$

6.5.8 Transition from 4b to 2a

Transition from 4b to 2a takes place when the resultant force at the contact between the bottom block and the base acts at point B and the moment on the mass x acceleration diagram with respect to that point exceeds the moment of the weight with respect to the same point, while rocking in configuration 4b. The condition for this transition is:

$$
\ddot{u}_g\{m_1\frac{h_1}{2} + m_2\left[h_1 + R_2\cos\left(\alpha_2 - \theta_2\right)\right]\} > I_2\ddot{\theta}_2 + g\{m_1\frac{b}{2} + m_2\left[b - R_2\sin\left(\alpha_2 - \theta_2\right)\right]\}
$$
$$
- m_2R_2\dot{\theta}_2^2\left[h_1\sin\left(\alpha_2 - \theta_2\right) + b\cos\left(\alpha_2 - \theta_2\right)\right]
$$
$$
+ m_2R_2\ddot{\theta}_2\left[R_2 + b\sin\left(\alpha_2 - \theta_2\right) - h_1\cos\left(\alpha_2 - \theta_2\right)\right]. \quad (6.115)
$$

6.6 Transition with impact

Each time an impact between two bodies happens during rocking the upper body switches from rotation around one corner to rotation around the other corner. So, when the top block hits the bottom block (and the gap between these two blocks closes) the top block transition from rotation around corner E to rotation around corner D or vice-versa, while when the bottom block hits the base (and the gap between these two bodies closes) the whole stack transition from rotation around corner A to rotation around corner B or vice-versa. Each time an impact happens, the angular velocities immediately after the impact momentarily change.

The new angular velocities are calculated from the angular momentum balance principle during the impact, i.e. between the time just before the impact, t^-, and the time immediately after the impact, t^+).

If the impact between the bottom block and the base occurs, the angular momentum of just the top block with respect to its edge acting as the centre of rotation (which did not change) is conserved. Also, the angular momentum of the whole stack with respect to the edge of the bottom block acting as the centre of rotation after the impact is conserved since we assume that the impact impulse acts on the system at that very point.

On the other hand, if the impact between the top and the bottom block happens, the angular momentum of the whole stack with respect to the edge of the bottom block acting as the centre of rotation (which did not change) is conserved. Also, the angular momentum of only the top block with respect to its edge acting as the new centre of rotation after the impact is conserved, providing the impact impulse acts at that point.

The formulas used to calculate the post-impact angular velocities are presented below.

6.6.1 Transition between configurations 4a and 4b

Based on the velocity diagrams in Figure 6.12, the angular momentum of the top block with respect to point D in configuration 4a before the impact (at time t^-) can be obtained as

$$J_{D,2}^- = I_{C2}\dot{\theta}_2^- + m_2\dot{u}^- R_2\cos\left(\alpha_2 + \theta_2\right) + R_2^2\dot{\theta}^- m_2\cos^2\left(\alpha_2 + \theta_2\right) \tag{6.116}$$

$$- R_2\dot{\theta}_2^- m_2\sin\left(\alpha_2 + \theta_2\right)\left[b_2 - R_2\sin\left(\alpha_2 + \theta_2\right)\right] \tag{6.117}$$

$$= I_{O2}\dot{\theta}_2^- + m_2R_2\left[\dot{u}^-\cos\left(\alpha_2 + \theta_2\right) - b_2\dot{\theta}_2^-\sin\left(\alpha_2 + \theta_2\right)\right], \tag{6.118}$$

while the angular momentum of the top block with respect to the same point after the impact is

$$J_{D,2}^+ = I_{O2}\dot{\theta}_2^+ + \dot{u}^- m_2 R_2\cos\left(\alpha_2 - \theta_2\right). \tag{6.119}$$
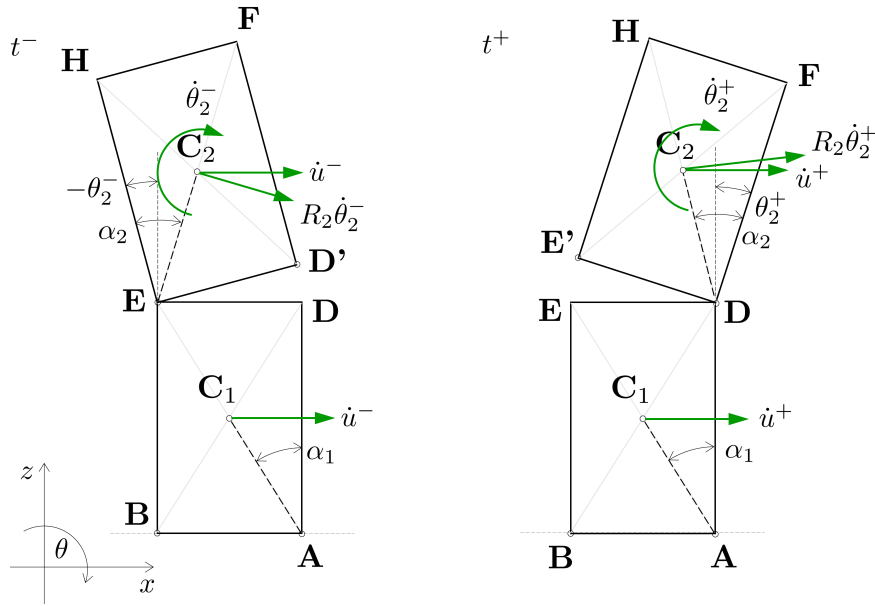
Figure 6.12: Velocity diagrams in configurations 4a and 4b

Likewise, the angular momentum of the top block with respect to point E in configuration 4b before and after the impact is

$$J_{E,2}^- = I_{C2}\dot{\theta}_2^- + m_2\dot{u}^- R_2\cos\left(\alpha_2 - \theta_2\right) + R_2^2\dot{\theta}^- m_2\cos^2\left(\alpha_2 - \theta_2\right) \tag{6.120}$$

$$- R_2\dot{\theta}_2^- m_2\sin\left(\alpha_2 - \theta_2\right)\left[b_2 - R_2\sin\left(\alpha_2 - \theta_2\right)\right] \tag{6.121}$$

$$= I_{O2}\dot{\theta}_2^- + m_2R_2\left[\dot{u}^-\cos\left(\alpha_2 - \theta_2\right) - b_2\dot{\theta}_2^-\sin\left(\alpha_2 - \theta_2\right)\right], \tag{6.122}$$

and

$$J_{E,2}^+ = I_{O2}\dot{\theta}_2^+ + \dot{u}^- m_2 R_2 \cos\left(\alpha_2 + \theta_2\right). \tag{6.123}$$

Since the angular momentum with respect to the new contact point (D or E here) is conserved when $t^+ \to t^-$ (i.e. for $\dot{u}^+ \to \dot{u}^-$ and both $\theta_2^- \to 0$ and $\theta_2^+ \to 0$), we obtain the relation between the post-impact and the pre-impact angular velocity as

$$\dot{\theta}_2^+ = \left(1 - \frac{m_2 b_2^2}{2I_{O2}}\right)\dot{\theta}_2^-, \tag{6.124}$$

i.e. the coefficient of restitution as

$$\eta_2 = 1 - \frac{m_2 b_2^2}{2I_{O2}} = 1 - \frac{3}{2}\sin\alpha_2, \tag{6.125}$$

which, as expected, coincides with the well-known Housner's restitution estimate [1].

6.6.2 Transition between configurations 3a and 3b

Based on the velocity diagrams in Figure 6.13, the angular momentum of the whole stack with respect to point A in configuration 3a before the impact (at time t^-) can be obtained as

$$\begin{aligned}
J_A^- = &\ I_{C1}\dot{\theta}_1^- + I_{C2}\dot{\theta}_2^- + m_1\dot{u}^- R_1 \cos\left(\alpha_1 + \theta_1\right) + m_2\dot{u}^- R_2' \cos\left(\alpha_2' + \theta_1\right) \\
&+ m_1 R_1^2 \dot{\theta}_1^- \cos^2\left(\alpha_1 + \theta_1\right) - m_1 R_1 \dot{\theta}_1^- \sin\left(\alpha_1 + \theta_1\right)\left[b - R_1 \sin\left(\alpha_1 + \theta_1\right)\right] \\
&+ m_2 R_2'^2 \dot{\theta}_1^- \cos^2\left(\alpha_2' + \theta_1\right) - m_2 R_2'^2 \dot{\theta}_1^- \sin^2\left(\alpha_2' + \theta_1\right), \tag{6.126}
\end{aligned}$$

while the angular momentum of the stack with respect to the same point after the impact is

$$J_A^+ = I_{O1}\dot{\theta}_1^+ + I_{O2}\dot{\theta}_2^+ + m_1\dot{u}^+ R_1 \cos\left(\alpha_1 - \theta_1\right) + m_2\dot{u}^+ R_2' \cos\left(\alpha_2' - \theta_1\right). \tag{6.127}$$
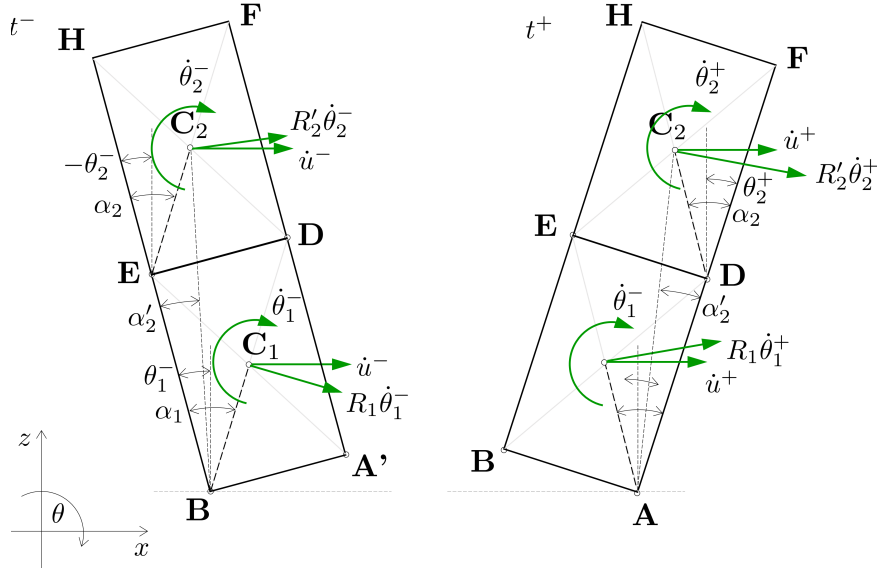
Figure 6.13: Velocity diagrams in configurations 3a and 3b

Likewise, the angular momentum of the whole stack with respect to point B in configuration 3b is

$$
\begin{aligned}
J_B^- = & I_{C1}\dot{\theta}_1^- + I_{C2}\dot{\theta}_2^- + m_1\dot{u}^- R_1 \cos\left(\alpha_1 - \theta_1\right) + m_2\dot{u}^- R_2' \cos\left(\alpha_2' - \theta_1\right) \\
& + m_1 R_1^2 \dot{\theta}_1^- \cos^2\left(\alpha_1 - \theta_1\right) - m_1 R_1 \dot{\theta}_1^- \sin\left(\alpha_1 - \theta_1\right)\left[b - R_1 \sin\left(\alpha_1 - \theta_1\right)\right] \\
& + m_2 R_2'^2 \dot{\theta}_1^- \cos^2\left(\alpha_2' - \theta_1\right) - m_2 R_2'^2 \dot{\theta}_1^- \sin^2\left(\alpha_2' - \theta_1\right), \quad (6.128)
\end{aligned}
$$

while the angular momentum of the stack with respect to the same point after the impact is

$$
J_B^+ = I_{O1}\dot{\theta}_1^+ + I_{O2}\dot{\theta}_2^+ + m_1\dot{u}^+ R_1 \cos\left(\alpha_1 + \theta_1\right) + m_2\dot{u}^+ R_2' \cos\left(\alpha_2' + \theta_1\right). \quad (6.129)
$$

Since the angular momentum with respect to the point acting as the post-impact centre of rotation (either A or B here) is conserved when $t^+ \to t^-$, $\dot{u}^+ \to \dot{u}^-$ and both $\theta_2^+ \to \theta_2^-$ (both $\theta_2^- \to 0$ and $\theta_2^+ \to 0$) and $\theta_1^+ \to \theta_1^-$ (both $\theta_1^- \to 0$ and $\theta_1^+ \to 0$), we obtain the relation between the post-impact and the pre-impact angular velocity

$$
\dot{\theta}_1+ = \left[1 - \frac{m_2 b^2}{2\left(I_O'\right)}\right]\dot{\theta}_1^-, \quad (6.130)
$$

i.e. the coefficient of restitution

$$
\eta_1 = \eta_2 = 1 - \frac{m_2 b^2}{2\left(I_O'\right)}. \quad (6.131)
$$

The same procedure should be followed in order to obtain the coefficient of restitution for the vice-versa transition (from 3b to 3a), which is the same as η_2 in equation (6.131).

126

6.6.3   Transition between configurations 1a and 2a

Based on the velocity plans shown in Figure 6.14 angular momentum of the top block with respect to point D before the impact (at time t^-) is

$$
\begin{aligned}
J_{D,2}^- = {} & I_{C2}\dot{\theta}_2^- + \dot{u}^- m_2 \left[-b \sin\left(-\theta_1\right) + R_2 \cos\left(\alpha_2 + \theta_2\right) \right] \\
& + R_2 \dot{\theta}_2^- m_2 \cos\left(\alpha_2 + \theta_2\right) \left[-b \sin\left(-\theta_1\right) + R_2 \cos\left(\alpha_2 + \theta_2\right) \right] \\
& - R_2 \dot{\theta}_2^- m_2 \sin\left(\alpha_2 + \theta_2\right) \left[b \cos\left(-\theta_1\right) - R_2 \sin\left(\alpha_2 + \theta_2\right) \right] \\
& + h_1 \dot{\theta}_1^- m_2 \cos\left(-\theta_1\right) \left[-b \sin\left(-\theta_1\right) + R_2 \cos\left(\alpha_2 + \theta_2\right) \right] \\
& + h_1 \dot{\theta}_1^- m_2 \sin\left(-\theta_1\right) \left[b \cos\left(-\theta_1\right) - R_2 \sin\left(\alpha_2 + \theta_2\right) \right], \quad (6.132)
\end{aligned}
$$

while after the impact (at time t^+) is

$$
\begin{aligned}
J_{D,2}^+ = {} & I_{O2}\dot{\theta}_2^+ + \dot{u}^+ m_2 R_2 \cos\left(\alpha_2 - \theta_2\right) + 2R_1 \dot{\theta}_1^+ m_2 \cos\left(\alpha_1 + \theta_1\right) R_2 \cos\left(\alpha_2 - \theta_2\right) \\
& - 2R_1 \dot{\theta}_1^+ m_2 \sin\left(\alpha_1 + \theta_1\right) R_2 \sin\left(\alpha_2 - \theta_2\right). \quad (6.133)
\end{aligned}
$$

The angular momentum of the whole stack with respect to point B before the impact (at time t^-) is

$$
\begin{aligned}
J_B^- = {} & I_{O1}\dot{\theta}_1^- + I_{C2}\dot{\theta}_2^- + \dot{u}^- m_1 R_1 \cos\left(\alpha_1 + \theta_1\right) + \dot{u}^- m_2 \left[h_1 \cos\left(-\theta_1\right) + R_2 \cos\left(\alpha_2 + \theta_2\right) \right] \\
& + R_2 \dot{\theta}_2^- m_2 \cos\left(\alpha_2 + \theta_2\right) \left[h_1 \cos\left(-\theta_1\right) + R_2 \cos\left(\alpha_2 + \theta_2\right) \right] \\
& + R_2 \dot{\theta}_2^- m_2 \sin\left(\alpha_2 + \theta_2\right) \left[-h_1 \sin\left(-\theta_1\right) + R_2 \sin\left(\alpha_2 + \theta_2\right) \right] \\
& + h_1 \dot{\theta}_1^- m_2 \cos\left(-\theta_1\right) \left[h_1 \cos\left(-\theta_1\right) + R_2 \cos\left(\alpha_2 + \theta_2\right) \right] \\
& - h_1 \dot{\theta}_1^- m_2 \sin\left(-\theta_1\right) \left[-h_1 \sin\left(-\theta_1\right) + R_2 \sin\left(\alpha_2 + \theta_2\right) \right], \quad (6.134)
\end{aligned}
$$

while the angular momentum of the stack with respect to the same point after the impact is

$$
\begin{aligned}
J_B^+ = {} & I_{O1}\dot{\theta}_1^+ + I_{C2}\dot{\theta}_2^+ + \dot{u}^+ m_2 \left[2R_1 \cos\left(\alpha_1 + \theta_1\right) + R_2 \cos\left(\alpha_2 - \theta_2\right) \right] \\
& + 2R_1 \dot{\theta}_1^+ m_2 \cos\left(\alpha_1 + \theta_1\right) \left[2R_1 \cos\left(\alpha_1 + \theta_1\right) + R_2 \cos\left(\alpha_2 - \theta_2\right) \right] \\
& + 2R_1 \dot{\theta}_1^+ m_2 \sin\left(\alpha_1 + \theta_1\right) \left[2R_1 \sin\left(\alpha_1 + \theta_1\right) - R_2 \sin\left(\alpha_2 - \theta_2\right) \right] \\
& + R_2 \dot{\theta}_2^+ m_2 \cos\left(\alpha_2 - \theta_2\right) \left[2R_1 \cos\left(\alpha_1 + \theta_1\right) + R_2 \cos\left(\alpha_2 - \theta_2\right) \right] \\
& - R_2 \dot{\theta}_2^+ m_2 \sin\left(\alpha_2 - \theta_2\right) \left[2R_1 \sin\left(\alpha_1 + \theta_1\right) - R_2 \sin\left(\alpha_2 - \theta_2\right) \right]. \quad (6.135)
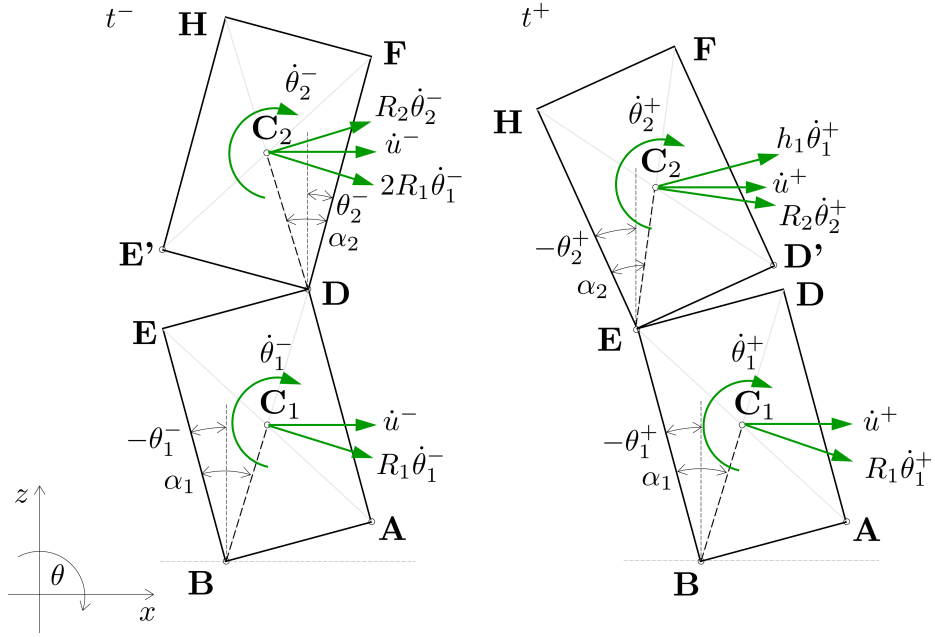\end{aligned}
$$
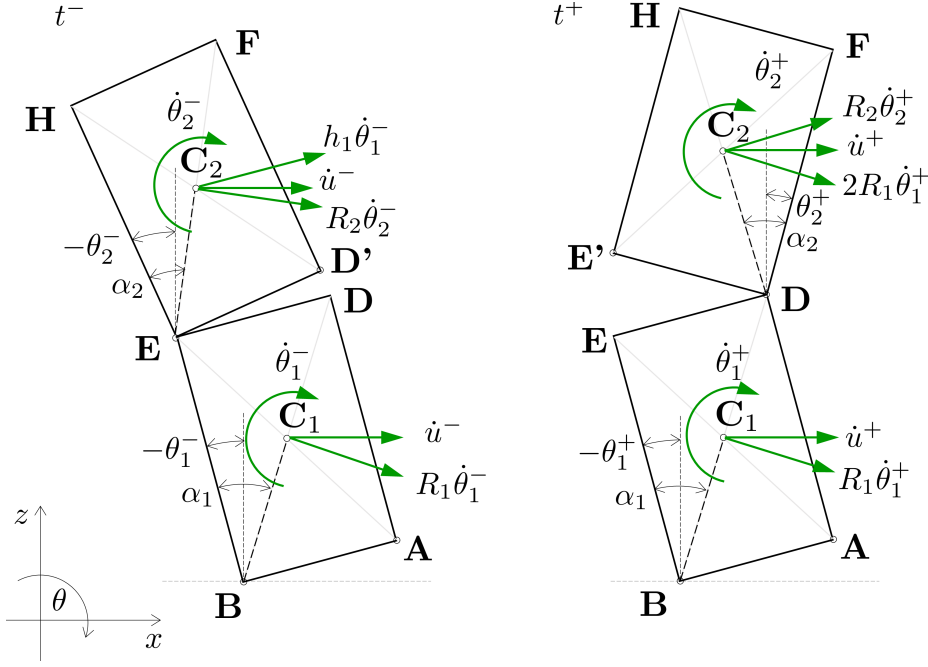
Figure 6.14: Velocity diagrams in configurations 1a and 2a

Following $J_B^- = J_B^+$ and $J_{D,2}^- = J_{D,2}^+$, we obtain

$$\begin{bmatrix} \zeta_1 & \zeta_2 \\ \zeta_3 & \zeta_4 \end{bmatrix} \begin{Bmatrix} \dot{\theta}_1^+ \\ \dot{\theta}_2^+ \end{Bmatrix} = \begin{Bmatrix} \lambda_1 \\ \lambda_2 \end{Bmatrix}, \tag{6.136}$$

where

$$\zeta_1 = I_{C1} + R_1^2 m_1 + 2R_1 m_2 \cos(\alpha_1 + \theta_1)\left[2R_1 \cos(\alpha_1 + \theta_1) + R_2 \cos(\alpha_2 - \theta_1)\right]$$
$$+ 2R_1 m_2 \sin(\alpha_1 + \theta_1)\left[2R_1 \sin(\alpha_1 + \theta_1) - R_2 \sin(\alpha_2 - \theta_1)\right]$$
$$= I_{C1} + R_1^2 m_1 + 4R_2^2 m_2 + 2R_1 R_2 m_1 \cos(\alpha_1 + \alpha_2), \quad (6.137)$$

$$\zeta_2 = I_{C2} + R_2 m_2 \cos(\alpha_2 - \theta_1)\left[2R_1 \cos(\alpha_1 + \theta_1) + R_2 \cos(\alpha_2 - \theta_1)\right]$$
$$- R_2 m_2 \sin(\alpha_2 - \theta_1)\left[1R_1 \sin(\alpha_1 + \theta_1) - R_2 \sin(\alpha_2 - \theta_1)\right]$$
$$= I_{C2} + R_2 m_2 + 2R_1 R_2 m_2 \cos(\alpha_1 + \alpha_2), \quad (6.138)$$

$$\zeta_3 = 2R_1 m_2 \cos(\alpha_1 + \theta_1) R_2 \cos(\alpha_2 - \theta_1)$$
$$- 2R_1 m_2 \sin(\alpha_1 + \theta_1) r_2 \sin(\alpha_2 - \theta_1)$$
$$= 2R_1^2 m_2 \cos(\alpha_1 + \alpha_2), \quad (6.139)$$

$$\zeta_4 = I_{C2} + R_2^2 m_2, \tag{6.140}$$

128

$$\lambda_1 = I_{C1}\dot{\theta}_1^- + I_{C2}\dot{\theta}_2^- + R_1^2 m_1 \dot{\theta}_1^- + R_2 \dot{\theta}_2^- m_2 \cos\left(\alpha_2 + \theta_1\right)\left[h_1 \cos\left(-\theta_1\right) + R_2 \cos\left(\alpha_2 + \theta_1\right)\right]$$

$$+ R_2 \dot{\theta}_2^- m_2 \sin\left(\alpha_2 + \theta_1\right)\left[-h_1 \sin\left(-\theta_1\right) + R - 2\sin\left(\alpha_2 + \theta_1\right)\right]$$

$$+ h_1 \dot{\theta}_1^- m_2 \cos\left(-\theta_1\right)\left[h_1 \cos\left(-\theta_1\right) + R_2 \cos\left(\alpha_2 + \theta_1\right)\right]$$

$$- h_1 \dot{\theta}_1^- m_2 \sin\left(-\theta_1\right)\left[-h_1 \sin\left(-\theta_1\right) + R_2 \sin\left(\alpha_2 + \theta_1\right)\right]$$

$$+ \dot{u}^- m_2 \left[h_1 \cos\left(-\theta_1\right) + R_2 \cos\left(\alpha_2 + \theta_1\right)\right] - \dot{u}^+ m_2 \left[2R_1 \cos\left(\alpha_1 + \theta_1\right) + R_2 \cos\left(\alpha_2 - \theta_1\right)\right]$$

$$= \left(I_{C1} + R_1^2 m_1 + h_1^2 m_2 + \frac{h_1 h_2}{2} m_2\right)\dot{\theta}_1^- + \left(I_{C2} + R_2^2 m_2 + \frac{h_1 h_2}{2} m_2\right)\dot{\theta}_2^-$$

$$+ \dot{u}^- m_2 \left[h_1 \cos\left(-\theta_1\right) + R_2 \cos\left(\alpha_2 + \theta_1\right)\right] - \dot{u}^+ m_2 \left[2R_1 \cos\left(\alpha_1 + \theta_1\right) + R_2 \cos\left(\alpha_2 - \theta_1\right)\right],$$

$$(6.141)$$

and

$$\lambda_2 = I_{C2}\dot{\theta}_2^- + R_2 \dot{\theta}_2^- m_2 \cos\left(\alpha_2 + \theta_1\right)\left[-b \sin\left(-\theta_1\right) + R_2 \cos\left(\alpha_2 + \theta_1\right)\right]$$

$$- R_2 \dot{\theta}_2^- m_2 \sin\left(\alpha_2 + \theta_1\right)\left[b \cos\left(-\theta_1\right) - R_2 \sin\left(\alpha_2 + \theta_1\right)\right]$$

$$+ h_1 \dot{\theta}_1^- m_2 \cos\left(-\theta_1\right)\left[-b \sin\left(-\theta_1\right) + R_2 \cos\left(\alpha_2 + \theta_1\right)\right]$$

$$+ h_1 \dot{\theta}_1^- m_2 \sin\left(-\theta_1\right)\left[b \cos\left(-\theta_1\right) - R_2 \sin\left(\alpha_2 + \theta_1\right)\right]$$

$$+ m_2 R_2 \dot{u}^- \cos\left(\alpha_2 \theta_1\right) - m_2 R_2 \dot{u}^+ \cos\left(\alpha_2 - \theta_1\right) - b m_2 \dot{u}^- \sin\left(-\theta_1\right)$$

$$= \left(I_{C2} + R_2^2 m_2\right)\dot{\theta}_2^- + \left(-\frac{b h_2}{2} m_2 + \frac{h_1 h_2}{2} m_2\right)\dot{\theta}_1^-$$

$$+ m_2 R_2 \dot{u}^- \cos\left(\alpha_2 \theta_1\right) - m_2 R_2 \dot{u}^+ \cos\left(\alpha_2 - \theta_1\right) - b m_2 \dot{u}^- \sin\left(-\theta_1\right). \quad (6.142)$$

Likewise, based on the velocity plans shown in Figure 6.14, the angular momentum of the top block with respect to point E before the impact (at time t^-) and after the impact (at time t^+), as well as the angular momentum of the stack with respect to point B before and after the impact are derived.

Figure 6.15: Velocity diagrams in configurations 2a and 1a

Following $J_B^- = J_B^+$ and $J_{E,2}^- = J_{E,2}^+$, we obtain

$$\begin{bmatrix} \zeta_1 & \zeta_2 \\ \zeta_3 & \zeta_4 \end{bmatrix} \begin{Bmatrix} \dot{\theta}_1^+ \\ \dot{\theta}_2^+ \end{Bmatrix} = \begin{Bmatrix} \lambda_1 \\ \lambda_2 \end{Bmatrix}, \tag{6.143}$$

where

$$\zeta_1 = I_{C1} + R_1^2 m_1 + \frac{h_1 h_2}{2} m_2, \tag{6.144}$$

$$\zeta_2 = I_{C2} + \frac{h_1 h_2}{2} m_2 + R_2^2 m_2, \tag{6.145}$$

$$\zeta_3 = \frac{h_1 h_2}{2} m_2, \tag{6.146}$$

$$\zeta_4 = I_{C2} + R_2^2 m_2, \tag{6.147}$$

$$\lambda_1 = \big[\big] I_{C1} + R_1^2 m_1 + 4 R_1^2 m_2 + 2 R_1 R_2 m_2 \cos(\alpha_1 + \alpha_2) \big] \dot{\theta}_1^-$$
$$+ \big[I_{C2} + R_2^2 m_2 + 2 R_1 R_2 m_2 \cos(\alpha_1 + \alpha_2) \big] \dot{\theta}_2^-$$
$$+ \dot{u}^- m_2 \left[2 R_1 \cos(\alpha_1 + \theta_1) + R_2 \cos(\alpha_2 - \theta_1) \right] - \dot{u}^+ m_2 \left[h_1 \cos(-\theta_1) + R_2 \cos(\alpha_2 + \theta_1) \right], \tag{6.148}$$

and

$$\lambda_2 = \left(I_{C2} - \frac{b h_2}{2} m_2 + R_2^2 m_2 \right) \dot{\theta}_2^- + \left[\frac{b h_1}{2} m_2 + 2 R_1 R_2 m_2 \cos(\alpha_1 + \alpha_2) \right] \dot{\theta}_1^-$$
$$+ \dot{u}^- m_2 \left[b \sin(-\theta_1) + R_2 \cos(\alpha_2 - \theta_1) \right] - \dot{u}^+ m_2 R_2 \cos(\alpha_2 + \theta_1). \tag{6.149}$$

130

6.6.4 Transition between configurations 1b and 2b

Following the same procedure as explained in Section 6.6.3 for transition between configurations 1a and 2a, here we obtain the post-impact velocities for transitions between configurations 1b and 2b.

Following $J_B^- = J_B^+$ and $J_{D,2}^- = J_{D,2}^+$, we obtain the post-impact velocities for transition from 1b to 2b as

$$\begin{bmatrix} \zeta_1 & \zeta_2 \\ \zeta_3 & \zeta_4 \end{bmatrix} \begin{Bmatrix} \dot{\theta}_1^+ \\ \dot{\theta}_2^+ \end{Bmatrix} = \begin{Bmatrix} \lambda_1 \\ \lambda_2 \end{Bmatrix}, \tag{6.150}$$

where

$$\zeta_1 = I_{C1} + R_1^2 m_1 + 4R_2^2 m_2 + 2R_1 R_2 m_1 \cos(\alpha_1 + \alpha_2), \tag{6.151}$$

$$\zeta_2 = I_{C2} + R_2 m_2 + 2R_1 R_2 m_2 \cos(\alpha_1 + \alpha_2), \tag{6.152}$$

$$\zeta_3 = 2R_1^2 m_2 \cos(\alpha_1 + \alpha_2), \tag{6.153}$$

$$\zeta_4 = I_{C2} + R_2^2 m_2, \tag{6.154}$$

$$\lambda_1 = \left(I_{C1} + R_1^2 m_1 + h_1^2 m_2 + \frac{h_1 h_2}{2} m_2 \right) \dot{\theta}_1^- + \left(I_{C2} + R_2^2 m_2 + \frac{h_1 h_2}{2} m_2 \right) \dot{\theta}_2^-$$
$$+ \dot{u}^- m_2 \left[h_1 \cos(\theta_1) + R_2 \cos(\alpha_2 - \theta_1) \right] - \dot{u}^+ m_2 \left[2R_1 \cos(\alpha_1 - \theta_1) + R_2 \cos(\alpha_2 + \theta_1) \right],$$

$$\tag{6.155}$$

and

$$\lambda_2 = \left(I_{C2} + R_2^2 m_2 \right) \dot{\theta}_2^- + \left(-\frac{bh_2}{2} m_2 + \frac{h_1 h_2}{2} m_2 \right) \dot{\theta}_1^-$$
$$+ m_2 R_2 \dot{u}^- \cos(\alpha_2 + \theta_1) - m_2 R_2 \dot{u}^+ \cos(\alpha_2 + \theta_1) - bm_2 \dot{u}^- \sin(\theta_1). \tag{6.156}$$

Following $J_B^- = J_B^+$ and $J_{E,2}^- = J_{E,2}^+$, we obtain the post-impact velocities for transition from 2b to 1b as

$$\begin{bmatrix} \zeta_1 & \zeta_2 \\ \zeta_3 & \zeta_4 \end{bmatrix} \begin{Bmatrix} \dot{\theta}_1^+ \\ \dot{\theta}_2^+ \end{Bmatrix} = \begin{Bmatrix} \lambda_1 \\ \lambda_2 \end{Bmatrix}, \tag{6.157}$$

where

$$\zeta_1 = I_{C1} + R_1^2 m_1 + \frac{h_1 h_2}{2} m_2, \tag{6.158}$$

$$\zeta_2 = I_{C2} + \frac{h_1 h_2}{2} m_2 + R_2^2 m_2, \tag{6.159}$$

$$\zeta_3 = \frac{h_1 h_2}{2} m_2, \tag{6.160}$$

131

$$\zeta_4 = I_{C2} + R_2^2 m_2, \tag{6.161}$$

$$\lambda_1 = \left[I_{C1} + R_1^2 m_1 + 4R_1^2 m_2 + 2R_1 R_2 m_2 \cos{(\alpha_1 + \alpha_2)} \right] \dot{\theta}_1^-$$
$$+ \left[I_{C2} + R_2^2 m_2 + 2R_1 R_2 m_2 \cos{(\alpha_1 + \alpha_2)} \right] \dot{\theta}_2^-$$
$$+ \dot{u}^- m_2 \left[2R_1 \cos{(\alpha_1 - \theta_1)} + R_2 \cos{(\alpha_2 + \theta_1)} \right] - \dot{u}^+ m_2 \left[h_1 \cos{(\theta_1)} + R_2 \cos{(\alpha_2 - \theta_1)} \right], \tag{6.162}$$

and

$$\lambda_2 = \left(I_{C2} - \frac{bh_2}{2} m_2 + R_2^2 m_2 \right) \dot{\theta}_2^- + \left[\frac{bh_1}{2} m_2 + 2R_1 R_2 m_2 \cos{(\alpha_1 + \alpha_2)} \right] \dot{\theta}_1^-$$
$$+ \dot{u}^- m_2 \left[b \sin{(\theta_1)} + R_2 \cos{(\alpha_2 + \theta_1)} \right] - \dot{u}^+ m_2 R_2 \cos{(\alpha_2 - \theta_1)}. \tag{6.163}$$

6.6.5   Transition between configurations 1a and 2b

Based on the velocity plans in Figure 6.16, the angular momentum of the top block
with respect to point E before the impact (at time t^-) is

$$J_{E,2}^- = I_{O2} \dot{\theta}_2^- + \dot{u}^- m_2 R_2 \cos{(\alpha_2 + \theta_2)} + h_1 \dot{\theta}_1^- m_2 \cos{(-\theta_1)} R_2 \cos{(\alpha_2 + \theta_2)}$$
$$- h_1 \dot{\theta}_1^- m_2 \sin{(-\theta_1)} R_2 \sin{(\alpha_2 + \theta_2)} \tag{6.164}$$

and after the impact (at time t^+) is

$$J_{E,2}^+ = I_{O2} \dot{\theta}_2^+ + \dot{u}^+ m_2 R_2 \cos{(\alpha_2 + \theta_2)} + 2R_1 \dot{\theta}_1^+ m_2 \cos{(\alpha_1 - \theta_1)} R_2 \cos{(\alpha_2 + \theta_2)}$$
$$- 2R_1 \dot{\theta}_1^+ m_2 \sin{(\alpha_1 - \theta_1)} R_2 \sin{(\alpha_2 + \theta_2)}. \tag{6.165}$$

The angular momentum of the whole stack with respect to the point A before the
impact (at time t^-) is

$$J_A^- = I_{C1} \dot{\theta}_1^- + I_{C2} \dot{\theta}_2^- + \dot{u}^- m_1 R_1 \cos{(\alpha_1 + \theta_1)} + R_1^2 \dot{\theta}_1^- m_1 \cos^2{(\alpha_1 + \theta_1)}$$
$$- R_1 \dot{\theta}_1^- m_1 \sin{(\alpha_1 + \theta_1)} \left[b - R_1 \sin{(\alpha_1 + \theta_1)} \right]$$
$$+ \dot{u}^- m_2 \left[h_1 \cos{(-\theta_1)} + R_2 \cos{(\alpha_2 + \theta_2)} \right]$$
$$+ h_1 \dot{\theta}_1^- m_2 \cos{(-\theta_1)} \left[h_1 \cos{(-\theta_1)} + R_2 \cos{(\alpha_2 + \theta_2)} \right]$$
$$+ h_1 \dot{\theta}_1^- m_2 \sin{(-\theta_1)} \left[b1 + h_1 \sin{(-\theta_1)} - R_2 \sin{(\alpha_2 + \theta_2)} \right]$$
$$+ R_2 \dot{\theta}_2^- m_2 \cos{(\alpha_2 + \theta_2)} \left[h_1 \cos{(-\theta_1)} + R_2 \cos{(\alpha_2 + \theta_2)} \right]$$
$$- R_2 \dot{\theta}_2^- m_2 \sin{(\alpha_2 + \theta_2)} \left[b + h_1 \sin{(-\theta_1)} - R_2 \sin{(\alpha_2 + \theta_2)} \right] \tag{6.166}$$

and after the impact (at time t^+) is

$$J_A^+ = I_{O1}\dot{\theta}_1^+ + I_{C2}\dot{\theta}_2^+ + \dot{u}^+ m_1 R_1 \cos(\alpha_1 - \theta_1)$$
$$+ \dot{u}^+ m_2 \left[2R_1 \cos(\alpha_1 - \theta_1) + R_2 \cos(\alpha_2 + \theta_2)\right]$$
$$+ R_2 \dot{\theta}_2^+ m_2 \cos(\alpha_2 + \theta_2) \left[2R_1 \cos(\alpha_1 - \theta_1) + R_2 \cos(\alpha_2 + \theta_2)\right]$$
$$- R_2 \dot{\theta}_2^+ m_2 \sin(\alpha_2 + \theta_2) \left[2R_1 \sin(\alpha_1 - \theta_1) - R_2 \sin(\alpha_2 + \theta_2)\right]$$
$$+ 2R_1 \dot{\theta}_1^+ m_2 \cos(\alpha_1 - \theta_1) \left[2R_1 \cos(\alpha_1 - \theta_1) + R_2 \cos(\alpha_2 + \theta_2)\right]$$
$$+ 2R_1 \dot{\theta}_1^+ m_2 \sin(\alpha_1 - \theta_1) \left[2R_1 \sin(\alpha_1 - \theta_1) - R_2 \sin(\alpha_2 + \theta_2)\right]. \quad (6.167)$$
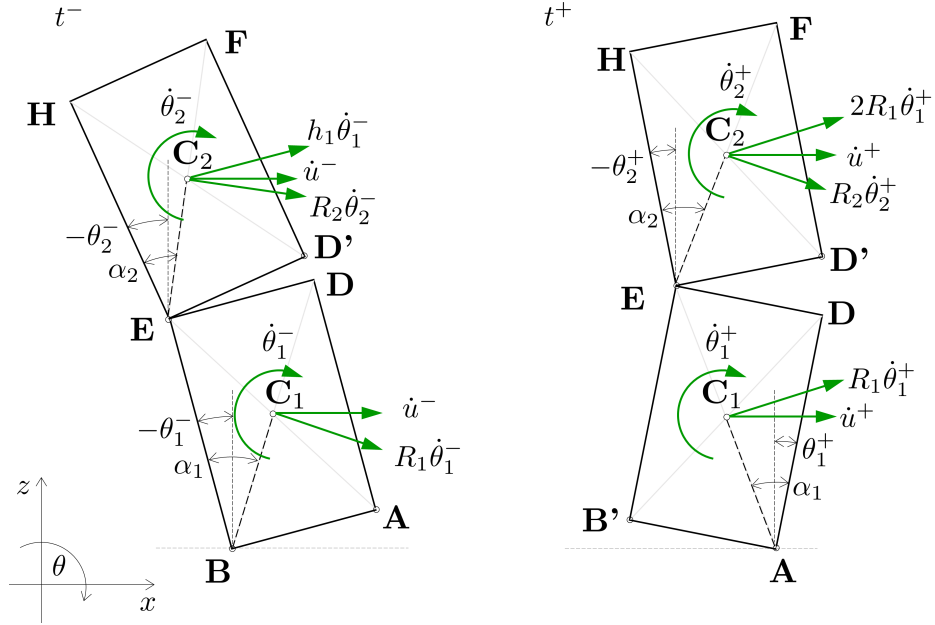
Figure 6.16: Velocity diagrams for configurations 1a and 2b

Following $J_A^- = J_A^+$ and $J_{E,2}^- = J_{E,2}^+$, we obtain the post-impact velocities for transition from 1a to 2b as

$$\begin{bmatrix} \zeta_1 & \zeta_2 \\ \zeta_3 & \zeta_4 \end{bmatrix} \begin{Bmatrix} \dot{\theta}_1^+ \\ \dot{\theta}_2^+ \end{Bmatrix} = \begin{Bmatrix} \lambda_1 \\ \lambda_2 \end{Bmatrix}, \quad (6.168)$$

where

$$\zeta_1 = I_{C1} + R_1^2 m_1 + h_1^2 m_2 + R_2 h_1 m_2 \cos(\alpha_2 + \theta_2), \quad (6.169)$$

$$\zeta_2 = I_{C2} + R_2^2 m_2 + 2R_1 R_2 m_2 \cos(\alpha_1 + \alpha_2 + \theta_2), \quad (6.170)$$

$$\zeta_3 = 2R_1 R_2 m_2 \cos(\alpha_1 + \alpha_2 + \theta_2), \quad (6.171)$$

$$\zeta_4 = I_{C2} + R_2^2 m_2, \quad (6.172)$$

133

$$\lambda_1 = \left[I_{C1} + R_1^2 m_1 - \frac{b^2}{2} m_1 + h_1^2 m_2 + h_1 R_1 m_2 \cos\left(\alpha_2 + \theta_2\right) \right] \dot{\theta}_1$$
$$+ \left[I_{C2} + R_2 h_1 m_2 \cos\left(\alpha_2 + \theta_1\right) + R_2^2 m_2 - R_2 b m_2 \sin\left(\alpha_2 + \theta_1\right) \right] \dot{\theta}_2^-, \quad (6.173)$$

and

$$\lambda_2 = \left(I_{C2} + R_2^2 m_2 \right) \dot{\theta}_2^- + \left[h_1 m_2 R_2 \cos\left(\alpha_2 + \theta_2\right) \right] \dot{\theta}_1^-. \quad (6.174)$$

Likewise, based on the velocity plans in Figure 6.17, the angular momentum of the top block with respect to point E before the impact (at time t^-) is

$$J_{E,2}^- = I_{C1} \dot{\theta}_1^- + \dot{u}^- m_1 R_1 \cos\left(\alpha_1 - \theta_1\right) + R_1^2 \dot{\theta}_1^- m_1 \cos^2\left(\alpha_1 - \theta_1\right)$$
$$- R_1 \dot{\theta}_1^- m_1 \sin\left(\alpha_1 - \theta_1\right) \left[b - R_1 \sin\left(\alpha_1 - \theta_1\right) \right]$$
$$+ \dot{u}^- m_2 \left[2 R_1 \cos\left(\alpha_1 - \theta_1\right) + R_2 \cos\left(\alpha_2 + \theta_2\right) \right]$$
$$+ R_2 \dot{\theta}_2^- m_2 \cos\left(\alpha_2 + \theta_2\right) \left[2 R_1 \cos\left(\alpha_1 - \theta_1\right) + R_2 \cos\left(\alpha_2 + \theta_2\right) \right]$$
$$+ R_2 \dot{\theta}_2^- m_2 \sin\left(\alpha_2 + \theta_2\right) \left[b - 2 R_1 \sin\left(\alpha_1 - \theta_1\right) + R_2 \sin\left(\alpha_2 + \theta_2\right) \right]$$
$$+ 2 R_1 \dot{\theta}_1^- m_2 \cos\left(\alpha_1 - \theta_1\right) \left[2 R_1 \cos\left(\alpha_1 - \theta_1\right) + R_2 \cos\left(\alpha_2 + \theta_2\right) \right]$$
$$- 2 R_1 \dot{\theta}_1^- m_2 \sin\left(\alpha_1 - \theta_1\right) \left[b - 2 R_1 \sin\left(\alpha_1 - \theta_1\right) + R_2 \sin\left(\alpha_2 + \theta_2\right) \right] \quad (6.175)$$

and after the impact (at time t^+) is

$$J_{E,2}^+ = I_{O1} \dot{\theta}_1^+ + I_{C2} \dot{\theta}_2^+ + \dot{u}^+ m_1 R_1 \cos\left(\alpha_1 + \theta_1\right)$$
$$+ \dot{u}^+ m_2 \left[h_1 \cos\left(-\theta_1\right) + R_2 \cos\left(\alpha_2 + \theta_2\right) \right] +$$
$$R_2 \dot{\theta}_2^+ m_2 \cos\left(\alpha_2 + \theta_2\right) \left[h_1 \cos\left(-\theta_1\right) + R_2 \cos\left(\alpha_2 + \theta_2\right) \right]$$
$$+ R_2 \dot{\theta}_2^+ m_2 \sin\left(\alpha_2 + \theta_2\right) \left[-h_1 \sin\left(-\theta_1\right) + R_2 \sin\left(\alpha_2 + \theta_2\right) \right]. \quad (6.176)$$

The angular momentum of the whole stack with respect to the point B before the impact (at time t^-) is

$$J_B^- = I_{O2} \dot{\theta}_2^- + \dot{u}^- m_2 R_2 \cos\left(\alpha_2 + \theta_2\right) + 2 R_1 m_2 \dot{\theta}_1^- \cos\left(\alpha_1 - \theta_1\right) R_2 \cos\left(\alpha_2 + \theta_2\right)$$
$$- 2 R_1 m_2 \dot{\theta}_1^- \sin\left(\alpha_1 - \theta_1\right) R_2 \sin\left(\alpha_2 + \theta_2\right) \quad (6.177)$$

and after the impact (at time t^+) is

$$J_B^+ = I_{O2} \dot{\theta}_2^+ + \dot{u}^+ m_2 R_2 \cos\left(\alpha_2 + \theta_2\right) + h_1 \dot{\theta}_1^+ m_2 \cos\left(-\theta_1\right) R_2 \cos\left(\alpha_2 + \theta_2\right)$$
$$- h_1 \dot{\theta}_1^+ m_2 \sin\left(-\theta_1\right) R_2 \sin\left(\alpha_2 + \theta_2\right). \quad (6.178)$$
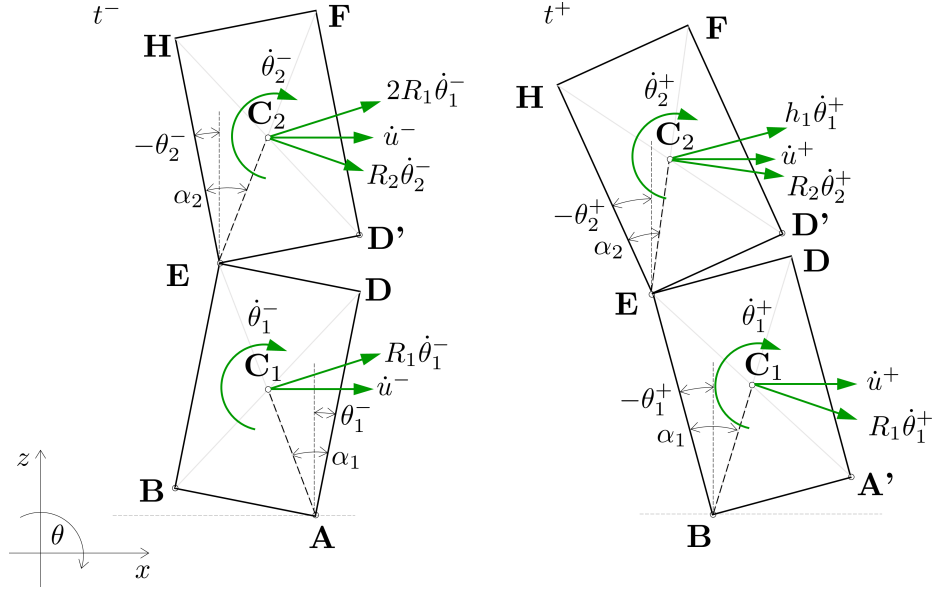
Figure 6.17: Velocity diagrams for configurations 2b and 1a

Following $J_B^- = J_B^+$ and $J_{E,2}^- = J_{E,2}^+$, we obtain the post-impact velocities for transition from 2b to 1a as

$$\begin{bmatrix} \zeta_1 & \zeta_2 \\ \zeta_3 & \zeta_4 \end{bmatrix} \begin{Bmatrix} \dot{\theta}_1^+ \\ \dot{\theta}_2^+ \end{Bmatrix} = \begin{Bmatrix} \lambda_1 \\ \lambda_2 \end{Bmatrix}, \tag{6.179}$$

where

$$\zeta_1 = I_{C1} + R_1^2 m_1 + 2h_1 R_2 m_2 \left[\cos\left(\alpha_2 + \theta_2\right) - \sin\left(\alpha_2 + \theta_2\right) \right], \tag{6.180}$$

$$\zeta_2 = I_{C2} + R_2^2 m_2 + R_2 m_2 h_1 \left[\cos\left(\alpha_2 + \theta_2\right) - \sin\left(\alpha_2 + \theta_2\right) \right], \tag{6.181}$$

$$\zeta_3 = h_1 m_2 R_2 \left[\cos\left(\alpha_2 + \theta_2\right) - \sin\left(\alpha_2 + \theta_2\right) \right], \tag{6.182}$$

$$\zeta_4 = I_{C2} + R_2^2 m_2, \tag{6.183}$$

$$\lambda_1 = \left\{ I_{C1} + \frac{h_1^2}{4} m_1 - \frac{b^2}{4} m_1 + h_1 m_2 \left[h_1 + R_2 \cos\left(\alpha_2 + \theta_2\right) \right] - b m_2 R_2 \sin\left(\alpha_2 + \theta_2\right) \right\} \dot{\theta}_1^-$$
$$+ \left[I_{C2} + R_2 m_2 h_1 \cos\left(\alpha_2 + \theta_2\right) + R_2^2 m_2 \right] \dot{\theta}_2^-, \tag{6.184}$$

and

$$\lambda_2 = \left(I_{C2} + R_2^2 m_2 \right) \dot{\theta}_2^- + \left[2R_1 R_2 m_2 \cos\left(\alpha_1 + \alpha_2 + \theta_2\right) \right] \dot{\theta}_1^-. \tag{6.185}$$

135

6.6.6 Transition between configurations 1b and 2a

Following the same procedure as explained in Section 6.6.3 for transition between configurations 1a and 2b, here the obtain the post-impact velocities for transitions between configurations 1b and 2a.

Following $J_B^- = J_B^+$ and $J_{D,2}^- = J_{D,2}^+$, we obtain the post-impact velocities for transition from 1b to 2a we obtain

$$\begin{bmatrix} \zeta_1 & \zeta_2 \\ \zeta_3 & \zeta_4 \end{bmatrix} \begin{Bmatrix} \dot{\theta}_1^+ \\ \dot{\theta}_2^+ \end{Bmatrix} = \begin{Bmatrix} \lambda_1 \\ \lambda_2 \end{Bmatrix}, \tag{6.186}$$

where

$$\zeta_1 = I_{C1} + R_1^2 m_1 + h_1^2 m_2 + R_2 h_1 m_2 \cos(\alpha_2 - \theta_2), \tag{6.187}$$

$$\zeta_2 = I_{C2} + R_2^2 m_2 + 2R_1 R_2 m_2 \cos(\alpha_1 + \alpha_2 - \theta_2), \tag{6.188}$$

$$\zeta_3 = 2R_1 R_2 m_2 \cos(\alpha_1 + \alpha_2 - \theta_2), \tag{6.189}$$

$$\zeta_4 = I_{C2} + R_2^2 m_2, \tag{6.190}$$

$$\lambda_1 = \left[I_{C1} + R_1^2 m_1 - \frac{b^2}{2} m_1 + h_1^2 m_2 + h_1 R_1 m_2 \cos(\alpha_2 - \theta_2) \right] \dot{\theta}_1$$
$$+ \left[I_{C2} + R_2 h_1 m_2 \cos(\alpha_2 - \theta_2) + R_2^2 m_2 - R_2 b m_2 \sin(\alpha_2 - \theta_2) \right] \dot{\theta}_2^-, \tag{6.191}$$

and

$$\lambda_2 = \left(I_{C2} + R_2^2 m_2 \right) \dot{\theta}_2^- + \left[h_1 m_2 R_2 \cos(\alpha_2 - \theta_2) \right] \dot{\theta}_1^-. \tag{6.192}$$

Following $J_A^- = J_A^+$ and $J_{D,2}^- = J_{D,2}^+$, we obtain the post-impact velocities for transition from 2a to 1b we obtain

$$\begin{bmatrix} \zeta_1 & \zeta_2 \\ \zeta_3 & \zeta_4 \end{bmatrix} \begin{Bmatrix} \dot{\theta}_1^+ \\ \dot{\theta}_2^+ \end{Bmatrix} = \begin{Bmatrix} \lambda_1 \\ \lambda_2 \end{Bmatrix}, \tag{6.193}$$

where

$$\zeta_1 = I_{C1} + R_1^2 m_1 + 2h_1 R_2 m_2 \left[\cos(\alpha_2 - \theta_2) - \sin(\alpha_2 - \theta_2) \right], \tag{6.194}$$

$$\zeta_2 = I_{C2} + R_2^2 m_2 + R_2 m_2 h_1 \left[\cos(\alpha_2 - \theta_2) - \sin(\alpha_2 - \theta_2) \right], \tag{6.195}$$

$$\zeta_3 = h_1 m_2 R_2 \left[\cos(\alpha_2 - \theta_2) - \sin(\alpha_2 - \theta_2) \right], \tag{6.196}$$

$$\zeta_4 = I_{C2} + R_2^2 m_2, \tag{6.197}$$

$$\lambda_1 = \left\{ I_{C1} + \frac{h_1^2}{4} m_1 - \frac{b^2}{4} m_1 + h_1 m_2 \left[h_1 + R_2 \cos(\alpha_2 - \theta_2) \right] - b m_2 R_2 \sin(\alpha_2 - \theta_2) \right\} \dot{\theta}_1^-$$
$$+ \left[I_{C2} + R_2 m_2 h_1 \cos(\alpha_2 - \theta_2) + R_2^2 m_2 \right] \dot{\theta}_2^-, \tag{6.198}$$

and

$$\lambda_2 = \left(I_{C2} + R_2^2 m_2 \right) \dot{\theta}_2^- + \left[2R_1 R_2 m_2 \cos(\alpha_1 - \alpha_2 + \theta_2) \right] \dot{\theta}_1^-. \tag{6.199}$$

6.7 Numerical procedure

6.7.1 Newmark's method

Rocking of the dual-block stack normally involves large rotations even for quite slender blocks subject to relatively weak base excitation, due to the fact that the top block lays on top of the bottom block and moves due to the rotation of the bottom block. Such motion should be analysed taking into account full nonlinearity of the equations of motion given in Section 6.2.1.

The set of two differential equations of motions, let us refer to them as $F_1\left(\theta_1,\theta_2,\dot{\theta}_1,\dot{\theta}_2,\ddot{\theta}_1,\ddot{\theta}_2\right)$ and $F_2\left(\theta_1,\theta_2,\dot{\theta}_1,\dot{\theta}_2,\ddot{\theta}_1,\ddot{\theta}_2\right)$, for each of the eight described configurations of rocking is integrated in time by dividing the time domain into a number of discrete time steps of size Δt and re-writing them at the end of a time step n (i.e. at time t_{n+1}) as $F_1\left(\theta_{1,n+1},\theta_{2,n+1},\dot{\theta}_{1,n+1},\dot{\theta}_{2,n+1},\ddot{\theta}_{1,n+1},\ddot{\theta}_{2,n+1}\right)$ and $F_2\left(\theta_{1,n+1},\theta_{2,n+1},\dot{\theta}_{1,n+1},\dot{\theta}_{2,n+1},\ddot{\theta}_{1,n+1},\ddot{\theta}_{2,n+1}\right)$. In the two discretised equations of motion the unknowns are $\theta_{1,n+1}$, $\theta_{2,n+1}$, and their derivatives with respect to time: $\dot{\theta}_{1,n+1}$, $\dot{\theta}_{2,n+1}$, $\ddot{\theta}_{1,n+1}$, and $\ddot{\theta}_{2,n+1}$.

Using Newmark's method of numerical integration [56, 63], the time derivatives $\dot{\theta}_{1,n+1}$, $\dot{\theta}_{2,n+1}$, $\ddot{\theta}_{1,n+1}$, and $\ddot{\theta}_{2,n+1}$ are approximated as

$$\dot{\theta}_{i,n+1} = \frac{\gamma\theta_{i,n+1} - \gamma\theta_{i,n}\left(\frac{\gamma}{\beta}\dot{\theta}_{i,n}\right) - \left(\frac{\gamma}{2\beta}-1\right)\ddot{\theta}_{i,n}}{\beta\Delta t} \tag{6.200}$$

and

$$\ddot{\theta}_{i,n+1} = \frac{\theta_{i,n+1} - \theta_{i,n} - \Delta t\dot{\theta}_{i,n} - \left(\frac{1}{2}-\beta\right)\Delta t^2\ddot{\theta}_{i,n}}{\beta\Delta t^2}, \tag{6.201}$$

where $i = 1, 2$. In this way we now obtain two equations of motion $F_1\left(\theta_{1,n+1},\theta_{2,n+1}\right)$ and $F_2\left(\theta_{1,n+1},\theta_{2,n+1}\right)$. The procedure of approximating the derivatives followed here is explained in detail in Section 3.2.1 for the case of a single block with only one unknown rotation.

6.7.2 Newton-Raphson iterative procedure

At each discrete time step the two equations of motion, $F_1\left(\theta_{1,n+1},\theta_{2,n+1}\right)$ and $F_2\left(\theta_{1,n+1},\theta_{2,n+1}\right)$, are nonlinear with respect to the unknown rotations $\theta_{1,n+1}$ and $\theta_{2,n+1}$, and need to be solved using an iterative procedure.

Newton-Raphson iterative procedure for the system of nonlinear equations with multiple unknowns is used here [57]. This procedure follows the iterative procedure for solving the equation of motion of a single block, explained in Section 3.2.2.

At the beginning of the analysis, given the known initial conditions for rotations $\theta_{1,0}$ and $\theta_{2,0}$, and angular velocities $\dot{\theta}_{1,0}$ and $\dot{\theta}_{2,0}$, the unknown angular accelerations $\ddot{\theta}_{1,0}$ and $\ddot{\theta}_{2,0}$ are calculated from the governing set of equations of motion corresponding to a particular configuration of rocking. After that, at each subsequent time step, the value of the rotations in the first iteration of a time step is the converged value of the rotations from the last time step, i.e.

$$\theta_{1,n+1,1} = \theta_{1,n} \tag{6.202}$$

and

$$\theta_{2,n+1,1} = \theta_{2,n}, \tag{6.203}$$

where the index 1 in $\theta_{1,n+1,1}$ and $\theta_{2,n+1,1}$ denotes the first interation. Inside each iteration, j, the two function values $F_1\left(\theta_{1,n+1,j}, \theta_{2,n+1,j}\right)$ and $F_2\left(\theta_{1,n+1,j}, \theta_{2,n+1,j}\right)$ following from a set of equations of motion for the current rocking configuration need to be calculated. If the values of *both* of these functions are lower than a given tolerance, *tol*, the solutions for the rotations obtained from the last iteration, $\theta_{1,n+1,j}$ and $\theta_{2,n+1,j}$, are taken to be the values of the converged rotations at that time step, $\theta_{1,n+1}$ and $\theta_{2,n+1}$.

If that is not the case, the first partial derivatives of the functions $F_1\left(\theta_{1,n+1}, \theta_{2,n+1}\right)$ and $F_2\left(\theta_{1,n+1}, \theta_{2,n+1}\right)$ with respect to the unknowns $\theta_{1,n+1}$ and $\theta_{2,n+1}$ need to be calculated at $\theta_{1,n+1,j}$ and $\theta_{2,n+1,j}$, i.e. the Jacobian of the system needs to be defined

$$\mathbf{J}_{n+1,j} = \left.\begin{bmatrix} \dfrac{\partial F_1\left(\theta_{1,n+1}, \theta_{2,n+1}\right)}{\partial \theta_{1,n+1}} & \dfrac{\partial F_1\left(\theta_{1,n+1}, \theta_{2,n+1}\right)}{\partial \theta_{2,n+1}} \\ \dfrac{\partial F_2\left(\theta_{1,n+1}, \theta_{2,n+1}\right)}{\partial \theta_{1,n+1}} & \dfrac{\partial F_1\left(\theta_{1,n+1}, \theta_{2,n+1}\right)}{\partial \theta_{2,n+1}} \end{bmatrix}\right|_{\substack{\theta_{1,n+1,j} \\ \theta_{2,n+1,j}}}. \tag{6.204}$$

In order to calculate the values of the unknown rotations $\theta_{1,n+1,j+1}$ and $\theta_{2,n+1,j+1}$ in the next iteration, $j + 1$, the corresponding discretised equations of motion are expanded into Taylor's series. If all the higher-order terms are ignored, this results

in a linear approximation as

$$F_1\left(\theta_{1,n+1,j+1}, \theta_{2,n+1,j+1}\right) = F_1\left(\theta_{1,n+1,j}, \theta_{2,n+1,j}\right) +$$
$$\left(\theta_{1,n+1,j+1} - \theta_{1,n+1,j}\right) \left.\frac{\partial F_1\left(\theta_{1,n+1}, \theta_{2,n+1}\right)}{\partial \theta_{1,n+1}}\right|_{\theta_{1,n+1,j};\theta_{2,n+1,j}} +$$
$$\left(\theta_{2,n+1,j+1} - \theta_{2,n+1,j}\right) \left.\frac{\partial F_1\left(\theta_{1,n+1}, \theta_{2,n+1}\right)}{\partial \theta_{2,n+1}}\right|_{\theta_{1,n+1,j};\theta_{2,n+1,j}} \equiv 0 \quad (6.205)$$

and

$$F_2\left(\theta_{1,n+1,j+1}, \theta_{2,n+1,j+1}\right) = F_2\left(\theta_{1,n+1,j}, \theta_{2,n+1,j}\right) +$$
$$\left(\theta_{1,n+1,j+1} - \theta_{1,n+1,j}\right) \left.\frac{\partial F_2\left(\theta_{1,n+1,j}, \theta_{2,n+1,j}\right)}{\partial \theta_{1,n+1,j}}\right|_{\theta_{1,n+1,j};\theta_{2,n+1,j}} +$$
$$\left(\theta_{2,n+1,j+1} - \theta_{2,n+1,j}\right) \left.\frac{\partial F_2\left(\theta_{1,n+1,j}, \theta_{2,n+1,j}\right)}{\partial \theta_{2,n+1,j}}\right|_{\theta_{1,n+1,j};\theta_{2,n+1,j}} \equiv 0. \quad (6.206)$$

The above set of equations obtained from expansion into Taylor's series can be written as

$$F_1\left(\theta_{1,n+1,j}, \theta_{2,n+1,j}\right) + \delta_{1,j} \left.\frac{\partial F_1\left(\theta_{1,n+1,j}, \theta_{2,n+1,j}\right)}{\partial \theta_{1,n+1,j}}\right|_{\theta_{1,n+1,j};\theta_{2,n+1,j}}$$
$$+ \delta_{2,j} \left.\frac{\partial F_1\left(\theta_{1,n+1,j}, \theta_{2,n+1,j}\right)}{\partial \theta_{2,n+1,j}}\right|_{\theta_{1,n+1,j};\theta_{2,n+1,j}} \equiv 0 \quad (6.207)$$

and

$$F_2\left(\theta_{1,n+1,j}, \theta_{2,n+1,j}\right) + \delta_{1,j} \left.\frac{\partial F_2\left(\theta_{1,n+1,j}, \theta_{2,n+1,j}\right)}{\partial \theta_{1,n+1,j}}\right|_{\theta_{1,n+1,j};\theta_{2,n+1,j}}$$
$$+ \delta_{2,j} \left.\frac{\partial F_1\left(\theta_{1,n+1,j}, \theta_{2,n+1,j}\right)}{\partial \theta_{2,n+1,j}}\right|_{\theta_{1,n+1,j};\theta_{2,n+1,j}} \equiv 0 \quad (6.208)$$

or shorter as

$$\boldsymbol{f}_{n+1,j} + \mathbf{J}_{n+1,j}\boldsymbol{\delta}_j \equiv 0, \quad (6.209)$$

where

$$\boldsymbol{f}_{n+1,j} = \left\{\begin{matrix} F_1\left(\theta_{1,n+1,j}, \theta_{2,n+1,j}\right) \\ F_2\left(\theta_{1,n+1,j}, \theta_{2,n+1,j}\right) \end{matrix}\right\} \quad (6.210)$$

and $\boldsymbol{\delta}_j$ is the vector of iterative corrections of the unknowns

$$\boldsymbol{\delta}_j = \left\{\begin{matrix} \delta_{1,j} \\ \delta_{2,j} \end{matrix}\right\} = \left\{\begin{matrix} \theta_{1,n+1,j+1} - \theta_{1,n+1,j} \\ \theta_{2,n+1,j+1} - \theta_{2,n+1,j} \end{matrix}\right\}. \quad (6.211)$$

Therefore, the vector of the corrections can be obtained from equation (6.209) as

$$\boldsymbol{\delta}_j = -\mathbf{J}_{n+1,j}\boldsymbol{f}_{n+1,j}. \quad (6.212)$$

This procedure is repeated within each time step until the absolute values of both functions $F_1\left(\theta_{1,n+1,j},\theta_{2,n+1,j}\right)$ and $F_2\left(\theta_{1,n+1,j},\theta_{2,n+1,j}\right)$ become lower than the given tolerance. When this condition is satisfied the values of rotations at time t_{n+1} $\theta_{1,n+1,j}$ and $\theta_{2,n+1,j}$ are taken to be the converged rotations at that time $\theta_{1,n+1}$ and $\theta_{2,n+1}$.

6.7.3 Contact detection procedure

To make the transition from one set of equations of motion to the other which happens when a transition between patterns due to an impact occurs, the time of each contact has to be detected precisely. As in Section 3.2.3, it can be argued that such contact-detection procedure is justified when a small number of contacts is expected.

The procedure proposed here is following the one for a single block explained in Section 3.2.3. The absolute rotation of the bottom block θ_1 and the relative rotation of the top block with respect to the bottom block $\theta_2 - \theta_1$ are monitored for the change of sign. When such change in one of these two terms is detected, for example at time t_{n+1}, the procedure to obtain the dynamic equilibrium over the time step is repeated but now for only one unknown rotation θ_i and the new unknown - the modified time step size $\Delta t'$. The condition followed here is that either the rotation of the bottom block is equal to zero, i.e. $\theta_{1,n+1} := 0$ or the relative rotation between the two blocks is equal to zero, i.e. $\theta_{2,n+1} - \theta_{1,n+1} := 0$ thus defining the two rotations to be the same $\theta_{1,n+1} = \theta_{2,n+1}$.

Such a set of equations with $\Delta t'$ and either $\theta_{1,n+1}$ or $\theta_{2,n+1}$ is still nonlinear and needs to be solved iteratively, following the same procedure as the one described in Section 6.7.2.

The Jacobian of this system now needs to be calculated as

$$\mathbf{J}_{n+1,j} = \left[\begin{array}{cc} \dfrac{\partial F_i\left(\theta_{i,n+1},\Delta t'\right)}{\partial \theta_{i,n+1}} & \dfrac{\partial F_1\left(\theta_{i,n+1},\Delta t'\right)}{\partial \Delta t'} \\[3mm] \dfrac{\partial F_2\left(\theta_{i,n+1},\Delta t'\right)}{\partial \theta_{i,n+1}} & \dfrac{\partial F_1\left(\theta_{i,n+1},\Delta t'\right)}{\partial \Delta t'} \end{array}\right]\Bigg|_{\substack{\theta_{i,n+1,j} \\ \Delta t'_j}} \tag{6.213}$$

and the system

$$\boldsymbol{f}_{n+1,j} + \mathbf{J}_{n+1,j}\boldsymbol{\delta}_j \equiv 0, \tag{6.214}$$

needs to be solved, where now

$$\boldsymbol{f}_{n+1,j} = \left\{\begin{array}{c} F_1\left(\theta_{i,n+1,j},\Delta t'_j\right) \\ F_2\left(\theta_{i,n+1,j},\Delta t'_j\right) \end{array}\right\} \tag{6.215}$$

140

and $\boldsymbol{\delta}_j$ is the vector with corrections of the unknowns defined as

$$\boldsymbol{\delta}_j = \begin{Bmatrix} \delta_{1,j} \\ \delta_{2,j} \end{Bmatrix} = \begin{Bmatrix} \theta_{i,n+1,j+1} - \theta_{i,n+1,j} \\ \Delta t'_{j+1} - \Delta t'_j \end{Bmatrix}, \tag{6.216}$$

where, depending on the configuration of motion, either $i = 1$ or $i = 2$.

Once the modified time-step size and the unknown rotation are both calculated, the pre-impact angular velocities, $\dot{\theta}_1^-$ and $\dot{\theta}_2^-$, and angular acceleration, $\ddot{\theta}_1^-$ and $\ddot{\theta}_2^-$, are calculated using Newmark's scheme following equations (6.200) and (6.201).

After the impact, the original time step size Δt is restored and the time-stepping procedure continues by switching to the new set of governing equations of motion corresponding to the current (new) rocking configuration at time $t^+ = t_n + \Delta t'$. However, the initial angular accelerations $\ddot{\theta}_1^+$ and $\ddot{\theta}_2^+$ need to be calculated at the beginning of that time step from the new governing equations of motion. Before that, the new angular velocities $\dot{\theta}_1^+$ and $\dot{\theta}_2^+$ are to be calculated from the equations involving the coefficient of restitution defined in Section 6.6 for each transition.

6.7.4   Numerical algorithm

The numerical procedure based on the nonlinear equations of motion derived in Section 6.2.1 which are integrated numerically using Newmark's integration method described in Section 6.7.1 and solved at each time step using Newton-Raphson iterative procedure described in Section 6.7.2, with the contact-detection procedure from Section 6.7.3 built-in, is illustrated in the flow-chart in Figure 6.18.
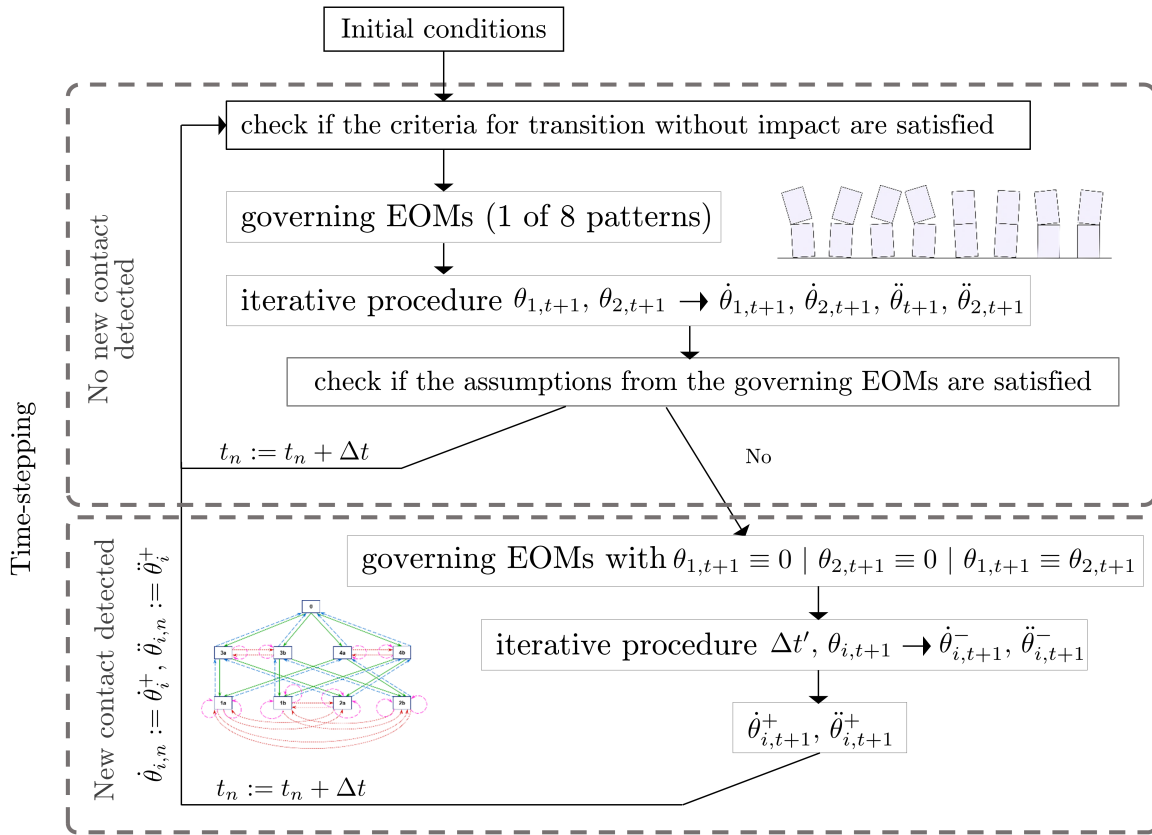
Figure 6.18: Algorithm for simulation of rocking of a dual-block stack

6.8 Validation against numerical benchmarks from the literature

Before going into the assessment of rocking stability and overturning conditions of the dual-block stack, the numerical procedure presented above is validated against the available numerical results in the literature [4].

The work by Kounadis et al. [4] investigates the dynamic response of a dual-block stack consisting of two identical blocks defined each by the length of the half-diagonal $R = 1.606$ m, the angle of slenderness $\alpha_1 = \alpha_2 = 0.25$ rad and the frequency parameter $p = \sqrt{\frac{3g}{4R}}$ s^{-1}. The attention of that work focuses on determining the minimum amplitude a_0 of the base acceleration for the excitation function $\ddot{u}_g = a_0 \sin(\omega t)$ needed to overturn the system.

The input parameters for the two cases of excitation analysed are given in Table 6.1, where $\alpha* = \frac{\alpha_1}{2} = 0.125$.

Table 6.1: Amplitude and frequency of the single sine-wave excitation

Case	a_0	ω
a	$10.8696g\alpha*$	12
b	$10.989g\alpha*$	12

The rotation time histories due to the two different single sine-wave excitations are shown in Figures 6.19 and 6.20. The numerical analyses are run with time-step size $\Delta t = 0.0001$ and a tolerance of $1 \cdot 10^{-8}$.
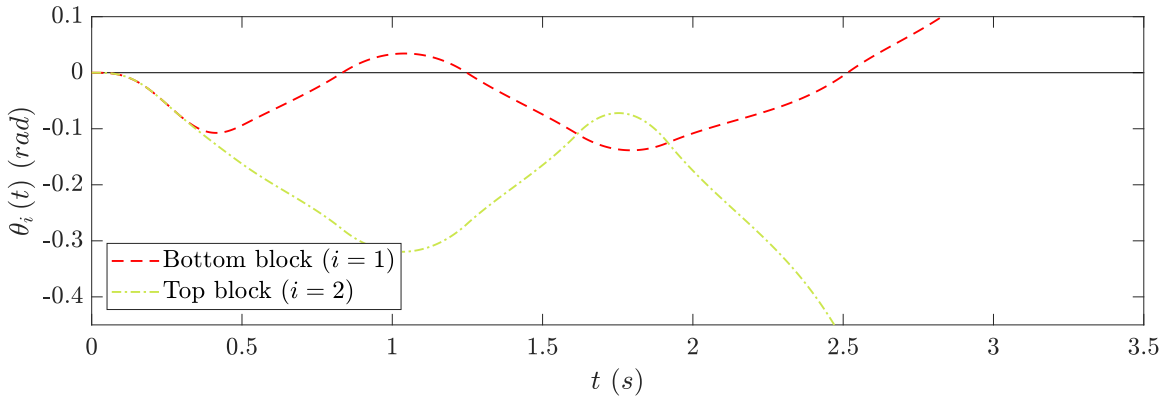
Figure 6.19: Rotation θ_1 and θ_2 time histories for the dual-block stack subject to a single sine-wave excitation with $a_0 = 10.8696g\alpha*$ and $\omega = 12$ rad/s (as in [4])
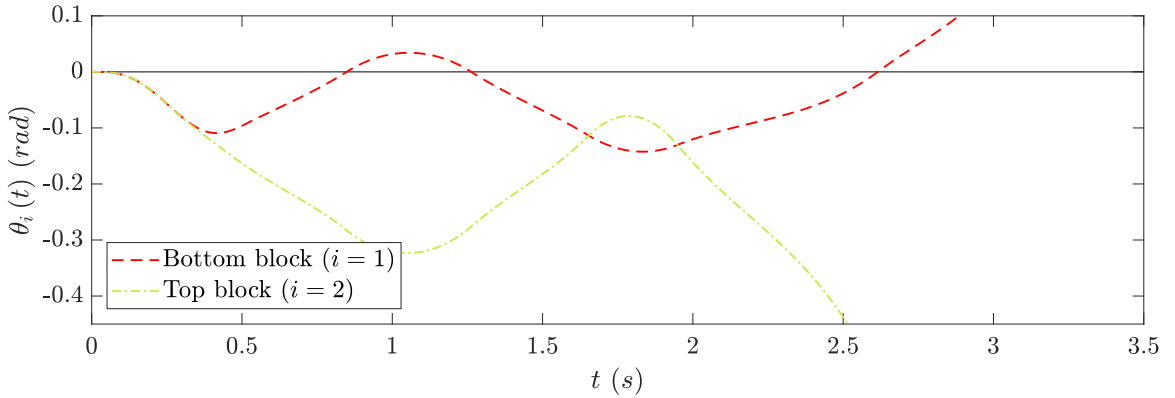
Figure 6.20: Rotation θ_1 and θ_2 time histories for the dual-block stack subject to a single sine-wave excitation with $a_0 = 10.989g\alpha*$ and $\omega = 12$ rad/s (as in [4])

The results in Figures 6.19 and 6.20 indicate that overturning of the top block occurs for both excitations, in oppose to the analysis in [4]. Also, overturning occurs significantly sooner here than in the reference research, as is the case with all the

transitions between configurations due to impacts between bodies. In general, the first part of the analysis (up to cca $t = 2$ s) corresponds well to the results from [4], while later (for $t > 2$ s) overturning occurs for both excitations cases.

However, behaviour similar to the first case reported in [4] (when only rocking occurs) is simulated numerically given slightly lower acceleration amplitudes here (cca 2 % lower). Rotation, angular velocity and angular acceleration time histories of the dual-block stack subject to a single sine-wave excitation with $a_0 = 10.7808g\alpha*$ and $\omega = 12$ rad/s are shown below.
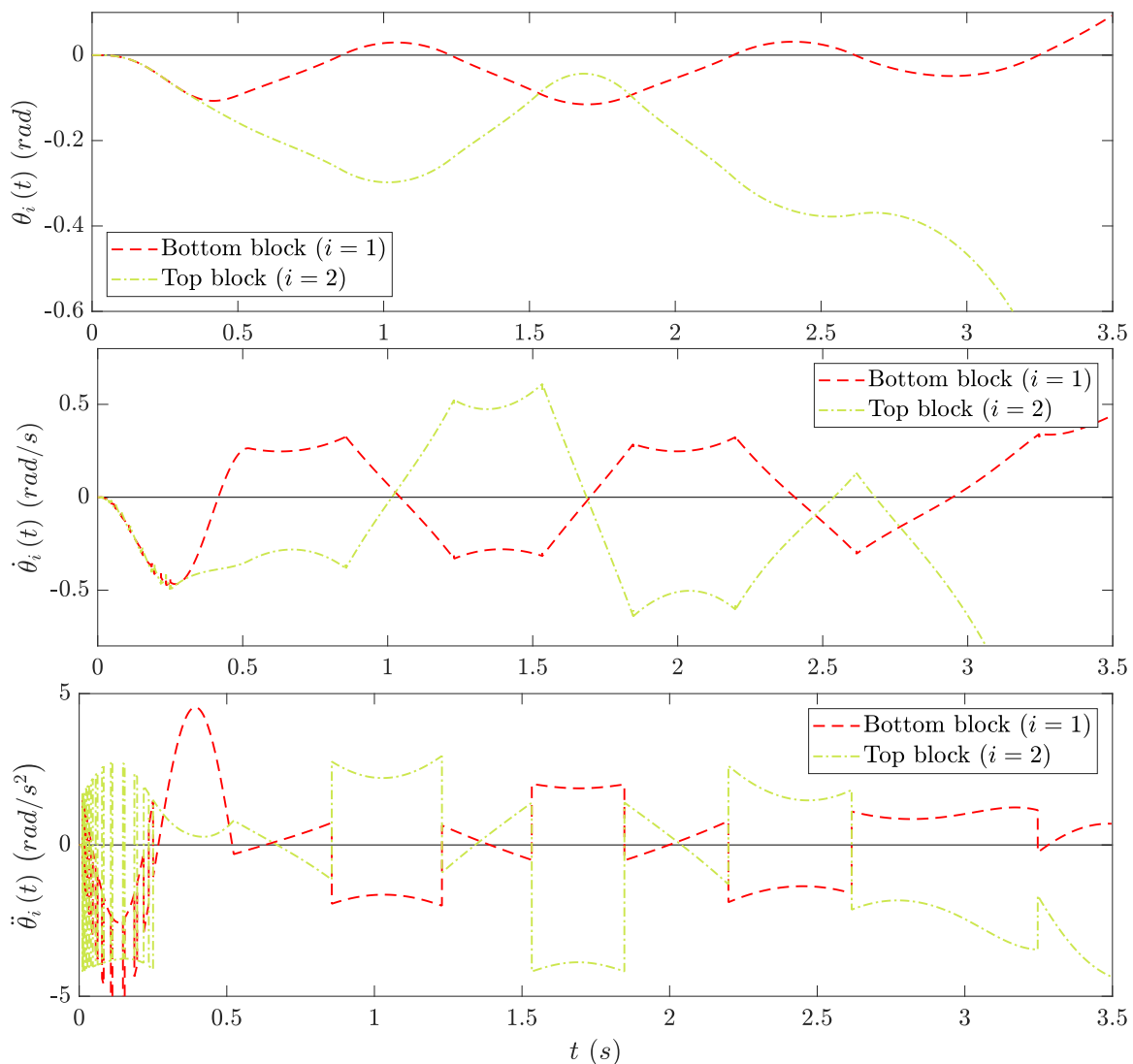
Figure 6.21: Rotation, angular velocity, and angular acceleration time histories for the dual-block stack subject to a single sine-wave excitation with $a_0 = 10.7808g\alpha*$ and $\omega = 12$ rad/s

This simulates stable rocking of the dual-block stack from [4]. The numerical

procedure here results in an interesting behaviour at the beginning of the simulation. The stack starts rocking as a single block with height $h_1 + h_2$ (configuration 3a), after which it transitions into one of the 'higher' configurations very soon, and during the first 0.25 seconds of the dynamic analysis it keeps transitioning between configurations 1a and 3a (see Figure 6.22). This is not reported in [4], where this first part of the analysis is considered pure rocking in configuration 3a. Nevertheless, the numerical procedure presented here manages to simulate rocking motion later on well, despite this initial behaviour.
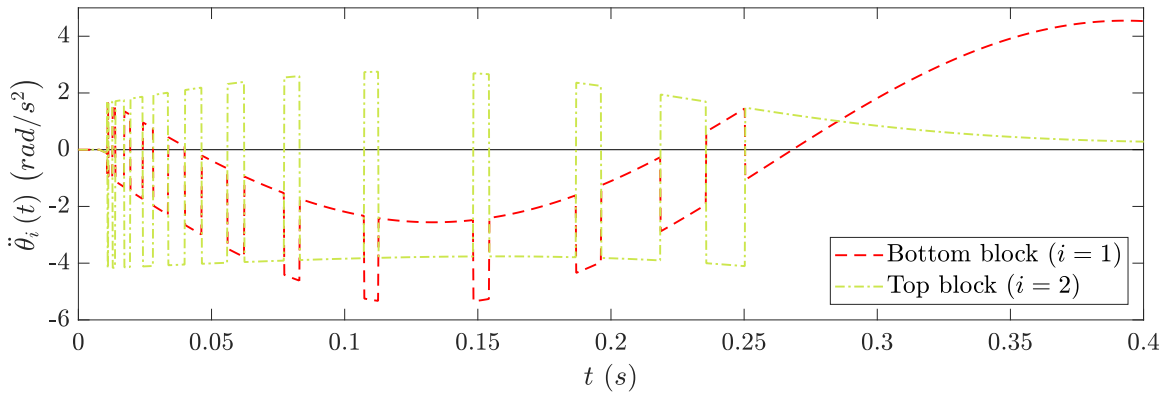
Figure 6.22: Angular acceleration time histories for $t < 0.45$ s of the dual-block stack subject to a single sine-wave excitation with $a_0 = 10.7808 g\alpha*$ and $\omega = 12$ rad/s

These numerically obtained results for the dual-block stack should ideally be validated experimentally. However, a dual-block stack with the geometry reported in [4] is not available within this research, so dual-block stacks with different geometries are analyses numerically and validated experimentally in Chapter 7.

6.9 Discussion and conclusion

Rocking of a dual-block stack is investigated numerically. The nonlinear equations of motion for the eight possible rocking configurations of the stack are derived from Lagrange's equation. The criteria for transition between configurations due to a kinematic conditions for initiation of 'higher' configurations are derived. The post-impact velocities after each impact between the bodies in the stack (either between the top and the bottom block or between the bottom block and the base) are derived from the condition that the angular momentum of only the top block and the whole stack needs to be conserved with respect to the points acting as centres of rotation after the impact.

A numerical procedure based on this equations is written. The procedure includes the Newmark's method for numerical integration, the Newton-Raphson iterative formula, and a procedure to detect exact time of each contact.

The numerical procedure is compared against available numerical results in the literature, before it is validated against experiments (in Chapter 7).

Chapter 7

Experimental benchmarks and modes of overturning of a dual-block stack

Forced rocking of a stack consisting of two rigid blocks of the same width is addressed here. The numerical procedure presented in Chapter 6 is used to simulate the dynamic behaviour of the dual-block stacks. Stacks subject to two cases of base acceleration function – constant base acceleration of finite duration and a single sine-wave excitation – are investigated. A set of experiments aiming to investigate rocking response of such dual-block stacks is designed and conducted and chosen numerical cases are validated against the experimentally obtained results.

7.1 Rocking due to a constant acceleration of finite duration

Rocking of the dual-block stack subject to a constant ground acceleration of finite duration is the simplest case of forced rocking. As such it is investigated in detail before going into the dynamic characterisation of the dual-block stack due to a more complex excitation.

7.1.1 Initiation of 'lower' configurations and overturning modes

A dual-block stack that is initially ideally vertical when subject to a base excitation can start rocking in one of the four 'lower' (simpler) configuration: either only the top block rocks (4a and 4b) or both blocks rock together as a single rigid body (3a and 3b). Whether the stack will start rocking in configuration 3a/3b or 4a/4b depends on the conditions for initiation of rocking given in Section 6.4.

Following initiation of rocking, the stack keeps transitioning between the eight configuration, until it settles to rest or it overturns. We distinguish three outcomes of the rocking analysis and two modes of overturning of the stack:

- **Stable rocking** if the block goes through rocking and it eventually settles to rest;

- **Partial overturning** if only the top block overturns either to the left or to the right side, while the bottom block settles to rest;

- **Total overturning** if the whole stack overturns (where we do not distinguish the case where both blocks overturn after rocking as a single rigid body, or they overturn separately).
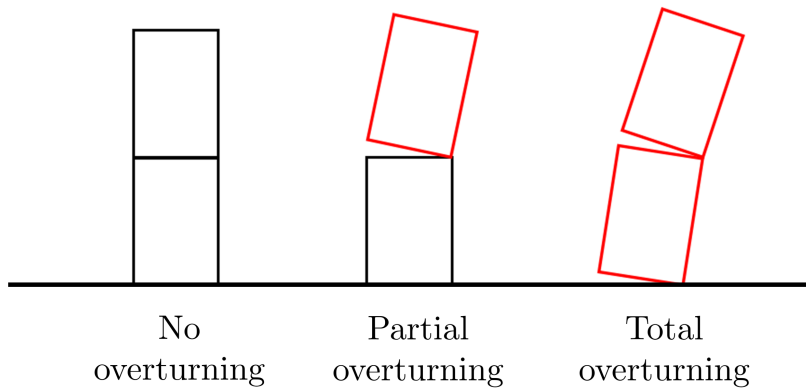
Figure 7.1: Modes of overturning of a dual-block stack

Conditions of the base excitation that specifically cause either partial or total overturning of the dual-block stack are of great interest in this study and are closely observed further on.

7.1.2   Experimental results

The experimental setup here involves the air track device and a slider connected to a mass via a string and pulley system, as described in Section 5.1.2 for a single block.

A range of measurements is made for the given mass of the slider $m_s = 120$ g and the dual-block stack of two equal blocks with width $b = 0.02$ m, height $h = 0.09$ m, mass $m = 95.5$ g, half-diagonal $R = 0.0461$ m, angle of slenderness $\alpha = 0.2187$ rad, and different values of the input data $(m_a, h_a) \Leftrightarrow (a_0, t_a)$, for which the block motion is characterised as translation, rocking, partial or total overturning by visual observation. The hanging masses are chosen from within the range $m_a \in [0.015\,\text{g}, 0.115\,\text{g}]$

and the vertical distances from within the range $h_a \in [0.2\,\text{cm}, 25.5\,\text{cm}]$. The results of the experiment are shown in Figure 7.2 for a variety of input data.
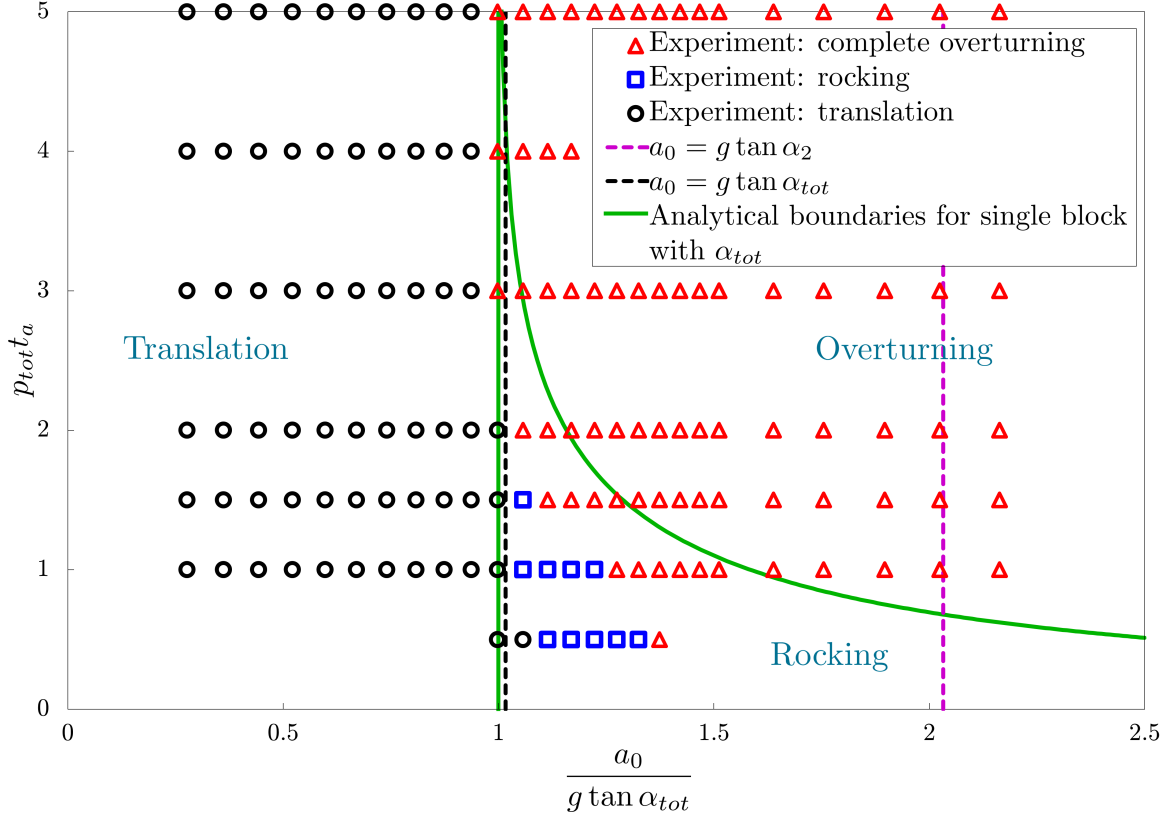
Figure 7.2: Experimental results for overturning/rocking/translation of the dual-block stack due to a constant acceleration of finite duration

The purple line with $a_0 = g\tan\alpha_2$ represents the threshold for immediate initiation of rocking in configurations 4a/b and we track whether partial overturning occurs when the stack is subject to an acceleration larger than $g\tan\alpha_2$. No partial overturning, as well as no rocking in configurations 4a/b, is noticed in these experiments.

7.2 Rocking due to a harmonic acceleration

Rocking outcome (no-overturning, partial or total overturning) for a dual-block stack subject to simple harmonic base excitation is investigated here. We analyse the stability of different dual-block stacks due to a single harmonic sine-wave acceleration.

The objective is to derive the conditions under which the stack overturns from multiple runs of the numerical algorithm presented in Chapter 6, and specifically

to distinguish the cases where partial overturning occurs from the cases where total overturning occurs, which may be of practical importance.

7.2.1   Geometry

Seven dual-block stacks of different geometry are investigated: The dual-block stack reported in [4], four stacks where the bottom and the top block are the same, i.e. $h_1 = h_2$, and two stacks where the top block is either significantly slenderer ($h_2 > h_1$) or bulkier ($h_2 < h_1$) than the bottom block. The geometry of all the observed stacks is given in Tables 7.1 and 7.2.

Table 7.1: Geometry of the dual-block stacks consisting of two blocks with the same heights ($h_1 = h_2$)

Stack	m_i [g]	b_i [m]	h_i [m]	$\frac{h_i}{b_i}$	h_{tot} [m]	$\frac{h_{tot}}{b_i}$	α_i	α_{tot}	R_i [m]	R_{tot} [m]
DB3M3M	544.4	0.045	0.10125	2.25	0.2025	4.5	0.4182	0.2187	0.0554	0.1037
DB6M6M	1089.6	0.045	0.2025	4.5	0.405	9	0.2187	0.1107	0.1037	0.2037
DB3L3L	1284.3	0.06	0.135	2.25	0.27	4.5	0.4182	0.2187	0.0739	0.1383
DB6L6L	2569.2	0.06	0.27	4.5	0.54	9	0.2187	0.1107	0.1383	0.2717

Table 7.2: Geometry of the dual-block stacks consisting of two block with different heights ($h_1 \neq h_2$)

Stack	$b_1 = b_2$ [m]	m_1 [g]	h_1 [m]	$\frac{h_1}{b_1}$	α_1	m_2 [g]	h_2 [m]	$\frac{h_2}{b_2}$	α_2	h_{tot} [m]	$\frac{h_{tot}}{b_i}$	α_{tot}	R_{tot} [m]
DB3M6M	0.045	544.4	0.10125	2.25	0.4182	1089.6	0.2025	4.5	0.2187	0.30375	6.75	0.1471	0.1535
DB6M3M	0.045	1089.6	0.2025	4.5	0.2187	544.4	0.10125	2.25	0.4182	0.30375	6.75	0.1471	0.1535

7.2.2 Numerical assessment of rocking stability due to a single sine-wave excitation

In a more extensive study of rocking behaviour, including assessment of rocking stability, presented here we are able to detect different modes of overturning (partial or total).

First the dual-block stacks with the same geometries of both blocks are observed. After that, two different stacks where the slenderness $\frac{h}{b}$ of the top block is either twice the slenderness of the bottom block or half of it are observed.

7.2.2.1 Dual-block stack documented in [4]

First, the dual-block stack investigated by Kounadis [4] is analysed numerically. The results from a series of numerical analyses with excitation amplitudes a_0 ranging from $0.1g \tan \alpha_{tot}$ to $30g \tan \alpha_{tot}$ and frequencies ω ranging from $0.1p_{tot}$ to $15p_{tot}$ are shown in Figure 7.3. The additional material restitution is $\eta_{mat} = 0.95$ between the two blocks and $\eta_{mat} = 1$ between the stack and the base, as reported in [4]. The results compare well with the results presented in [4], with the exception that for the frequencies between cca $11p_{tot}$ and $13p_{tot}$ the boundary between overturning and no-overturning areas is higher with respect to the amplitudes than in the reference [4].
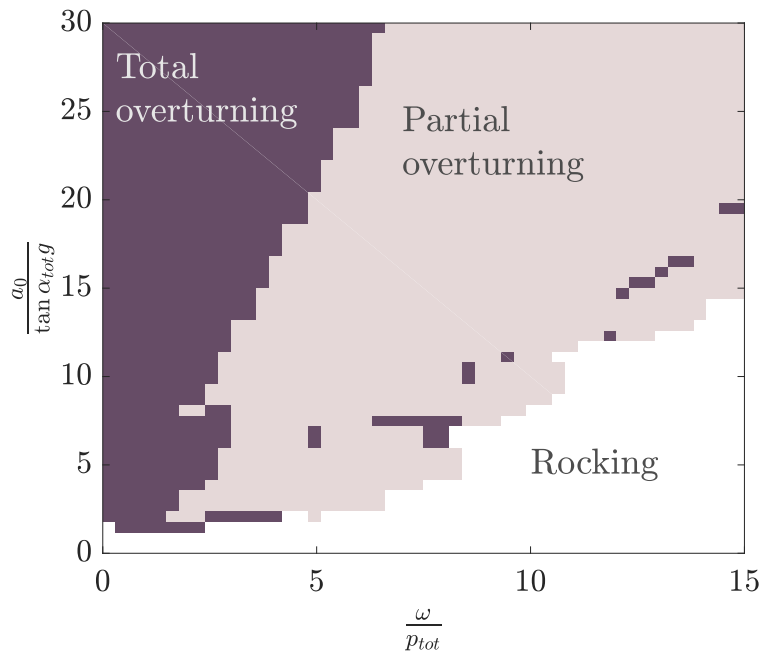
Figure 7.3: Stability graph for a single sine-wave acceleration of a dual-block stack from [4]

7.2.2.2 Dual-block stacks with $h_1 = h_2$

The results from a series of numerical analyses with excitation amplitudes a_0 ranging from $0.1g \tan \alpha_{tot}$ to $30g \tan \alpha_{tot}$ and frequencies ω ranging from $0.1p_{tot}$ to $15p_{tot}$ are shown in Figures 7.4 and 7.5 for the smaller and the larger stack of overall slenderness $\frac{h_{tot}}{b} = 4.5$ (DB3M3M and DB3L3L), respectively. Material dissipation is here accounted for with an additional 5% decrease in the angular velocities at each impact, as suggested in [4]. The results for the two stacks are very similar.
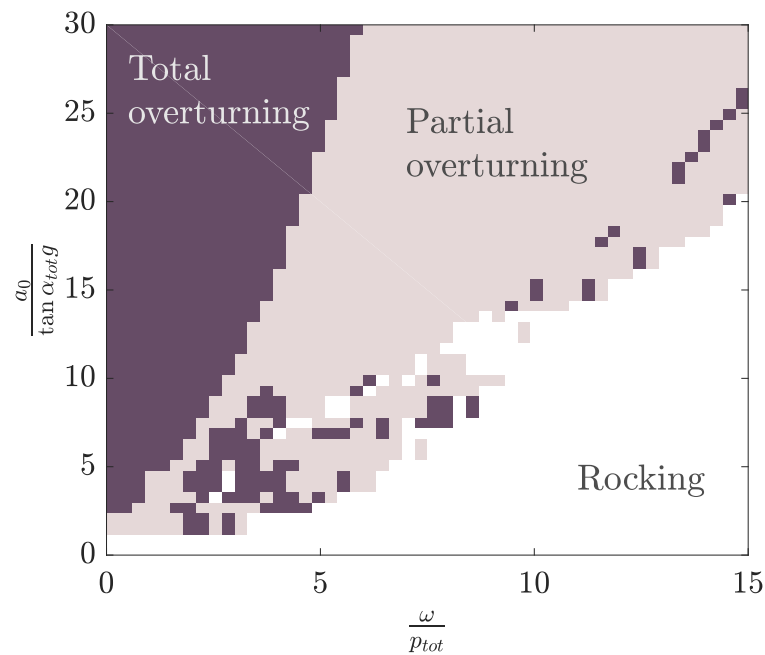
Figure 7.4: Stability graph for a single sine-wave acceleration of a dual-block stack with $h_{tot}/b = 4.5$ (DB3M3M)
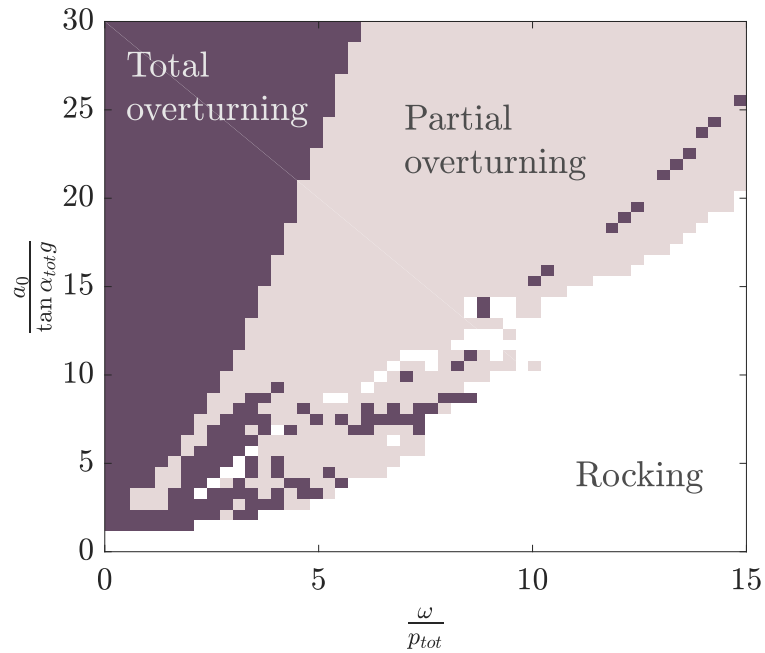
Figure 7.5: Stability graph for a single sine-wave acceleration of a dual-block stack with $h_{tot}/b = 4.5$ (DB3L3L)

The results from a series of numerical analysis with excitation amplitudes a_0 ranging from $0.1g \tan \alpha_{tot}$ to $30g \tan \alpha_{tot}$ and frequencies ω ranging from $0.1p_{tot}$ to $15p_{tot}$ are shown in Figures 7.6 and 7.7 for the smaller and the larger stack (DB6M6M and DB6L6L) of overall slenderness $\frac{h_{tot}}{b} = 9$, respectively. The results for the two stacks are again similar.
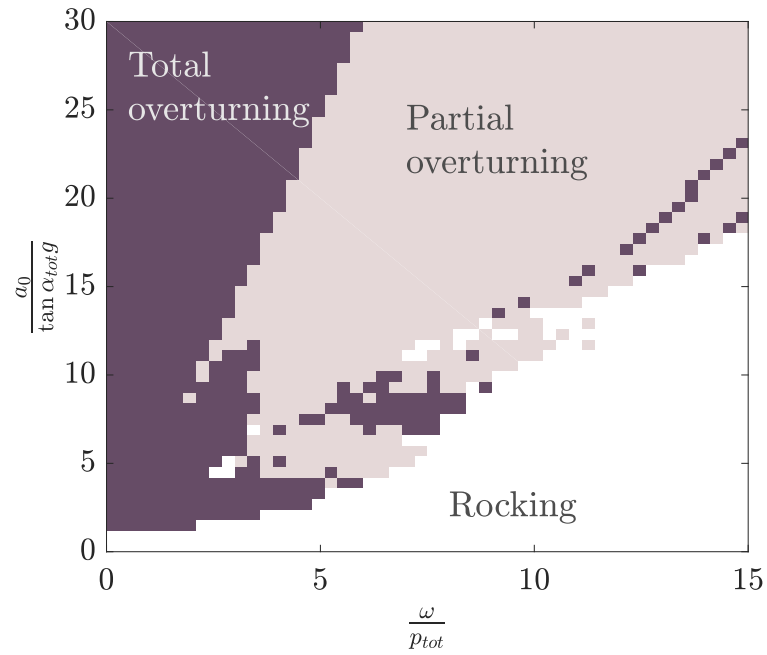
Figure 7.6: Stability graph for a single sine-wave acceleration of a dual-block stack with $h_{tot}/b = 9$ (DB6M6M)
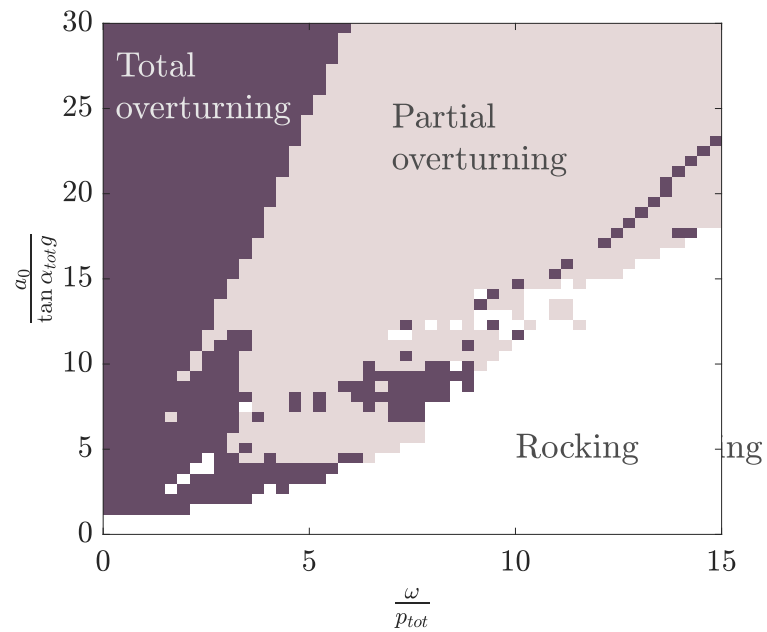
Figure 7.7: Stability graph for a single sine-wave acceleration of a dual-block stack with $h_{tot}/b = 9$ (DB6L6L)

7.2.2.3 Dual-block stack with $h_2 > h_1$

Rocking stability of the dual-block stack with the top block more slender than the bottom block, i.e. $h_2 > h_1$ (but $b_1 = b_2$) is addressed here. The results from the numerical simulations for a variety of excitation amplitudes and frequencies are shown in Figure 7.8. In comparison to the previously presented stability graphs for stacks consisting of two equal blocks (Section 7.2.2.2), we can see that the overall overturning area now consists of a larger area where partial overturning happens. This is to be expected, since such geometry can sometimes result in initiation of rocking in configuration 4a/b, as oppose to the stack of two equal blocks.
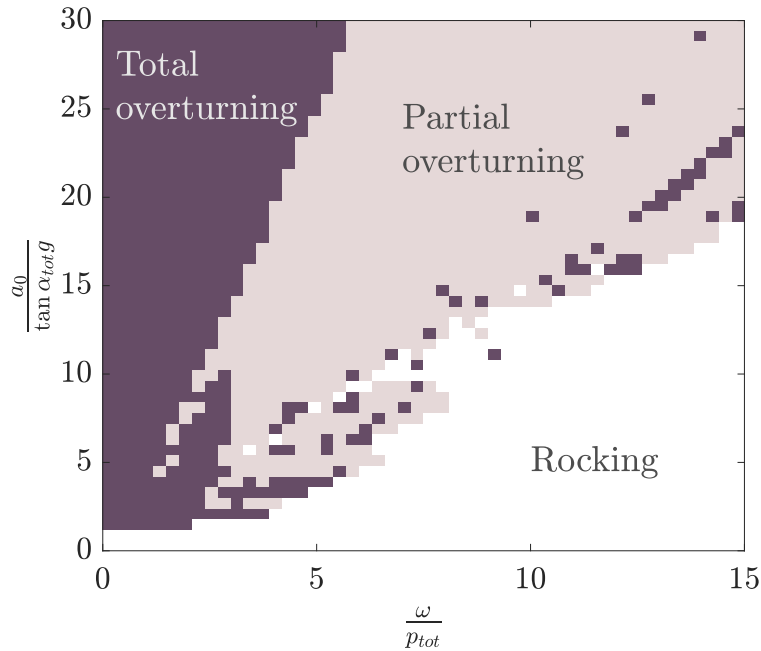
Figure 7.8: Stability graph for a single sine-wave acceleration of a dual-block stack with $h_{tot}/b = 6.75$ where $h_2 > h_1$ (DB3M6M)

7.2.2.4 Dual-block stack with $h_2 < h_1$

When assessing rocking stability of a stack consisting of two blocks where the top block is significantly bulkier than the bottom one, the opposite behaviour is expected. The results from the numerical simulations for a variety of excitation amplitudes and frequencies are shown in Figure 7.9. We can now notice that total overturning mode dominates the overall overturning area, if compared to the overturning modes for a stack consisting of two of the same blocks (presented in Section 7.2.2.2).
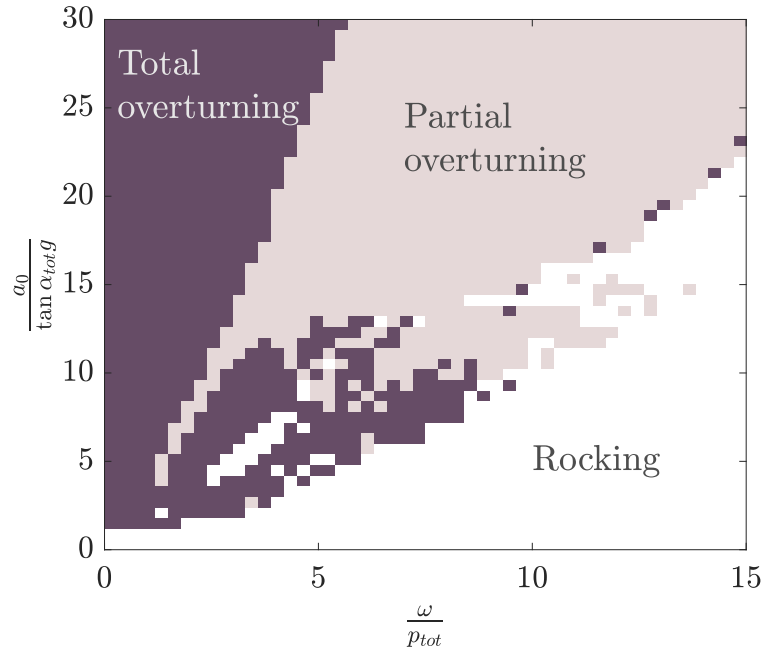
Figure 7.9: Stability graph for a single sine-wave acceleration of a dual-block stack with $h_{tot}/b = 6.75$ where $h_2 < h_1$ (DB6M3M)

7.2.3 Experimental results

The set of two dual-block stacks (stacks DB3M3M and DB3L3L from Table 7.1) subject to a sine-wave excitation is chosen for experimental validation. As described in Section 5.2.3.2, the acceleration function is input via a single sine-wave displacement function added to a linear displacement function (equation (5.5)).

The experiments are performed for each acceleration amplitude starting from the highest frequency. After each experiment resulting in stable rocking the frequency is lowered and the procedure repeated. When overturning occurs, the amplitude is increased.

7.2.3.1 Stack DB3M3M

The experimentally obtained results for the dual-block stack DB3M3M are shown in Figure 7.10, along with the simulation results from Figure 7.4. These experiments roughly confirm the inner boundary between the overturning and the no-overturning area obtained by simulation. On the other hand, the numerically obtained results show overturning in cases when the experiments result in no overturning for the range of amplitudes between cca $7.5g \tan \alpha_{tot}$ and $10g \tan \alpha_{tot}$ and frequencies between cca $7p_{tot}$ and $8p_{tot}$.
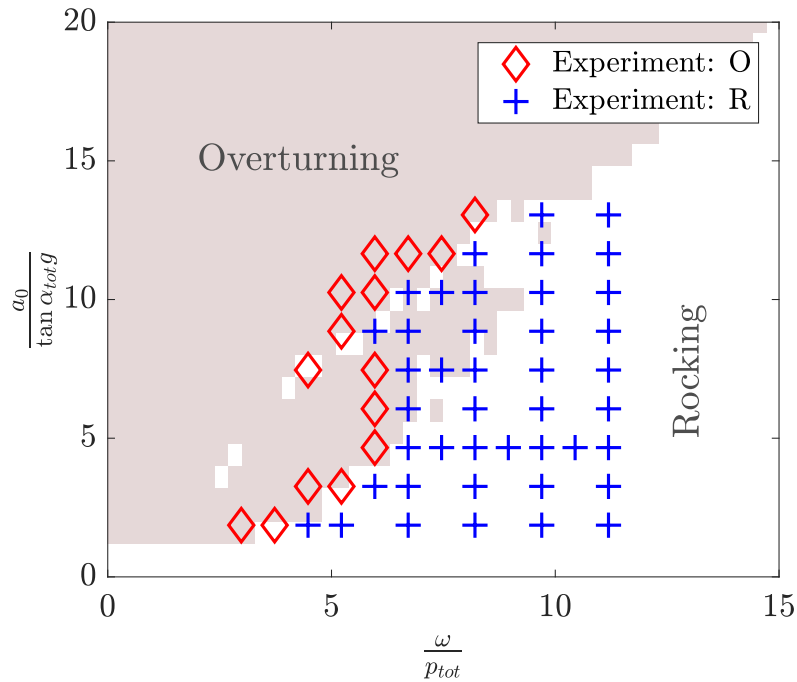
Figure 7.10: Stability graph for a single sine-wave acceleration of a dual-block stack with $h_{tot}/b = 4.5$ (DB3M3M): numerically and experimentally obtained results (O - overturning, R - rocking)

7.2.3.2 Stack DB3L3L

The experimentally obtained results for the dual-block stack DB3L3L are shown in Figure 7.11, along with the numerically obtained results from Figure 7.5. The experiments again validate the inner simulation boundary between the overturning and the no-overturning areas. The middle part of the overturning area obtained from the simulations is not confirmed experimentally, since the blocks rock in a stable fashion here.
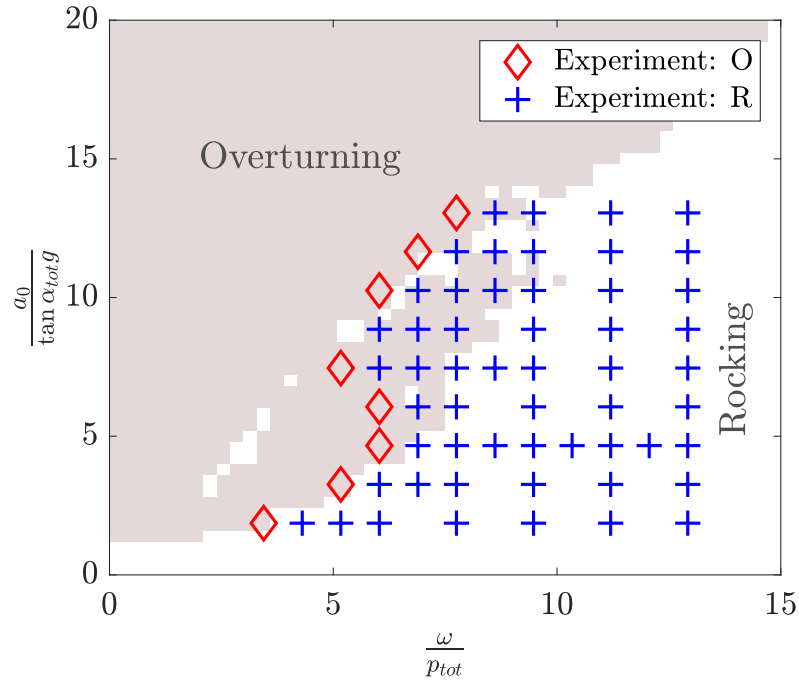
Figure 7.11: Stability graph for a single sine-wave acceleration of a dual-block stack with $h_{tot}/b = 4.5$ (DB3L3L): numerically and experimentally obtained results (O - overturning, R - rocking)

7.3 Discussion and conclusion

The rocking stability of the dual-block stack to a constant base acceleration of finite duration is investigated experimentally first. It is shown that the analytical, numerical and experimental boundary between translation and rocking coincide. Furthermore, it is shown that only total overturning of the stack as a single body happens even when the acceleration is high enough that it satisfied both the condition for immediate initiation of rocking configuration where both blocks rock together (configuration 3a/b) and the condition for immediate initiation of rocking of only the top block (configuration 4a/b).

A series of controlled experiments with aluminium dual-block stacks on a shaking table subject to a single sine-wave excitation function is deigned and carried out.

The experiments partially validate the numerically obtained results, i.e. the inner boundary between overturning and no-overturning is validated experimentally, while the smaller overturning area at the bottom is only partially validated experimentally. The simulations carried out show larger overturning area than the one noticed in the experiments.

Chapter 8

Overturning of multiple block stacks - sensitivity parameters and modes of overturning

This chapter is based on the results and discussion from paper [64]:
Čeh, N., Camenen, J. F., Bićanić, N., Pellegrino, A., and Petrinić, N, "Overturning of multiple-block stacks - dynamic sensitivity parameters and scaling effect", International Journal of Masonry Research and Innovation

Experimental dynamic sensitivity of a single block and multiple-block stack subject to a double pulse base excitation is examined. Series of test experiments is conducted at the Impact Engineering Laboratory at University of Oxford on a bespoke platform for a controlled double (initial and reverse) pulse base excitation history. Different overturning modes (forward, backward, total or partial) in the experiments are characterised as a function of the peak initial base velocity and the timing of the reverse impulse, controlled by the gap distance between the base and the stopper. The influence of the block sample scales is also examined. The conducted set of validation benchmarks is believed to be valuable for researchers, code developers, safety case engineers, and industry regulators.

8.1   Introduction

In order to better understand as well as to predict the highly nonlinear mechanical response of natural and/or engineered discontinuous, blocky structures, comprising evolving contact conditions and including friction between their components or constituent parts, it is important to develop robust analytical capabilities for simulations

of such systems. In spite of extraordinary advances in nonlinear computational mechanics and simulations paradigms, the validation and verification of their predictive powers remains one of the main challenges in order to promote their incorporation into the industry relevant procedures. It can be safely argued that a major research attention in nonlinear structural dynamics today has noticeably moved from considering a detailed response of a very specific structural system to a defined excitation, towards a more generic predictive capability for a class of structural configurations.

8.2   Experimental setup and preliminary notes

In the context of a joint research project between the universities of Rijeka, Durham and Oxford, a comprehensive series of experiments is conducted at the Oxford Impact Engineering Laboratory on a bespoke platform for a controlled double pulse base excitation, inspired by the classic ingenious simple experimental test device at Roorkee University [65], where the railway wagons on inclined planes and hellical springs were used to generate varying controlled double half sine pulse base excitations and the associated input kinetic energy was correlated to a scalar measure of damage experienced by the test structures.

8.2.1   Double-pulse excitation device *ROORI1*

The experimental setup at the University of Oxford (named ROORI-1 as an hommage to both Roorkee and Rijeka Universities) comprises an impact device based on a pin-ball mechanism with a spring used to launch a wooden projectile, with a Teflon PTFE base and a stopper aligned to the impact device and attached to the optical bench (Figures 8.1 and 8.2). An aluminium sliding base, sitting on the low friction Teflon PTFE surface is positioned at a predefined distance from the stopper (BD). The dimensions of the sliding base are the following: length 0.2 m, width 0.02 m and thickness 0.01 m. The base excitation is triggered with an initial impulse (different intensities are controlled by the different initial pin-ball spring positions) followed by a reverse impulse (provided by the base hitting the stopper), after a given time delay (controlled by the distance between the base and the stopper). The wooden projectile used to induce the impulse is of a cylindrical shape with a length of 0.079 m, a diameter 0.0179 m and a mass of 0.0081 kg. A rubber cushion is glued to the front and the back face of the aluminium base to act as a pulse shaper.
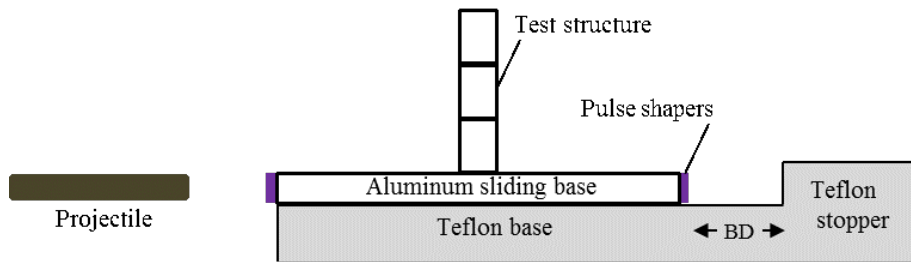
Figure 8.1: Experimental set-up of the double-pulse type excitation device ROORI1
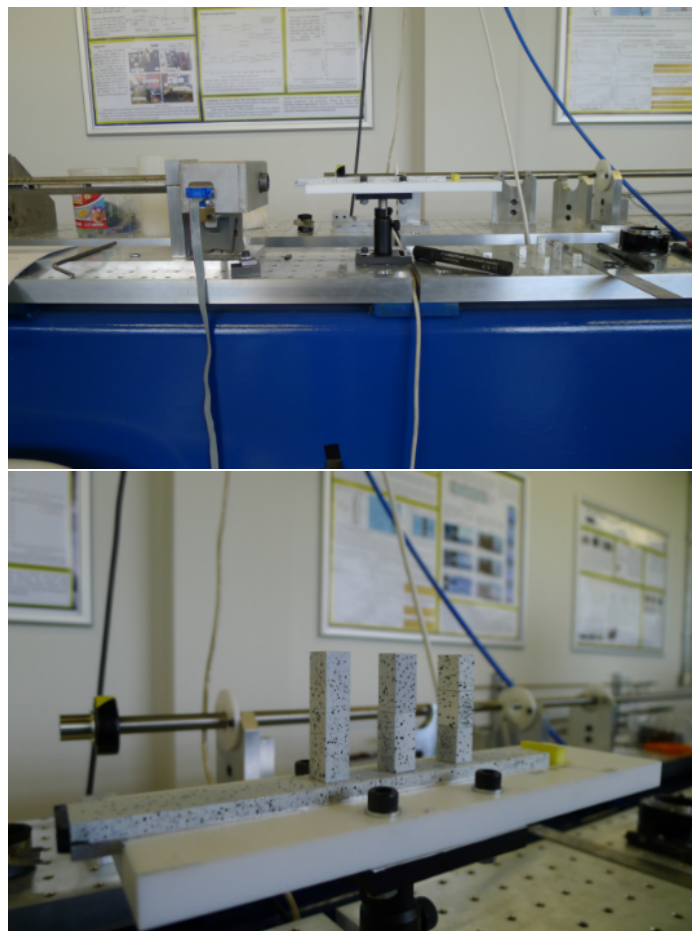
Figure 8.2: Optical bench and ROORI1 test facility (top); samples of multi-block structures on the sliding base (bottom)

The input impact energy and projectile velocity is imparted to the sliding base. The resulting post first impact peak base velocity, achieved after a very short rise time, reflects not only the initial projectile position but also the consequences of the energy dissipation during impact, on the projectile/base mass ratio and the influence of the rubber cushion. Both the incoming projectile velocity and the post impact base

163

velocity ae measured. The projectile velocity is measured by means of two laser curtains with given distance, while the post-impact base velocity is measured by means of the non-contact optical system (described in Section 8.2.3). A separate restitution study concluded that the peak base velocity post first impact is directly proportional to the projectile velocity (Figure 8.3) irrespective of the projectile velocity level, corresponding to a constant restitution.
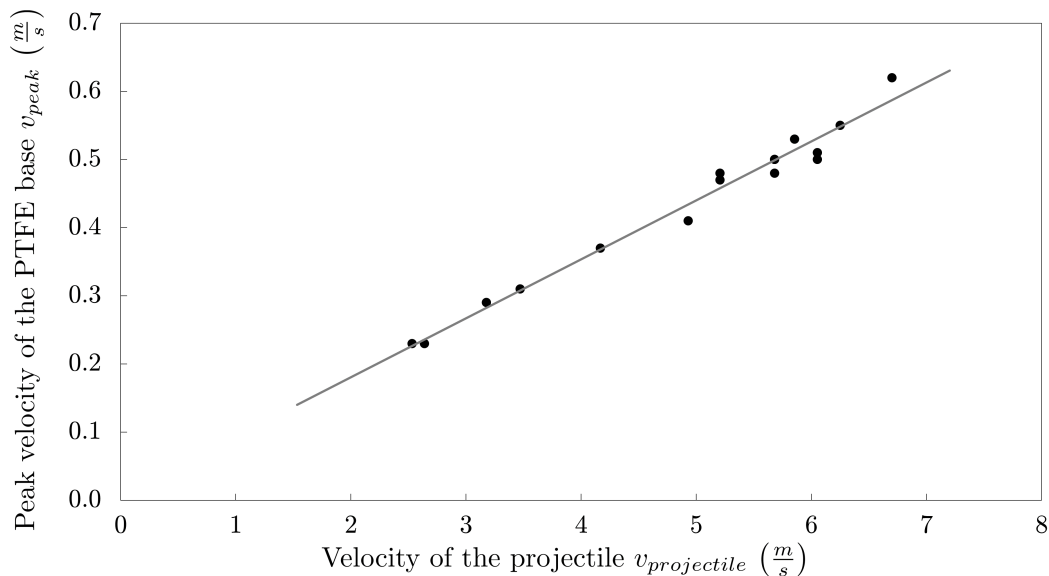
Figure 8.3: Velocity of the projectile vs. peak velocity of the base on the ROORI1 device

During the double impulse experiment, the base excitation history comprises four sections shown in Figure 8.4:

a. Initial impact between the projectile and the base (via rubber cushion),

b. Sliding of the base (free travel) with a gradual decrease in the sliding base velocity due to the friction between the sliding aluminium base and the teflon PTFE surface,

c. Second, reverse impact between the sliding base and the stopper (via rubber cushion), and

d. Sliding of the base in the opposite direction, again associated with a decrease in velocity due to the friction between the aluminium base and the teflon PTFE surface.

164
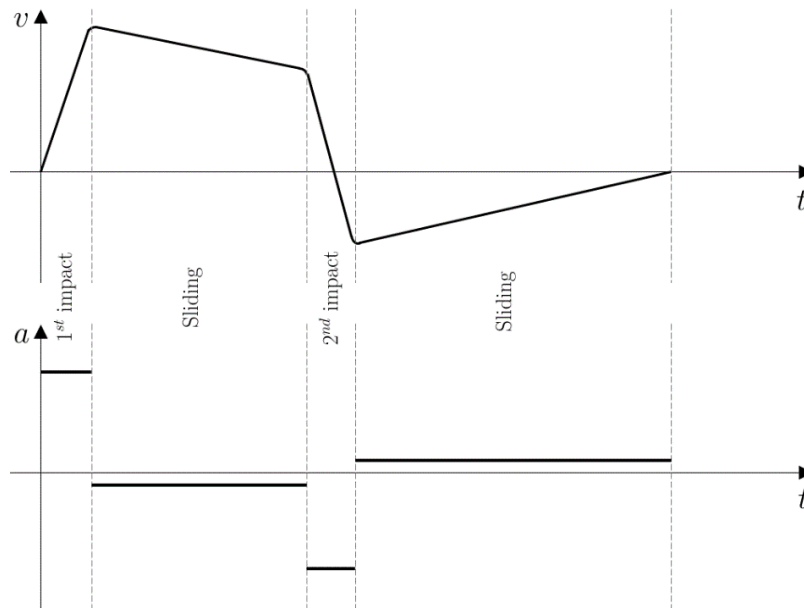
Figure 8.4: Velocity and acceleration time-histories obtained from ROORI1 device

Such velocity (and acceleration) profile can cause various modes of overturning of a single block and a multiple-block stack, which is discussed in detail below.

8.2.2 Sample preparation

On top of the sliding base the test structure (either a single block or a stack of three blocks) is positioned and aligned to the projectile and the Teflon PTFE base (Figure 8.1, left). Surface roughness of the sliding base-block interface and of each of the inter-block surfaces is achieved by using sandpaper with P60 grit (scraping aluminium surface along the sandpaper surface), to exclude sliding. Simple experiments have given the inter-blocks and the block-base surfaces the friction coefficient of 0.54, while the friction coefficient between the sliding base and the Teflon PTFE surface is 0.23. All the experiments have been triggered manually and a good repeatability are achieved, however the results for some experimental scenarios appear to be quite sensitive to small changes in initial conditions.

8.2.3 Optical measurement

Advanced non-contact optical measuring technique based on the GOM Aramis and Pontos system [59] and the corresponding processing software has been applied to replace conventional displacement measuring systems. Every experiment is recorded with either the Phantom or the Photron video camera with a resolution of 800x600

pixels and a frame rate of 2000 fps. The camera is triggered by a laser-beam curtain. Every video is then converted into a series of images (in .jpg format). Each series of images is post-processed using GOM Aramis v6.3.1 software for optical deformation and displacement analysis.

8.3   Experimental results for single blocks

A series of single aluminium block experiments subject to different double pulse type base excitations on two different scales is carried out. The dimensions of test samples on the smaller scale (Scale 1) are h_1=45 mm, b_1=10 mm and l_1=10 mm, whereas for the larger scale (Scale 2) the dimensions are h_2=90 mm, b_2=20 mm and l_2=20 mm. The final state of the samples as an outcome of the controlled double-pulse excitation is characterised by either its stable state (which includes pure translation along with the base and stable rocking) or by a specific mode of overturning, for each experiment (see Figure 8.5):

- Mode of overturning **A** if the block remains stable at the end of the experiment, and

- Mode of overturning $\mathbf{B}_L$ or $\mathbf{B}_R$ if the block overturns to the left or to the right side, respectively.
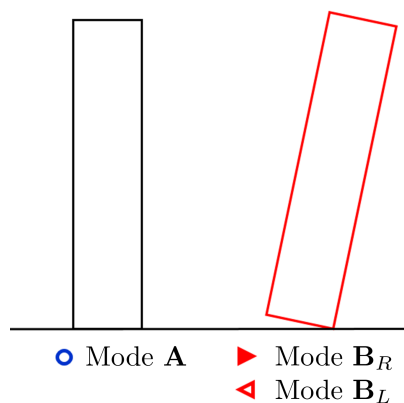
Figure 8.5: Modes of overturning of a single block

8.3.1   Scale 1

Experimental results of the overturning behaviour for a single block (Scale 1) due to the double pulse-type base excitation are shown in Figure 8.6 with respect to the distance between the base and the stopper BD and the initial (peak) sliding

base velocity v_{peak}. For the low-peak base velocities, the sliding base does not reach high enough velocity to overturn the block (experiments with projectile velocity of 0.1 m/s in Figure 8.3). For higher velocities the block starts rocking but in the experiments where the distance between the sliding base and the stopper is small, the base experiences a reverse pulse, which results in an acceleration in opposite direction, causing the block to start rocking about the opposite corner. Such behaviour may eventually result in block stability even for very high velocity (left part of the graph in Figure 8.6).
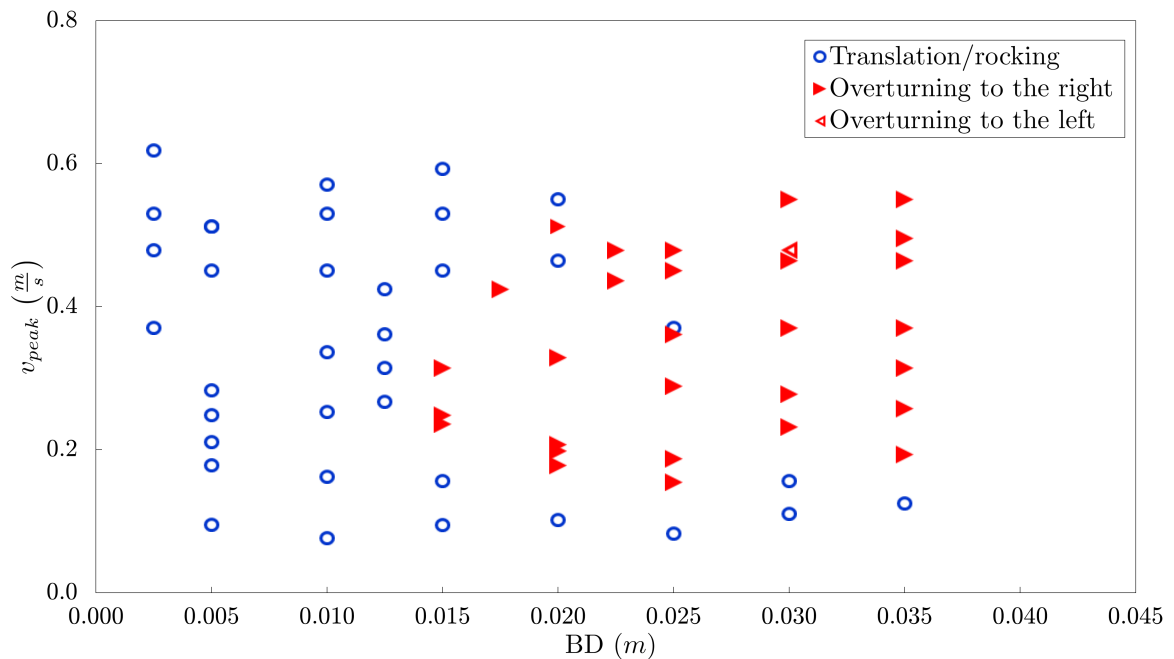
Figure 8.6: Modes of overturning of a single block (scale 1) obtained from the experimental study

8.3.2 Scale 2

Experimental results of the overturning behaviour of a single block at Scale 2 due to double pulse-type base excitation are shown in Figure 8.7 and the end states are characterised in the same way as the experiments at Scale 1. In comparison to the experimental results for the smaller single block larger velocities are required to overturn the larger block, as expected. Longer travel times (larger distances between the base and the stopper) lead to more stable behaviour for larger blocks.
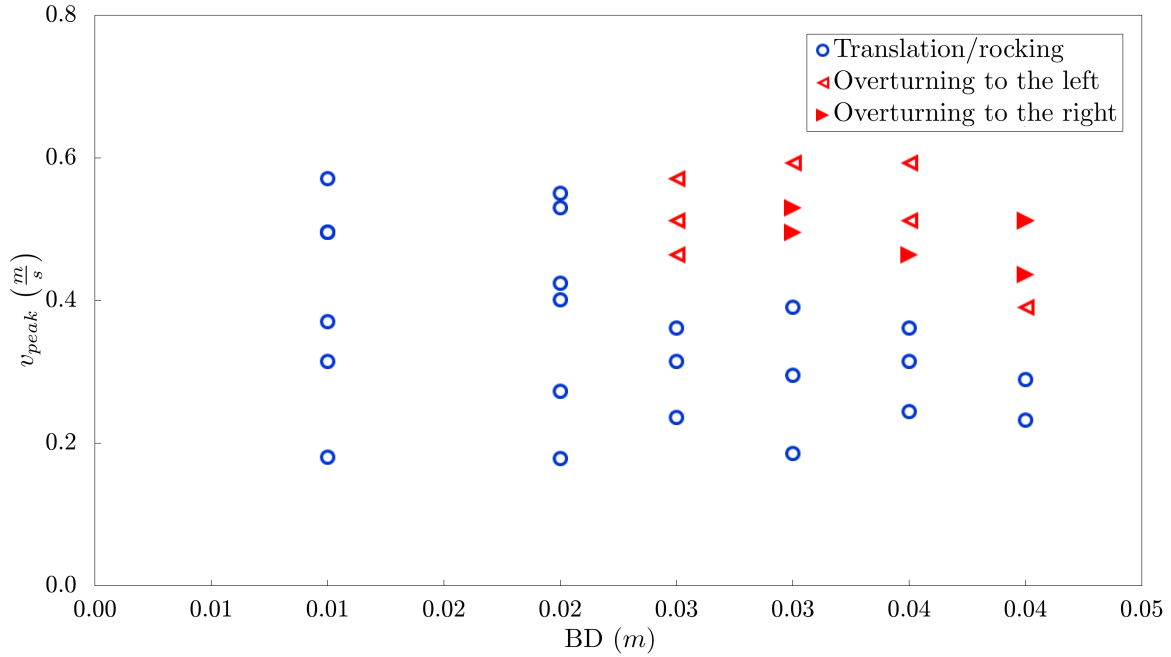
Figure 8.7: Modes of overturning of a single block (scale 2) obtained from the experimental study

8.3.3 Comments on the scaling effect

Scaling effect in rocking behaviour of blocky structures was addressed in [28], where the angle of slenderness α was suggested to scale the amplitude of excitation. In this study with blocks on two scales it is clear that larger amplitude of excitation (impact type) is needed to overturn the larger block, whereas the angle of slenderness is the same for both scales. The results are plotted so that the amplitude of excitation is expressed as the input kinetic energy and scaled using the mass of the block (ratio of the larger block mass to the smaller block mass is $\frac{m_2}{m_1} = 6.83$). Housners frequency parameter p [1] is adopted to scale the frequency of the excitation. The frequency parameter ratio of the larger block to the smaller block is $\frac{p_2}{p_1}$=0.707 and the period of excitation T_d can be estimated as the sum of the impulse duration and the analytically approximated free sliding time before the base reaches the stopper with the assumption of zero friction. The combined experimental results of blocks on both scales are shown in Figure 8.8.
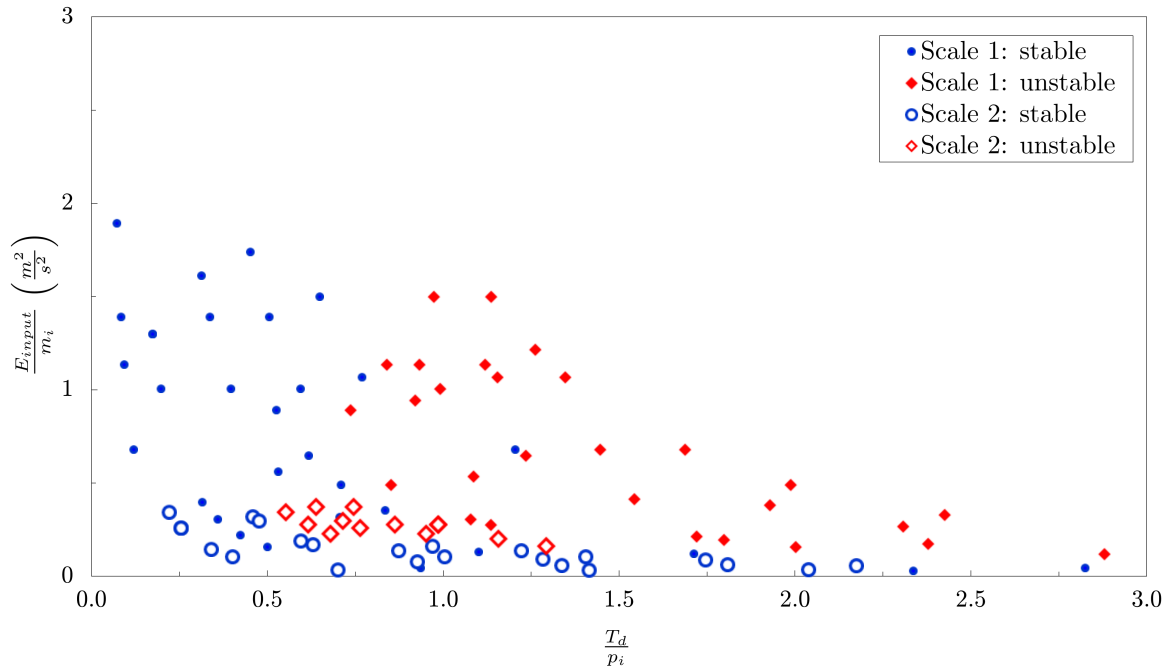
Figure 8.8: Areas of overturning (red marks) and no overturning (blue marks) for single block (Scale 1 is represented with filled marks, Scale 2 is represented with empty marks) obtained from the experimental study

8.3.4 Detailed study of single block overturning modes

In Sections 8.3.1 and 8.3.2 a simplified characterisation of the final overturning modes is described as the observed outcome of an experiment (stable, overturning forward and overturning backward), without considering how these eventual overturning modes have been achieved. Near the boundary between the stability and instability range in the overturning graphs, it is to be expected that small changes in the excitation condition (projectile velocity v_{peak} and/or base to stopper distance BD) may influence the overturning mode.

For a single block, as an illustration, Figure 8.9 and Figure 8.10 show substantial differences of the eventual overturning modes for the two cases, which are subject to very similar projectile velocities. It can be noted that these differences in the outcome are primarily associated with the actual timing of the reverse shock (i.e. at what stage of rocking does the reverse impact with stopper take place) which in turn is obviously related to different distances between the base and the stopper (as well as to different peak base velocities). The graphs in Figure 8.9 (detail extracted by zooming Figure 8.7) show the case where the single block starts rocking about its left edge due to the initial acceleration of the base, but when the reverse impact of

the base with the stopper happens, the block starts rocking back and finally ends up
rocking around its right corner, eventually overturning to the right side.
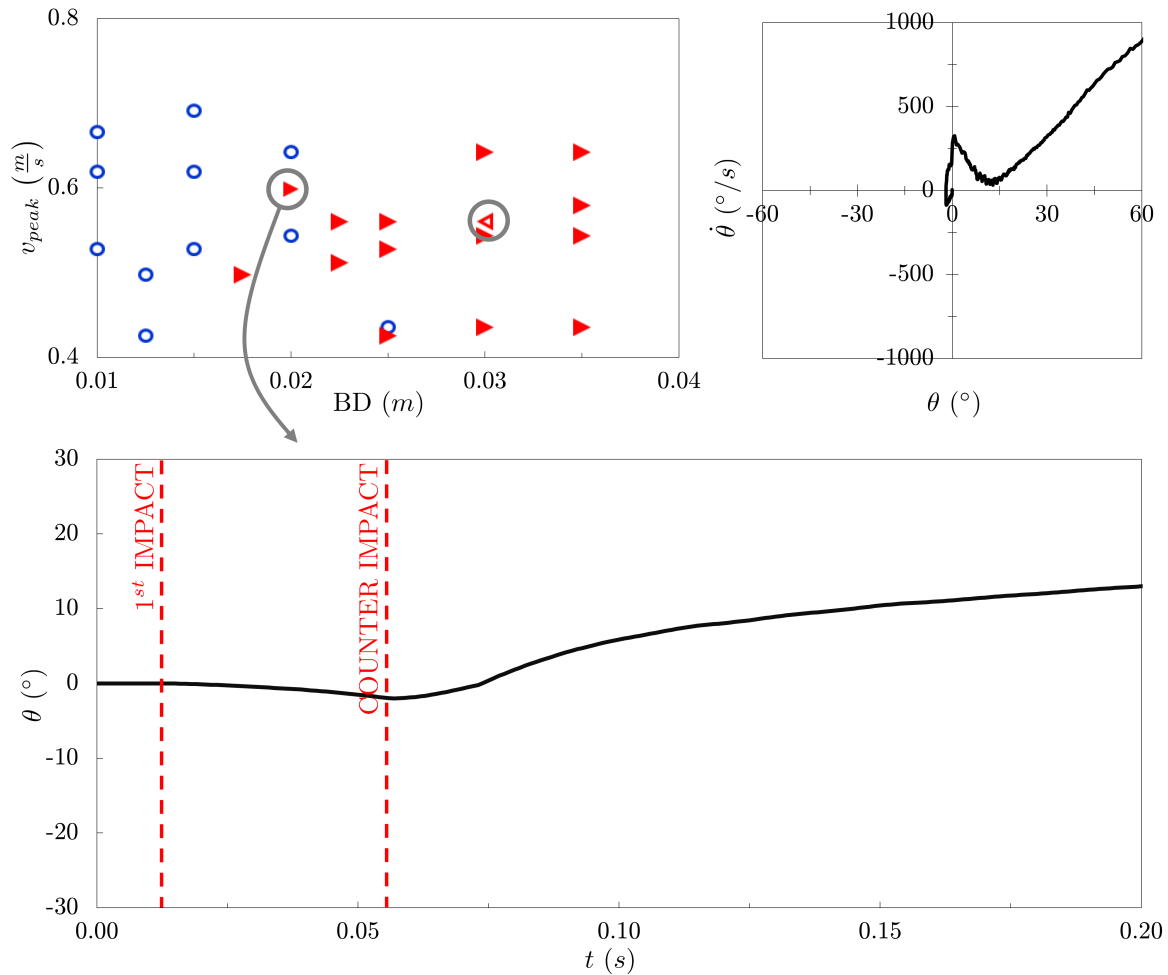
Figure 8.9: Phase plane view (above on the right) and rotation time history (below) of
the experiment of a single block (Scale 1) motion with initial conditions $v_{peak} = 0.59$
$\frac{m}{s}$, BD= 2.0 cm

The graphs in Figure 8.10 show the case with a very similar base velocity, but a
larger distance between the base and the stopper (hence a longer time of free travel
of the base), where the block starts rocking around its left edge and when the reverse
impact happens it starts to rotate back to its initial vertical position - however the
angular velocity at that instant is such that the block ends up eventually overturning
to the left side.
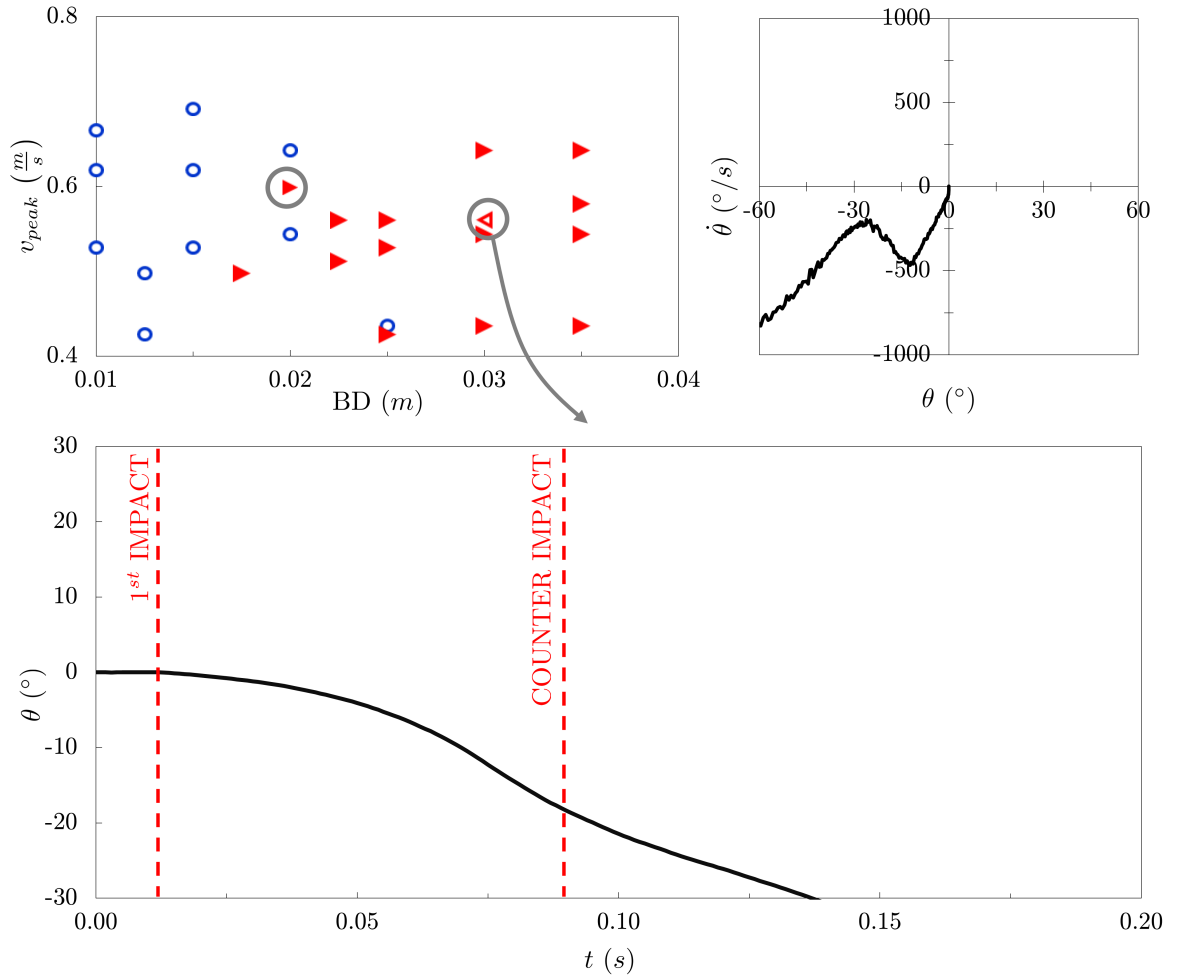
Figure 8.10: Phase plane view (above on the right) and rotation time history (below) of the experiment of a single block (Scale 1) motion with initial conditions $v_{peak} = 0.56$ $\frac{m}{s}$, BD= 3.0 cm

Both experimental cases are accompanied by a phase plane plot, which would enable the detection of any attractor points in such dynamic behaviour.

Tracing the details of the overturning histories provides not only an additional angle in the interpretation of the reasons for the eventual overturning modes (the time instant of the reverse impact while the block is either leaning forward or backward as a result of the initial shock) - it also provides additional detailed information and forms a part of the benchmarking and validation of various simulation frameworks.

8.4 Experimental results for multiple-blocks stack

A series of multi-block-stack experiments on two different scales comprising three blocks, positioned one on top of the other, subject to a double pulse base excitation

is carried out. Sample dimensions on the smaller scale (Scale 1) are $h_1 = 15$ mm, $b_1 = 10$ mm and $l_1 = 10$ mm, while the larger scale (Scale 2) samples dimensions are $h_2 = 30$ mm, $b_2 = 20$ mm and $l_2 = 20$ mm. The end state for each experiment and for each simulation is again categorised using different modes of overturning (see Figure 8.11):

- Mode of overturning **A** if all the blocks from the stack remain stable at the end of the experiment,

- Mode of overturning $\mathbf{B}_L$ or $\mathbf{B}_R$ if the top block from the stack overturns to the left or to the right side, respectively,

- Mode of overturning $\mathbf{C}_L$ or $\mathbf{C}_R$ if the two upper blocks from the stack overturn to the left or to the right side, respectively, and

- Mode of overturning $\mathbf{D}_L$ or $\mathbf{D}_R$ if the whole stack overturns to the left or to the right side, respectively.

○ Mode **A**   ● Mode $\mathbf{B}_R$ ▶ Mode $\mathbf{C}_R$ ▶ Mode $\mathbf{D}_R$
○ Mode $\mathbf{B}_L$ ◀ Mode $\mathbf{C}_L$ ◀ Mode $\mathbf{D}_L$
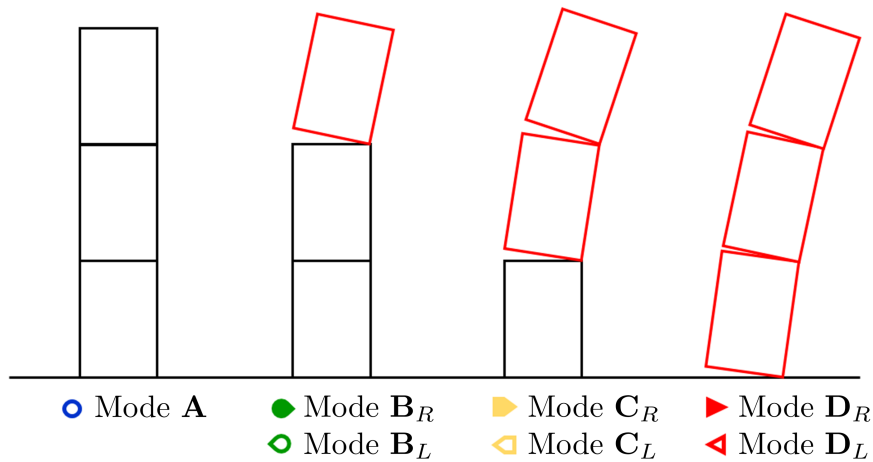
Figure 8.11: Modes of overturning of a three-block stack

8.4.1   Scale 1

Experimental results of the overturning behaviour of the stack of three blocks (Scale 1) due to pulse-type excitation are shown in Figure 8.12. Impacts with the projectile with velocity lower than 3.5 m/s are not resulting in overturning of any of the blocks. Impacts with higher velocities result in different modes of overturning (Figure 8.12).
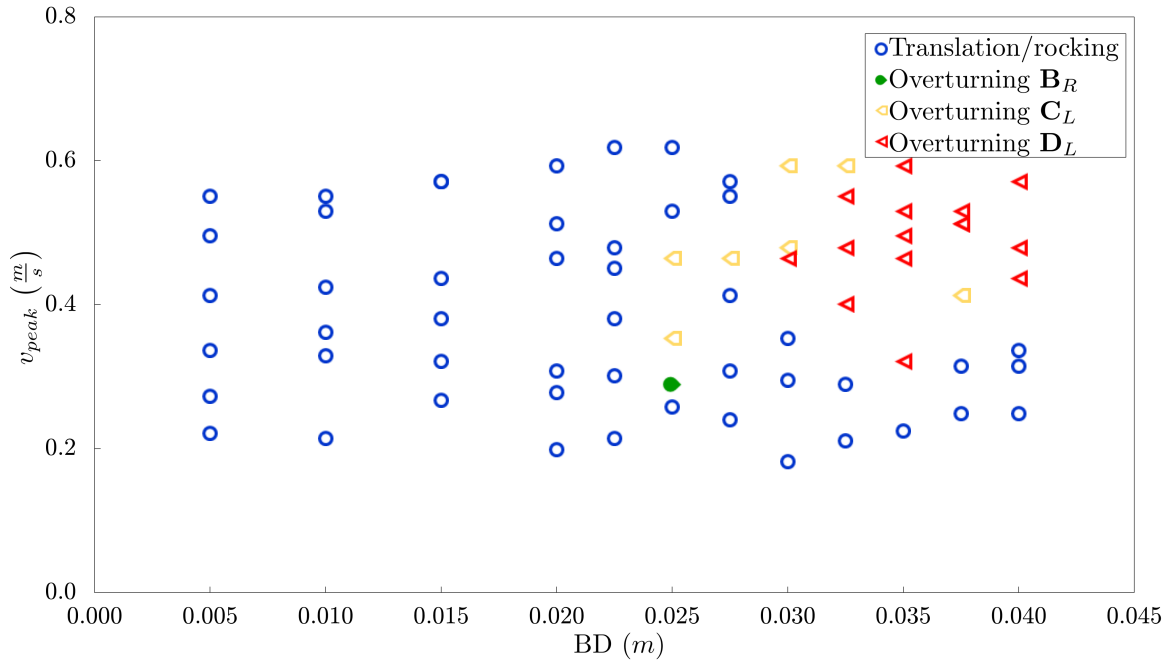
Figure 8.12: Modes of overturning of a three/block stack (scale 1) obtained from the experimental study

8.4.2   Scale 2

Experimental results of the overturning behaviour of a stack of three blocks (Scale 2) due to the pulse-type excitation are shown in Figure 8.13. In comparison to the experimental results for the stack of smaller blocks, the stack with larger blocks requires higher projectile velocities and consequently higher base velocities to overturn. The stack with larger blocks indicates a larger stability region with respect to the distance between the base and the stopper.
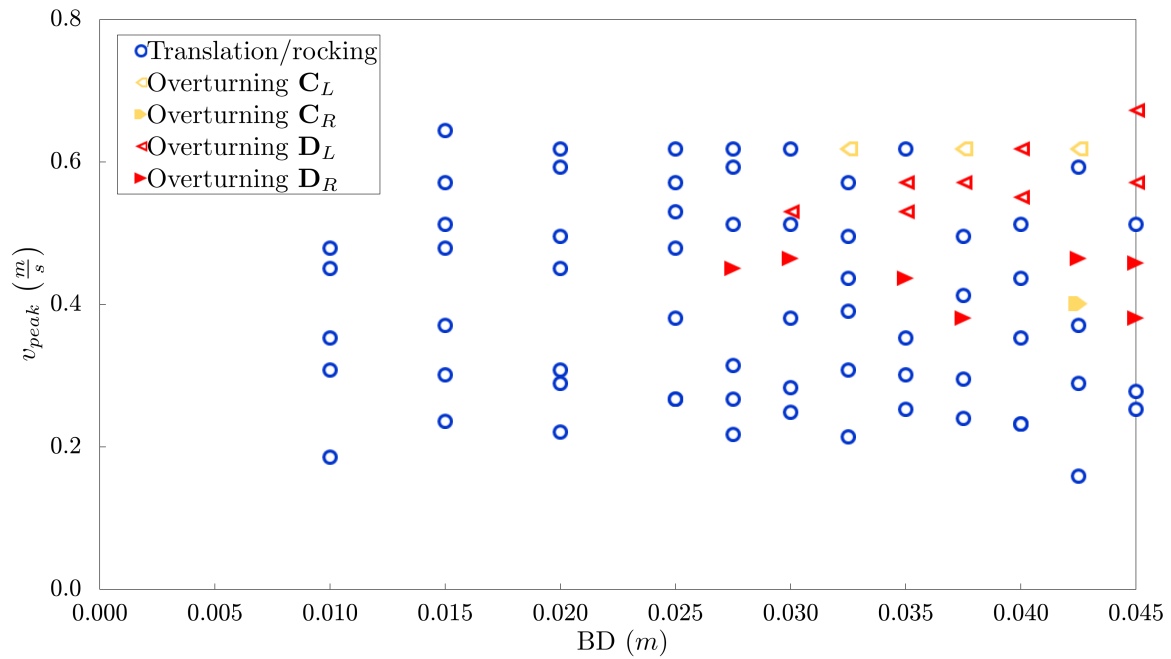
Figure 8.13: Modes of overturning of a three/block stack (scale 2) obtained from the experimental study

8.4.3 Comments on the scaling effect

In a similar way as shown earlier for a single block, experimental results from both scales of the three block stack are plotted in a single, combined graph in Figure 8.14. The frequency parameter analytically obtained for the case of a single block with corresponding overall dimensions of the stack of three blocks is used to scale the excitation frequency, while the overall mass of the stack is used to scale the input kinetic energy of the system.
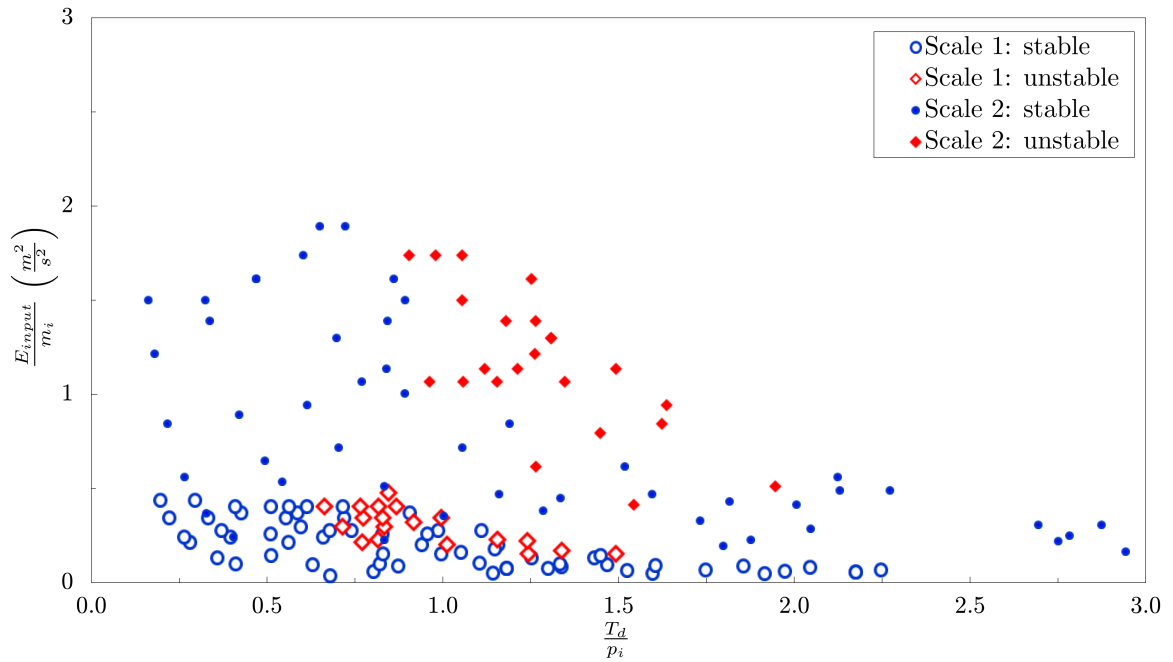
Figure 8.14: Areas of overturning (red marks) and no overturning (blue marks) for the three/block stack (Scale 1 is represented with filled marks, Scale 2 is represented with empty marks) obtained from the experimental study

8.4.4 Detailed study of the three-block stack overturning modes

Overturning modes of the three block stack also depend significantly on the timing of the reverse impact with the stopper. Figures 8.15 and 8.16 illustrate the significant differences between the overturning modes of the stack with the same initial velocity of the base, but with a perturbation in the BD distance. The experiment shown in Figure 8.15 shows a case where the entire stack starts rotating around the left edge, but the reverse impact happens exactly in time to produce a small push to the left side so that the bottom block starts rotating backwards and finally ends up in the vertical position, while the two upper blocks overturn to the left side.
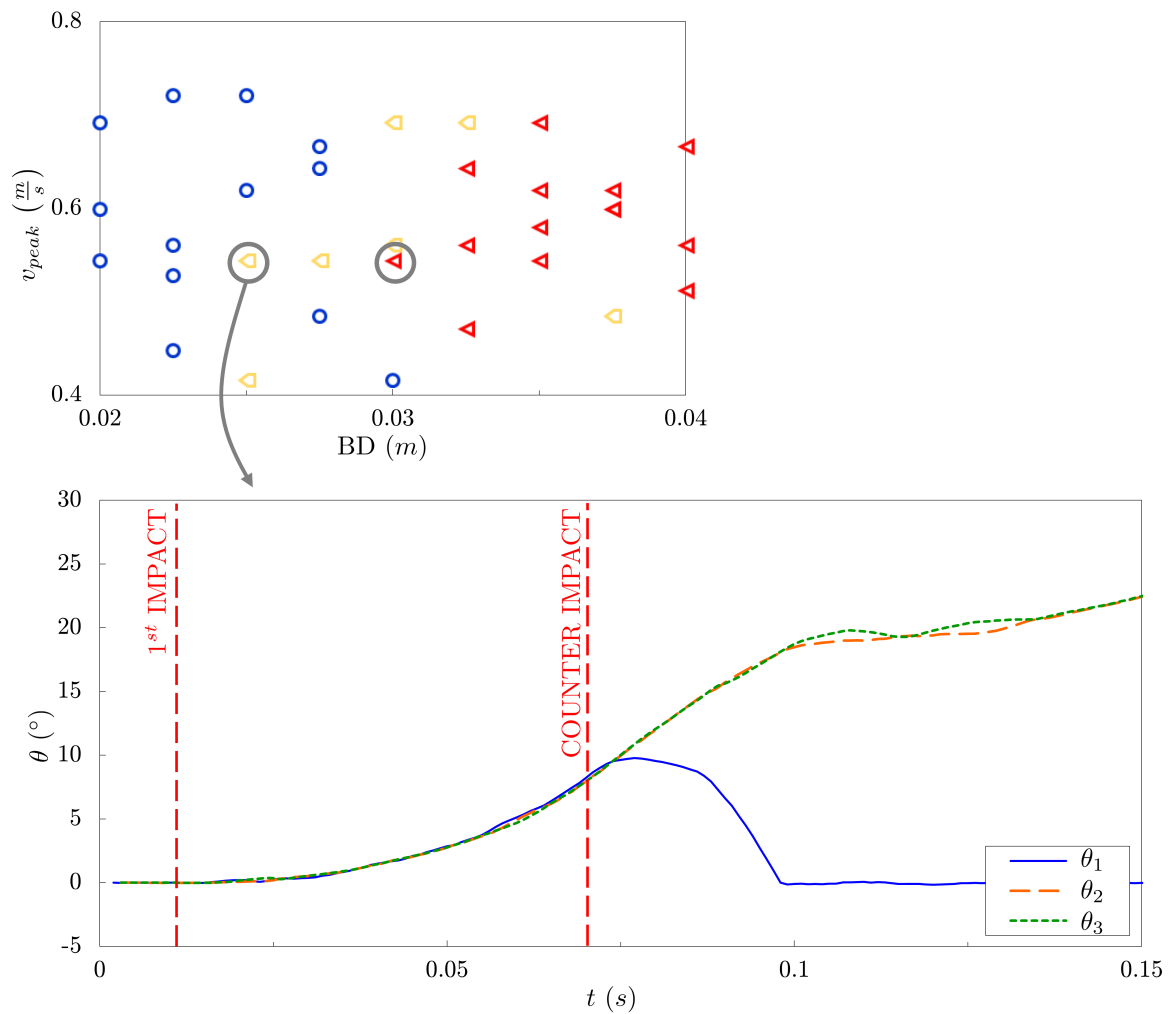
Figure 8.15: Rotation time history (below) of the experiment of a three-block stack (Scale 1) motion with initial conditions $v_{peak} = 0.54 \frac{m}{s}$, BD= 2.5 cm

The experiment shown in Figure 8.16 starts with a behaviour similar to the case just described, but the reverse impact happens later (due to the larger BD distance) and even though the bottom block clearly experiences a decrease in angular velocity (indicating a tendency to rotate in the opposite direction) the entire stack ends up overturning to the left.
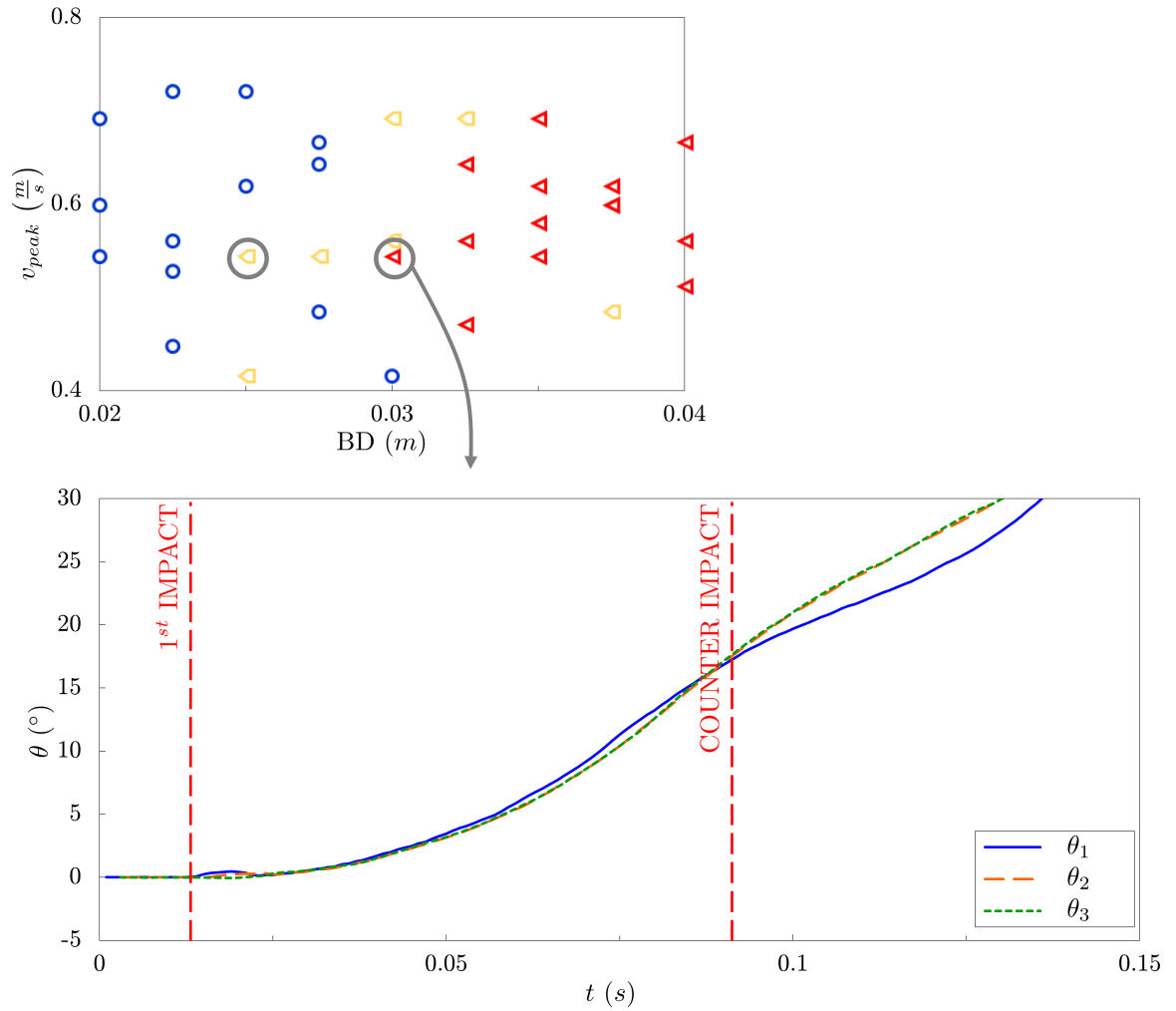
Figure 8.16: Rotation time history (below) of the experiment of a three-block stack (Scale 1) motion with initial conditions $v_{peak} = 0.54 \frac{m}{s}$, BD= 3.0 cm

The results for the two cases described above are further illustrated in Figure 8.17 (corresponding to the case shown earlier in Figure 8.15) and Figure 8.18 (corresponding to the case shown earlier in Figure 8.16) by means of the rotation phase plane views for the entire stack comprising three blocks, as well as for each of the three blocks individually. Rotation-phase-plane view enables an easier insight into the dynamic behaviour of each of the bodies within a multiple body system during the course of the experiment (or simulation). Rotation-phase-plane view of the whole stack and of the bottom block in Figure 8.17 shows counter-clockwise rocking motion of the bottom block (as well as the upper two blocks) up until the time the counter-impact takes place, which is followed by a clockwise direction of rotation of the bottom block leading finally to a stable end state of the bottom block, while the top two blocks overturn, hence this case leads to a partial stack overturning.

177
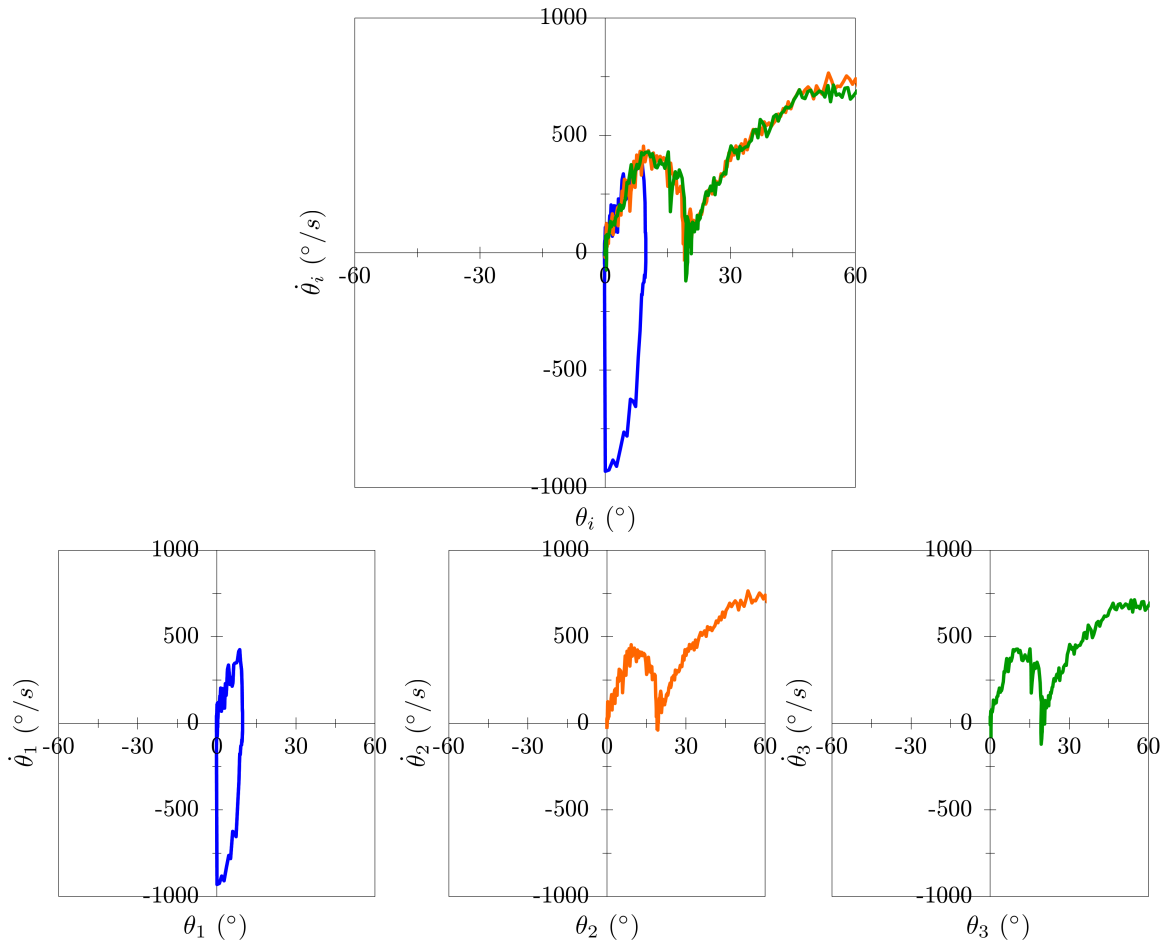
Figure 8.17: Phase-plane views of the experiment of a three-block stack (Scale 1) motion with initial conditions $v_{peak} = 0.54 \frac{m}{s}$, BD= 2.5 cm

The corresponding rotation-phase-plane views in Figure 8.18, where the BD distance is larger, show the initial counter-clockwise rocking motion of the three blocks up until the counter-impact takes place, which is again followed by a clockwise motion and a tendency to a stable end state. Since the BD distance is larger such a stable position is not reached and a global overturning of the stack as the whole takes place.
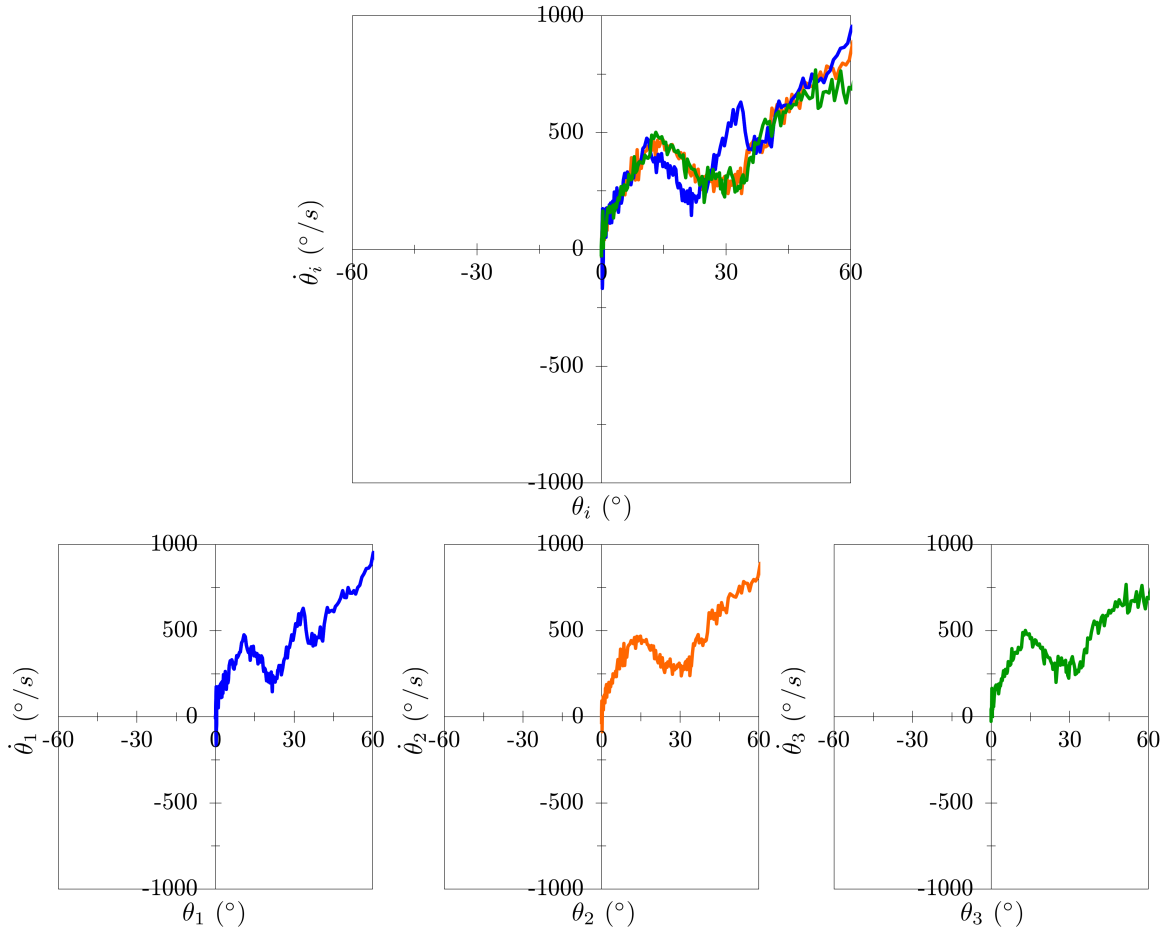
Figure 8.18: Phase-plane views of the experiment of a three-block stack (Scale 1) motion with initial conditions $v_{peak} = 0.54 \frac{m}{s}$, BD= 3.0 cm

8.5 Discussion and conclusion

Preliminary results of experiments, related to the single-block and the multiple-block stacks overturning study due to the controlled double pulse excitation are given. A particular attention is given to the excitation conditions (impulse intensities and time delay between the initial and reverse impulse) leading to a partial overturning mode.

The coarse, predominantly descriptive, characterisation of the eventual overturning modes is augmented by a more detailed study tracing the manner in which the eventual overturning modes are achieved. The sources of the result scatter emanate from the difficulties and imperfections to manually align the blocks along the same plane, as well as on top of one another during the experiments, and the inability to completely prevent sliding motion between the bodies by means of rough surfaces.

The results of the scaling study to render the observed overturning modes dimen-

179

sionless are inconclusive and require further research, starting with obtaining a series of experimental (and computational) results of dynamic behaviour of a single-block and three-block stack on a third (larger) scale due to a double impulse type base excitation.

Chapter 9

Ordered confined multiple-body assembly

This chapter is based on the results and discussion from paper [66]:
Bićanić, N., Camenen, J. F., Čeh, N., and Koziara, T., "Characterisation of pattern formation in constrained multiblock assembly subjected to horizontal harmonic excitation", International Journal of Masonry Research and Innovation

Pattern formation for a constrained one-dimensional assembly comprising a number of blocks undergoing external harmonic excitation of the basin boundary is investigated. The importance of the relationship between the excitation amplitude and the basin size which leads to repeatable response patterns of the single and multiple blocks is established, considering in addition the role of the energy dissipation due to inter-block collisions and collisions with the moving boundary. Experimental results for the four- and eight-block assembly control problems, exposed to various amplitudes and frequencies, are included. In the characterisation of the dynamic sensitivity response of the multi-block assemblies, several attributes and indices (kinetic energy index, block-assembly mass centroid and moment of inertia index, presented through time histories and phase planes) are extracted from the experimental results.

9.1   Introduction

This chapter aims to examine a particular class of structured, ordered multi block assemblies of simple block shapes. The observed system comprises assemblies where any rearrangement of block neighbours or repositioning is either impossible (due to small clearances) or such a rearrangement would directly imply a structural or functional

failure. It explores observations about the blocks pattern formation by studying the simple case of a one-dimensional model i.e. a row comprising N rigid blocks in 1D, driven by a harmonic excitation of the side container boundaries, while the blocks are subject to dissipative inter-block collisions, collisions with the side boundary, as well as the frictional dissipation in contact with the container sliding base. The interior domain comprising N blocks is subject to repeated collisions with the exterior domain, which follows a prescribed harmonic motion and in between these collisions the blocks experience either a free travel or their motion is affected by inter block collisions and the effects of base friction. The paper provides an initial exploration of characterising dynamic sensitivity of multi block assemblies, i.e. whether there are relationships between the basin size, the blocks and gap sizes and the excitation amplitudes and frequencies leading to a repeatable response pattern and how they are affected by dissipation mechanisms through block collisions and base friction.

9.2   Single block study

Even the consideration of harmonic excitation of a single block (Figure 9.1) of a block with mass m and size s, within a container basin of mass $M >> m$ and size d, corresponding to a free travel of the block $(d - s)$, points distinctly to the importance of the problem geometry in the nature of the dynamic response. The simplest case to be considered is the case of a single rigid block, subject to harmonic excitation $x_b = u_0 \sin(\Omega t)$, $\dot{x}_b = u_0 \Omega \cos(\omega t)$, assuming an elastic collision with both boundaries $(e = 1)$, no base friction, with the initial block position directly next to the left boundary $\left(x_c = \frac{s}{2} \right)$. As $M >> m$, the initial block velocity is $v_0 = 2u_0\Omega$, twice the maximum boundary velocity.
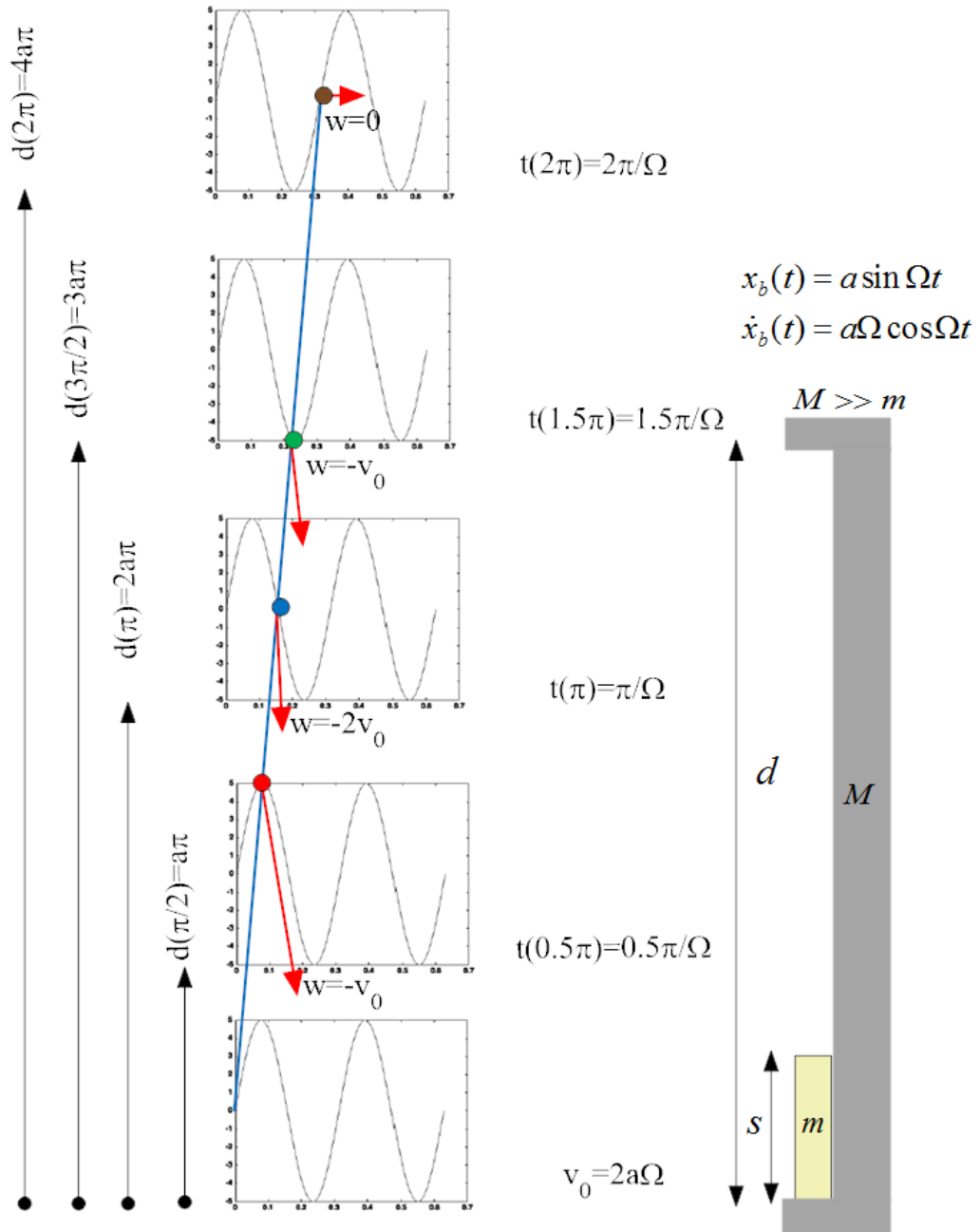
Figure 9.1: Rigid block, elastic collision. Maximum rebound velocity corresponds to a distinct geometry $d = s + 2u_0\pi\,(1 + 2n)$, $n = 0, 1, 2, ...$ between the container basin size d and the excitation amplitude u_0. This relationship is independent of the excitation frequency

By equating the block free travel arrival time to the other boundary $T_{travel} = \frac{d-s}{v_0}$ to the time instances of a maximum boundary velocity in the opposite direction $T_{max} = \frac{\pi}{\Omega} + 2n\pi$, it is possible to analytically determine that the basin size $d =$

$s + 2u_0\pi\left(1 + 2n\right)$, $n = 0, 1, 2, ...$ leading to a maximum rebound velocity, double the initial block velocity v_0. This maximum condition is purely geometric - it is the relationship between the boundary amplitude and the basin size, independent of the excitation frequency. Any larger basin size corresponding to different values of $n = 0, 1, 2, 3, ...$ will also lead to doubling of the rebound velocity upon collision, as an equivalent contact location is achieved due to the time shift $\frac{2\pi}{\Omega}$ in the harmonic boundary motion. Different basin sizes will clearly induce a whole range of rebound velocities upon the first collision. The block always leaves its initial position with the initial velocity $v_0 = 2u_0\Omega$, but the rebound velocity will depend on the boundary velocity at the time instant the block reaches the opposite boundary. The whole range of rebound velocities between $(0 - 2v_0)$ is possible. It can be concluded that for a given boundary amplitude there is a critical basin size, corresponding to an unfavourable maximum block rebound velocity. Similarly, there are critical excitation amplitudes for a given basin size.

Table 9.1: Basin sizes for a given amplitude u_0 and excitation amplitudes for a given basin size d

$d_{\frac{\pi}{2}} = \left(1 + e\right)u_0\frac{\pi}{2}\left(1 + 4n\right) + s - u_0$	$u_{0,\frac{\pi}{2}} = \dfrac{d - s}{\left(1 + e\right)\frac{\pi}{2}\left(1 + 4n\right) - 1}$
$d_\pi = \left(1 + e\right)u_0\pi\left(1 + 2n\right) + s$	$u_{0,\pi} = \dfrac{d - s}{\left(1 + e\right)\pi\left(1 + 2n\right)}$
$d_{\frac{3\pi}{2}} = \left(1 + e\right)u_0\frac{3\pi}{2}\left(1 + \frac{4}{3}n\right) + s + a$	$u_{0,\frac{3\pi}{2}} = \dfrac{d - s}{\left(1 + e\right)\frac{3\pi}{2}\left(1 + \frac{4}{3}n\right) + 1}$
$d_{2\pi} = \left(1 + e\right)u_02\pi\left(1 + n\right) + s$	$u_{0,2\pi} = \dfrac{d - s}{\left(1 + e\right)2\pi\left(1 + n\right)}$

The above argument can be extended to an inelastic collision with the boundary $(e \neq 1)$, where the collision is associated with a degree of energy dissipation. For a given boundary amplitude u_0, the critical basin sizes for the block to reach contact points $(\frac{\pi}{2}, \pi, \frac{3\pi}{2}, 2\pi)$ on the first collision are given in Table 9.1, which also includes the converse relationship of the critical amplitudes for the block to reach contact points $(\frac{\pi}{2}, \pi, \frac{3\pi}{2}, 2\pi)$ if a given basin size is d. As the container mass M (the exterior domain undergoing prescribed motion $x_b = u_0\sin\left(\Omega t\right)$, $\dot{x}_b = u_0\Omega\cos\left(\omega t\right)$) is significantly larger that the block mass m (the interior domain), the initial block velocity depends on the restitution coefficient $v_0 = \left(1 + e\right)u_0\Omega$, and hence the initial kinetic energy of the block is $E_{kin}^0 = 0.5mv_0^2 = 0.5m\left(1 + e\right)^2u_0^2\Omega^2$. If – for a given amplitude u_0 – the container size d is tuned to ensure the first collision at contact

points A, B, C or D ($\frac{\pi}{2}$, π, $\frac{3\pi}{2}$, 2π), the rebound block velocity can be analytically determined, as given in Table 9.2. Note that at 2π, for an elastic collision, the block comes to a stop and rebounds on boundary return at π, whereas for the fully plastic collision the block remains in persistent contact with the boundary until its release at π.

Table 9.2: Block rebound velocity $\tilde{v}_m$ following the first collision

Collison point	Mass velocity v_m	Boundary velocity v_M	Rebound velocity $\tilde{v}_m$
A, $\frac{\pi}{2}$	$(1+e)\,u_0\Omega$	0	$-ev_0 = -e\,(1+e)\,u_0\Omega$
B, π	$(1+e)\,u_0\Omega$	$-u_0\Omega$	$-(1+e)\,v_0 = -e\,(1+e)^2\,u_0\Omega$
C, $\frac{3\pi}{2}$	$(1+e)\,u_0\Omega$	0	$-ev_0 = -e\,(1+e)\,u_0\Omega$
D, 2π	$(1+e)\,u_0\Omega$	$u_0\Omega$	$(1-e)\,v_0 = (1-e)^2\,u_0\Omega$
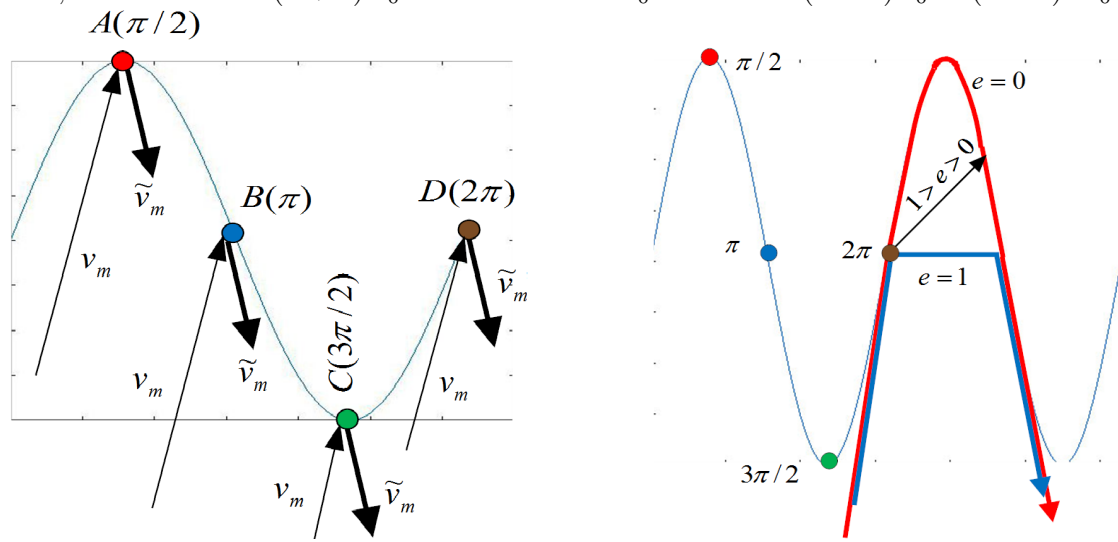
The role of the restitution coefficient in the nature of the subsequent block response to external excitation is now further considered (Figures 9.2, 9.3 and 9.4) by following both the block trajectories and the kinetic energy index $\dfrac{E_{kin}\,(t)}{E_{kin}^0}$ time histories for the two initial contact cases at B and D (π, 2π). The elastic collision case ($e = 1$) reveals that the block trajectory is noisy and that the kinetic energy index increases up to 6 times if the container size corresponds to the first collision at π (maximum rebound velocity).
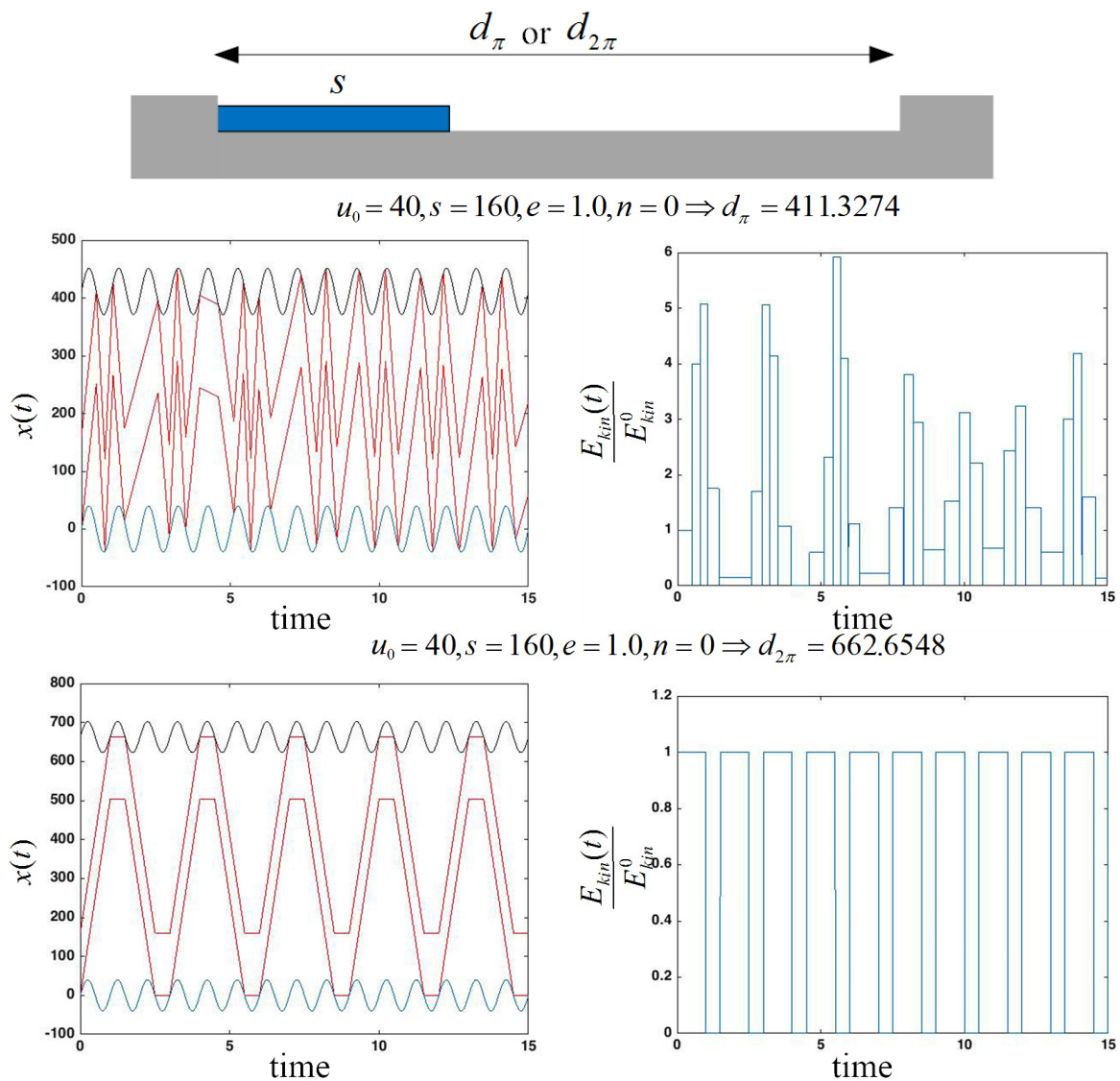
Figure 9.2: Trajectory and kinetic energy index time-histories for a fully elastic collision ($e = 1$) between the block and the moving boundary for the first collision at contact points $(\pi, 2\pi)$

The block trajectory is periodic and the kinetic energy index never exceeds 1.0, if the container size is such that the collision occurs at 2π. Trajectory for the fully plastic collision case ($e = 0$) remains periodic for both container sizes corresponding to collisions at both $(\pi, 2\pi)$ and the kinetic energy index never exceeds 1.0.
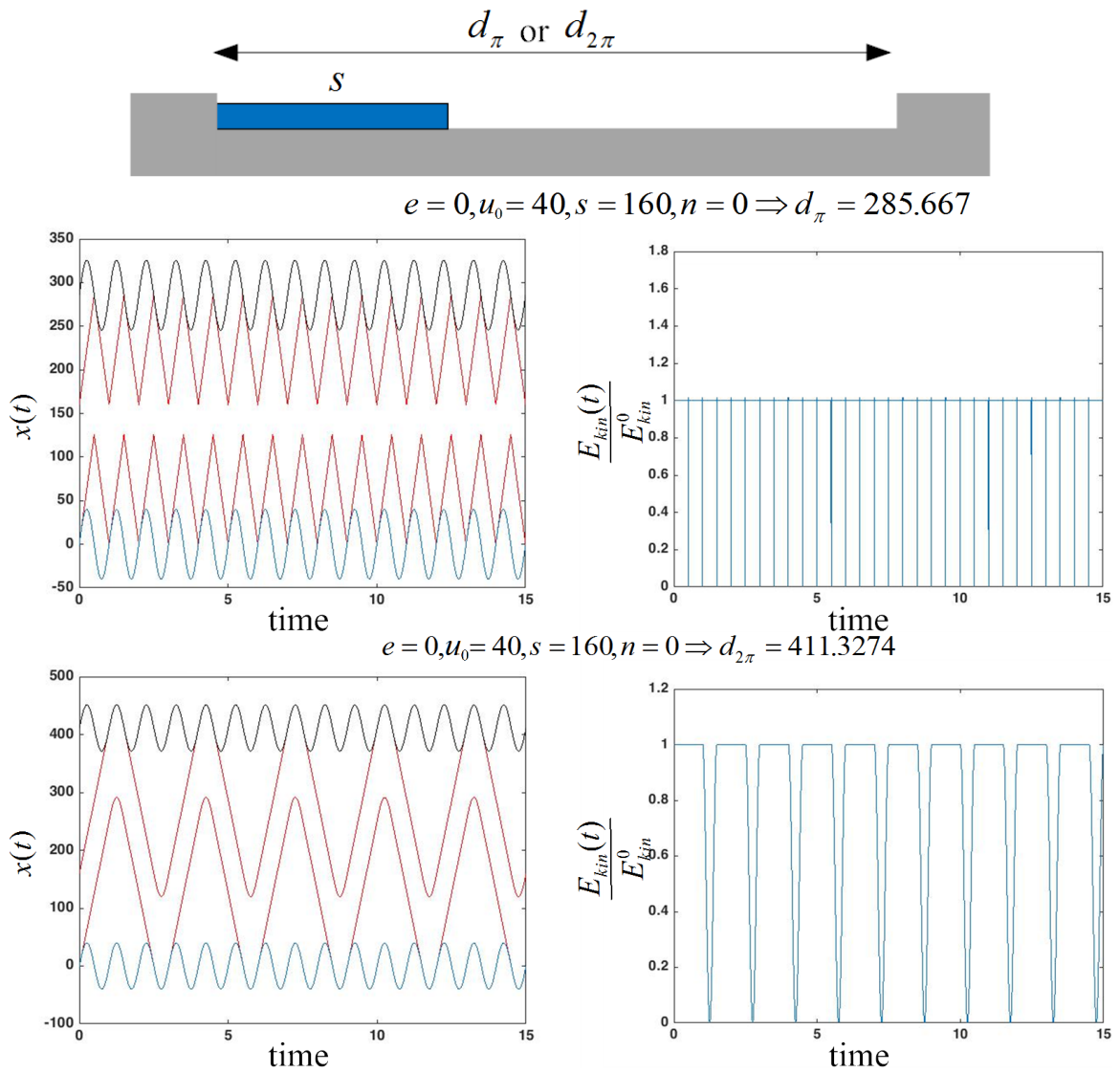
Figure 9.3: Trajectory and kinetic energy index time-histories for fully plastic collision ($e = 0$) between the block and the moving boundary for the first collision at contact points ($\pi, 2\pi$)

The intermediate case of ($1 > e = 0.8 > 0$) does not lead to any periodicity in subsequent block response for $d_{2\pi}$ basin size and the kinetic energy index remains above 1.0.
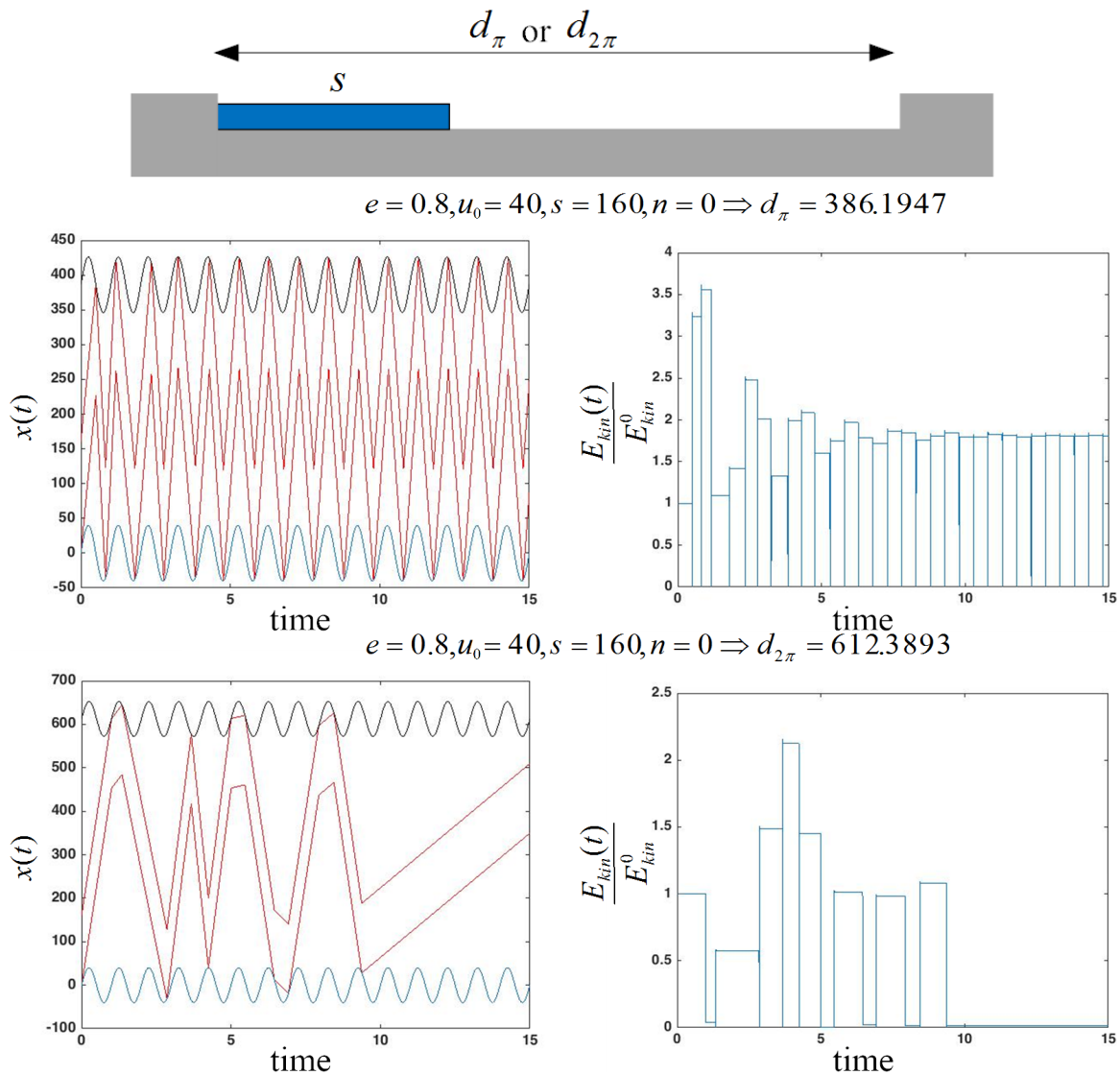
Figure 9.4: Trajectory and kinetic energy index time-histories for an intermediate restitution coefficient $(1 > e > 0)$ between the block and the moving boundary for the first collision at contact points $(\pi, 2\pi)$

It is worth noting again that there are distinct geometry and restitution cases where the block response is periodic, whereas in some other arrangements this is not the case. The above arguments firmly indicate that the relationship between the excitation amplitude and the problem geometry (the length of the free travel path, defined by the block and clearance sizes, as well by the size of the basin itself) is likely to be of importance in the response of multi-block assemblies to harmonic external excitation.

9.3 Patterns with subdivided block

The single block benchmark problems are here extended by subdividing the block of size s into N blocks (4 or 8 respectively), with the first block aligned next to the boundary, where the initial configuration may or may not include gaps g between the blocks. The purpose of this illustrative series is to explore if and how does the pattern of the block assembly response change due to such subdivision and due to gaps and clearances. Clearly an additional restitution coefficient e_2 is now introduced, to represent the energy dissipation during collisions between blocks, which may be different to the restitution coefficient e_1 between the blocks and the boundary. Only one basin size is considered d_π, where the basin size corresponds to the maximum rebound velocity after the first collision in the original single block case.
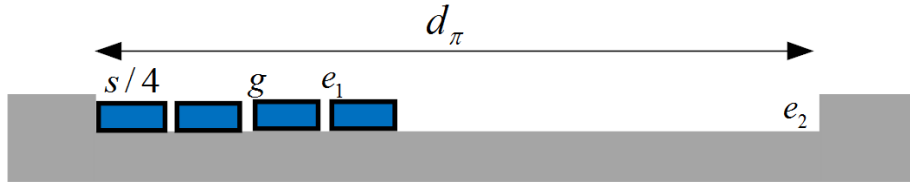
Figure 9.5: Four-blocks subdivision
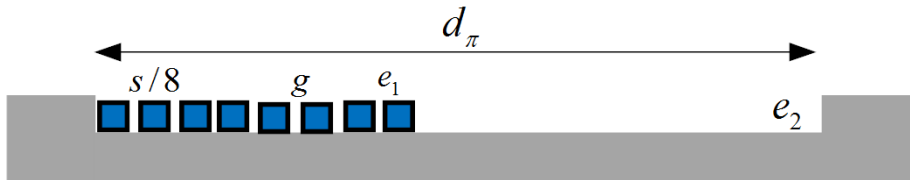
Figure 9.6: Eight-blocks subdivision

9.4 N-block problem

In the N-block study, the exterior boundary and the interior domain (blocks assembly) are subject to interaction through numerous collisions. The interior domain is dissipating energy through the inter-block collisions, through collisions with the external boundary, as well as through base friction. The presented N-block benchmark problem includes a series of experiments.

Apart from an obvious intention to computationally validate experimental results, the principal research question remains the same, i.e. to investigate whether - for a given basin size, excitation frequency and amplitude, after an initial transient adjustment stage - the response of the interior domain converges asymptotically to a state

with some repeatable trajectories. Furthermore, if yes, the question remains of what are the associated block assembly patterns or block clustering modes, similarly to the ones observed with granular material in harmonically excited containers [53].

It is believed that these patterns depend on the inter-block dissipative mechanical interactions, on the problem geometry, on the initial configuration of the assembly and also on the frequencies and amplitudes of the external excitation. The intention here is to explore and possibly characterise oscillatory 'repeatable patterns', associated with distinct frequencies or amplitudes as well as to study transient and possible steady state and asymptotic response of a multi-block assembly (including whether such a steady state exists at all).

9.5   Experimental setup

The behaviour of an assembly of four and eight rigid blocks respectively, subject to external harmonic excitation due to collisions with a rigid basin boundary undergoing a prescribed displacement history is considered. A series of experiments shown below was conducted in the Structural Dynamics Laboratory at the Faculty of Civil Engineering at the University of Rijeka. Each rectangular block with the dimensions 113 mm x 40 mm x 10 mm and mass 52.24 g is fabricated using a 3D printer Connex 500. The entire block assembly is placed on top of a layer of albumin beads with diameter 5 mm used to provide as low friction as possible between the blocks and the basin floor underneath (Figure 9.7). The Plexiglas rectangular basin with an interior free space dimensions 114 mm x 394 mm x 20 mm is attached to the top surface of the shaking table.
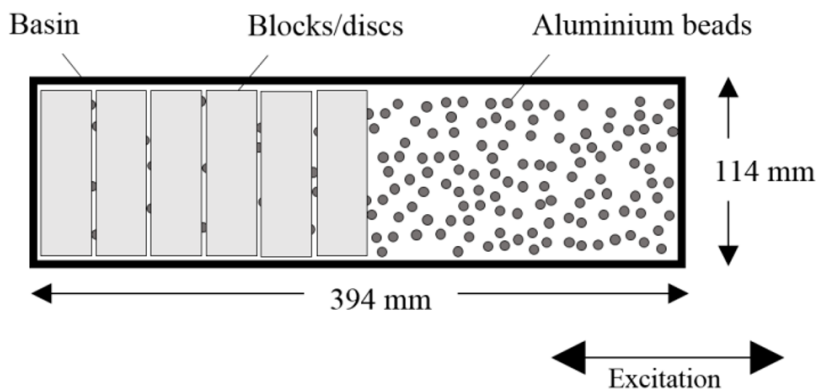
Figure 9.7: Assembly of N blocks inside a rectangular basin – experimental set-up

The biaxial shaking table Quanser ST-III (described in Section 5.2.3.2) is used to

provide a given excitation in form of the boundary displacement history. To avoid extreme difficulties that would occur if accelerometers were used to trace the dynamic response of the assembly (such as the effect of the wires and the mass of the devices on the dynamic response of each block as well as the possibility of device damage during impacts between discs) every experiment is recorded using a set of two cameras as part of the GOM Aramis/Pontos non-contact optical measuring system. The characteristics of Quanser ST-III set of biaxial shaking tables are given in Section 5.2.3.2 and of GOM optical measuring system in Section 4.3.3. All the videos are recorded using the frame rate 100 fps with a resolution 2400x1728 pixels which provides long enough exposure time with respect to the lighting conditions.

The results of displacement history of the shaking table obtained from GOM optical system are compared to the readings from an encoder on the shaking table surface which has shown that GOM Pontos system has provided sufficiently accurate displacement measurements. The limiting parameter for the optical system in this case is the low frame rate, unable to capture high frequency displacements of the discs during the impacts with either other discs or the basin boundary, which can be seen as gaps in the position histories in some of the results below.

The coefficient of friction and coefficients of restitution between two discs and the disc and the basin are obtained experimentally using the GOM optical system to record the free movement of a disc inside the basin on top of the aluminium beads (Table 9.5).

Table 9.3: Coefficient of friction and restitution coefficients obtained experimentally

Dynamic coefficient of friction	μ_{dyn}	0.03
Restitution coefficient 1 (collision between two blocks)	e_1	0.6
Restitution coefficient 2 (collision between block and basin wall)	e_2	0.3

9.5.1 Samples

Benchmark problems with four (series A) or eight (series B) identical rectangular rigid blocks are considered. All block sizes are $s = 40$ mm and the block cross section 10x113 mm^2 (mass density 1200 $\frac{kg}{m^3}$, hence block masses are equal to 52.24 g) the blocks are initially in contact with one other, within a horizontal container of a width of 114 mm and a length of 394 mm (which implies a free travel space of 234 mm and 74 mm within the basin for series A and B, respectively). The first block is initially in contact with the moving side boundary. The basin is driven horizontally by a series of sinusoidal motions $x_b(t) = u_0 \sin(\Omega t)$ and the selected cases are presented below.

9.6 Characterisation of multi-block assembly response

Dynamic sensitivity of the N block assembly under harmonic excitation is studied by extracting time histories and phase plane representations of the two scalar parameters to assist in the pattern recognition and characterisation of dynamic sensitivities for the multi block assembly

a. the mass centroid,

b. the moment-of-inertia index,

which are conveniently captured from the experimental results.

9.6.1 Mass centroid

Trajectories of both the left and the right sides of each block as well as the constrained moving boundary are traced, allowing for an easy visualisation of shocks between the blocks themselves and between the end blocks and the basin boundary. The time-history of the centre of mass for the multi block assembly is given by

$$x_{cm}(t) = \frac{\sum m_i x_i(t)}{\sum m_i}, \tag{9.1}$$

where x_i are the positions of the blocks with mass m_i inside the assembly.

9.6.2 Moment of inertia with respect to the centroid

The block assembly moment of inertia with respect to its mass centroid is defined as

$$I_z(t) = \sum m_i \left[x_i(t) - x_{cm}(t)\right]^2. \tag{9.2}$$

9.6.3 Moment-of-inertia index

We define the moment-of-inertia index as

$$I_z^{ind}(t) = \frac{I_z(t)}{I_z^{ref}}, \tag{9.3}$$

i.e. as the current moment of inertia normalised with respect to the most compact configuration the multi block assembly can form. Here the initial configuration is assumed as the reference configuration $I_z^{ref} = I_z(0)$.

9.7 Experimental results

Benchmark problems with four (series A) or eight (series B) identical rectangular rigid blocks are considered. All block sizes are $s = 40$ mm and the block cross-section 10×113 mm^2 (mass density 1200 kg/m^3, hence block masses are equal to 52.24 g), the blocks are initially in contact with one other, within a horizontal container of a width of 114 mm and a length of 394 mm (which implies a free travel space of 234 mm and 74 mm within the basin for series A and B, respectively). The first block is initially in contact with the moving side boundary. The basin is driven horizontally by a series of sinusoidal motions $x_b(t) = u_0 \sin(\Omega t)$, with an amplitude $u_0 = 40$ mm, with frequencies $f = \frac{\Omega}{2\pi} = (1.5; 2; 2.5; 3)$ Hz. The friction between the blocks and the base is taken as $\mu = 0.03$ and the restitution coefficient for the collision between the blocks is equal to $e_1 = 0.6$ and between the block and the basin is equal to $e_2 = 0.6$.

9.7.1 Series A - four-block assembly

9.7.1.1 Excitation 1 - no impact with the sides

First, the four-block assembly subject to excitation with $u_0 = 40$ mm and $f = 1$ Hz is shown in Figures 9.8, 9.9 and 9.10. The positions of both edges of each blocks are presented (full line for one edge, dashed line for the other edge), along with the positions of the boundaries (basin). No periodic behaviour is detected in the mass centroid of the assembly (Figure 9.9), as well as in the inertia index history (Figure 9.10).
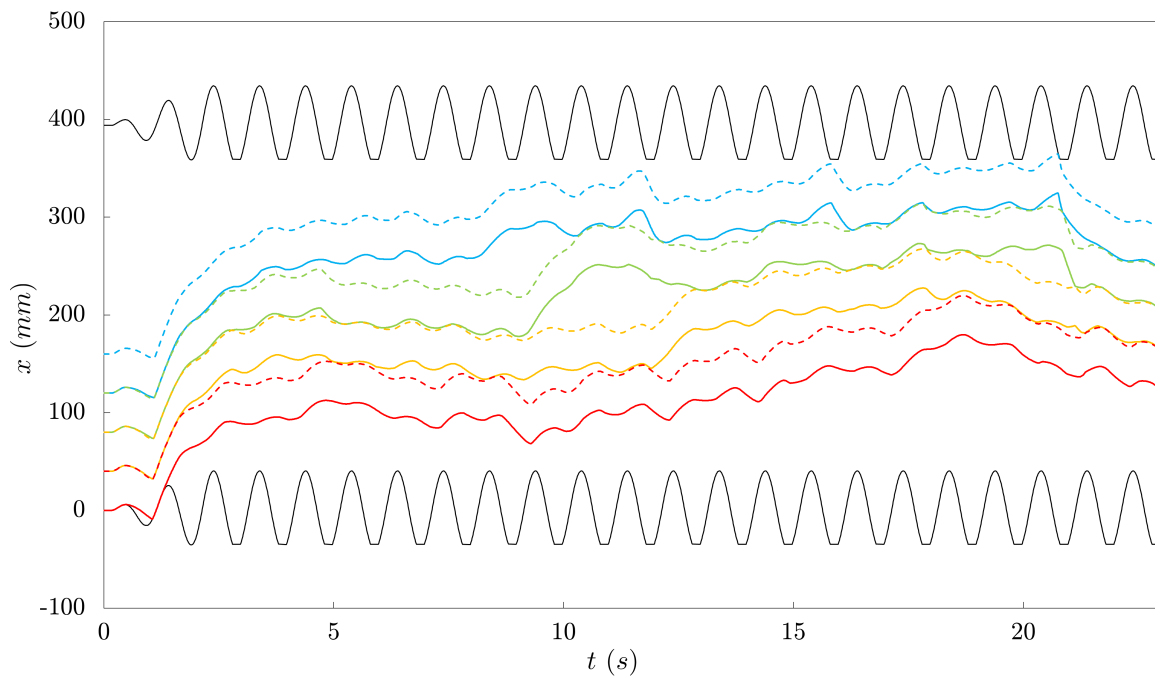
Figure 9.8: Position time-histories of a four-block assembly subjected to harmonic excitation with $u_0 = 40$ mm and $f = 1$ Hz
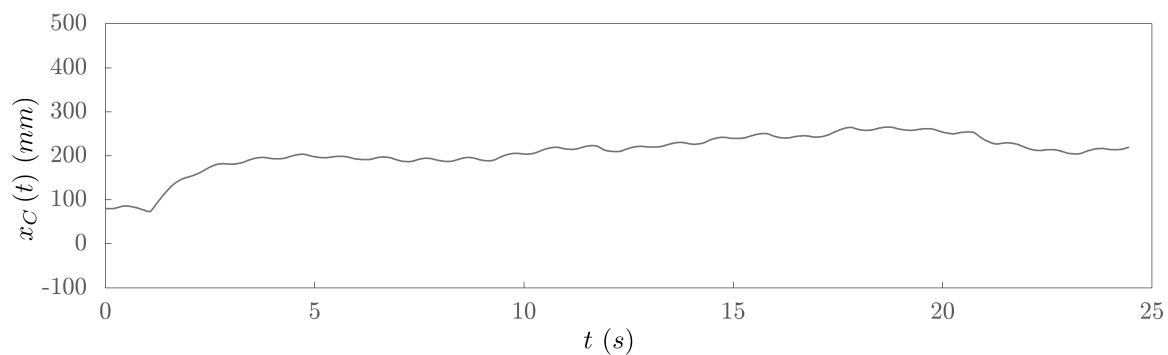
Figure 9.9: Position od the centre of mass of a four-block assembly subjected to harmonic excitation with $u_0 = 40$ mm and $f = 1$ Hz

194
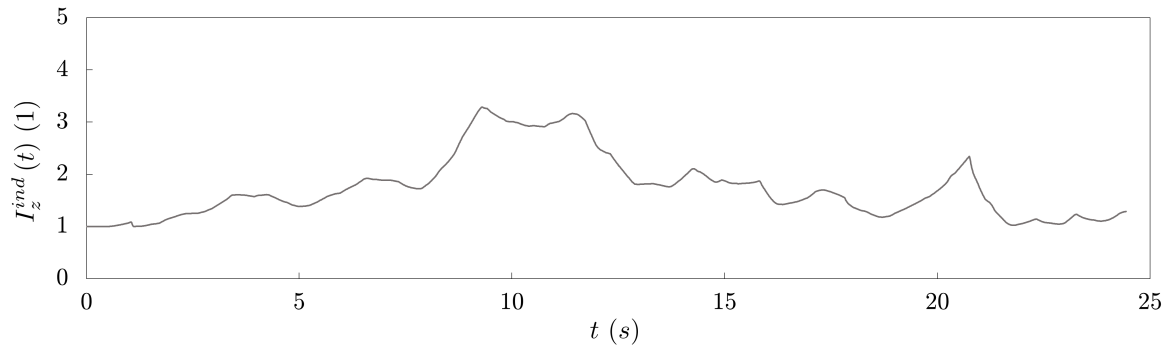
Figure 9.10: Moment-of-inertia index histories of a four block assembly subjected to harmonic excitation with $u_0 = 40$ mm and $f = 1$ Hz

9.7.1.2 Excitation 2 - impact with the sides

The four-block assembly is then subject to excitation with $u_0 = 40$ mm and $f = 2$ Hz, which is shown in Figure 9.11.

As it is seen from the experimental results (Figure 9.11), there is a large number of missing readings as the image processing software Pontos could not utilise the video images, due to either an insufficient resolution or insufficient light. It is also noted that the shaking tables need a lead on time to achieve the desired amplitude for the boundary harmonic motion.
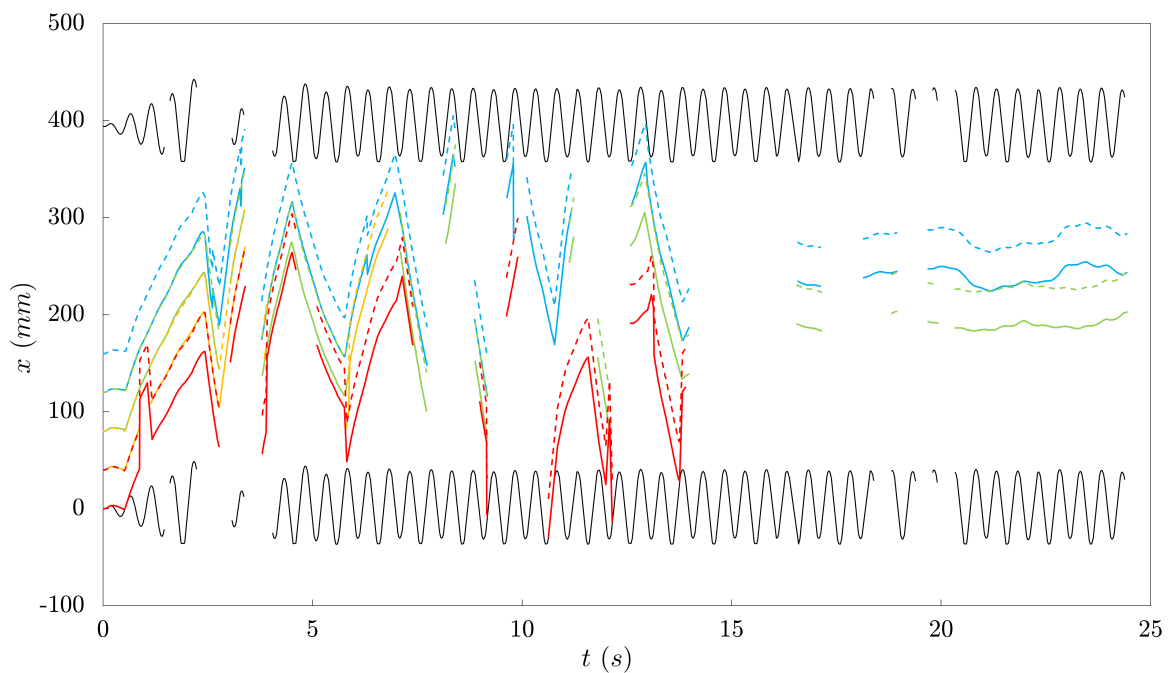
Figure 9.11: Time-histories of the blocks' edges and the container for the case with excitation $u_0 = 40$ mm and $f = 2$ Hz obtained from the experimental data

195

The time-histories in Figure 9.11 indicate that the entire assembly nearly reaches a repeatable pattern in the first part of the analysis, moving largely as one single block

9.7.2 Series B - eight-block assembly

9.7.2.1 Excitation 1 - no impact with the sides

When the eight-block assembly is subject to the excitation with $u_0 = 8$ mm and $f = 4$ Hz, repeatable configuration patterns are noticed neither in the centroid of the whole assembly (Figure 9.13), nor in the moment-of-inertia index (Figure 9.14). This indicate that the assembly mostly moves together as a single body and a low number of inter block impacts is detected. For this problem, the quality of the recorded images allows for the full set of experimental results for Pontos post-processing (Figures 9.12, 9.13 and 9.14).
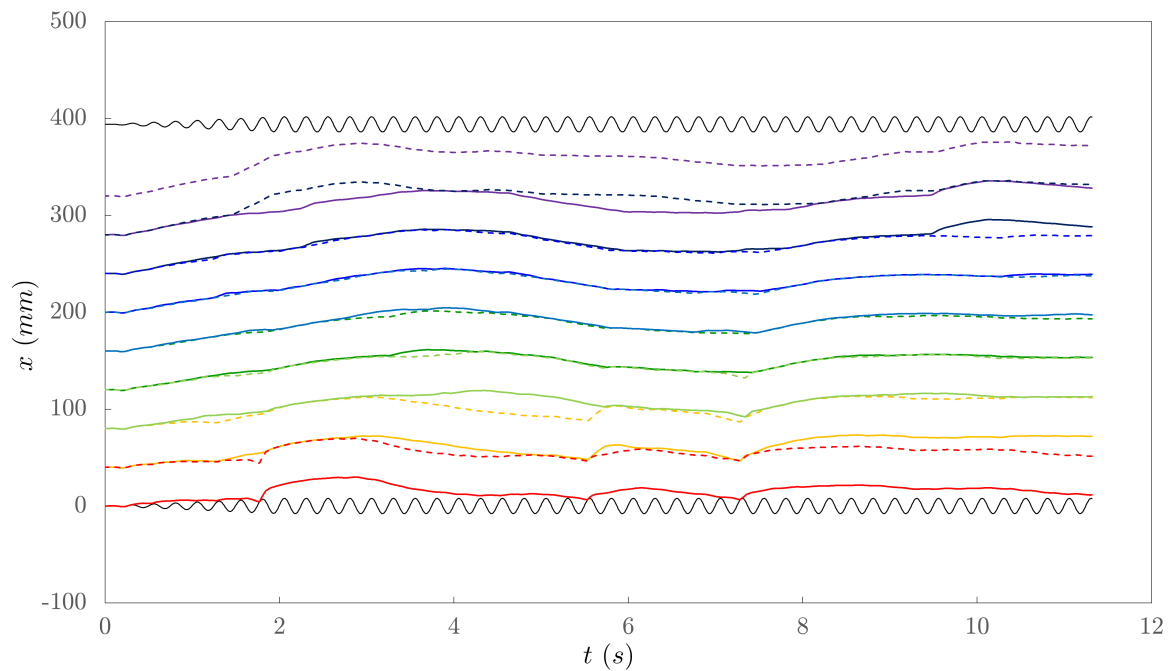
Figure 9.12: Position time histories of an eight-block assembly subjected to harmonic excitation with $u_0 = 8$ mm and $f = 4$ Hz
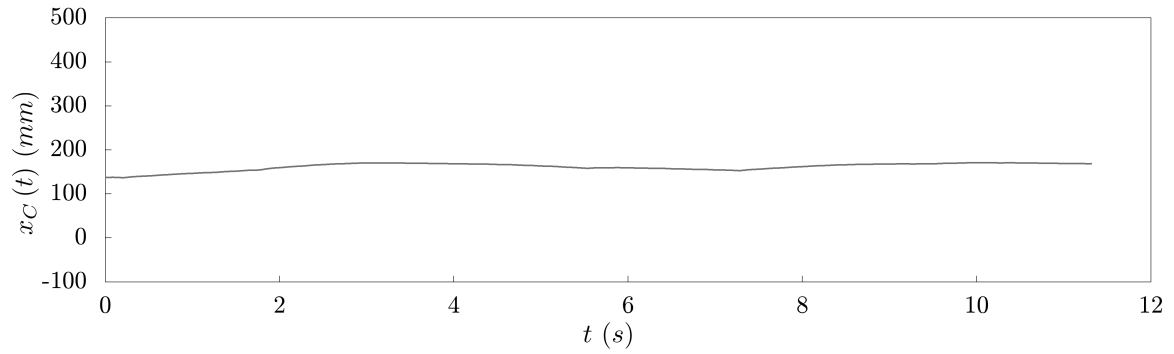
Figure 9.13: Position of the centre of mass time histories of an eight-block assembly subjected to harmonic excitation with $u_0 = 8$ mm and $f = 4$ Hz
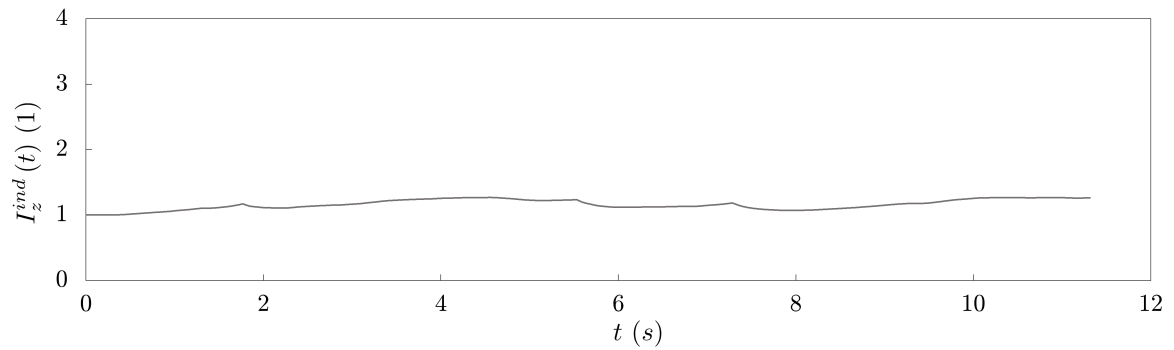
Figure 9.14: Moment-of-inertia index time histories of an eight-block assembly subjected to harmonic excitation with $u_0 = 8$ mm and $f = 4$ Hz

9.7.2.2 Excitation 2 - impact with the base

When the four-block assembly is subject to excitation with $a = 75$ mm and $f = 0.5$ Hz, strong repeatability in the assembly's behaviour is noticed. The quality of the recorded images allows for the full set of experimental results for Pontos post processing, even when the blocks succumb larger velocities (Figures 9.15, 9.16 and 9.17).
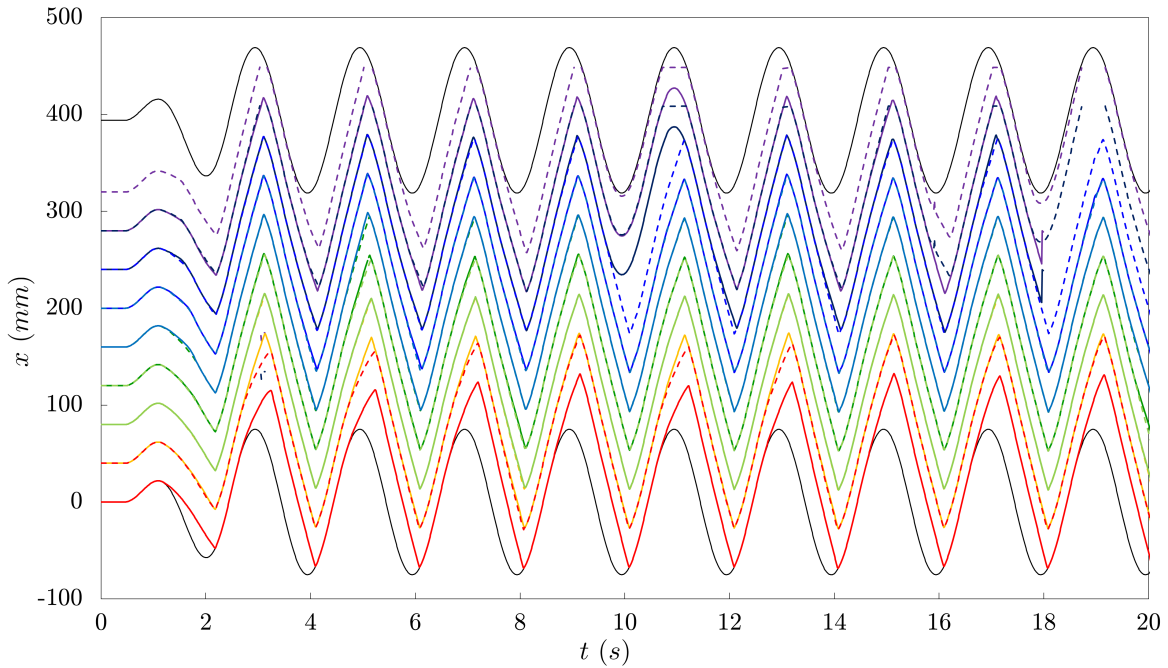
Figure 9.15: Position time-histories of the blocks' edges and the container sides for the case with excitation $u_0 = 75$ mm and $f = 0.5$ Hz

Note again that the boundary trace indicates the very clear rise time before the desired excitation amplitude is reached (see Figure 9.15).

Periodicity also exists in the behaviour of the mass centroid of the assembly (Figure 9.16), as well as in the moment-of-inertia index of the assembly (Figure 9.17).
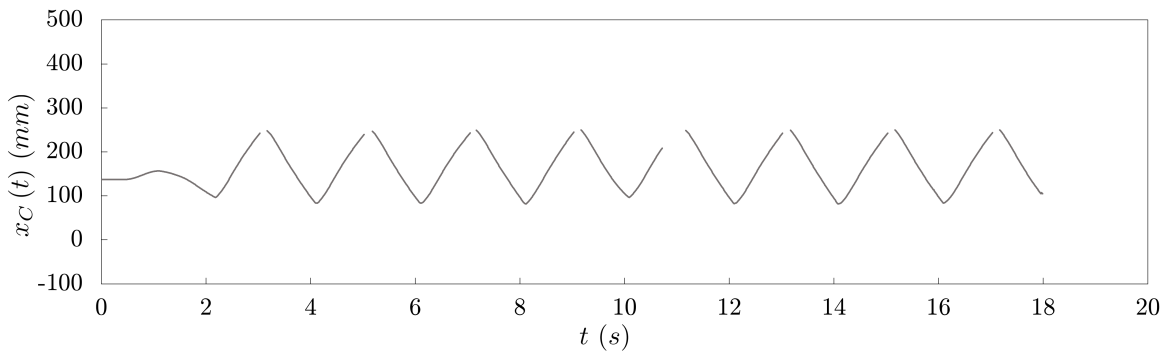
Figure 9.16: Position of mass centroid time-history for the case with excitation $a = 75$ mm and $f = 0.5$ Hz

The time history of the mass inertia index (Figure 9.17) shows a response of the block assembly mainly as one single block, with the inertia index periodically hovering around the value of 1.0. The latter indicates a repeatable behaviour with

198

a large number of inter block impacts, thus exposing a parameter to characterise a possible undesirable event.
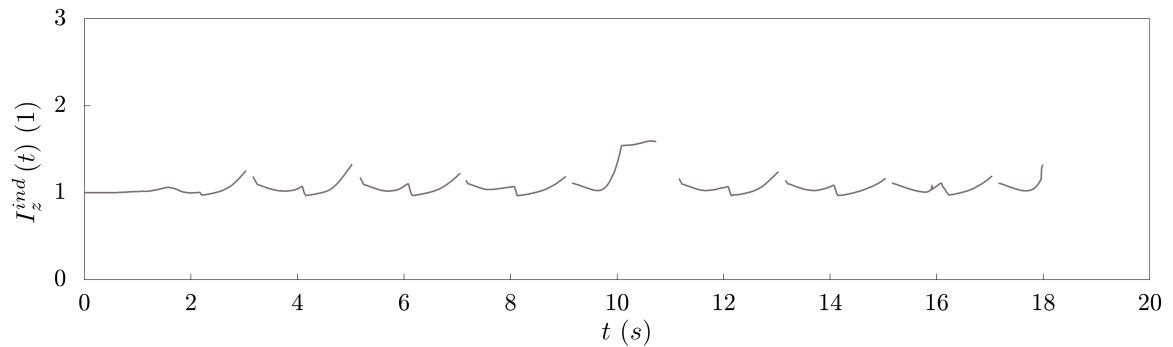
Figure 9.17: Mass inertia index of the assembly time-history for the case with excitation $a = 75$ mm and $f = 0.5$ Hz

9.8   Discussion and conclusion

Several indices characterising the dynamic sensitivity and the asymptotic response pattern formation of an ordered dissipative block assembly are considered in this preliminary study. The characterisation of the multi-block-assembly patterns reveals that for specific conditions a repeatable sustainable assembly response is possible, although very minor changes in the excitation frequency and amplitudes lead to different response patterns (multi block assembly responding as a single block, or the blocks separating and coming together in a repeatable fashion or 'modes').

The presented study has dealt with only one problem geometry, hence it is clearly limited and serves only as an initial exploration. Further studies are needed to generalise the current tentative findings.

Chapter 10

Summary of collected results and conclusions

The results from every chapter along with the conclusions drawn are collected here.

In **Chapter 1** the motivation for the presented research is given. The motivation arises from a set of practical problems to characterise the dynamic behaviour of discontinuous blocky structures, as well as to provide a well-documented set of experimental benchmarks.

In **Chapter 2** an extensive literature review is provided for both rocking of simple blocky structures and self-organisation of ordered blocky assemblies, subject to a given excitation function.

In **Chapter 3** rocking of a single rigid rectangular block is investigated. Free and forced rocking motion are investigated analytically (where applicable), and numerically. A numerical procedure involving the well-known Newmark integration formula for time-stepping, the Newton-Raphson iterative procedure for solving the nonlinear equations of motion, and an own contact detection procedure are developed and tested.

We show that the full geometrical nonlinearity of the rocking problem needs to be taken into account in order to simulate rocking behaviour properly by presenting the differences between the rotation time-histories and stability graphs obtained from the linearised and the nonlinear analysis. The linear and the nonlinear analysis provide similar results for a slender block (slenderness $\frac{h}{b} = 4.5$), but different results for a

201

bulkier block (slenderness $\frac{h}{b} = 1.5$). In the presented case the linearised analysis underestimates the rocking stability of bulky blocks, especially when subject to larger acceleration amplitudes. In general, the nonlinear analysis should be used to assess rocking stability of single blocks.

Furthermore, the equation of motion describing small rotations of bulky blocks, which is thus linear with respect to the unknown rotation, has limited use - it is shown that it can be used only in cases when the block really succumbs only to small rotations. Otherwise, such equation of motion gives a much shorter period of rocking than the fully nonlinear equation of motion.

Last, sensitivity of the rocking problem to perturbation in initial verticality of the block is examined. Here we (again) show that the conditions required to overturn the block change when the block is subject to small initial tilt, thus showing how a small variation in initial conditions can significantly affect the stability.

In **Chapter 4** free rocking motion and the coefficient of restitution defining the energy-loss are investigated. An extensive experimental program conducted is described and combined with the previously presented numerical procedure in order to experimentally obtain a better estimate of the restitution coefficient than those available in the literature. The experimental program involves a non-contact optical measuring system to track the motion of free rocking blocks, and a specifically designed procedure to assure the correct initial conditions (the non-zero initial tilt with a zero initial angular velocity).

It is again experimentally confirmed that Housner's restitution mainly overestimates the energy loss, as reported in previous experiments. An approach to estimate the position of the impact impulse between the block and the base is presented, arising from two sets of experiments: the full- and the specifically designed edge- contact experiments (both with a special system of tapes used to prevent sliding and jumping od the block). The latter set of experiments manages to limit the length of the contact between the block and the base in order to minimise the range of possible positions of the impact impulse. With this position obtained and known, it is shown that the modified restitution formula is a much more suitable estimate of the energy loss in rocking.

Additionally,, it is shown that the position of the impact impulse moves away from the edge with the increase in size for the examined set of samples, which indicates that larger blocks tend to lose less energy during each impact in comparison to the

smaller ones. This indicates that the energy loss (and thus the restitution coefficient) cannot be established independently of the size of the block, thus opening a question of whether the previously used and often-reported dimensionless stability graphs for the rocking problem should be modified so that the real restitution involving the size effect is accounted for. As a result of this research, such stability graphs are obtained and presented.

In **Chapter 5** forced rocking is analysed both numerically, with the help of the algorithm presented in Chapter 3, and experimentally. Two excitation cases are investigated: a constant base acceleration of finite duration, and a single-wave harmonic excitation.

The stability due to a constant acceleration of finite duration is investigated experimentally on an air-track device with a slider (acting as the base) connected to a hanging mass via a string-and-pulley system. This enables achieving a constant acceleration followed by a constant velocity of the base. This set of experiments validates the analytically and the numerically obtained boundaries between translation and rocking behaviour, while it shows a larger overturning area in comparison to the analytically and numerically obtained one.

Following the questions about the size effect to the rocking stability raised in Chapter 4, rocking response of a single block subject to a single sine- and cosine-wave acceleration is investigated numerically, while selected cases are also validated experimentally. Stability graphs due to these excitations for blocks of various slenderness and size are presented, which take into account the restitution coefficients as obtained in the free rocking study in Chapter 4. The experimental program involves a shaking platform to provide the source of excitation combined with the system of tapes to prevent sliding and jumping and assure pure rocking of the block. The experimental results validate the boundary between the area with overturning conditions and the area with no-overturning conditions, especially if the exact restitution for a given geometry of a block is taken into account based on the exact position of the contact impulse (in contrast to the average position of the contact impulse for a given size of the block obtained from a range of slendernesses).

Last, it is (again) experimentally proven that Housner's original restitution should not be used to assess rocking stability for blocks subject to base excitation since it overestimates the real energy loss and does not provide safe enough overturning area.

In **Chapter 6** rocking of a stack consisting of two rigid rectangular blocks is analysed numerically. A numerical procedure involving Newmark's time-stepping scheme, the Newton–Raphson iterative procedure to solve the nonlinear equations of motion, transitions between different configurations of rocking due in various situations, and a contact-detection procedure are developed and tested against available numerical results in the literature.

The equations of motion are derived from Lagrange's equation by defining the potential and kinetic energy of the stack in each of the eight possible rocking configurations. The initiation of 'lower' configurations from a vertical initial state, as well as transitions from 'lower' to 'higher' configurations occurring when a new contact opens are described by presenting the kinematic conditions for transition that need to be satisfied.

The transitions between configurations happening due to an impact between the bodies (either between the two blocks in the stack, or between the top and the bottom block) are treated so that the exact time of each contact is detected, thus enabling us to calculate the exact velocities and accelerations of the system at the end of a configuration, and defining the energy loss during each impact. The energy loss, i.e. the restitution coefficients, for both angular velocities of the blocks, are derived from the angular momentum balance principle with respect to the points acting as the post-impact centres of rotation.

The developed algorithm is run and compared against the available numerical results in the literature, where it is shown that a slightly lower amplitude required to overturn the block is obtained from such numerical procedure than reported in the literature.

In **Chapter 7** the rocking stability of dual-block stacks consisting of two blocks is assessed both numerically (using the developed algorithm presented in Chapter 6), as well as experimentally.

First, stability of the stack subject to a constant base acceleration of finite duration is investigated experimentally on the air track device. It is proven that only total overturning of the stack as a single body occurs when the stack is subject to an instant acceleration, even when this acceleration exceeds the threshold required to initiate rocking of only the top block.

Rocking stability of the dual-block stack subject to a single sine-wave excitation is investigated after that. Stacks with both blocks bulky and both blocks slender,

as well as a slender block on top of a bulky block and a bulky block on top of a slender block are chosen. Conditions for total or partial overturning of the stack are specifically investigated. The results have shown that, for lower excitation frequencies total overturning usually takes place (for a whole range of acceleration amplitudes), while when the frequency is increased partial overturning becomes prevalent. The analysis of the stacks with blocks with different slenderness have shown that, when the slender block is on top of the bulky block, partial overturning is the failure mode that occurs under many of the excitation conditions that would otherwise result in total overturning if the stack of two equal blocks, and especially the stack with bulky block on top of a slender block, were considered.

The experimental program on a seismic platform conducted manages to validate the inner boundary between the overturning and the no-overturning area. On the other hand, the experiments result in rocking in a stable fashion for some of the cases that have numerically resulted in overturning in the smaller area defined by another (outer) boundary.

In **Chapter 8** we proceed with the complex dynamic response of a single block or a stack consisting of three blocks subject to a double-pulse type excitation, which is investigated experimentally. The experimental setup involves a specifically designed device with an impactor, a sliding base (with the block or stack upon it), a stopper (for the counter-impact), and a high-speed camera to track the motion, as well as the excitation of the base. The contact surfaces between the blocks and the base are roughened to reduce sliding, which is, however, not completely prevented. Different modes of overturning (with the emphasis on total and partial overturning) are addressed.

The overturning and no-overturning excitation conditions for the double-pulse-type excitation are given for a single block, as well as for the stack of three blocks. For the stack of three blocks, overturning modes (partial or total overturning) are defined and presented with respect to the excitation parameters.

An attempt is made to scale the results of such excitation, however, without significant success.

Last, overturning modes are investigated in more detail considering the exact timing of the counter-impact in the double-pulse-type excitation. We conclude that this timing plays a significant role in whether total or partial overturning occurs, as well as in whether overturning to the left or to the right side occurs.

In **Chapter 9** the dynamic response od a single block, a horizontal assembly of four blocks and a horizontal assembly of eight blocks inside a rectangular container subject to a 1D harmonic excitation is investigated, as a brief insight into the second class of problems regarding the dynamic characterisation of blocky structures. The system parameters of the whole assembly, such as the mass centroid position and the moment-of-inertia index, are used to characterise the dynamic behaviour of such assemblies, as well as its periodicity.

10.1   Hypotheses

The first hypothesis:

A classical rocking model (the so called inverted-pendulum model) with rotational degrees of freedom can satisfactorily describe rocking behaviour and predict failure conditions of a single block and a dual-block stack

is confirmed both for the single block and for the dual-block stack. The single block model is tested for a variety of base acceleration functions and the numerically obtained results are in very good agreement with the experimentally obtained results, provided that the correct amount of energy-loss is taken into account via s proper coefficient of restitution. The coefficient of restitution is obtained experimentally from an independent set of experiments and it shown that it is affected by the size of the block.

The second hypothesis:

The global parameters such as the moment-of-inertia index and the mass centroid position of a constrained ordered multiple-block assembly enable characterisation of the dynamic response of the assembly

is confirmed. Tracking the time histories and the change of these time histories provides a clear information about the (non)existence of periodicity in the system.

Such periodicity showed to also appear in the the density of the multi-block assembly, so patterns of rarification and densification are addressed.

List of Figures

iv

vi

Bibliography

[1] G. W. Housner, "The behavior of inverted pendulum structures during earthquakes," *Bulletin of the Seismological Society of America*, vol. 53, no. 2, pp. 403–417, 1963.

[2] D. Kalliontzis, S. Sritharan, and A. Schultz, "Improved Coefficient of Restitution Estimation for Free Rocking Members," *Journal of Structural Engineering*, vol. 142, no. 12, 2016.

[3] M. N. Chatzis, M. Garcia Espinosa, and A. W. Smyth, "Examining the Energy Loss in the Inverted Pendulum Model for Rocking Bodies," *Journal of Engineering Mechanics*, vol. 143, no. 5, 2017.

[4] A. Kounadis, G. Papadopoulos, and D. Cotsovos, "Overturning instability of a two-rigid block system under ground excitation," *ZAMM - Journal of Applied Mathematics and Mechanics / Zeitschrift für Angewandte Mathematik und Mechanik*, vol. 92, no. 7, pp. 536–557, 2012.

[5] H. Smoljanovic, Z. Nikolic, N. Zivaljic, and I. Balic, "Stability of rigid blocks exposed to single-pulse excitation," *Acta Mechanica*, vol. 227, pp. 1671–1684, jun 2016.

[6] N. Makris, "A half-century of rocking isloation," *Earthquakes and Structures*, vol. 7, no. 6, pp. 1187–1221, 2014.

[7] L. Dihoru, A. Crewe, C. Taylor, and T. Horgan, "Shaking Table Experimental Programme," in *Modelling and Measuring Reactor Core Graphite Properties and Performance*, 2011.

[8] P. D. Spanos and A.-S. Koh, "Rocking of rigid blocks due to harmonic shaking," *J. Eng. Mech.*, vol. 110, no. 11, pp. 1627–1642, 1985.

1

[9] A. Sinopoli, "Earthquakes and large block monumental structures," *Annali di Geofisica*, vol. XXXVIII, no. 5-6, pp. 737–751, 1995.

[10] B. Shi, A. Anooshehpoor, Y. Zeng, and J. N. Brune, "Rocking and overturning of precariously balanced rocks by earthquakes," *Bulletin of the Seismological Society of America*, vol. 86, no. 5, pp. 1364–1371, 1996.

[11] N. Makris and Y. Roussos, "Response and Overturning of Equipment under Horizontal Pulse-Type Motions," tech. rep., University of California, Berkeley, 1998.

[12] N. Makris and J. Zhang, "Rocking Response and Overturning of Anchored Equipment under Seismic Excitations," tech. rep., University of California, Berkeley, 1999.

[13] N. Makris and J. Zhang, "Rocking Response of Anchored Blocks under Pulse-Type Motions," *Journal of Engineering Mechanics*, vol. 127, pp. 484–493, may 2001.

[14] T. Winkler, K. Meguro, and F. Yamazaki, "Response of rigid body assemblies to dynamic excitation," *Earthquake Engineering & Structural Dynamics*, vol. 24, no. 10, pp. 1389–1408, 1995.

[15] E. Dimitrakopoulos and M. DeJong, "Overturning of Retrofitted Rocking Structures under Pulse-Type Excitations," *Journal of Engineering Mechanics*, vol. 138, no. 8, pp. 936–972, 2012.

[16] E. G. Dimitrakopoulos and A. I. Giouvanidis, "Seismic Response Analysis of the Planar Rocking Frame," *Journal of Engineering Mechanics*, vol. 141, p. 04015003, jul 2015.

[17] E. G. Dimitrakopoulos and T. S. Paraskeva, "Dimensionless fragility curves for rocking response to near-fault excitations," *Earthquake Engineering & Structural Dynamics*, vol. 44, pp. 2015–2033, sep 2015.

[18] M. J. Dejong, *Seismic Assessment Strategies for Masonry Structures*. PhD thesis, Massachusetts Institute of Technology, 2009.

[19] U. Andreaus and P. Casini, "On the rocking-uplifting motion of a rigid block in free and forced motion: influence of sliding and bouncing," *Acta Mechanica*, vol. 138, no. 3-4, pp. 219–241, 1999.

[20] H. Zhang and B. Brogliato, "The planar rocking-block: analysis of kinematic restitution laws, and a new rigid-body impact model with friction," tech. rep., Inria, 2011.

[21] J. Zhang and N. Makris, "Rocking Response of Free-Standing Blocks under Cycloidal Pulses," *Journal of Engineering Mechanics*, vol. 127, no. 5, pp. 473–483, 2001.

[22] N. Makris and D. Konstantinidis, "The Rocking Spectrum and the Shortcomings of Design Guidlines," tech. rep., University of California, Berkeley, 2001.

[23] R. N. Iyengar and C. Manohar, "Rocking response of rectangular rigid blocks under random noise base excitations," *International Journal of Non-Linear Mechanics*, vol. 26, no. 6, pp. 885–892, 1991.

[24] S. J. Hogan, "On the Dynamics of Rigid-Block Motion Under harmonic Forcing," *Proceedings of the Royal Society A: Mathematical, Physical and Engineering Sciences*, vol. 425, no. 1869, pp. 441–476, 1989.

[25] S. J. Hogan, "The Effect of Damping on Rigid Block Motion under Harmonic Forcing," *Proceedings of the Royal Society A: Mathematical, Physical and Engineering Sciences*, vol. 437, no. 1899, pp. 97–108, 1992.

[26] S. J. Hogan, "Damping in rigid block dynamics contained between side-walls," *Chaos Solitons & Fractals*, vol. 11, no. 4, pp. 495–506, 2000.

[27] S. J. Hogan, "Rigid Block Dynamics Confined between Side-Walls," *Philosophical Transactions of the Royal Society A: Mathematical, Physical and Engineering Sciences*, vol. 347, no. May, pp. 411–419, 1994.

[28] E. G. Dimitrakopoulos and M. J. DeJong, "Revisiting the rocking block: closed-form solutions and similarity laws," *Proceedings of the Royal Society A: Mathematical, Physical and Engineering Sciences*, vol. 468, no. 2144, pp. 2294–2318, 2012.

[29] C.-S. Yim, A. K. Chopra, and J. Penzien, "Rocking Response of Rigid Blocks to Earthquakes," *Earthquake Engineering and Structural Dynamics*, vol. 8, pp. 565–587, 1980.

[30] P. D. Spanos, P. C. Roussis, and N. P. a. Politis, "Dynamic analysis of stacked rigid blocks," *Soil Dynamics and Earthquake Engineering*, vol. 21, no. 7, pp. 559–578, 2001.

[31] C. Casapulla, "On the Resonance Conditions of Rigid Rocking Blocks," *International Journal of Engineering and Technology*, vol. 7, no. 2, pp. 760–771, 2015.

[32] Y. Ishiyama, "Motions of Rigid Bodies and Criteria for Overturning By Earthquake Excitations," *Earthquake Engineering & Structural Dynamics*, vol. 10, no. November 1981, pp. 635–650, 1982.

[33] M. Chatzis and A. Smyth, "Modeling of the 3D rocking problem," *International Journal of Non-Linear Mechanics*, vol. 47, pp. 85–98, may 2012.

[34] N. Ogawa, "A Study on Rocking and Overturning of Rectangular Column," tech. rep., National Research Center for Disaster Prevention, 1977.

[35] M. J. N. Priestley, R. J. Evison, and A. J. Carr, "Seismic response of structures free to rock on their foundations," *Bulletin of the New Zealand National Society fro Earthquake Engineering*, vol. 11, no. 3, pp. 141–150, 1978.

[36] F. Peña, F. Prieto, P. B. Lourenço, A. Campos-Costa, and J. V. Lemos, "On the dynamics of rocking motion of single rigid-block structures," *Earthquake Engineering & Structural Dynamics*, vol. 36, no. 15, pp. 2383–2399, 2007.

[37] M. Aslam, D. T. Scalise, and W. G. Godden, "Earthquake Rocking Response of Rigid Bodies," *Journal of the Structural Division*, vol. 106, no. 2, pp. 377–392, 1980.

[38] W. Fielder, L. Virgin, and R. Plaut, "Experiments and simulation of overturning of an asymmetric rocking block on an oscillating foundation," *European Journal of Mechanics, A/Solids*, vol. 16, no. 5, pp. 905–923, 1997.

[39] K. Muto, H. Umemura, and Y. Sonobe, "Study of the overturning vibrations of slender structures," in *Proc. 2nd World Congress Earthquake Engineering*, pp. 1239–1261, 1960.

[40] P. R. Lipscombe, *Dynamics of rigid block structures*. PhD thesis, University of Cambridge, 1990.

[41] J. A. Bachmann, M. Strand, M. F. Vassiliou, M. Broccardo, and B. Stojadinović, "Is rocking motion predictable?," *Earthquake Engineering & Structural Dynamics*, vol. 42, pp. 535–552, oct 2017.

[42] A. I. Giouvanidis and E. G. Dimitrakopoulos, "Nonsmooth dynamic analysis of sticking impacts in rocking structures," *Bulletin of Earthquake Engineering*, vol. 15, pp. 2273–2304, may 2017.

[43] H. Zhang, B. Brogliato, and C. Liu, "Comparisons between numerical and experimental data for the planar rocking-block dynamics Part I: free-rocking," 2011.

[44] V. Acary, "Projected event-capturing time-stepping schemes for nonsmooth mechanical systems with unilateral contact and Coulomb's friction," tech. rep., INRIA, Grenoble - Rhone-Alpes, 2012.

[45] I. N. Psycharis, "Dynamic behaviour of rocking two-block assemblies," *Earthquake Engineering & Structural Dynamics*, vol. 19, no. December 1989, pp. 555–575, 1990.

[46] A. Kounadis, "New findings in the rocking instability of one and two rigid block systems under ground motion," *Acta Mechanica*, vol. 50, no. 9, pp. 2219–2238, 2015.

[47] G. Minafo, L. Stella, and G. Amato, "Rocking Behaviour of Multi-Block Columns Subjected to Pulse-Type Ground Motion Accelerations," *The Open Construction & Building Technology Journal*, vol. 10, pp. 150–157, 2016.

[48] M. J. DeJong and E. G. Dimitrakopoulos, "Dynamically equivalent rocking structures," *Earthquake Engineering & Structural Dynamics*, vol. 43, pp. 1543–1563, aug 2014.

[49] N. Makris and M. F. Vassiliou, "Planar rocking response and stability analysis of an array of free-standing columns capped with a freely supported rigid beam," *Earthquake Engineering & Structural Dynamics*, vol. 42, no. 3, pp. 431–449, 2013.

[50] M. Demesthenous and G. C. Manos, "Dynamic response of rigid bodies subjected to horizontal base motions," in *Earthquake Engineering, Tenth World Conference*, (Rotterdam), pp. 2817–2821, 1992.

[51] F. Peña and A. Campos-costa, "Experimental dynamic behavior of free standing multi- block structures under seismic loadings," pp. 1–39, 1992.

[52] R. J. Y. Greenbaum, A. W. Smyth, and M. N. Chatzis, "Monocular Computer Vision Method for the Experimental Study of Three-Dimensional Rocking Motion," *Journal of Engineering Mechanics*, vol. 142, no. 1, 2016.

[53] S. Luding, E. Clément, A. Blumen, J. Rajchenbach, and J. Duran, "Studies of columns of beads under external vibrations," *Physical Review E*, vol. 49, pp. 1634–1646, feb 1994.

[54] G. Lumay, S. Dorbolo, O. Gerasymov, and N. Vandewalle, "Experimental study of a vertical column of grains submitted to a series of impulses," *The European Physical Journal E*, vol. 36, p. 16, feb 2013.

[55] N. Čeh and G. Jelenić, "Rocking motion of a single rigid rectangular block analysis of the block slenderness assumption," in *Proceedings of the 8th International Congress of Croatian Society of Mechanics*, 2015.

[56] N. M. Newmark, "A method of computation for structural dynamics," *Journal of the Engineering Mechanics Division*, vol. 85, no. 3, pp. 67–94, 1959.

[57] S. C. Chapra and R. P. Canale, *Numerical methods for engineers.* McGraw Hill Education, 2015.

[58] N. Čeh, G. Jelenić, and N. Bićanić, "Analysis of restitution in free rocking of single rigid rectangular block," *Acta Mechanica (online first)*, 2018.

[59] V. Pickerd, "Optimisation and Validation of the ARAMIS Digital Image Correlation System for use in Large-scale High-strain-rate Events.," tech. rep., Maritime Division, Defence Science and Technology Organisation, Victoria, 2013.

[60] G. Jelenić, N. Čeh, and N. Bućanić, "Rocking of single and dual rigid-block systems subject to ground excitation: experimental and computational analysis of overturning conditions," in *Proceedings of the 25th Conference on Computational Mechanics*, pp. 244–247, 2017.

[61] N. Čeh and G. Jelenić, "Rocking stability of rigid prismatic blocks during single-wave harmonic excitation: numerical investigation and experimental validation," *Experimental Techniques (submitted)*, 2018.

[62] D. A. Wells, *Schaum's outline of theory and problems of Lagrangian dynamics, with a treatment of Euler's equations of motion, Hamilton's equations and Hamilton's principle.* Schaum Pub. Co, 1967.

[63] E. L. Wilson, *Three-Dimensional Static and Dynamic Analysis of Structures.* Berkeley: Computers and Structures, Inc., third edit ed., 2002.

[64] N. Čeh, J. F. Camenen, N. Bićanić, A. Pellegrino, and N. Petrinić, "Overturning of multiple-block stacks - dynamic sensitivity parameters and scaling effect," *International Journal of Masonry Research and Innovation*, vol. 1, no. 4, p. 351, 2016.

[65] M. Qamaruddin, B. Chandra, and A. S. Arya, "Dynamic testing of brick building models," vol. 77, no. 3, pp. 353–365, 1984.

[66] N. Bićanić, J. F. Camenen, N. Čeh, and T. Koziara, "Characterisation of pattern formation in constrained multiblock assembly subjected to horizontal harmonic excitation," *International Journal of Masonry Research and Innovation*, vol. 1, no. 4, p. 375, 2016.

Nina Čeh

Born on 16 June 1989 in Rijeka, Croatia. Attended high school in Buzet from 2004 to 2008. Attended Faculty of Civil Engineering at the University of Rijeka from 2008 to 2013 and received a bachelor (*magna cum laude*) and a master's (*suma cum laude*) degree. The master's thesis titled *Transient Response of Plate Structures to Excitation Induced by Human Movement* was awarded for the best master's thesis in Civil engineering, Structural engineering by the Association of Croatian Civil Engineering Faculties.

Briefly after graduation, entered the postgraduate doctoral study programme in Civil Engineering and started working full-time as a teaching and research assistant at the Faculty of Civil Engineering, University of Rijeka.

Participated in the scientific projects *Evidence Based Characterisation of Dynamic Sensitivity for Multiblock Structures – Computational Simulation and Experimental Validation*, financed by the Unity Through Knowledge Fund under the supervision of Prof. Nenad Bićanić, and *Configuration-dependent Approximation in Non-linear Finite-element Analysis of Structures*, financed by the Croatian Science Foundation under the supervision of Prof. Gordan Jelenić.

During 2015 and 2016 spent three months at the Impact Engineering Laboratory, University of Oxford under the supervision of Prof. Nikica Petrinić.

List of Publications

[1] N. Čeh and I. Žigo, "Strength parameters of the flysch rock mass from the Pazin Paleogene Flysch Basin, Istrian Peninsula, Croatia", *Proceedings of the International Summer Conference of Civil Engineering Students ISUCCES*, 2013.

[2] N. Čeh and N. Bićanić, "Study of periodicity in non-smooth dynamic behavior of solid block due to harmonic excitation", *Proceedings of the 6th meeting of the Croatian Society of Mechanics*, 2014.

[3] N. Čeh and N. Lustig, "Beskontaktno mjerenje pomaka i deformacija pri statičkim i dinamičkim laboratorijskim ispitivanjima", *Proceedings of the Conference of young researchers Zajednicki temelji*, 2014.

[4] N. Čeh, A. Pellegrino, J.-F. Camenen, N. Petrinić, G. Jelenić, T. Koziara, and N. Bićanić, "Dyanmic sensitivity of multi-block stacks subjected to pulse base excitation – Experimental evidence and non-smooth contact dynamics simulations", *Proceeding of the 5th International Conference COMPDYN*, 2015.

[5] J.-F. Camenen, N. Čeh, N. Bićanić, and T. Koziara, "Dynamic Sensitivity of a Multi-block Stack Subjected to Horizontal Harmonic Excitation", *Proceedings of the 22^{emme} Congres Francais de Mechanique*, 2015.

[6] J.-F. Camenen, N. Čeh, N. Petrinić, G. Jelenić, T., Koziara, and N. Bićanić, "Dynamic Sensitivity of a Multi-block Assembly Subjected to Horizontal Harmonic Excitation", *Proceedings of the 8th International Congress of Croatian Society for Mechanics*, 2015.

[7] N. Čeh, A. Pellegrino, J.-F. Camenen, N. Bićanić, N. Petrinić, and M. Tuhtan, "Overturning of multiple-block stack – synamic sensitivity parameters and scaling effect", *Proceedings of the 8th International Congress of Croatian Society for Mechanics*, 2015.

[8] N. Čeh and G. Jelenić, "Rocking motion of a single rigid rectangular block – analysis of the block slenderness assumption", *Proceedings of the 8th International Congress of Croatian Society for Mechanics*, 2015.

[9] N. Čeh and N. Bićanić, "Djelomično prevrtanje slobodno položenog blokovskog stupca pri dinamičkoj pobudi", *Zbornik radova 7. susreta Hrvatskoga društva za mehaniku*, 2016.

[10] N. Čeh, N. Bićanić, J.-F. Camenen, A. Pellegrino and N. Petrinić, "Overturning of multiple-block stacks – dynamic sensitivity parameters and scaling effect", *International Journal of Masonry Research and Innovation*, vol. 1, no. 4, pp. 351-374, 2016.

[11] N. Bićanić, J.-F. Camenen, N. Čeh and T. Koziara, T., "Characterisation of pattern formation in constrained mutliblock assembly subjected to horizontal harmonic excitation", *International Journal of Masonry Research and Innovation*, vol. 1, no. 4, pp. 375-397, 2016.

[12] N. Čeh, I. Hlača, S. Dobrilla, G. Jelenić and N. Bićanić, "Eksperimentalna i numerička dinamička analiza grednih nosača pod utjecajem nejednolike potresne pobude oslonaca", *Zbornik radova Osmog susreta Hrvatskoga društva za mehaniku*, 2017.

[13] N. Čeh, L. Theophile, G. Jelenić and N. Bićanić, "Prevrtanje stupca od dva bloka uslijed konstantnog i impulsnog ubrzanja podloge", *Zbornik radova Osmog susreta Hrvatskoga društva za mehaniku*, 2017.

[14] N. Čeh, G. Jelenić and N. Bićanić, "Rocking of single and dual rigid-block systems subjected to free rocking and constant ground acceleration of finite duration: equations of motion and contact detection", *Proceedings of the 3rd International Conference on Multiscale Computational Methods for Solids and Fluids* 2017.

[15] S. Dobrilla, N. Čeh, M. Tuhtan and G. Jelenić, "Experimental analysis of structure response to non-uniform support excitation", *Zbornik radova Građevinskog fakulteta u Rijeci, Knjiga XX*, 2017.

[16] N. Čeh, G. Jelenić and N. Bićanić, "Analysis of restitution in rocking of single rigid blocks", *Acta Mechanica (online first)*, 2018.

[17] N. Čeh and G. Jelenić, "Rocking stability of rigid prismatic blocks during single-wave harmonic excitation: numerical investigation and experimental validation", *Experimental Techniques (submitted)*